12-15-2016

Fundamental Parameters of Eclipsing Binaries in the Kepler Field of View

Rachel A. Matson

FUNDAMENTAL PARAMETERS OF ECLIPSING BINARIES
IN THE *KEPLER* FIELD OF VIEW

by

RACHEL A. MATSON

Under the Direction of Douglas R. Gies

ABSTRACT

Accurate knowledge of stellar parameters such as mass, radius, effective temperature, and composition inform our understanding of stellar evolution and constrain theoretical models. Binaries and, in particular, eclipsing binaries make it possible to measure directly these parameters without reliance on models or scaling relations. In this dissertation we derive fundamental parameters of stars in close binary systems with and without (detected) tertiary companions to test and inform theories of stellar and binary evolution. A subsample of 41 detached and semi-detached short-period eclipsing binaries observed by NASA's *Kepler* mission and analyzed for eclipse timing variations form the basis of our sample. Radial velocities and spectroscopic orbits for these systems are derived from moderate resolution optical spec-

tra and used to determine individual masses for 34 double-lined spectroscopic binaries, five of which have detected tertiaries. The resulting mass ratio M_2/M_1 distribution is bimodal, dominated by binaries with like-mass pairs and semi-detached classical Algol systems that have undergone mass transfer. A more detailed analysis of KIC 5738698, a detached binary consisting of two F-type main sequence stars with an orbital period of 4.8 days, uses the derived radial velocities to reconstruct the primary and secondary component spectra via Doppler tomography and derive atmospheric parameters for both stars. These parameters are then combined with *Kepler* photometry to obtain accurate masses and radii through light curve and radial velocity fitting with the binary modeling software ELC. A similar analysis is performed for KOI-81, a rapidly-rotating B-type star orbited by a low-mass white dwarf, using UV spectroscopy to identify the hot companion and determine masses and temperatures of both components. Well defined stellar parameters for KOI-81 and the other close binary systems examined in this dissertation enable detailed analyses of the physical attributes of systems in different evolutionary stages, providing important constraints for the formation and evolution of close binary systems.

INDEX WORDS: astronomy, binaries, binaries: eclipsing, binaries: spectroscopic, stars: fundamental parameters, stars: evolution, stars: individual (KIC 5738698), stars: individual (KOI-81)

FUNDAMENTAL PARAMETERS OF ECLIPSING BINARIES IN THE *KEPLER* FIELD OF VIEW

by

RACHEL A. MATSON

A Dissertation Submitted in Partial Fulfillment of the Requirements for the Degree of

Doctor of Philosophy

in the College of Arts and Sciences

Georgia State University

2016

FUNDAMENTAL PARAMETERS OF ECLIPSING BINARIES
IN THE *KEPLER* FIELD OF VIEW

by

RACHEL A. MATSON

Committee Chair:	Douglas R. Gies
Committee:	Todd J. Henry
	Harold A. McAlister
	Guillermo Torres
	Russel J. White
	Joshua S. Von Korff

Electronic Version Approved:

Office of Graduate Studies

College of Arts and Sciences

Georgia State University

December 2016

ACKNOWLEDGMENTS

Special Thanks goes to:

My advisor Doug Gies, who was always full of new ideas and projects to challenge me and excite my curiosity. His guidance and confidence in me has made me the researcher I am today.

To my classmates and colleagues: Stephen Williams, Zhao Guo, Saida Caballero-Nieves, Travis Fischer, Joe Eggen, Jeremy Maune, Emily Bowsher, Jen Winters, Nic Scott, and everyone else. Thank you for the lessons in both life and astronomy, I will cherish the time we spent together at Georgia State.

To the other members of my dissertation committee, who provided endless encouragement and the occasional lesson in letting off steam along this journey: Russel White, Hal McAlister, Guillermo Torres, and especially Todd Henry.

To my family, especially my parents, who instilled in me a love of science and astronomy, who taught me I could do anything, and who loved and supported me throughout this long journey.

To my husband, who I don't think knew what he was getting into when he signed on, but who became my rock and biggest supporter through all the ups and down the last few years.

TABLE OF CONTENTS

LIST OF TABLES

LIST OF FIGURES

CHAPTER 1
INTRODUCTION

Stars are fundamental to our understanding of the Universe. Their structure and evolution dictate energetic processes that shape the interstellar medium, feedback processes in galaxy evolution, and the overall chemical enrichment history of the Universe. In order to understand such processes we need to understand stars and how they interact with their environments. It is therefore vital to have accurate knowledge of stellar parameters such as mass, radius, luminosity, composition, and age. Accurate knowledge of these parameters allows us to develop models of star formation and evolution in order to understand the physical processes within stars and how they interact with the interstellar medium. Binary stars and, in particular, eclipsing binaries are the primary source of fundamental stellar parameters as they make it possible to measure directly stellar properties without reliance on models or scaling relations. While such fundamental astrophysics has been overshadowed by cutting edge research into cosmological questions concerning dark energy, black holes, and how the Universe began as well as the hunt for habitable planets and life in the Universe, there are few areas in modern astronomy that do not rely to some extent on our knowledge of the basic properties of stars.

In addition, binary stars make up approximately half of all Sun-like stars, with more massive stars more likely to have companions (Raghavan et al. 2010; Duchêne & Kraus 2013). Binaries, therefore, represent a significant portion of the stellar populations in both our Galaxy and others, and are particularly important in understanding star formation.

Studies of their intrinsic parameters, such as mass and orbital period, can reveal the angular momentum contained in such systems, constraining formation and evolution scenarios for binary stars as well as single stars and planetary systems. Furthermore, the variety of components found in binaries, including stellar, sub-stellar, variable, peculiar, and evolved stars, allows such objects to be thoroughly studied in ways which might not otherwise be possible.

1.1 Eclipsing Binaries

1.1.1 Observational Characteristics

An eclipsing binary consists of two stars whose orbit is aligned in such a way that the stars periodically pass in front of one another along our line of sight, temporarily blocking a portion of the total light from the system, as demonstrated in Figure 1.1. Eclipsing binaries are typically too far away to resolve the individual stars, so the brightness variation is the primary way these objects are identified and studied. By recording the changes in brightness over time and determining the periodicity of the eclipses the *light curve*, a graph of brightness variation versus orbital phase (ϕ), can be classified and analyzed. The timing and durations of the eclipses contain information about the shape and orientation of the binary orbit, while the eclipse depth and duration provides information about the relative sizes of the stars and their flux ratio. Stellar radii, relative to their separation, are estimated from the duration of a total eclipse using the following times (in units of fractional phases): start of eclipse ingress (ϕ_1), start of total eclipse (ϕ_2), end of total eclipse (ϕ_3), and end of eclipse egress

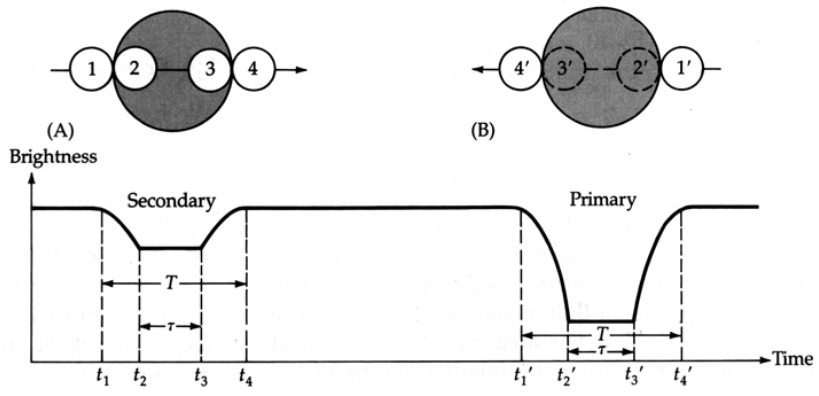

Figure 1.1: Diagram depicting the orientation and resulting light curve of an eclipsing binary. Times of ingress (t_1), total eclipse beginning (t_2), total eclipse end (t_3), and egress (t_4) represent the same times given in fractional phases (ϕ) in the text. [From `http://ircamera.as.arizona.edu/astr_250/images/ecl_bin1.gif`]

(ϕ_4). For a circular orbit we can then derive the radius of the smaller, transiting star (R_2) from

$$(\phi_2 - \phi_1) = (\phi_4 - \phi_3) = 2R_2/(2\pi a) \tag{1.1}$$

and the radius of the larger, occulting star (R_1) as

$$(\phi_3 - \phi_1) = (\phi_4 - \phi_2) = 2R_1/(2\pi a), \tag{1.2}$$

where a is the separation between the stars (Hilditch 2001). The fractional radii (R/a) are then related to the inclination (i) and eclipse duration (e.g. $\phi_{1,4}$) by

$$\cos^2 i + \sin^2 i \sin^2 \phi_{1,4} = (R_2/a)^2(1 + R_1/R_2)^2 \tag{1.3}$$

and

$$\cos^2 i + \sin^2 i \sin^2 \phi_{2,3} = (R_2/a)^2(R_1/R_2 - 1)^2. \tag{1.4}$$

In order for eclipses to appear i must be near 90°, which serves as an additional constraint on the system geometry. However, if the orbit is significantly eccentric the durations of the two eclipses will differ, as the orbital speeds of the two stars change with orbital phase, and the phase of the secondary will not be at $\phi = 0.5$ relative to the primary eclipse. If information about the stars' motions is also available, such as with radial velocity measurements, it is possible to deduce the scale of the system and measure the absolute radius for each star.

In addition to the stellar sizes and orientation of the binary, light curves depend on physical proximity effects between the two stars. One of the most accurate approximations of the geometry of binary systems is the Roche model, in which stellar shapes are determined by the equipotentials they fill if the orbit is assumed to be circular and the gravitational field generated by the two stars is like that of two point masses (Iben & Livio 1993). Depending on the ratio of stellar radius to Roche radius, close binaries are classified into three distinct groups (Kopal 1955). *Detached binaries* are systems where neither star fills its Roche lobe and the stars have not interacted via mass transfer. These stars are therefore effectively gravitationally bound single stars that have evolved independent of one another, making them ideal for studying the properties of individual stars and testing models of stellar evolution. Typical detached binaries consist of relatively spherical stars[1], so that as they orbit each other the out-of-eclipse light remains fairly constant, resulting in essentially flat-topped

[1]Fast-spinning stars may be flattened at the poles, as well as stars that fill their Roche lobes.

light curves. When both stars are spherical and move in a circular orbit, the depth of the eclipses is primarily due to the temperature difference between the two stars because the amount of surface area eclipsed at both eclipses must be the same. Therefore, more light is lost when the hotter component with larger surface intensity is eclipsed, resulting in a deeper eclipse, referred to as the primary eclipse throughout this dissertation. As the width of the eclipses is a function of the sizes of the individual stars and the orbital inclination of the system, when stars fill a larger portion of their respective Roche lobes their shapes begin to distort because of gravitational tidal forces, causing them to elongate. This causes the out-of-eclipse light to vary due to the amount of light we receive from the varying stellar cross-section.

Semi-detached binaries occur when one star entirely fills its Roche lobe while the other star remains bound within a separate equipotential surface. Such systems are created when the more massive component in a close binary evolves faster, increasing in radius until it fills its Roche lobe. As the star continues to expand it will overflow the critical surface, transferring mass to its companion through the inner Lagrangian point. The smaller, secondary star accretes much of the mass lost by the primary and becomes the more massive component. The binary then consists of an evolved low-mass star (usually a sub-giant) orbiting a more massive, early-type main sequence star and is known as an *Algol* system after the eclipsing binary Algol, which consists of a B8 main-sequence star and a K2-type sub-giant (Hilditch 2001).

When both stars fill their Roche lobes, the binaries are called *contact* or *overcontact*

systems as they are in contact with each other at the inner Lagrangian point. The stars typically possess disparate temperatures and continuously varying light levels as they are both distorted from spheres.

1.1.2 Deriving Stellar Parameters

Equations characterizing the orbits, stellar surfaces (via the Roche model), and radiative properties of two stars in a close binary (Kopal 1959; Lucy 1968) allowed researchers to produce models that explained the light curves of non-spherical stars with non-uniform distributions of surface brightness orbiting a common center of mass. Modern methods of light curve analysis, called *light curve synthesis*, use such models to produce a synthetic light curve for the binary in question, adjusting input parameters until the model matches the observations, allowing physical parameters of the system to be derived. Theoretical models include all known physical processes that define the temperature of surface elements across a star as well as the geometrical effects of the orientation of the orbit and resulting visibility of different stellar regions. Typically, the specific intensity of radiation emitted by a star is approximated by the Planck function evaluated for the effective temperature of the star. This intensity varies across the stellar surface based upon the angle at which the radiation leaves the photosphere, known as *limb darkening*. Limb darkening is described by one of several relations, either linear, quadratic, root-square, logarithmic, or a 4-coefficient law, with coefficients for these relations tabulated for stars of various temperatures, gravities ($\log g$), and chemical compositions in numerous bandpasses (e.g., Claret & Bloemen 2011). The models also calculate the tidal deformation and resulting *gravity darkening* of the component

stars. Gravity darkening occurs when a rapidly rotating star becomes distorted, with the equatorial radius becoming larger than the polar radii. This results in the poles of the star, when compared to the equatorial regions, having higher $\log g$ values so that the polar regions are characterized by higher temperatures and larger fluxes. So, compared to a slowly rotating star, the poles will appear gravity brightened while the equator appears gravity darkened.

The Wilson-Devinney (WD) code (Wilson & Devinney 1971) is the most successful and widely-used light curve synthesis program, and it has been extensively expanded and improved upon over the years (e.g. Wilson & Sofia 1976; Wilson 1979, 1990; Milone et al. 1992; Kallrath et al. 1998; VanHamme & Wilson 2003). More recently Prša & Zwitter (2005) developed PHOEBE (PHysics Of Eclipsing BinariEs), a modeling package for eclipsing binary stars built on top of the WD program that incorporates observational spectra of eclipsing binaries into the solution-seeking process, extraction of individual temperatures from observed color indices, main sequence constraints, and numerical innovations, including improved minimization algorithms, heuristic scans, and parameter kicking to escape from local minima. PHOEBE also includes both a graphical user interface and back-end scripter which have made it a popular tool for the analysis of eclipsing binaries.

The Eclipsing Light Curve (ELC) code of Orosz & Hauschildt (2000) further advanced the development of light curve modeling by directly incorporating model stellar atmospheres to describe the specific intensity on the surface of a star, eliminating the need for blackbody approximations and analytical limb darkening laws. More recent incarnations of the WD code have since adopted this technique, and now use models of stellar atmospheres as inputs

(van Hamme & Wilson 2003). ELC uses a grid of photometric bandpass-integrated intensities (standard Johnson filters) at various temperatures, $\log g$'s, and emergent angles to assign an intensity for the surface elements of each star. Model light (and radial velocity) curves are then computed via Roche geometry using one of several optimizers to reduce iteratively a chi-squared function and find the best global solution between the model and observations. Details of our use of ELC to derive stellar and orbital parameters, including inclination, relative stellar radii, temperature ratio, eccentricity, and longitude of periastron from *Kepler* data can be found in Section 4.4.

1.2 Spectroscopic Binaries

1.2.1 Observational Characteristics

Binary systems exhibiting periodic shifts of their spectral lines due to the Doppler effect are known as spectroscopic binaries. The orbital motion about the center-of-mass of a binary results in line-of-sight or radial motion that manifests as the periodic displacement of the spectral lines. A binary system where the Doppler shifted spectral features of only one component are observed is known as a *single-lined spectroscopic binary* (SB1). If spectral features from both components are detected, then the system is a *double-lined spectroscopic binary* (SB2). Figure 1.2 shows the double-lined spectrum of one of the stars targeted in this work, KIC 5738698, with the spectral features of each component shifted in opposite directions during phases of maximum velocity separation.

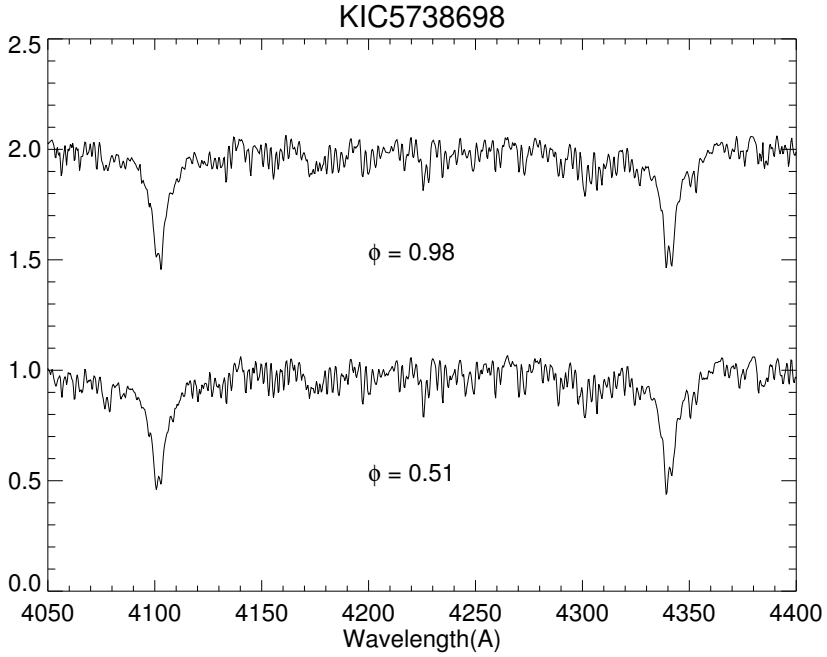

Figure 1.2: Spectra of the double-lined spectroscopic binary KIC 5738698 depicting double-lines due to the doppler shift of both components in opposite directions at quadrature phases. Both spectra have been normalized in flux, with the top spectrum offset for clarity. See Chapter 4 for more details.

The observed radial velocity due to orbital motion is given by the relation

$$V = K\left[\cos(\theta + \omega) + e\cos\omega\right] + \gamma, \tag{1.5}$$

where θ is the true anomaly, an angular coordinate that describes the location of the star in its orbit relative to the closest approach at periastron, ω is the longitude of periastron, which describes the orientation of the periastron location relative to the plane of the sky, e is the orbital eccentricity, and γ is the radial velocity of the center of mass or *systemic velocity* of the binary relative to our Solar System. The velocity semi-amplitude, K, is given by

$$K_{1,2} = \frac{2\pi a_{1,2} + \sin i}{P\sqrt{1-e^2}} \tag{1.6}$$

where $a_{1,2}$ is the fractional semi-major axis of the orbit for each component, i is the orbital inclination, and P is the orbital period. More details and a full derivation are available in Chapters 2 and 3 of Hilditch (2001).

1.2.2 Deriving Stellar Parameters

By measuring the radial velocities of binary stars we can therefore derive orbital elements that define the binary orbit in space as the radial velocity is a function of K, e, ω, T, P, and γ (with P and the reference epoch T entering the equation via the true anomaly, θ). In practice, the orbital elements are determined by fitting a Keplerian orbit to the radial velocity measurements via an iterative least-squares technique. This requires a set of observations that are well distributed in orbital phase and cover the phases of velocity maximum and minimum known as *quadrature* phases.

For a single-lined spectroscopic binary, the information about the binary orbit from a single radial velocity curve can be combined with Kepler's Third Law to derive the binary mass function in solar masses, which when rewritten using Newton's laws of gravity and the relation $m_1/m_2 = K_2/K_1$, is

$$f(m) = \frac{m_2^3 \sin^3 i}{(m_1 + m_2)^2} = 1.036149 \times 10^{-7} (1 - e^2)^{3/2} K_1^3 P, \tag{1.7}$$

with the orbital velocity semi-amplitude K in km s^{-1} and the period P in days (Hilditch 2001). The projected semi-major axis, $a_{1,2} \sin i$, can also be derived directly from the semi-amplitude via

$$a_{1,2} \sin i = \frac{(1 - e^2)^{1/2}}{2\pi} K_{1,2} P. \tag{1.8}$$

For a double-lined spectroscopic orbit where the velocity curves of both components can be determined from observations, the individual minimum masses and the projected semi-major axis can be derived from

$$m_{1,2} \sin^3 i = 1.036149 \times 10^{-7} (1 - e^2)^{3/2} (K_1 + K_2)^2 K_{2,1} P \tag{1.9}$$

and

$$a \sin i = 1.976682 \times 10^{-2} (1 - e^2)^{1/2} (K_1 + K_2) P, \tag{1.10}$$

where the orbital velocity semi-amplitudes K are in km s^{-1}, the orbital period P is in days, the masses m are in solar masses, the orbital semi-major axis a is in solar radii, and i is the inclination in degrees (Torres et al. 2010). Inclination is defined to be 90° when the plane of the orbit is in the line of sight of the observer (i.e., edge-on). Therefore, assuming the orbit is edge-on in the above relations results in the derivation of minimum values for the mass and semi-major axis of the binary system. The true masses and semi-major axis can only be determined if the inclination of the binary system is known from the projected orbit of a visual binary or from the light curve of an eclipsing binary.

1.3 Fundamental Stellar Parameters

The most basic physical properties of a star are its mass, radius, effective temperature, luminosity, and chemical composition. These characteristics allow us to describe generally the formation, evolution, and death of any star. The determination of fundamental stellar properties is a classic discipline in astronomy that enabled the characterization of stars and

led to the discovery of correlations between stellar parameters that provide insight into their internal structures. The crucial role of binaries in measuring physical properties of stars is difficult to overstate. While some stellar parameters can be inferred from spectroscopy, population studies, and evolutionary modeling, the direct determination of the mass of any astronomical object requires measurable gravitational interaction between at least two observable objects. Binary stars are therefore the main source of stellar mass measurements, as the gravitational force between the two components is proportional to the product of their masses. However, as shown above, the inclination must be known to derive the actual masses and scale of the system from spectroscopy. We also noted how the favorable alignment between the line of sight and the orbital plane of eclipsing binaries allows for the determination of the orbital inclination, relative radii, and temperature ratio but cannot provide the absolute dimensions of the binary. Therefore the full determination of absolute eclipsing binary parameters requires both a light curve and a radial-velocity curve for each component. Masses and radii determined via double-lined eclipsing binaries do not rely on any external data or calibrations and are therefore vital to linking observations, theories of stellar structure and evolution, and stellar atmosphere models.

Double-lined eclipsing binaries have long been the primary source of fundamental parameters for stars and continue to provide increasingly accurate results ($\lesssim 3\%$) with improved instruments and techniques. However, similar advances have enabled other methods for deriving fundamental parameters to reach comparable accuracies ($\lesssim 5\%$). For example, long-baseline interferometry and direct imaging can determine the astrometric orbit of the

secondary relative to the primary star for spatially resolved binaries. When combined with double-lined spectroscopic binaries, the absolute masses of both stars can be determined as well as the luminosity (e.g., Boden et al. 2006; Baines et al. 2016). If radial velocities are only available for one component, independent knowledge of the trigonometric parallax is needed to derive individual masses for both stars (Torres 2014). Long-baseline interferometry can also yield very precise measurements of stellar radii, effective temperatures, and absolute luminosities of the stars using trigonometric parallaxes and measured bolometric fluxes (e.g., Berger et al. 2006; Boyajian et al. 2012), but are usually only available for single stars. In addition, asteroseismology, the study of stellar interiors via their natural oscillation frequencies, can be used to determine fundamental parameters for stars with solar-like oscillations. For oscillations driven by surface convection, the average frequency separation and frequency of maximum oscillation power can be tied to the mass and radius of a star through solar-scaled asteroseismic relations (Rawls et al. 2016). These asteroseismic scaling relations, together with the star's effective temperature, provide an estimation of the radius, mass, mean density, and surface gravity independent of stellar evolutionary theory and binary modeling (Chaplin & Miglio 2013). Comparisons with interferometry and eclipsing binaries find radius estimates from asteroseismology are precise within a few percent, though the masses are less precise (Epstein et al. 2014). Advances in such techniques have steadily improved their contributions to our knowledge of accurate fundamental parameters, testing and enhancing those derived from double-lined eclipsing binaries.

Perhaps the most important application of such precise measurements of stellar parame-

ters is to improve our understanding of stellar structure and stellar evolution, as the combination of observational characteristics and correlations with theoretical expressions governing the pressure, density, and energy production and transport within a star have allowed astronomers to develop an understanding of stellar internal structure and create theoretical stellar models. The determination of stellar properties therefore informs our understanding of stars as a whole, with new and accurate fundamental properties providing the means to test and update models of stellar structure and evolution.

Much of the progress in understanding stars has come from constructing theoretical models of their structure and evolution, and comparing the predicted results with observations. Stellar models should, for an input mass and chemical composition, be able to describe the radius, effective temperature, and internal structure of a star at a given age using various parameterizations to describe the physical processes in the star's interior. Determining whether or not the adopted treatments are adequate requires comparisons between model outputs and observations of real stars (Andersen 1991).

For two stars in the same binary, their individual masses and radii must be fit by models with the same initial composition and age[2]. Further constraints may be added with knowledge of additional stellar parameters such as effective temperature and chemical composition of the stars, as well as their rotational velocities and interstellar reddening. The most informative comparison of stellar models with real stars is obtained when the mass, radius, temperature, and chemical composition are accurately known for both stars in a binary system. Furthermore, if the stars differ significantly in mass and degree of evolution, fitting

[2]Assuming that the stars formed together simultaneously and have not been externally affected since.

both stars simultaneously for a single age provides a more stringent test of the models. Such comparisons are limited to detached binaries because the components can be expected to have evolved as if they were single.

Beyond simple comparisons with models, stars with highly accurate parameters allow the affects of main-sequence evolution and chemical composition on the masses and radii of main-sequence stars to be studied, as well as tests of stellar structure calculations with different treatments of physical effects like opacity and energy transport (Andersen 1991). Accurate determinations of fundamental stellar parameters can also expose the importance of additional physical parameters like rotational velocity, and begin to constrain exposed shortcomings in models due to simplistic treatments of processes including mass loss and convective efficiency. Furthermore, such data allow for the derivation of empirical relationships between fundamental stellar parameters that provide good estimates of masses and radii for single stars with reliable determinations of $T_{\rm eff}, \log g$, and metallicity (Torres et al. 2010).

While semi-detached binaries cannot be compared to theoretical stellar evolution models of single stars, evolutionary models that take into account the influence of a companion can be compared to astrophysical parameters of evolved systems. If a binary has one component filling its Roche lobe, such as an Algol system, it means the system has passed through at least one stage of mass transfer or mass loss from one or both components. Binary evolutionary models must therefore incorporate the limited volume of a star's Roche lobe and changes in mass, angular momentum, separation, and period of the two stars that are a consequence

of mass exchange (Hilditch 2001). Few Algols have precisely determined masses and other parameters, but comparison with binary evolutionary models and analysis of their general properties have shown that non-conservative mass and angular momentum transfer/loss are necessary to explain their present properties (Giuricin et al. 1983).

1.4 Eclipsing Binary Research

Binary stars have been studied for more than two centuries, yet the number of systems with accurate masses and radii make up only a small percentage of the many thousands of known eclipsing binaries (Torres 2014). The determination of stellar masses and radii with accuracies of $\lesssim 3\%$ can lead to much greater astrophysical insight than merely improving mean mass and radii relations. Early reviews of the field by Popper (1967, 1980) listed only two and seven systems, respectively, with masses known to 3% or better. A significant effort by Danish astronomers in the 1970's increased the number dramatically, resulting in 45 binaries known to better than 3% for the next review by Andersen (1991). Since then, improvements in observational techniques and the analysis of eclipsing binaries have more than doubled the number of well studied systems (95) in the latest review (Torres et al. 2010). However, the number of systems with empirically determined stellar parameters still represents a tiny fraction of the known eclipsing binaries.

More recent studies have used improved observational and analysis techniques to consistently derive accurate radial velocities that lead to masses and radii with errors less than $1 - 3\%$. Many such efforts have concentrated on systems with unequal mass components

(Garcia et al. 2014), low-mass stars (Torres et al. 2014a), red giants (Hełminiak et al. 2015), and evolved stars sensitive to the treatment of convective overshooting (Clausen et al. 2010a; Torres et al. 2014b) in order to explore and quantify uncertainties and mismatches with current models. Detailed chemical analyses from high resolution spectra (Brogaard et al. 2011; Torres et al. 2015) are also being used to better determine stellar ages, while eclipsing binaries are providing distance determinations to nearby clusters (Southworth et al. 2007; Rozyczka et al. 2014).

By far the biggest impact on modern eclipsing binary science, however, has been the advent of large-scale photometric surveys. Such surveys have provided thousands of newly discovered eclipsing binaries in a wide range of environments including the Galactic Bulge (e.g., Soszyński et al. 2015), Galactic Disk (e.g., Pietrukowicz et al. 2013), and Magellanic Clouds (e.g., Muraveva et al. 2014; Kim et al. 2014), useful for determining statistical properties of binaries and finding rare systems. In addition to large numbers of new eclipsing binaries, the space-based missions CoRoT[3] (COnvection, ROtation and planetary Transits) and *Kepler* (Borucki et al. 2010) have produced light curves of unprecedented accuracy, with regular sampling of 1 s to 29 m, extending over time spans of months, and with very high duty cycles (Maceroni et al. 2012). In this work, we take advantage of the data from *Kepler*, in particular, to target intermediate mass eclipsing binaries.

[3]The CoRoT space mission was developed and is operated by the French space agency CNES, with participation of ESA's RSSD and Science Programmes, Austria, Belgium, Brazil, Germany, and Spain; complete information is available at `http://corot.oamp.fr`

1.4.1 Impact of Kepler

NASA's *Kepler* mission was specifically designed to find Earth-size planets by continuously monitoring more than 150,000 stars to detect transiting planets via unparalleled photometric precision. A byproduct of the mission is the discovery and monitoring of thousands of variable stars, more than 2800 of which are eclipsing binaries, representing 1.3% of all observed *Kepler* targets (Prša et al. 2011; Slawson et al. 2011; Kirk et al. 2016). The photometric accuracy and essentially uninterrupted observations have revolutionized the study of eclipsing binaries through the surge in data quality, detection efficiency, interpretation possibilities, and the ability to confront theoretical predictions with detailed observations (Prša et al. 2012). Individual systems consisting of detached binaries (e.g., Yakut et al. 2015; Matson et al. 2016), low-mass stars (e.g., Ofir et al. 2012; Bass et al. 2012), and red-giants (e.g., Gaulme et al. 2013; Beck et al. 2014), have provided accurate mass and radius measurements in addition to probing our understanding of proximity effects and intrinsic stellar variability. *Kepler* has also opened a new window into stellar interiors via asteroseismology, with pulsating eclipsing binaries enabling the determination of stellar parameters by two independent methods (e.g. Southworth et al. 2011; Lehmann et al. 2013; Maceroni et al. 2014; Guo et al. 2016) as well as the discovery of heartbeat stars (Thompson et al. 2012), a subclass of eccentric ellipsoidal variables, many with tidally induced pulsations (e.g. Maceroni et al. 2009; Hambleton et al. 2013; Smullen & Kobulnicky 2015). The sensitivity and long time span of *Kepler* observations have further enabled the search for triple stellar systems via multiple transits (e.g. Carter et al. 2011b; Alonso et al. 2015) and periodic variations in

the eclipse times (Gies et al. 2012; Conroy et al. 2014; Zasche et al. 2015; Gies et al. 2015; Borkovits et al. 2016), as well as the discovery of circumbinary planets (Doyle et al. 2011; Welsh et al. 2012; Orosz et al. 2012; Kostov et al. 2016).

However, the wealth of new systems and ultra-precise data have illuminated deficiencies in even the best models used to describe the physical and geometric properties of binaries. State-of-the-art models, including the WD code, PHOEBE, and ELC, show systematics for a range of binary light curves partly due to approximations embedded in the models and partly due to missing and/or inadequate physics that have yet to be accounted for, hindering the reliability and scope of binary star solutions (Prša et al. 2012). ELC has begun to address the characteristics of *Kepler* data and the additional astrophysical phenomena detected in the light curves by including specific intensities from the *Kepler* bandpass, data smoothing to match the long cadence interval of 29.4244 minutes, and enabling faster computation times for immense datasets, as well as accounting for aperture contamination and Doppler boosting (see Section 4.4.2.2). PHOEBE, meanwhile, is undergoing a massive redevelopment[4] to allow for high-precision modeling of new observables and increased physics.

1.5 Motivation and Goals

One of the many opportunities created by *Kepler* was the long term monitoring of binary eclipses for periodic perturbations caused by a third star. An eclipsing binary with a tertiary companion will orbit the common center-of-mass, slightly changing the line-of-sight distance the light from the binary travels, causing a delay in the eclipse arrival time known as the

[4] `http://phoebe-project.org`

light travel time effect (LTTE) or Roemer delay. If the third star is in an eccentric or inclined orbit, additional dynamical perturbations to the inner binary orbit can also cause changes in the eclipse arrival times. Detection of changes in the eclipse times of binaries has been successfully used in the past to infer the presence of third bodies from the ground (summarized in Pribulla & Rucinski 2006), however the observations are usually intermittent. *Kepler*, on the other hand, supplied nearly continuous observations of more than 2800 eclipsing binaries for 3.5 years. This led to a targeted study of 41 eclipsing binaries in the *Kepler* data set to search for tertiary companions via eclipse timing by Gies et al. (2012, 2015). The main goal of this dissertation is to characterize these 41 systems to constrain and inform formation and evolutionary scenarios for short-period/close binaries.

While there have been great strides in theories of star formation, we do not yet fully understand the circumstances and dynamics involved, especially in the formation of binary and higher order stellar systems. The preferred mechanism for producing the wide range of observed binary systems is fragmentation of a collapsing molecular cloud (Bate 2015). There are two main ways fragmentation can occur to form binary and multiple star systems, including large scale fragmentation due to structure in a gravitationally unstable cloud and smaller scale disk fragmentation (Tobin et al. 2016). When a protostellar binary first forms via fragmentation it is usually embedded in a massive envelope of infalling molecular gas from which it accretes to reach its final mass. As the system grows in mass, its mass ratio, separation, and eccentricity will change (Bate & Bonnell 1997). The final state of the binary therefore depends on the accretion of, and interaction with, the remaining cloud material

as it falls on the system. The most important quantity in determining the final state of the system is the specific angular momentum of the accreted material relative to the binary (Bate 2015). If the specific angular momentum of the gas is much less than that of the binary, the mass ratio and orbital separation of the binary will decrease. The infalling gas will also be preferentially accreted by the primary as the material falls to the center of mass of the system, nearest the primary. For gas with a specific angular momentum greater than that of the binary, the binary separation increases and the secondary accretes more than the primary, driving the system toward equal mass components (Bate 1997). This implies that binaries with medium to large separations are expected to exhibit a wide range of mass ratios, whereas close binaries are more likely to have mass ratios near unity as closer systems are expected to receive a greater fraction of their initial mass from high angular momentum accretion during formation. However, while fragmentation has been shown to readily create wide binaries there are severe difficulties with fragmentation producing close binaries directly (Bate et al. 2002). In particular, close binary systems ($P \lesssim 7\,\mathrm{d}$) cannot have formed in their current configurations as the protostellar radii would be too large to fit inside their present day orbits (Rappaport et al. 2013). Theoretical studies, however, suggest that a significant number of close binaries have a distant tertiary companion that could provide a natural mechanism, through the eccentric Kozai-Lidov mechanism (Fabrycky & Tremaine 2007; Naoz 2016), for the initially wide binary to lose angular momentum and shrink to its current state. Observational evidence of such systems has been found by Pribulla & Rucinski (2006), Tokovinin et al. (2006), Raghavan et al. (2010), and Zakirov (2010). By

determining fundamental parameters of this sub-sample of short-period eclipsing binaries, both with and without (detected) tertiary companions, this work will provide insight into the characteristics, dynamics, and evolution of such systems.

1.5.1 Outline

This chapter reviewed the utility of photometric and spectroscopic observations of binaries and how they are used to measure directly stellar properties capable of testing and refining theoretical stellar evolution models. It has also motivated the need for detailed studies of double-lined eclipsing binaries in short-period systems as well as the suitability of *Kepler* for such a project. In Chapter 2 we will take a closer look at the 41 binaries on which this project is based and detail the steps necessary to process the *Kepler* light curves. A quick summary of the eclipse timing results of Gies et al. (2012, 2015) is also presented. Chapter 3 presents a spectroscopic study of all 41 binaries in the sample, including obtaining and reducing the data as well as determining radial velocities and spectroscopic orbits for each system, followed by an analysis of the results. Building on the spectroscopic work, Chapter 4 details the binary modeling of the radial velocities and light curve of KIC 5738698, a detached binary consisting of two F-type main sequence stars with an orbital period of 4.8 days, including comparisons with stellar models. These results also appear in the *Astronomical Journal* by Matson et al. (2016). Chapter 5 presents a similar analysis of KOI-81, a B-type star orbited by a subdwarf discovered via *Kepler* observations. This chapter encompasses work contributed by several co-authors and published by Matson et al. (2015) in the *Astrophysical Journal*. Finally, Chapter 6 discusses additional directions for this project and the impact

of such work, before concluding with a summary of the main results of this dissertation.

CHAPTER 2
KEPLER LIGHT CURVES OF ECLIPSING BINARIES

2.1 Sample Selection

The 41 systems studied in this dissertation constitute a sample of eclipsing binaries selected for observation with *Kepler* in order to measure the eclipse arrival times of each system and to look for light travel time variations that may indicate the presence of a tertiary companion. This project began as a *Kepler* Guest Observer program with 20 eclipsing binaries observed in the first cycle, and 40 and 41 binaries in the second and third cycles, respectively. Most systems were identified as eclipsing binaries prior to the launch of *Kepler* and were selected from the All Sky Automated Survey (Pigulski et al. 2009), the Hungarian-made Automated Telescope Network (HATNet) survey (Hartman et al. 2004), Vulcan survey (Borucki et al. 2001; Mjaseth et al. 2007), and early *Kepler* results (Prša et al. 2011). To facilitate the measurement of eclipse times, detached and semi-detached systems with 'pristine' light curves and deep primary eclipses (> 0.2 mag) were chosen. Furthermore, as the goal of this project was to search for tertiary companions, which have been shown to be plentiful around short-period binaries (Tokovinin et al. 2006), only eclipsing binaries with periods less than seven days were considered. The final sample consists of systems with orbital periods of $0.6 - 6$ days. As the primary goal for *Kepler* was to identify planets in the habitable zones of main-sequence stars, the target field in Cygnus was chosen to optimize the number of main-sequence (primarily G-type stars) stars brighter than 16th magnitude (Batalha et al. 2010). Because of this, and our need for stars bright enough for ground-based optical spectroscopy,

our targets have primary star effective temperatures in the range $5200-11000\,\mathrm{K}$ according to the *Kepler* Input Catalog (the result of an extensive campaign to classify millions of stars in the *Kepler* field of view that includes stellar magnitudes, effective temperatures, and surface gravities; Brown et al. 2011), corresponding to B through G spectral types. The *Kepler* Input Catalog number (KIC), alternate ID, and *Kepler* magnitude (K_p) for each system are given in Table 3.3.

2.2 *Kepler* Data

The *Kepler* spacecraft was launched in 2009 with the primary goal of searching for Earth-size exoplanets in the habitable zones of late-type main-sequence stars using the transit method. The scientific objectives of the mission closely dictated the spacecraft design and data characteristics, requiring observations of one region of sky encompassing a large number of stars, carefully selected to provide an appropriate density of target stars, continuously for the life of the mission. To satisfy these requirements, the on-board photometer consists of 42 charge-coupled devices (CCDs) that collect data over a 105° field of view (FOV), with 'postage stamp' regions defined around each target so only the desired pixels are collected. A set integration time of 6.54 seconds (including readout) is used to prevent saturation, then co-added into long and short cadence data sets of 29.4244 minutes and 58.8488 seconds, respectively (Gilliland et al. 2010). Approximately $170,000$ targets can be observed in long cadence (LC) mode and up to 512 in short cadence (SC) mode depending on the desired science. Data are collected in quarters corresponding to spacecraft rolls that occur

approximately every three months (93 days) to maintain optimal solar panel illumination and ensure the radiator is pointed away from the Sun (Haas et al. 2010). Each quarter, new apertures are defined due to the 90° roll and to re-prioritize targets observed for exoplanet detection as well as asteroseismology, astrometry, and the guest observer program.

After nearly four years of observations, two of *Kepler*'s reaction wheels failed, resulting in the inability to point at the same field of view as precisely as necessary. The telescope has since been repurposed as *K2* to continue precision photometry for a wider variety of science cases in regions of the sky distributed along the ecliptic plane. For this dissertation, however, we use data from the original *Kepler* mission corresponding to Quarters $0 - 17$ (Q0−Q17; 2009 May 2 – 2013 May 8). The eclipse timing campaign of Gies et al. (2012, 2015) was a Guest Observer program that began with 20 targets in the first cycle ($Q2 - 5$) before being expanded to all 41 systems ($Q6 - 13$), guaranteeing observations of these systems for most of the original mission. Long cadence data are therefore available from Quarter $0 - 17$ for a majority of the eclipsing binaries, with minor gaps typically due to spacecraft outages or failing CCDs. Short cadence data also exist for some of the systems but are not routinely included in this work.

Data collected by *Kepler* are processed and calibrated through the *Kepler* Science Pipeline[1] and available at the Mikulski Archive for Space Telescopes (MAST[2]). The pipeline converts raw data numbers, pixel locations, and ancillary engineering data into calibrated counts and astrometric coordinates. The counts within each aperture are then summed to create

[1] `http://keplerscience.arc.nasa.gov/pipeline.html`
[2] `http://archive.stsci.edu/kepler/`

calibrated light curves, with adjustments made to estimate and subtract background light as well as cosmic ray hits on the detectors. Additional processing of the calibrated light curves applies a series of corrections based on known instrumental and spacecraft anomalies as well as artifacts found in the data. This final step (Pre-search Data Conditioning, PDC) prepares the light curves for a numerical search for candidate planetary transit events, ideal for detecting planets, but which can interfere with the signal of an eclipsing binary. Since we want to preserve the eclipses, we use the light curves output from simple aperture photometry (SAP) in the previous step and correct for varying flux levels in the data ourselves. To do so, data from each quarter were binned according to the number of bins that gave the minimum scatter in out-of-eclipse phases, and a cubic spline was fit through the mean of the upper 50% of each section. The light curve was then divided by the spline fit and outliers between eclipses greater than 3σ from the out-of-eclipse median magnitude were removed. The detrended light curves from each quarter were then combined into a single light curve per target.

This method adequately removes the large scale trends found within and between quarters due to the systematic trends and instrumental artifacts inherent in *Kepler* data. It does not completely account for jumps, drifts, and outliers, but does mitigate their effects while maintaining the binary signature. The eclipse timing analysis by Gies et al. (2012, 2015) further normalized the light curves to unity at the maximum between eclipses, resulting in the varying flux levels having little influence on the eclipse times. To model the light curves and derive system parameters for an eclipsing binary (see Section 4.2.1) we phase fold the

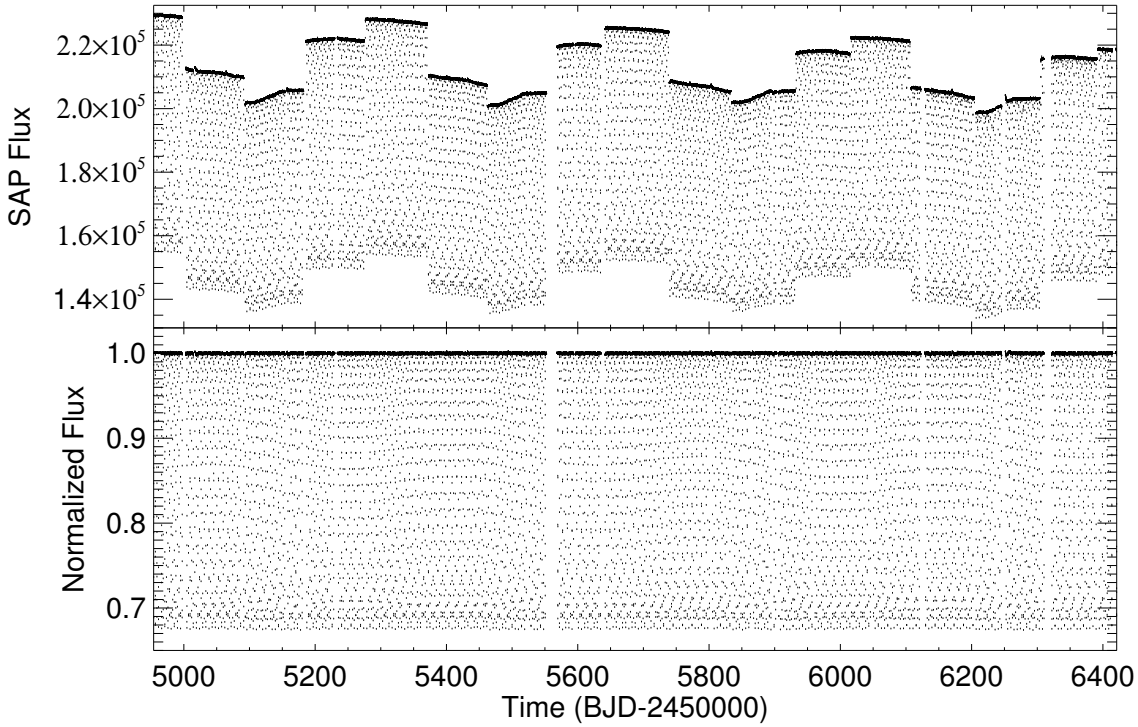

Figure 2.1: Top: the SAP light curve of KIC 5738698 from Q0 to Q17, showing the changes in flux levels between quarters. Bottom: the detrended and normalized light curve.

light curve, which should randomize any remaining artifacts and merely add to the overall scatter of the residuals. An example of the SAP and detrended light curves for KIC 5738698 are shown in Figure 2.1.

2.3 *Kepler* Light Curves

Figure 2.2 depicts detrended, phased light curves for KIC 3241619 and 4665989 in terms of *Kepler* magnitudes. While the precision and uninterrupted observations of *Kepler* are evident in the light curves, many exhibit varying flux levels due to spacecraft settling, time-dependent light losses from the target flux falling out of the pixel apertures, contamination

of neighboring sources moving around within the pixel apertures, and variations based on the nature of the binary (discussed below). Binned light curves for all 41 systems are shown in Figure 2.3 to depict clearly the characteristics of each light curve and reduce the number of plotted points. We note that KIC 4678873 was listed as an eclipsing binary by the ASAS and HATNET surveys and was included in the *Kepler* Eclipsing Binary Catalogs of Prša et al. (2011) and Slawson et al. (2011). However, subsequent analysis revealed it to be a 'false positive' in which the variations in its light curve are caused by a neighboring eclipsing binary, believed to be KIC 4678875, five arc seconds north and slightly fainter than KIC 4678873 (Rowe et al. 2015). The light curve of this object suffers from large flux variations throughout and between quarters due to the inconsistent flux contributions from KIC 4678875. The PyKE6[3] software was therefore used to extract the flux of this target using a larger aperture that included both stars (Gies et al. 2015). The final light curve is plotted in Figure 2.3 as KIC 4678875.

Despite being chosen for their pristine light curves and similar characteristics, there is considerable variety among the light curves. The most obvious features are the eclipse depths, with most systems showing either approximately equal eclipses or one deep and one shallow eclipse. By convention, the deeper eclipse is known as the primary and occurs when the hotter component is eclipsed. Unequal eclipses usually indicate a large temperature difference between the two stars. The eclipses themselves can contain additional information about the shape and orientation of the binary beyond the conditions necessary for eclipses. For instance, if an eclipse has a 'flat-bottom' or interval of constant brightness, it indicates a

[3] `http://keplerscience.arc.nasa.gov/software.html`

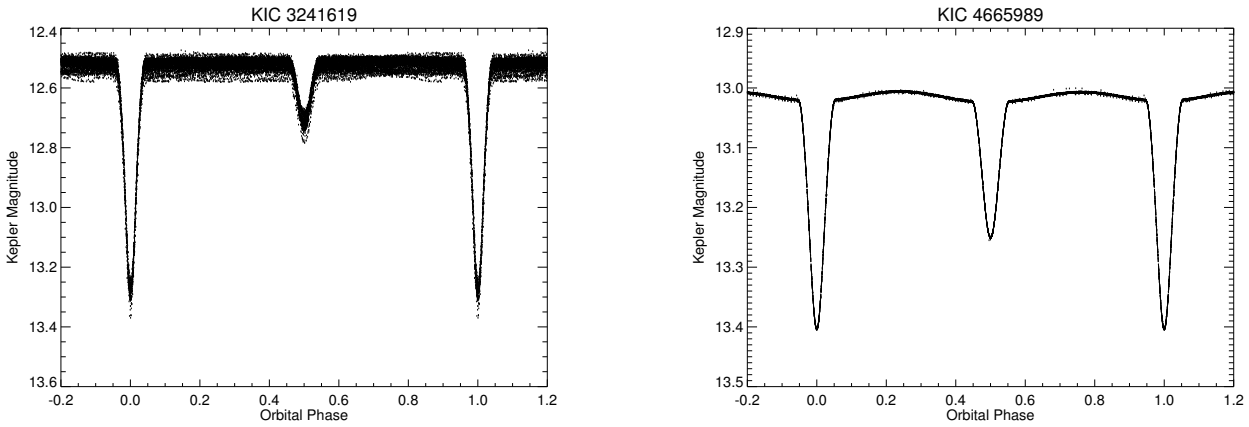

Figure 2.2: Detrended, phased light curves for KIC 3241619 and 4665989 in terms of *Kepler* magnitudes. The light curve of KIC 3241619 is strongly modulated by starspots, while KIC 4665989 has slight variations indicative of pulsations.

total eclipse where the stars fully overlap. In this case the duration of the minima provides directly the relative size of the eclipsed star, while the depth indicates the total amount of light it contributes to the system, providing stricter constraints for determining binary parameters. The light curves of KIC 10661783 and 10686876 both show total eclipses.

The effect of the system geometry on the light curve can also be seen when the stars are in non-circular orbits, as the position of the secondary eclipse relative to the primary is displaced and the durations of the eclipses may differ. The displacement of the secondary eclipse from the circular-orbit value of $\phi = 0.5$ depends on the orbital eccentricity e and the longitude of periastron ω as demonstrated in the light curves of KIC 4544587 and 8196180, where the secondary eclipses occur at $\phi \approx 0.65$ and $\phi \approx 0.40$, respectively.

Another prominent feature in the light curves of these systems is the shape of the region between eclipses. As noted earlier, in detached systems with nearly spherical stars the amount of light received from each component is constant throughout the orbit, resulting

in a flat out-of-eclipse light curve such as those seen in KIC 3241619, 3327980, 4848423, 5738698, 10156064, and 10686876. When one or both stars fill a larger portion of their Roche lobes and elongate due to tidal forces, the out-of-eclipse portion of the light curve is no longer constant. This distortion of the light curve, historically called *ellipsoidal variation* due to early efforts to model the light curve with ellipsoids, is periodic with half the orbital period resulting in a 'bump' between eclipses. This effect can be mild as in KIC 2305372, 4665989, and 5444392 or more pronounced as the stars become more tidally distorted as in KIC 4660997, 6206751, and 9592855. Additional modulations in the out-of-eclipse region can be caused by the *reflection effect* due to radiation from the hotter star heating the facing hemisphere of the cooler star and creating a region of enhanced brightness. The effect is periodic with the orbital period and peaks when the heated hemisphere of the cooler star is in the line-of-sight ($\phi = 0.5$ in circular systems), demonstrated in the light curve of KIC 7368103 where the flux around the secondary eclipse is greater than that around the primary eclipse.

Intrinsic variations of one or both components can also affect the appearance of an eclipsing binary light curve, causing increased scatter as the changes in brightness occur on timescales that differ from the orbital period. Pulsations caused by radial and non-radial monements of a star's surface result in rapid flux variations most easily seen outside of eclipse. Oscillations in Sun-like stars are typically small and fast and cannot be resolved with *Kepler* long cadence data as variability gets averaged over $\sim$30 min. However, evidence of pulsations with large amplitudes can be visible in long cadence light curves, as in

KIC 4665989 (Fig. 2.2). Slight variations due to pulsations can also be seen in the binned light curves of KIC 4851217, 6206751, 7368103, 9159301, 10486425, and 10619109. Studying the oscillation frequencies of pulsating stars or *asteroseismology* can also determine accurate parameters of stars through knowledge of their interior structures. As stated in Chapter 1, *Kepler* has enabled the discovery and analysis of a wide variety of pulsating stars through short cadence (Sun-like stars) and long cadence (classical variables and evolved stars) and the derivation of masses and radii via asteroseismology. Many of the stars in this sample exhibit radial and non-radial pulsations on shorter timescales, including KIC 10661783, analyzed by Southworth et al. (2011) and Lehmann et al. (2013), and KIC 9851944, studied by Guo et al. (2016). Pulsational analyses of more systems are underway (e.g. KIC 8262223; Guo et al. in prep.) but are, in general, beyond the scope of this dissertation.

Stars with temperatures $T_{\rm eff} \lesssim 6500\,K$ also experience starspot activity that results in brightness variations outside of eclipse due to changes in the surface intensity and center of

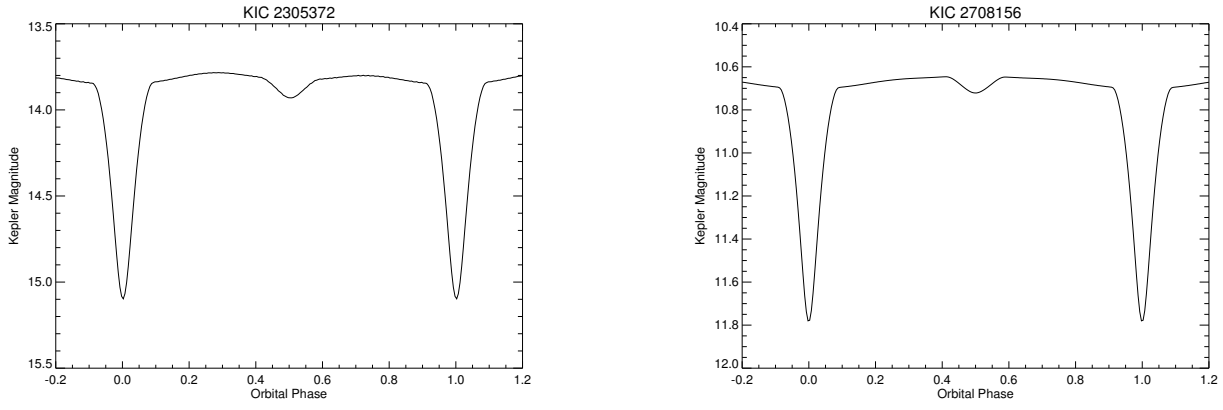

Figure 2.3: Binned, phased light curves for all 41 eclipsing binaries in terms of *Kepler* magnitudes.

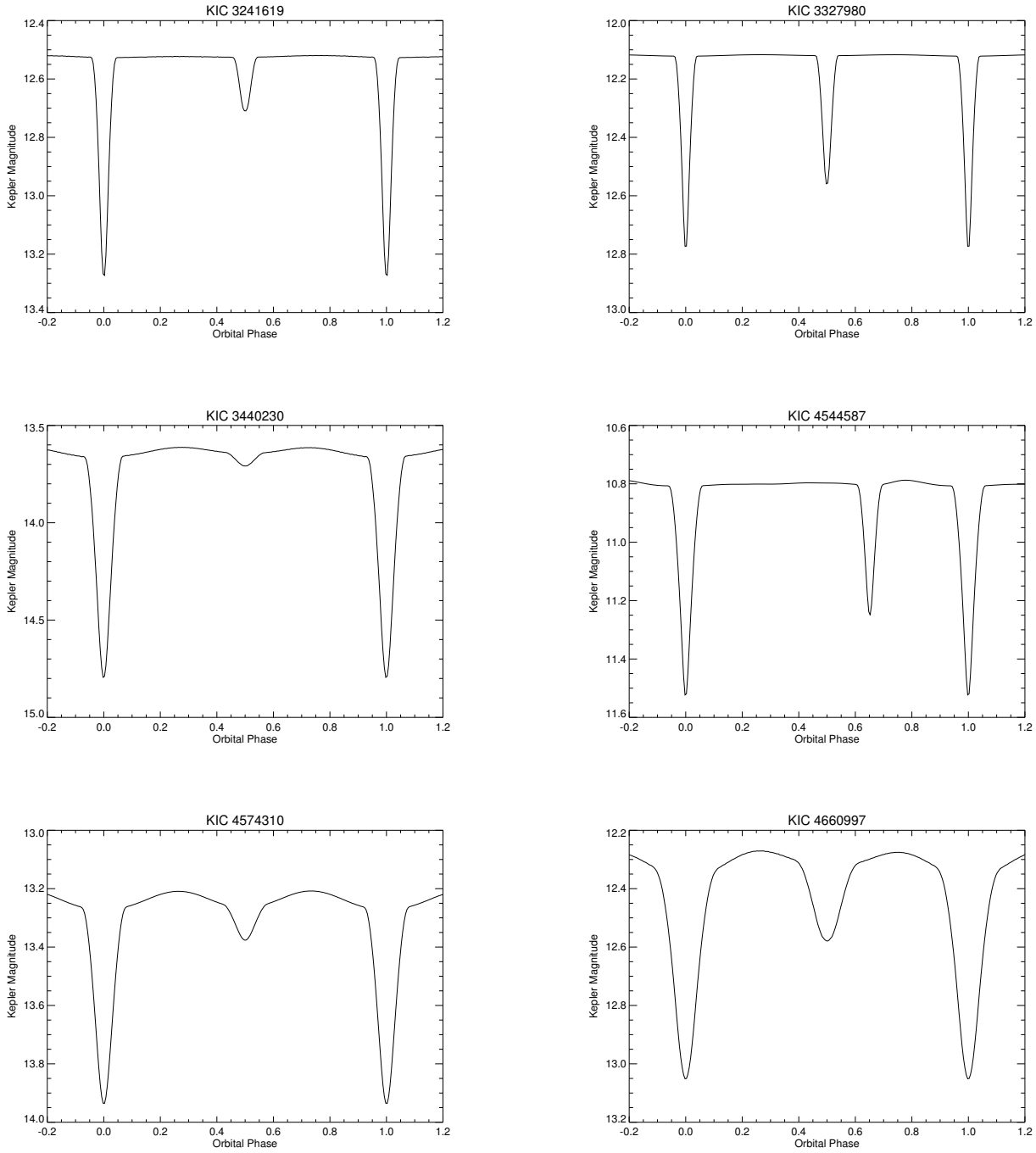

Figure 2.3: Binned, phased light curves for all 41 eclipsing binaries in terms of *Kepler* magnitudes.

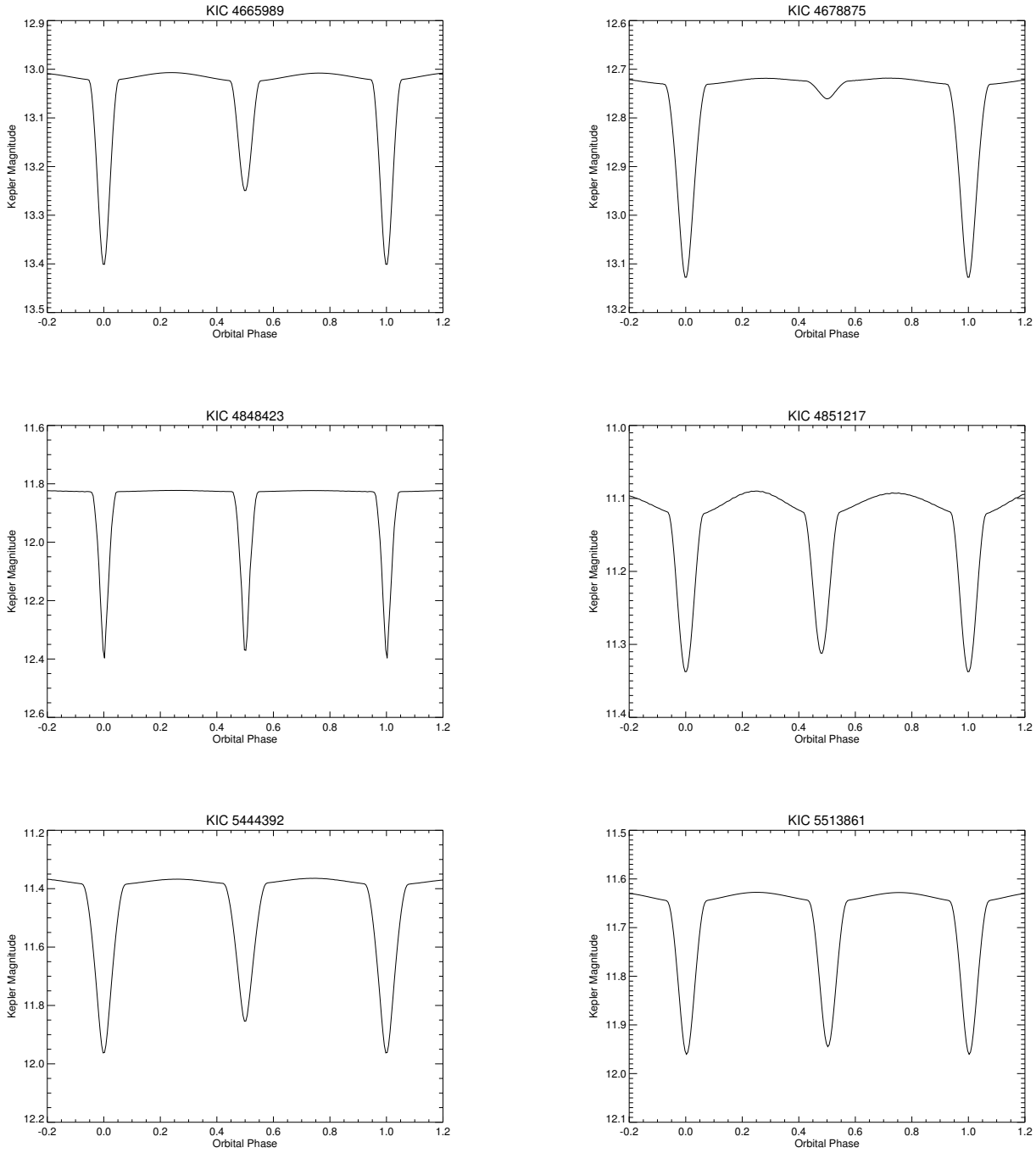

Figure 2.3: Binned, phased light curves for all 41 eclipsing binaries in terms of *Kepler* magnitudes.

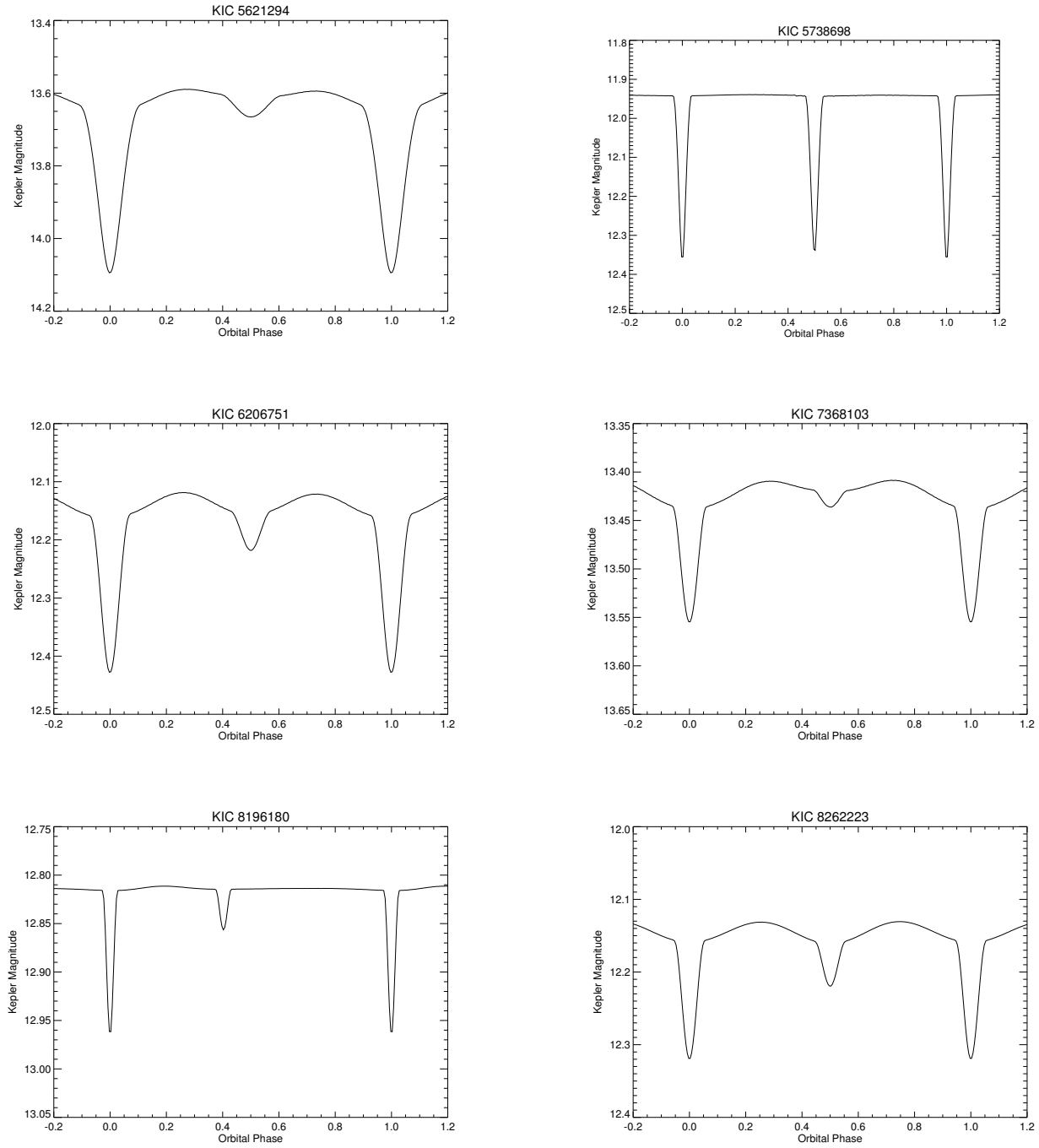

Figure 2.3: Binned, phased light curves for all 41 eclipsing binaries in terms of *Kepler* magnitudes.

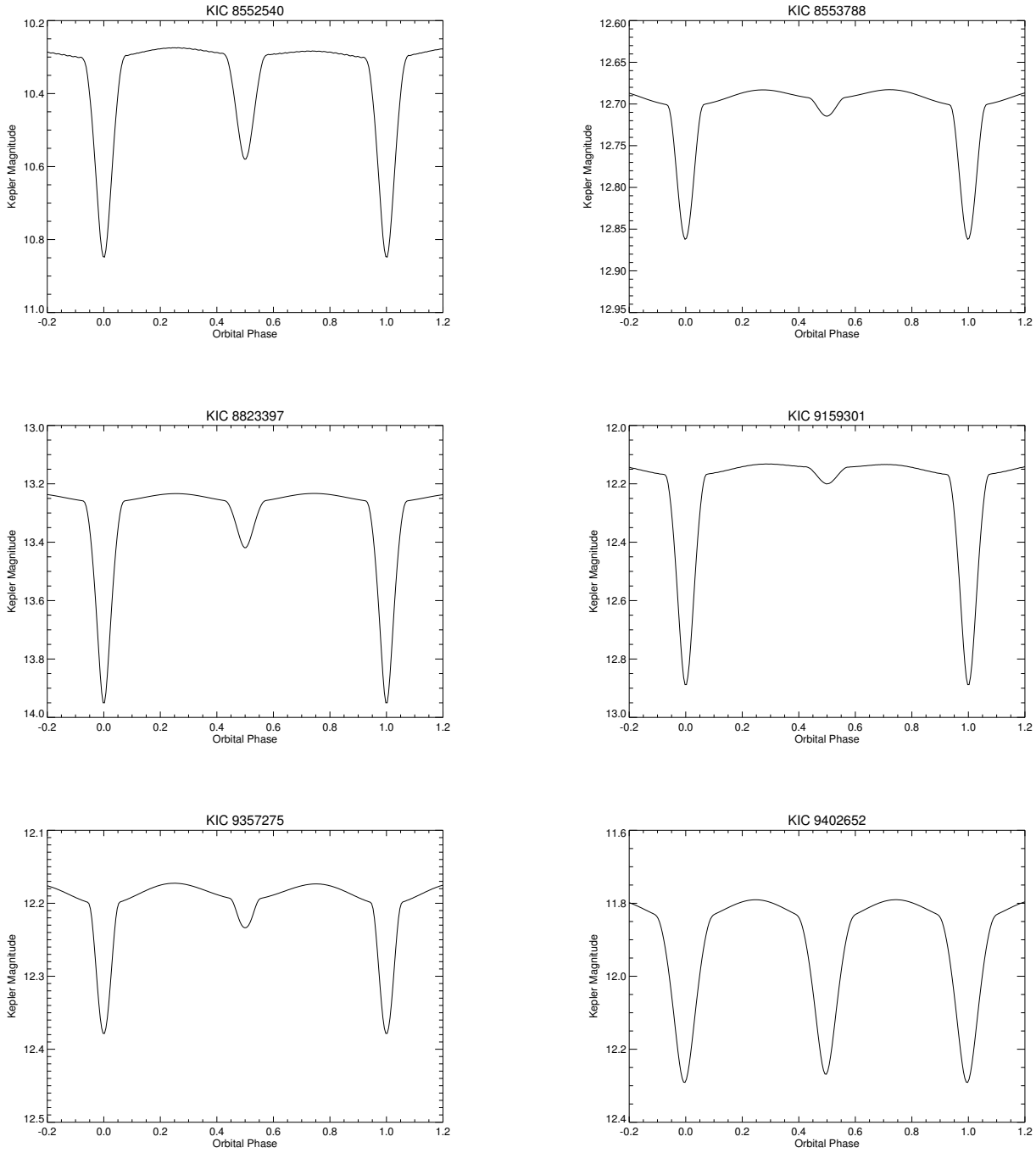

Figure 2.3: Binned, phased light curves for all 41 eclipsing binaries in terms of *Kepler* magnitudes.

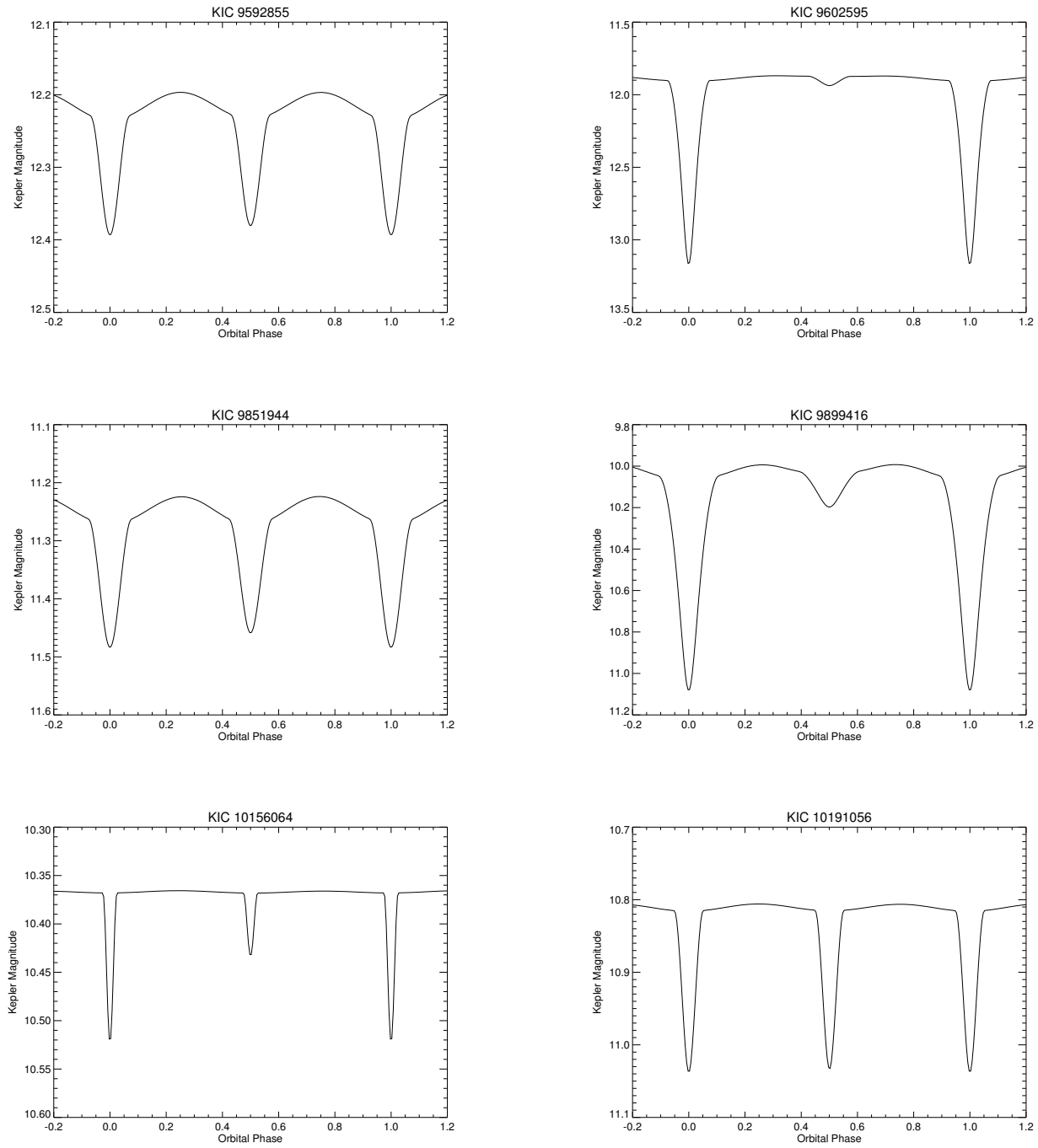

Figure 2.3: Binned, phased light curves for all 41 eclipsing binaries in terms of *Kepler* magnitudes.

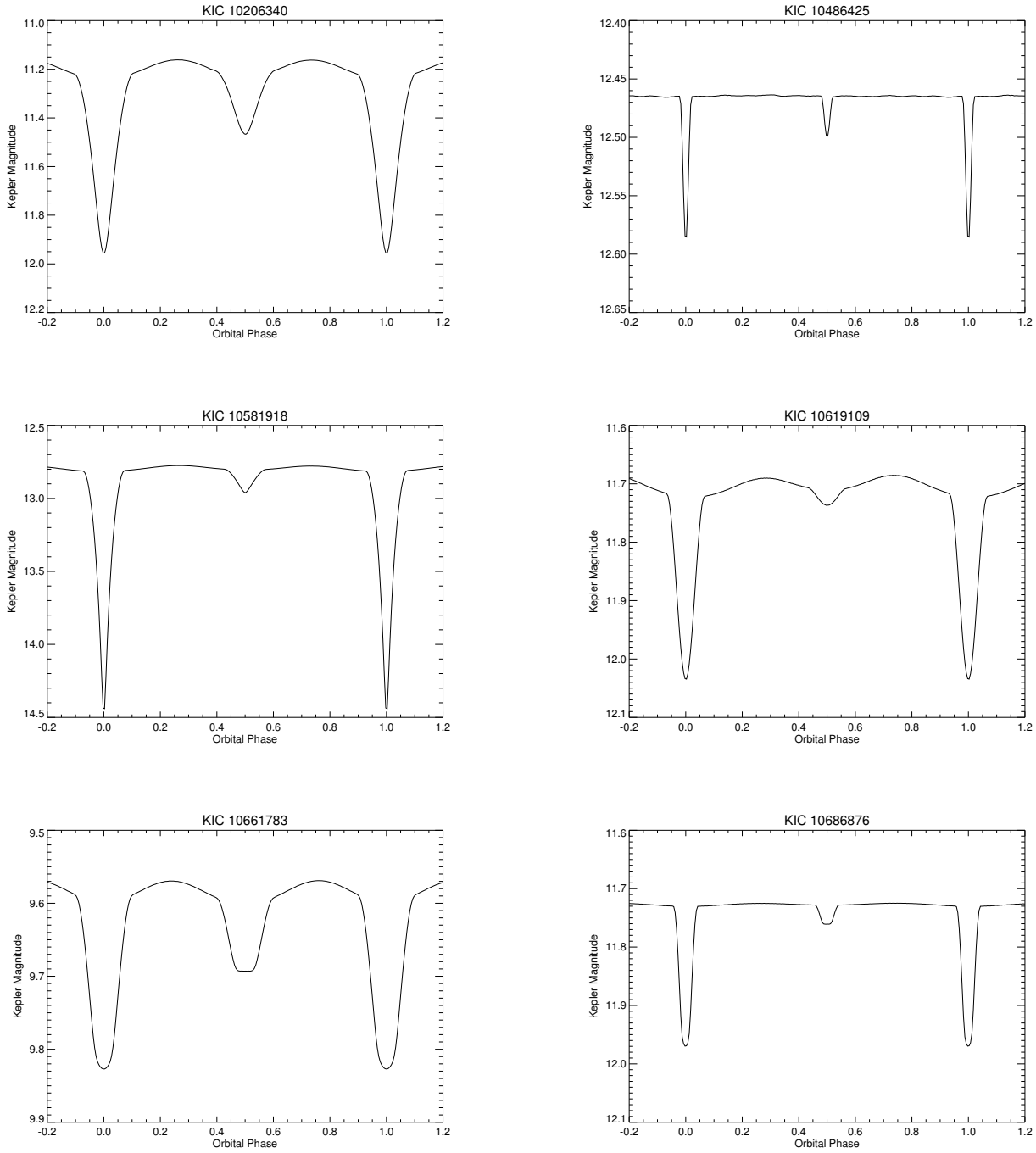

Figure 2.3: Binned, phased light curves for all 41 eclipsing binaries in terms of *Kepler* magnitudes.

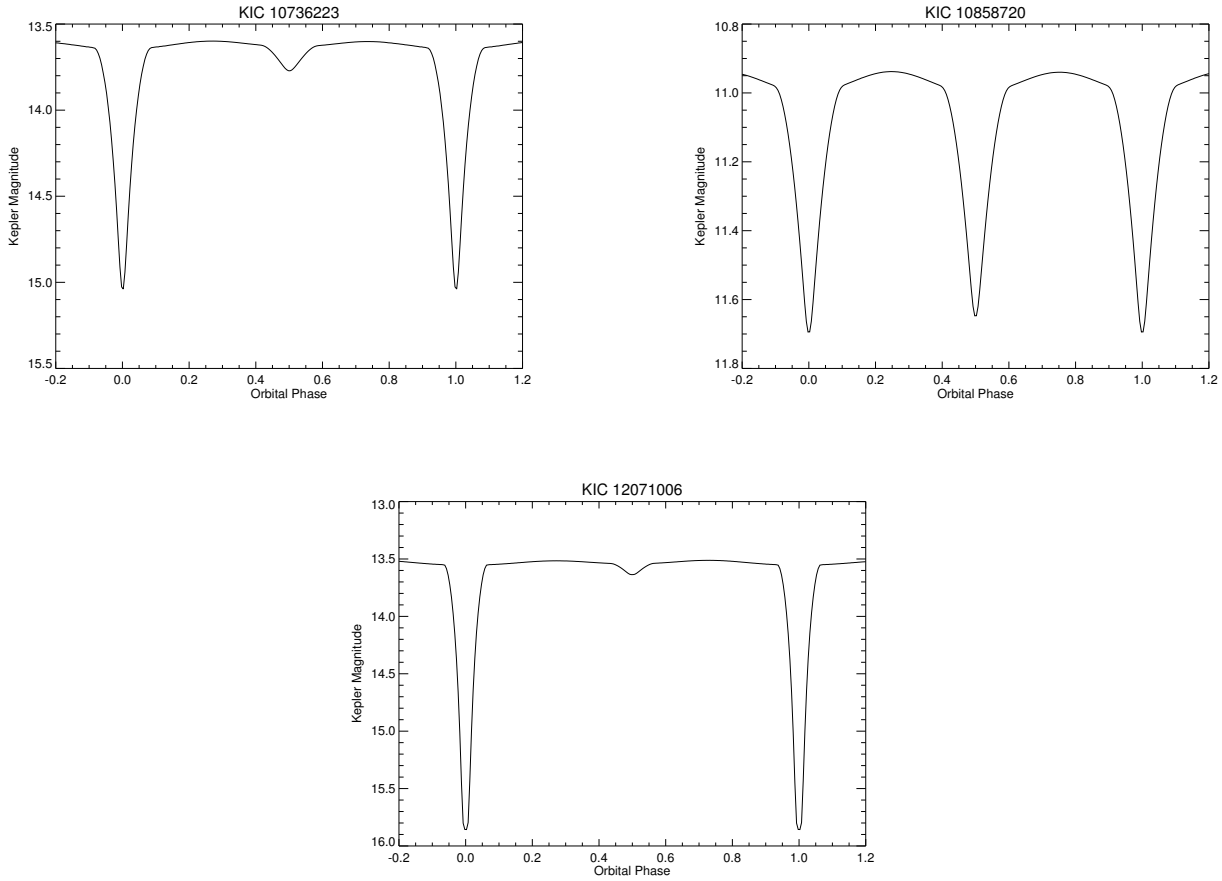

Figure 2.3: Binned, phased light curves for all 41 eclipsing binaries in terms of *Kepler* magnitudes.

light over the visible hemisphere. Gies et al. (2012) reported spot activity in 25 of the binaries, with spot rotations faster than the orbital period, slower than the orbit, and where both trends are visible. The effect of spots is evident in the un-binned light curve of KIC 3241619 (Fig. 2.2) and can be seen as slight out-of-eclipse variations in the binned light curves of KIC 2305372, 2708156, 3241619, 4660997, 5444392, 6206751, 8196180, 8552540, 8553788, 9602595, 9899416, 10206340, 10581918, 10686876, 10736223, and 12071006.

2.4 Finding Hierarchical Triples using Eclipse Timing

Eclipse timing analysis looks for changes in the arrival times of eclipses by searching for periodic features in the observed minus calculated ($O-C$) eclipse times. Gies et al. (2015) formed an eclipse template by binning all available data in orbital phase according to an estimated period P and epoch of minimum light T for the primary and secondary eclipses individually. The template was then smoothed by convolution with a Gaussian function and recentered by fitting a parabola to the lowest 20% of each eclipse, with the epochs updated accordingly. Each individual eclipse was then fit with the template to derive the times of eclipse and find the best match to parameters for the phase offset and an eclipse depth scaling factor. The phase offset was multiplied by the period to determine the eclipse times and $O-C$ (after subtraction of the normal linear progression of eclipse times with cycles $T+PE$, where E is the number of eclipses since the reference epoch T). Graphical representations of the $O-C$ results (some enhanced by additional eclipse timings from Zasche et al. 2015) can be seen in Gies et al. (2015). Updated periods and epochs of primary minima from the fitting process are also given in their Table 1 and adopted throughout this dissertation (see Table 3.5).

Trends in the $O-C$ diagrams of Gies et al. (2015) display a variety of features related to starspots, apsidal motion (procession of the major axis of an eccentric orbit primarily due to tidal deformation), long-term period changes, and light time changes associated with orbital motion about a third star. $O-C$ variations consistent with a third star in an orbit short enough to be detected within the four year time-span of *Kepler* were detected in

seven systems: KIC 2305372, 4574310, 4848423, 5513861, 8553788, 9402652, and 10686876. The orbital periods for the third bodies range from $\sim 3 - 11$ years and have mass functions $f(m_3)$ of $0.01 - 0.08\,M_\odot$, with two exceptions: KIC 2305372, which has a larger mass function ($f(m_3) = 0.25\,M_\odot$) and the longest tertiary orbital period ($P = 11.338$ yr), and KIC 4574310, which has the smallest mass function of $f(m_3) = 0.000032\,M_\odot$. Seven additional systems showed large parabolic variations in the primary and secondary eclipses, though the small observed fraction of any potential orbital period was not enough to detect definitively a companion or to derive orbital fits as in the previous seven systems.

The 17% detection rate (7 of 41) for triples in Gies et al. (2015) is similar to that of other, larger samples. For instance, Rappaport et al. (2013) surveyed approximately 2100 eclipsing binaries from Q0−Q13 in the *Kepler* dataset and presented dynamical solutions for 39 candidate triple systems with short outer periods of $49\,\mathrm{d} < P < 960\,\mathrm{d}$. Extrapolating their results, Rappaport et al. estimate at least 20% of all close binaries have tertiary companions. A catalog of eclipse times for short-period, mostly over-contact binaries presented by Conroy et al. (2014) detected third bodies in ∼20% of their sample, but only ∼10% for outer periods less than 1400 days. The most recent study by Borkovits et al. (2016) measured eclipse time variations for more than 2600 eclipsing binaries from the *Kepler* Eclipsing Binary Catalog[4] (Prša et al. 2011; Slawson et al. 2011; Kirk et al. 2016). They found strong indications of tertiaries in 222 systems via light travel time or dynamical effect delays, resulting in a detection rate of approximately 8%, lower than previous studies. However, taking into account the incompleteness of their sample for outer periods longer than 2000 days, Borkovits

[4] `http://keplerebs.villanova.edu`

et al. estimate at least 30% of all binaries are located in triples, and likely closer to unity.

2.5 Summary

The unprecedented photometric precision and coverage of *Kepler* data are seen in the light curves of the 41 eclipsing binaries included in this study. Detrending the processed light curves accounts for many of the large scale features introduced by the spacecraft, enabling the measurement of eclipse times and updated ephemerides as well as insight into the binary orbits and stellar components. The light curves are used to enhance our understanding of the spectroscopic orbital parameters derived in Chapter 3, as well as in the determination of fundamental parameters for KIC 5738698 in Chapter 4 and other systems in the future (see Chapter 6).

CHAPTER 3
SPECTROSCOPIC STUDIES OF ECLIPSING BINARIES

3.1 Introduction

Of the 41 eclipsing binaries selected for eclipse timing analysis via *Kepler*, approximately two-thirds were reported only recently to be eclipsing based on automated variability surveys such as the Hungarian-made Automated Telescope Network (HATnet), whose goal is to detect transiting extrasolar planets using small-aperture robotic telescopes (Hartman et al. 2004), and the All Sky Automated Survey (ASAS) which monitors V-band variability among stars brighter than 14th magnitude visible in the southern hemisphere (Pigulski et al. 2009). Most of the remaining binaries have been known since the 1930s or 1960s, but typically have little more than times of eclipse minima and orbital ephemerides published. In order to characterize further this set of eclipsing binaries as well as to derive spectroscopic orbital elements, estimate stellar parameters, compare with evolutionary codes, and explore pulsational properties of the component stars, we completed a large set of spectroscopic observations. An average of 11 ground-based optical spectra were collected per binary and used to measure radial velocities and derive spectroscopic orbits for each system. Ideally, when measuring radial velocities, high resolution spectra and complete phase coverage of the orbit are desired. However, moderate resolution ($R = \lambda/\delta\lambda \approx 6000$) optical spectra in the wavelength range $3930 - 4600$Å provide a high density of astrophysically important atomic lines and molecular bands (traditionally used for stellar classification) that allowed us to derive accurate radial velocities of intermediate-mass stars. In addition, the ephemerides

determined in the eclipse timing analysis (Gies et al. 2015) enabled us to concentrate our observations during velocity extrema to best constrain the spectroscopic orbits with a modest number of spectra. Details of the data collection and analysis are presented in Sections 3.2 and 3.3, with a discussion of the radial velocity results, mass ratio trends, and suspected triple systems given in Section 3.4.

3.2 Observations & Data Reduction

Spectra for all 41 eclipsing binaries were obtained over the course of six observing runs between 2010 June and 2013 August at Kitt Peak National Observatory (KPNO) with the 4 m Mayall telescope and R-C Spectrograph. Using the BL380 grating (1200 grooves mm^{-1}) in second order provides wavelength coverage of $3930-4600$Å with an average resolving power of $R = \lambda/\delta\lambda \approx 6200$. For wavelength calibration purposes, spectra of HeNeAr comparison lamps were taken either immediately before or after each science exposure, and numerous bias and flat-field exposures were taken each night.

Additional observations of the brighter systems ($K_p \lesssim 12$) were made at the Anderson Mesa Station of Lowell Observatory between 2010 July and 2012 November. The 1.8 m Perkins telescope and the DeVeny Spectrograph were used along with a 2160 grooves mm^{-1} grating to obtain a resolving power of $R = \lambda/\delta\lambda \approx 6000$ over the wavelength range $4000 - 4530$Å. Calibration exposures with HgNeArCd Pen-Ray lamps were taken before or after each exposure while bias and flat-field frames were taken nightly.

Ten of the binaries were also observed at the Dominion Astrophysical Observatory (DAO)

Table 3.1. Spectroscopic Observation Parameters

Observatory	Wavelength Range (Å)	Average Resolving Power ($\lambda/\delta\lambda$)	Average S/N	Number of Spectra
KPNO	$3930 - 4600$	6200	100	367
Lowell	$4000 - 4530$	6000	40	48
DAO	$4260 - 4600$	4200	30	39

1.8 m Plaskett telescope in 2010 July. The Cassegrain Spectrograph was used with the 1200B grating in first order to obtain wavelength coverage from $4260 - 4600$Å and an average resolving power of $R = \lambda/\delta\lambda \approx 4200$. Bias and flat-field exposures were taken nightly and FeAr comparison lamp spectra were taken immediately before or after each science exposure for wavelength calibration. A summary of the observations and spectral characteristics for all three setups is provided in Table 3.1.

All spectra were reduced and extracted using the Image Reduction and Analysis Faculty (IRAF[1]). The raw data are transformed via calibration data including bias frames and flat fields, which account for the inherent background level of the detector and pixel to pixel variations in gain, including uneven illumination of the detector. Series of bias and flat field exposures are median combined into master images that are then used to subtract and divide out the bias and flat field images, respectively, from the raw data.

Spectrum extraction and wavelength calibration were performed using IRAF and the corresponding comparison lamp spectra for KPNO and DAO observations. However, spectra

[1]IRAF is distributed by the National Optical Astronomy Observatory, which is operated by the Association of Universities for Research in Astronomy (AURA), Inc., under cooperative agreement with the National Science Foundation.

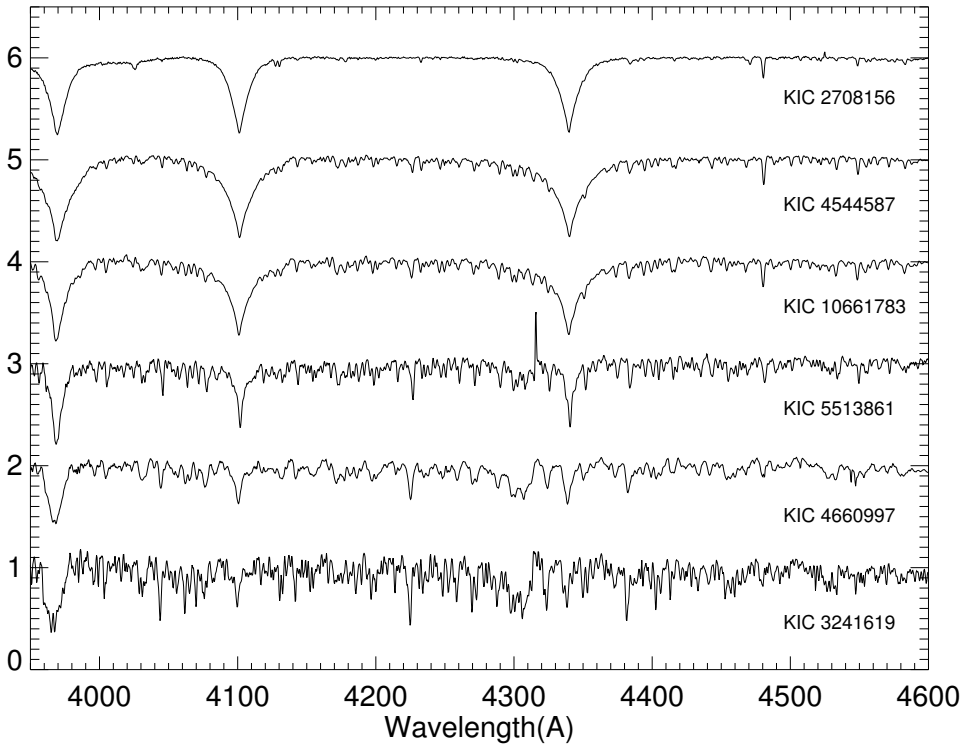

Figure 3.1: Representative spectra of six systems spanning B (top) through G (bottom) spectral types. The weakening of the hydrogen Balmer lines, Hγ (4340Å), Hδ (4102Å), and Hϵ (3970Å), with decreasing temperature is evident, while the metal lines strengthen and the molecular G-band near 4300Å develops.

from Lowell required observations of standard velocity stars to aid in the determination of the dispersion solution as the comparison lamps only produce three measurable emission lines in the wavelength region $4000 - 4530$Å (Hg I $\lambda 4046, 4077, 4358$). Different subsets of seven standard velocity stars, depending on the time of year, were observed $2 - 4$ times per night. Properties of each star are given in Table 3.2. Model spectra from the UVBLUE[2] libraries of Rodríguez-Merino et al. (2005) interpolated to the appropriate temperatures and gravities were transformed to the topocentric velocity of each standard star and convolved

[2] `http://www.inaoep.mx/~modelos/uvblue/download.html`

Table 3.2. Standard Velocity Stars

Star	T_{eff} (K)	log g (cgs)	V_r (km s^{-1})	Sources
HD 37160	4668	2.46	99.29	Cenarro et al. 2007; Massarotti et al. 2008
HD 82106	4868	4.80	29.84	Nidever et al. 2002; Valenti & Fischer 2005
HD 102870	6109	4.20	4.45	Nidever et al. 2002; Cenarro et al. 2007
HD 144579	5395	4.75	-59.43	Nidever et al. 2002; Luck & Heiter 2006
HD 187691	6107	4.30	-0.15	Cenarro et al. 2007; Molenda-Zakowicz et al. 2007
HD 194071	5486	2.70	-9.43	Latham & Stefanik 1992; Gray 2008
HD 213947	4973	2.10	16.58	Famaey et al. 2005; Gray 2008

for instrumental broadening. We then used the comparison lamp exposures taken with each standard velocity star to determine an initial fit of wavelength to pixel number. The observed spectra and appropriate model were then cross-correlated in 40 sub-regions across the spectrum to get the mean pixel and wavelength values for each region. These values were then fit with a cubic polynomial to remove any systematic effects across the chip. Finally, dispersion corrections were applied to the science spectra observed nearest in time to each standard based on the cubic polynomial and individual pixel shifts determined from the comparison lamp spectra.

After wavelength calibration, all spectra were rectified to a unit continuum and transformed to a common heliocentric wavelength grid of 1733 spectral steps in $\log \lambda$ increments equivalent to Doppler shift steps of 26.2 km s^{-1} over the range 3950 to 4600Å. Six reduced and transformed spectra are shown in Figure 3.1, demonstrating the range of spectral types (B−G) in the sample and highlighting the changing spectral features visible in our wavelength range.

3.3 Spectral Analysis

3.3.1 Radial Velocities

To determine radial velocities, Doppler shifts of the spectra are measured by cross-correlating the observed spectrum against an assumed template. The relative velocity shifts are then given by the correlation maximum. In double-lined spectroscopic binaries the observed spectra are composites of the spectral features of both stars, which produce cross-correlations with two peaks. However, when the relative velocity of the two components is smaller than the intrinsic width of the correlation peaks, the individual maxima can blend together making it difficult or impossible to resolve the two peaks. Two-dimensional cross correlation minimizes this problem by calculating the correlation of the observed spectrum against two templates combined over a range of velocity shifts (Zucker 2012). One of the most widely used implementations of this technique is TODCOR, which stands for TwO-Dimensional CORrelation, developed by Zucker & Mazeh (1994). The algorithm calculates cross-correlation functions of the observed spectrum with a template for the primary, the observed spectrum with a template for the secondary, and the first template with the second template, and these are combined in a multiple correlation statistic $R\,(s_1, s_2, \alpha)$ that is a function of Doppler shifts s_1 and s_2 for the primary and secondary star, respectively, and the monochromatic flux ratio $\alpha = F_2/F_1$ (see eq. A3 in Zucker & Mazeh 1994).

Here we use our own implementation of two-dimensional cross-correlation (see Appendix B), employing two templates to determine the velocity separation of the secondary component relative to the primary followed by the absolute velocity of the primary, based on the method

Table 3.3. Eclipsing Binary System Parameters

KIC	Other ID	K_p (mag)	Template T_1 (K)	Template T_2 (K)	Flux ratio (f_2/f_1)	Source
2305372	2MASS J19275768+3740219	13.821	6208	4097[a]	0.01	A
2708156	UZ Lyr	10.672	11061	5671	0.01	S
3241619	2MASS J19322278+3821405	12.524	5715	4285	< 0.01	A
3327980	2MASS J19084227+3826005	12.119	7321	6424	0.26	S
3440230	2MASS J19215310+3831428	13.636	8300	4897[a]	0.05	spec
4544587	TYC 3124-1348-1	10.801	8600	7750	0.66	H
4574310	2MASS J19395847+3938341	13.242	7153	4077	0.05	A
4660997	V1130 Cyg	12.317	5587	4215[a]	0.05	A
4665989	2MASS J19390335+3945102	13.016	7559	6846	0.12	A
4678873	TYC 3140-587-1	12.725	7496	5698	0.01	S
4848423	KOI-3560/TYC 3140-2904-1	11.825	6239	6176	0.83	A
4851217	HD 225524	11.108	7022	6804	2.00	A
5444392	TYC 3138-829-1	11.378	5965	5726	0.86	A
5513861	TYC 3123-2012-1	11.638	6479	6411	0.59	A
5621294	2MASS J19285262+4053359	13.613	8425	5560[a]	0.03	S
5738698	TYC 3141-1400-1	11.941	6792	6773	0.82[b]	M
6206751	2MASS J19293751+4130469	12.142	6965	4885	0.02	S
7368103	2MASS J19333970+4255021	13.419	7838	5212[a]	0.01	S
8196180	2MASS J20023258+4403122	12.814	7114	5934	0.04	S
8262223	TYC 3162-1562-1	12.146	9128	6849	0.12	G2
8552540	V2277 Cyg	10.292	5948	5252[a]	0.17	A
8553788	2MASS J19174291+4438290	12.691	8045	5328	0.02	S
8823397	2MASS J19342636+4501070	13.249	8540	5724	0.07	S
9159301	TYC 3556-2697-1	12.146	7959	4209	0.02	S
9357275	2MASS J19484858+4550595	12.186	7545	5580	0.01	S
9402652	V2281 Cyg	11.823	6641	6587[a]	1.18	S
9592855	2MASS J19350483+4614117	12.216	7290	7087	0.64	S
9602595	V995 Cyg	11.882	9679	5705	0.04	A
9851944	TYC 3558-939-1	11.249	7026	6902	1.24	G1
9899416	BR Cyg	10.028	11056	6278	0.06	A
10156064	TYC 3561-1283-1	10.367	7424	6268	0.07	S
10191056	BD+47 2717	10.811	6588	6455	0.48	S
10206340	V850 Cyg	11.203	5844	4856[a]	0.09	A
10486425	2MASS J19495442+4739323	12.465	7018	5847	0.08	S
10581918	WX Dra	12.796	8300	5544[a]	0.05	spec
10619109	TYC 3562-985-1	11.704	7028	3903	< 0.01	S
10661783	TYC 3547-2135-1	9.586	7764	6001	< 0.01	L
10686876	TYC 3562-961-1	11.727	7944	5842	< 0.01	S
10736223	V2290 Cyg	13.621	7797	5069	0.01	S
10858720	V753 Cyg	10.971	7282	7223	0.90	A
12071006	V379 Cyg	13.533	7338	4660	0.01	S

[a]Temperature ratio from Armstrong et al. (2014) used to determine secondary temperature

[b]Flux ratio adopted from Matson et al. (2016)

Note. — Template temperature sources: A - Armstrong et al. (2014), S - Slawson et al. (2011), spec - observed spectral type, H - Hambleton et al. (2013), M - Matson et al. (2016), G1 - Guo et al. (2016), G2 - Guo et al. (2016b, in prep), L - Lehmann et al. (2013). All flux ratios derived by maximizing the average cross-correlation functions unless otherwise noted (see Section 3.3.3 for details).

used in PROCOR by R.W. Lyons (see Gies & Bolton 1986). Model templates were selected from the UVBLUE grid of high resolution model spectra based on LTE calculations using ATLAS9 model atmospheres and the SYNTHE spectral synthesis code of R. L. Kurucz (Rodríguez-Merino et al. 2005). Templates for the primary and secondary were selected based on temperatures determined via the *Kepler* Input Catalog and temperature ratio as derived by Slawson et al. (2011) or using spectral energy distribution (SED) fits by Armstrong et al. (2014). The temperatures that best matched the observed spectral type and preliminary mass estimates were adopted and are given in Table 3.3. In a few cases the temperature ratio determined from the light curve and used as a prior in Armstrong et al. (2014) was used to provide a more reasonable temperature for the secondary. Detailed analyses of five systems (KIC 4544587, 5738698, 8262223, 9851944, and 10661783) include previously derived temperatures via spectroscopy and light curve analysis that we adopt instead. Gravities ($\log g$), projected rotational velocities ($v \sin i$), and initial estimates of the relative flux contribution of each star were calculated based on the temperatures, assuming main sequence stars and solar metallicity. Each model spectrum was then rebinned onto the observed wavelength grid ($3950 - 4600$Å) and convolved with functions for the projected rotational velocity and instrumental broadening. The adopted temperatures and flux ratios for each system are shown in Table 3.3 along with the *Kepler* Input Catalog (KIC) number, alternate object names, and *Kepler* magnitude (K_p).

Using the times of observation and orbital elements estimated from the period and epoch of primary eclipse from Gies et al. (2015) and the temperatures and inclinations of Slawson

et al. (2011), we predicted radial velocities for each observation and determined trial velocity separations for the primary and secondary. These trial separations were used to make a series of composite model spectra over a grid of separations, which were then cross-correlated against the observed spectra. The maximum of each cross-correlation function was plotted against the corresponding trial separation for each spectrum, with the optimal separation determined from the interpolated maximum nearest the predicted velocity. A final cross-correlation was then performed using this separation to get the absolute velocity of the primary, and by extension the secondary. The uncertainties in the resulting velocities were estimated using the method of Zucker (2003). Because the radial velocity measurements are derived from different instruments, we might also expect systematic differences in the velocities from KPNO, Lowell, and DAO. However, we believe any such differences to be below our measurement sensitivities and see no visible trends in our derived radial velocities. More careful examination of this for KIC 5738698 (see Chapter 4) and KIC 9851944 (Guo et al. 2016) similarly revealed no offsets in the data.

As broad hydrogen (and diffuse helium) lines are usually omitted when determining radial velocities from individual lines because blending effects can cause the line centers to appear displaced in wavelength (Petrie et al. 1967), we chose to omit the Balmer lines (Hϵ, Hδ, Hγ) from the cross-correlation. This was accomplished by blanking out the relevant pixels in each spectrum and using a Tukey (tapered cosine) window to smooth the edges and minimize systematic offsets in the derived radial velocities. To further aid in the accurate determination of radial velocities, we used the estimated velocity separation to guide which

peak was chosen in the event of multiple peaks in the cross-correlation maxima versus separation plot. When multiple peaks were blended together, we performed a local rectification of the cross-correlation function by fitting a linear slope to the relevant side of the background peak and subtracting out its contribution to the desired peak. The uncertainties in the secondary velocities were determined via the newly rectified peak in the same way as before, with occasional anomalously large errors due to tiny peaks replaced by errors determined via the method of Kurtz et al. (1992).

Once initial radial velocities were determined using the estimated flux ratio based on the ratio of the stellar radii and blackbody fluxes from the template temperatures, cross-correlations were repeated over a grid of flux ratios for each system. The average maximum correlation functions for each flux ratio were then plotted to find the interpolated maximum via the numerical derivative. The flux ratio corresponding to this peak, reported in Table 3.3, was used to perform a final set of cross-correlations and derive radial velocities for each system. In a few cases, the average maximum correlation function continued to increase for progressively smaller flux ratios approaching zero. We believe this reflects discrepancies in our adopted temperatures and the difficulty of measuring cross-correlation functions with varying slopes and backgrounds, rather than a true flux ratio of zero. For these systems we therefore list $f_2/f_1 < 0.01$ in Table 3.3 and use 0.01 for the derivation of radial velocities.

The radial velocities are presented in Table 3.4, which lists the *Kepler* Input Catalog (KIC) number, time of observation in heliocentric Julian date (HJD), orbital phase, radial velocities (V), uncertainties (σ), and observed minus calculated ($O - C$) residuals from the

spectroscopic fit (§ 3.3.3) for both components in all 41 systems, as well as the observatory where the observation was made. Orbital phase is determined relative to T_0, taken to be the epoch of primary eclipse from Gies et al. (2015). Note the period of KIC 4848423 is adopted from Gies et al. (2015) and is consistent with our velocity measurements, whereas Rowe et al. (2015) included the system as a transiting planet candidate with half the period.

Table 3.4: Radial Velocity Measurements

Object (KIC)	Date (HJD−2,400,000)	Orbital Phase[a]	V_1 (km s^{-1})	σ_1 (km s^{-1})	$(O-C)_1$ (km s^{-1})[b]	V_2 (km s^{-1})	σ_2 (km s^{-1})	$(O-C)_2$ (km s^{-1})[b]	Source (Obs.)
2305372	55367.8978	0.143	−77.09	1.21	−1.14	103.07	21.81	−1.04	KPNO
2305372	56078.7768	0.218	−92.72	1.07	−1.16	126.70	21.69	−8.42	KPNO
2305372	56079.8403	0.975	4.00	2.95	5.11	23.75	34.03	···	KPNO
2305372	56081.9033	0.444	−39.07	1.25	2.02	46.51	22.33	5.24	KPNO
2305372	56486.8313	0.712	61.71	1.71	−2.14	−186.40	25.64	−25.53	KPNO
2305372	56522.8387	0.346	−77.17	1.78	2.06	95.86	25.48	−17.31	KPNO
2708156	55368.8339	0.164	−68.39	1.19	2.41	129.39	19.68	−50.14	KPNO
2708156	55368.9349	0.217	−74.35	1.24	3.02	39.07	···	···	KPNO
2708156	55718.8555	0.236	−73.72	2.71	4.59	−8.64	···	···	Lowell
2708156	55719.8914	0.784	25.45	2.86	−2.75	−256.29	31.55	1.12	Lowell
2708156	55720.9486	0.343	−64.05	4.11	5.50	−99.07	···	···	Lowell
2708156	55734.8661	0.702	29.56	1.64	2.58	−249.80	21.87	1.92	KPNO
2708156	55734.9794	0.762	30.69	1.76	1.40	−247.63	22.82	14.48	KPNO
2708156	55735.7758	0.183	−70.87	1.45	2.91	313.26	20.61	···	KPNO
2708156	55735.9293	0.264	−78.49	1.64	−0.19	259.81	21.78	47.04	KPNO
2708156	55753.8980	0.765	51.57	3.05	22.37	−239.01	33.73	22.72	Lowell
2708156	55754.7917	0.237	−82.85	1.49	−4.51	242.10	21.92	29.25	Lowell
2708156	55755.8035	0.772	28.26	1.50	−0.64	−247.51	22.22	12.94	Lowell
2708156	55755.9211	0.835	17.27	1.36	−4.72	−233.24	21.71	−3.06	Lowell
2708156	56077.8059	0.030	−55.33	1.34	−20.74	38.86	19.50	20.04	KPNO
2708156	56077.8979	0.078	−49.64	1.33	0.44	96.70	20.37	9.41	KPNO
2708156	56234.6275	0.949	2.90	1.39	10.31	−98.16	20.76	3.15	Lowell

Continued on Next Page...

Table 3.4: Radial Velocity Measurements

Object (KIC)	Date (HJD−2,400,000)	Orbital Phase[a]	V_1 (km s^{-1})	σ_1 (km s^{-1})	$(O-C)_1$ (km s^{-1})[b]	V_2 (km s^{-1})	σ_2 (km s^{-1})	$(O-C)_2$ (km s^{-1})[b]	Source (Obs.)
2708156	56522.8612	0.351	−62.34	1.98	5.67	173.66	25.28	5.40	KPNO
3241619	55367.8007	0.201	−135.82	0.90	−0.53	82.91	14.87	1.67	KPNO
3241619	55368.7557	0.762	44.45	0.95	−0.70	−189.56	15.26	−8.31	KPNO
3241619	55431.8255	0.789	41.55	0.82	−1.10	−187.01	14.50	−9.39	KPNO
3241619	55730.7169	0.262	−137.43	0.87	1.87	76.20	14.93	−10.91	KPNO
3241619	55734.7762	0.645	27.39	0.79	1.32	−156.46	14.23	−3.02	KPNO
3241619	55734.9169	0.728	44.87	0.82	0.35	−181.70	14.44	−1.39	KPNO
3241619	55815.7410	0.178	−130.72	0.88	−0.48	72.53	14.64	−1.37	KPNO
3241619	55815.8400	0.236	−140.36	0.90	−1.15	75.52	15.16	−11.44	KPNO
3327980	55368.8406	0.949	31.76	1.61	−6.10	−17.24	3.75	4.23	KPNO
3327980	55733.7069	0.185	−68.24	1.42	3.07	105.74	3.30	1.18	KPNO
3327980	56078.6839	0.721	99.55	1.58	2.23	−87.95	3.56	2.56	KPNO
3327980	56078.8019	0.748	96.12	1.50	−2.71	−97.68	3.51	−5.47	KPNO
3327980	56078.9259	0.778	100.86	1.58	3.37	−83.26	3.64	7.35	KPNO
3327980	56082.7124	0.673	95.44	2.66	6.86	−86.52	5.46	−6.03	KPNO
3327980	56082.9033	0.718	96.06	1.52	−0.97	−94.05	3.53	−3.87	KPNO
3327980	56486.8086	0.181	−79.90	3.59	−9.68	92.06	7.30	−11.25	KPNO
3440230	55368.8775	0.404	−30.09	1.68	−3.41	93.01	9.27	12.59	KPNO
3440230	55734.7169	0.383	−29.15	1.59	1.40	91.06	8.89	−4.86	KPNO
3440230	55735.7537	0.743	31.71	2.18	−0.37	−164.78	11.37	−8.84	KPNO
3440230	55813.7689	0.821	31.49	1.39	3.08	−122.71	8.02	18.75	KPNO
3440230	55813.8563	0.852	25.49	1.79	0.77	−110.47	9.43	16.25	KPNO
3440230	56077.7209	0.436	−21.67	1.63	−1.64	81.70	9.00	27.92	KPNO
3440230	56078.8888	0.842	24.27	1.52	−1.79	−132.31	8.68	−0.24	KPNO
3440230	56078.9460	0.862	21.47	1.52	−1.81	−122.91	8.56	−1.98	KPNO
3440230	56082.9251	0.243	−43.65	1.35	−0.75	153.88	8.01	8.78	KPNO
3440230	56488.9395	0.166	−31.68	2.04	6.15	125.18	10.57	0.65	KPNO
4544587	55366.8921	0.552	−72.59	3.55	−18.42	50.15	4.65	32.34	KPNO
4544587	55367.9578	0.038	−57.05	2.27	−22.03	12.07	3.05	17.16	KPNO
4544587	55403.8256	0.423	−94.10	19.26	11.24	12.63	···	···	DAO
4544587	55463.7559	0.799	69.39	3.81	···	−91.91	···	···	Lowell

Continued on Next Page...

Table 3.4: Radial Velocity Measurements

Object (KIC)	Date (HJD−2,400,000)	Orbital Phase[a]	V_1 (km s^{-1})	σ_1 (km s^{-1})	$(O-C)_1$ (km s^{-1})[b]	V_2 (km s^{-1})	σ_2 (km s^{-1})	$(O-C)_2$ (km s^{-1})[b]	Source (Obs.)
4544587	55718.8310	0.319	−104.53	3.62	4.88	97.64	4.54	14.12	Lowell
4544587	55719.8645	0.791	126.56	3.48	15.41	−200.02	4.40	−20.94	Lowell
4544587	55720.8965	0.263	−108.65	4.56	−5.29	75.43	5.68	−0.87	Lowell
4544587	55730.7363	0.758	121.84	2.36	5.32	−190.23	3.07	−4.78	KPNO
4544587	55731.7476	0.220	−84.94	3.08	10.66	59.97	4.01	−7.09	KPNO
4544587	55731.8155	0.251	−95.02	2.72	6.42	67.25	3.55	−6.76	KPNO
4544587	55732.7925	0.697	72.13	2.42	−15.77	−136.89	3.16	14.45	KPNO
4544587	55753.7640	0.277	−80.87	5.59	24.45	58.58	7.02	−20.05	Lowell
4544587	55754.7381	0.722	103.68	2.69	−2.03	−163.47	3.47	9.09	Lowell
4544587	55755.8282	0.220	−102.51	3.58	−6.87	43.14	4.62	−23.96	Lowell
4544587	55813.7983	0.701	80.21	2.35	−10.98	−136.79	3.06	18.47	KPNO
4544587	56235.5909	0.378	−147.12	3.40	···	47.23	4.30	···	Lowell
4574310	55367.7634	0.257	−86.71	1.24	0.02	133.84	7.70	−9.38	KPNO
4574310	55431.7942	0.277	−83.16	1.31	3.01	134.57	7.96	−6.20	KPNO
4574310	55730.8331	0.211	−85.30	1.22	0.22	130.49	7.71	−7.35	KPNO
4574310	55732.8358	0.745	−0.99	1.07	0.64	−234.80	7.12	−3.16	KPNO
4574310	55732.9268	0.814	−6.38	1.16	−1.36	−232.01	7.47	−15.25	KPNO
4574310	55813.7461	0.687	−4.39	1.10	0.52	−231.00	7.36	−13.87	KPNO
4574310	55815.7921	0.253	−88.47	1.55	−1.71	130.13	8.68	−13.22	KPNO
4660997	55366.9202	0.911	35.87	2.04	−6.08	−115.52	12.26	15.65	KPNO
4660997	55730.7454	0.641	88.99	1.92	13.48	−166.36	12.06	7.18	KPNO
4660997	55733.7577	0.995	−37.62	1.93	−9.35	−139.31	12.50	···	KPNO
4660997	55733.8014	0.073	−96.79	1.94	−2.75	44.89	12.09	−3.10	KPNO
4660997	55733.8524	0.164	−152.52	1.76	−0.88	140.86	10.92	16.49	KPNO
4660997	55735.7213	0.486	−23.78	2.18	20.85	46.25	12.61	···	KPNO
4660997	56486.9044	0.778	99.41	3.65	−5.53	−196.89	17.95	16.45	KPNO
4660997	56488.8791	0.288	−161.16	1.79	6.52	150.91	11.05	4.46	KPNO
4660997	56521.9127	0.008	−63.89	2.29	−24.67	28.52	12.63	···	KPNO
4665989	55368.7394	0.259	−126.23	1.12	0.58	117.60	4.41	10.14	KPNO
4665989	55432.8240	0.766	72.68	1.46	−0.23	−169.61	5.22	−9.00	KPNO
4665989	55432.8843	0.792	68.94	1.29	−0.90	−159.20	4.87	−2.69	KPNO

Continued on Next Page...

Table 3.4: Radial Velocity Measurements

Object (KIC)	Date (HJD−2,400,000)	Orbital Phase[a]	V_1 (km s^{-1})	σ_1 (km s^{-1})	$(O-C)_1$ (km s^{-1})[b]	V_2 (km s^{-1})	σ_2 (km s^{-1})	$(O-C)_2$ (km s^{-1})[b]	Source (Obs.)
4665989	55730.6977	0.268	−125.06	1.23	1.29	119.08	4.64	12.23	KPNO
4665989	55730.8556	0.338	−110.49	1.28	1.55	76.14	4.74	−11.54	KPNO
4665989	55731.7710	0.745	74.22	1.08	0.87	−163.24	4.24	−2.04	KPNO
4665989	55732.8019	0.204	−125.64	1.33	−2.87	108.96	4.84	6.93	KPNO
4665989	55732.9084	0.251	−127.84	1.22	−0.87	116.41	4.58	8.73	KPNO
4665989	55733.8769	0.682	64.17	1.09	−0.20	−132.43	4.32	16.70	KPNO
4665989	55814.8067	0.682	64.32	1.12	0.02	−123.65	4.63	25.38	KPNO
4678873	55369.8474	···	24.85	1.12	···	···	···	···	KPNO
4678873	55733.7799	···	20.03	1.12	···	···	···	···	KPNO
4678873	55733.9391	···	18.91	0.88	···	···	···	···	KPNO
4678873	55734.7425	···	16.67	0.87	···	···	···	···	KPNO
4678873	55734.8721	···	18.04	0.93	···	···	···	···	KPNO
4678873	55734.9575	···	15.45	0.91	···	···	···	···	KPNO
4678873	55735.9410	···	14.41	0.90	···	···	···	···	KPNO
4678873	56081.7941	···	18.95	1.31	···	···	···	···	KPNO
4678873	56082.8400	···	13.60	1.23	···	···	···	···	KPNO
4848423	55369.8095	0.926	46.42	2.37	−12.50	−50.15	2.66	−21.28	KPNO
4848423	55732.8746	0.801	97.25	1.97	−7.47	−88.99	2.21	−8.22	KPNO
4848423	55813.6718	0.701	107.10	1.78	2.04	−77.34	2.00	3.75	KPNO
4848423	55813.8059	0.745	112.44	1.89	3.10	−82.15	2.13	3.83	KPNO
4848423	56077.8358	0.649	99.89	1.76	8.40	−57.27	1.98	8.39	KPNO
4848423	56077.9455	0.685	104.74	1.86	2.83	−72.59	2.09	4.91	KPNO
4848423	56079.7246	0.277	−73.92	1.90	−2.29	119.99	2.13	0.60	KPNO
4848423	56079.8997	0.336	−57.54	1.85	2.53	105.59	2.08	−0.72	KPNO
4848423	56082.7363	0.280	−71.29	1.88	0.06	119.89	2.11	0.81	KPNO
4848423	56486.6881	0.767	101.51	2.49	−7.33	−97.83	2.76	−12.40	KPNO
4848423	56486.8539	0.822	89.90	3.12	−10.19	−82.38	3.45	−6.85	KPNO
4848423	56487.9584	0.190	−91.03	2.05	···	93.66	2.29	···	KPNO
4851217	55368.6964	0.919	26.45	4.37	−7.31	−74.63	2.87	4.25	KPNO
4851217	55369.6875	0.320	−138.28	3.22	−3.89	80.46	2.10	3.73	KPNO
4851217	55369.7405	0.341	−137.22	3.48	−10.18	74.33	2.31	4.40	KPNO

Continued on Next Page...

Table 3.4: Radial Velocity Measurements

Object (KIC)	Date (HJD−2,400,000)	Orbital Phase[a]	V_1 (km s^{-1})	σ_1 (km s^{-1})	$(O-C)_1$ (km s^{-1})[b]	V_2 (km s^{-1})	σ_2 (km s^{-1})	$(O-C)_2$ (km s^{-1})[b]	Source (Obs.)
4851217	55369.7709	0.354	−120.84	3.19	1.07	63.50	2.07	−1.68	KPNO
4851217	55369.8190	0.373	−107.08	3.16	5.48	53.27	2.05	−3.26	KPNO
4851217	55401.8413	0.336	−144.06	6.35	−14.85	72.96	4.41	1.02	DAO
4851217	55401.9126	0.364	−110.21	6.31	6.70	59.84	4.36	−0.71	DAO
4851217	55405.7796	0.930	25.74	7.11	−1.42	−62.75	4.88	10.02	DAO
4851217	55431.7139	0.428	−65.02	3.88	14.49	14.66	2.45	−11.28	KPNO
4851217	55432.7500	0.847	71.84	3.10	3.46	−110.99	1.99	−0.07	KPNO
4851217	55432.7820	0.860	67.42	3.18	4.16	−106.47	2.06	−0.29	KPNO
4851217	55432.8480	0.887	58.27	3.62	7.28	−93.67	2.37	1.15	KPNO
4851217	55432.9085	0.911	35.85	3.68	−2.08	−75.32	2.30	7.42	KPNO
4851217	55716.9126	0.875	50.85	3.23	−5.97	−105.56	2.05	−5.34	Lowell
4851217	55753.8661	0.833	70.88	3.58	−2.34	−127.31	2.35	−11.92	Lowell
4851217	55815.8161	0.910	27.82	3.65	−10.66	−79.26	2.27	3.98	KPNO
4851217	56234.6485	0.452	−62.81	3.47	0.08	1.40	2.22	−9.17	Lowell
4851217	56235.6521	0.858	68.45	3.65	4.24	−95.52	2.39	11.54	Lowell
4851217	56488.6784	0.282	−134.76	5.29	7.38	102.47	3.65	18.57	KPNO
5444392	55367.7893	0.712	107.37	2.32	0.21	−132.96	2.58	−1.33	KPNO
5444392	55367.8407	0.745	111.15	2.14	0.44	−135.20	2.40	−0.07	KPNO
5444392	55367.9203	0.798	104.99	2.18	−0.24	−130.09	2.44	−0.39	KPNO
5444392	55368.6683	0.290	−130.22	2.40	2.81	107.34	2.67	1.76	KPNO
5444392	55368.7124	0.319	−125.74	2.47	−0.29	98.72	2.75	0.62	KPNO
5444392	55383.8562	0.285	−129.37	3.42	4.54	109.14	3.73	2.68	Lowell
5444392	55386.8193	0.235	−137.63	2.91	−1.25	105.04	3.20	−3.86	Lowell
5444392	55402.9012	0.819	97.88	4.78	−1.55	−116.89	5.18	7.08	DAO
5444392	55734.6810	0.162	−120.94	2.44	−2.28	92.48	2.71	1.06	KPNO
5444392	55734.7988	0.240	−138.40	2.37	−1.73	107.29	2.63	−1.90	KPNO
5513861	55366.7480	0.647	102.97	1.83	−2.91	−107.74	2.66	−6.75	KPNO
5513861	55366.8105	0.689	117.58	1.86	−3.80	−123.26	2.70	−4.70	KPNO
5513861	55366.8592	0.721	126.10	1.85	−2.15	−137.69	2.67	−11.34	KPNO
5513861	55366.9053	0.752	131.57	1.75	1.31	−127.27	2.53	1.36	KPNO
5513861	55366.9560	0.785	127.75	1.80	0.42	−126.07	2.61	−0.75	KPNO

Continued on Next Page...

Table 3.4: Radial Velocity Measurements

Object (KIC)	Date (HJD−2,400,000)	Orbital Phase[a]	V_1 (km s^{-1})	σ_1 (km s^{-1})	$(O-C)_1$ (km s^{-1})[b]	V_2 (km s^{-1})	σ_2 (km s^{-1})	$(O-C)_2$ (km s^{-1})[b]	Source (Obs.)
5513861	55367.6647	0.254	−113.89	1.84	−1.40	140.99	2.66	−5.32	KPNO
5513861	55367.7101	0.284	−111.51	1.79	−1.80	131.32	2.59	−11.85	KPNO
5513861	55367.7512	0.312	−105.81	1.72	−2.26	125.23	2.50	−10.97	KPNO
5513861	55730.9715	0.822	122.34	2.19	4.20	−113.90	3.07	1.02	KPNO
5513861	55755.7130	0.205	−98.44	2.31	9.19	153.75	3.19	12.96	Lowell
5513861	56077.7097	0.418	−36.80	3.00	14.11	77.62	4.15	1.01	KPNO
5513861	56077.8145	0.487	5.01	1.78	5.70	14.07	2.55	−5.67	KPNO
5513861	56077.9028	0.546	48.35	2.37	4.94	−31.32	3.38	−1.10	KPNO
5513861	56522.9017	0.207	−87.67	2.92	20.38	143.03	3.94	1.76	KPNO
5621294	55369.6957	0.198	−36.00	2.21	−0.55	248.79	46.43	5.50	KPNO
5621294	55734.8111	0.072	−14.58	2.35	−8.52	91.89	45.54	−27.91	KPNO
5621294	56078.7018	0.339	−29.31	2.32	0.38	185.44	45.78	−36.28	KPNO
5621294	56081.8050	0.644	66.85	2.41	2.80	−215.99	46.06	−49.45	KPNO
5621294	56488.9164	0.247	−34.48	2.31	4.01	114.31	···	···	KPNO
5621294	56488.9645	0.298	−33.81	2.40	2.09	351.06	46.74	···	KPNO
5738698	55366.7614	0.296	−76.26	2.44	0.20	99.74	2.78	3.19	KPNO
5738698	55368.7913	0.718	99.58	2.44	5.32	−80.43	2.77	2.89	KPNO
5738698	55368.8630	0.733	92.91	2.49	−2.61	−86.16	2.82	−1.49	KPNO
5738698	55368.9200	0.745	95.19	2.55	−0.79	−90.33	2.89	−5.17	KPNO
5738698	55368.9649	0.754	93.03	2.40	−2.97	−84.50	2.74	0.68	KPNO
5738698	55402.9316	0.818	63.72	3.38	···	−83.08	3.85	−6.08	Lowell
5738698	55431.7764	0.816	91.93	2.75	3.37	−74.31	3.13	3.08	KPNO
5738698	55431.8614	0.834	85.99	3.02	1.86	−67.76	3.42	4.98	KPNO
5738698	55731.8001	0.207	−74.64	2.44	2.25	101.33	2.78	4.39	KPNO
5738698	55734.7638	0.823	89.32	2.61	2.45	−75.34	2.97	0.28	KPNO
5738698	55813.7096	0.240	−80.28	2.47	−0.35	96.56	2.80	−3.61	KPNO
5738698	55813.8211	0.263	−81.26	2.40	−1.48	98.14	2.72	−1.89	KPNO
5738698	55813.8798	0.276	−79.91	2.59	−0.95	96.81	2.92	−2.36	KPNO
6206751	55367.7213	0.205	−76.97	0.84	−0.89	135.89	11.75	−2.99	KPNO
6206751	55431.8376	0.690	−25.70	0.96	−0.20	−254.34	12.23	−10.28	KPNO
6206751	55431.8794	0.723	−24.40	0.92	−0.42	−260.29	12.00	−4.71	KPNO

Continued on Next Page...

Table 3.4: Radial Velocity Measurements

Object (KIC)	Date (HJD−2,400,000)	Orbital Phase[a]	V_1 (km s^{-1})	σ_1 (km s^{-1})	$(O-C)_1$ (km s^{-1})[b]	V_2 (km s^{-1})	σ_2 (km s^{-1})	$(O-C)_2$ (km s^{-1})[b]	Source (Obs.)
6206751	55730.7923	0.748	−21.73	0.99	1.89	−248.04	12.00	10.38	KPNO
6206751	55730.8824	0.820	−27.40	0.97	−1.21	−241.37	11.79	−2.31	KPNO
6206751	55733.8983	0.242	−76.73	0.97	0.38	151.96	11.95	5.24	KPNO
6206751	55733.9578	0.290	−75.42	0.98	0.89	141.68	12.08	0.96	KPNO
7368103	55369.7453	0.287	−43.32	0.93	−1.37	···	···	···	KPNO
7368103	55733.7355	0.062	−27.75	0.78	1.94	···	···	···	KPNO
7368103	55733.9119	0.143	−37.62	0.80	0.39	···	···	···	KPNO
7368103	55734.6906	0.500	−21.28	0.84	0.47	···	···	···	KPNO
7368103	55734.8358	0.567	−15.98	0.87	−2.66	···	···	···	KPNO
7368103	55734.9352	0.612	−6.41	0.86	1.90	···	···	···	KPNO
7368103	55735.7875	0.003	−22.20	1.01	−0.11	···	···	···	KPNO
7368103	56081.7668	0.526	−17.91	0.96	0.50	···	···	···	KPNO
7368103	56082.7739	0.987	−24.05	1.29	−3.96	···	···	···	KPNO
8196180	55369.9433	0.264	−70.54	1.07	−2.21	···	···	···	KPNO
8196180	55735.6994	0.880	25.09	0.96	0.77	···	···	···	KPNO
8196180	55735.8912	0.932	5.89	0.92	1.03	···	···	···	KPNO
8196180	55814.8287	0.431	−5.29	0.71	2.29	···	···	···	KPNO
8196180	55814.8993	0.450	−1.66	0.78	−0.19	···	···	···	KPNO
8196180	56078.9126	0.356	−33.68	0.88	0.38	···	···	···	KPNO
8196180	56082.7964	0.414	−11.63	0.90	1.71	···	···	···	KPNO
8196180	56082.8632	0.432	−6.38	0.98	0.91	···	···	···	KPNO
8196180	56082.9613	0.459	−0.73	0.87	−1.82	···	···	···	KPNO
8196180	56487.9122	0.750	41.14	1.16	−3.90	···	···	···	KPNO
8196180	56487.9738	0.766	42.12	1.49	−2.13	···	···	···	KPNO
8196180	56522.8764	0.273	−67.05	1.05	−1.70	···	···	···	KPNO
8262223	55369.9232	0.191	2.07	1.07	−0.69	212.28	4.33	2.11	KPNO
8262223	55732.8574	0.195	1.49	1.11	−1.09	205.63	4.44	−6.17	KPNO
8262223	55815.8979	0.676	41.49	1.62	−1.14	−161.93	5.51	−0.93	KPNO
8262223	56077.9534	0.139	7.58	1.10	1.24	182.67	4.58	5.94	KPNO
8262223	56078.7629	0.641	40.59	1.11	0.56	−138.54	4.68	−1.78	KPNO
8262223	56078.8440	0.692	42.68	1.07	−0.80	−173.24	4.48	−4.34	KPNO

Continued on Next Page...

Table 3.4: Radial Velocity Measurements

Object (KIC)	Date (HJD−2,400,000)	Orbital Phase[a]	V_1 (km s^{-1})	σ_1 (km s^{-1})	$(O-C)_1$ (km s^{-1})[b]	V_2 (km s^{-1})	σ_2 (km s^{-1})	$(O-C)_2$ (km s^{-1})[b]	Source (Obs.)
8262223	56078.9357	0.748	46.08	1.18	1.15	−181.91	4.85	0.62	KPNO
8262223	56079.7925	0.280	5.07	1.23	3.41	212.05	4.87	−8.52	KPNO
8262223	56081.9642	0.626	37.53	1.25	−1.10	−119.83	4.87	3.84	KPNO
8262223	56082.8204	0.157	4.08	1.09	−0.84	194.75	4.54	4.78	KPNO
8262223	56082.8833	0.196	1.17	1.12	−1.37	212.94	4.66	0.70	KPNO
8262223	56082.9468	0.235	1.47	1.14	0.09	224.05	4.47	0.94	KPNO
8262223	56488.7439	0.812	46.72	2.70	3.42	−158.55	9.18	8.92	KPNO
8552540	55366.8248	0.648	87.30	1.52	2.58	−132.52	4.89	1.50	KPNO
8552540	55366.8735	0.694	109.84	1.39	8.57	−147.14	4.60	7.89	KPNO
8552540	55366.9337	0.751	110.76	1.43	2.08	−158.92	4.65	5.64	KPNO
8552540	55369.6616	0.320	−122.52	1.51	−0.37	138.39	4.78	11.14	KPNO
8552540	55406.7586	0.253	−129.88	2.48	3.62	131.18	8.81	−10.21	DAO
8552540	55406.8217	0.312	−116.15	2.61	8.19	117.39	9.23	−12.60	DAO
8552540	55432.7569	0.735	105.45	1.22	−2.70	−167.05	4.19	−3.21	KPNO
8552540	55432.7894	0.766	107.03	1.64	−1.08	−167.01	4.98	−3.14	KPNO
8552540	55432.7978	0.773	104.05	1.24	−3.32	−169.00	4.23	−6.03	KPNO
8552540	55432.8707	0.842	84.01	1.35	−4.95	−144.24	4.46	−4.35	KPNO
8552540	55730.6861	0.288	−128.97	1.28	1.05	135.85	4.32	−1.25	KPNO
8552540	55733.7740	0.196	−129.82	1.30	−3.16	132.06	4.36	−0.53	KPNO
8552540	56235.6171	0.771	109.11	1.60	1.46	−159.60	4.89	3.71	Lowell
8553788	55369.6658	0.172	18.31	0.78	−2.03	···	···	···	KPNO
8553788	55732.8862	0.314	21.27	0.87	1.26	···	···	···	KPNO
8553788	55813.8364	0.713	36.24	0.77	−0.04	···	···	···	KPNO
8553788	55814.8626	0.352	18.85	0.95	−2.19	···	···	···	KPNO
8553788	56078.9698	0.786	36.44	0.86	0.15	···	···	···	KPNO
8553788	56079.6847	0.231	19.74	1.59	0.35	···	···	···	KPNO
8553788	56079.7743	0.287	21.19	1.03	1.63	···	···	···	KPNO
8553788	56079.8793	0.352	22.89	0.89	1.85	···	···	···	KPNO
8553788	56486.7582	0.675	40.89	1.44	5.30	···	···	···	KPNO
8823397	55368.9396	0.473	−25.51	1.21	0.26	61.17	6.66	46.06	KPNO
8823397	55734.8936	0.389	−35.61	1.45	0.73	97.23	7.11	−22.37	KPNO

Continued on Next Page...

Table 3.4: Radial Velocity Measurements

Object (KIC)	Date (HJD−2,400,000)	Orbital Phase[a]	V_1 (km s^{-1})	σ_1 (km s^{-1})	$(O-C)_1$ (km s^{-1})[b]	V_2 (km s^{-1})	σ_2 (km s^{-1})	$(O-C)_2$ (km s^{-1})[b]	Source (Obs.)
8823397	56078.8547	0.706	−1.99	1.25	−1.59	−244.33	6.31	−8.17	KPNO
8823397	56079.9248	0.416	−31.74	1.64	1.42	78.32	7.84	−9.82	KPNO
8823397	56081.9282	0.746	−0.74	1.22	−1.18	−250.23	6.27	−5.62	KPNO
8823397	56487.9324	0.247	−46.58	2.24	−2.29	201.16	9.41	3.20	KPNO
8823397	56488.7631	0.798	1.38	1.77	1.96	−233.58	8.36	1.05	KPNO
8823397	56488.8100	0.830	2.58	2.43	4.87	−211.35	10.06	6.43	KPNO
8823397	56522.8113	0.399	−31.20	2.37	3.96	100.46	10.08	−7.48	KPNO
9159301	55369.7756	0.798	33.28	0.96	−2.89	−152.25	11.03	−13.22	KPNO
9159301	55732.9539	0.077	−14.99	0.92	0.47	75.04	10.66	5.58	KPNO
9159301	55735.7364	0.991	6.13	0.83	2.61	77.77	···	···	KPNO
9159301	55735.9594	0.064	−11.45	1.01	1.36	101.93	11.84	···	KPNO
9159301	55751.8454	0.282	−33.57	1.06	0.60	127.35	11.14	−18.23	Lowell
9159301	55813.7240	0.605	27.93	0.85	4.29	−84.83	10.19	3.08	KPNO
9159301	56078.7384	0.644	29.36	0.95	−0.62	−113.42	10.48	0.19	KPNO
9159301	56079.8097	0.996	3.83	0.89	1.36	64.65	···	···	KPNO
9159301	56079.9468	0.041	−12.40	1.03	−4.69	92.58	11.41	···	KPNO
9159301	56081.6945	0.615	28.32	1.36	2.91	−103.87	12.93	−8.81	KPNO
9159301	56081.8717	0.673	32.60	0.95	−1.00	−159.99	10.98	−31.69	KPNO
9159301	56082.9143	0.015	−8.12	0.91	−6.11	110.69	10.73	···	KPNO
9159301	56488.7904	0.318	−26.80	1.44	4.84	−102.96	13.23	···	KPNO
9159301	56521.9511	0.209	−35.09	1.09	−1.41	138.24	11.18	−5.13	KPNO
9357275	55369.8726	0.794	65.59	0.92	−2.61	···	···	···	KPNO
9357275	55716.8688	0.265	−92.20	1.43	−1.03	···	···	···	Lowell
9357275	55731.8229	0.680	65.13	0.86	1.59	···	···	···	KPNO
9357275	55735.8129	0.192	−84.90	1.16	1.26	···	···	···	KPNO
9357275	55735.9145	0.256	−94.84	1.11	−3.39	···	···	···	KPNO
9357275	56079.7052	0.708	66.31	1.02	−2.22	···	···	···	KPNO
9357275	56079.7567	0.741	71.78	0.99	0.60	···	···	···	KPNO
9357275	56079.8617	0.807	68.54	0.99	2.34	···	···	···	KPNO
9357275	56488.7019	0.215	−89.07	1.20	0.42	···	···	···	KPNO
9357275	56488.8570	0.312	−80.35	1.56	5.03	···	···	···	KPNO

Continued on Next Page...

Table 3.4: Radial Velocity Measurements

Object (KIC)	Date (HJD−2,400,000)	Orbital Phase[a]	V_1 (km s^{-1})	σ_1 (km s^{-1})	$(O-C)_1$ (km s^{-1})[b]	V_2 (km s^{-1})	σ_2 (km s^{-1})	$(O-C)_2$ (km s^{-1})[b]	Source (Obs.)
9402652	55366.6998	0.311	−119.60	2.69	0.04	150.61	2.42	2.05	KPNO
9402652	55366.7364	0.345	−109.15	2.74	−3.99	133.87	2.46	−0.16	KPNO
9402652	55366.7978	0.402	−65.13	3.56	3.93	97.13	3.20	−0.74	KPNO
9402652	55366.8468	0.448	−37.60	3.59	−5.25	67.83	3.22	6.71	KPNO
9402652	55367.8523	0.385	−76.86	3.37	4.50	103.92	3.03	−6.27	KPNO
9402652	55403.7707	0.856	123.58	6.74	−3.64	−98.89	6.17	−0.74	DAO
9402652	55434.7970	0.769	159.65	2.79	2.49	−127.60	2.52	0.61	KPNO
9402652	55730.7776	0.586	97.18	3.41	8.80	−69.47	3.06	−9.85	KPNO
9402652	55813.6353	0.799	152.53	2.56	1.21	−122.11	2.29	0.21	KPNO
9402652	55813.6860	0.847	138.02	2.66	5.56	−100.69	2.38	2.70	KPNO
9402652	55814.7846	0.870	117.61	3.55	−1.31	−86.89	3.21	2.94	KPNO
9402652	55814.8490	0.930	75.85	3.53	0.70	−46.86	3.16	−0.86	KPNO
9402652	55815.7578	0.777	150.55	2.49	−5.53	−128.62	2.22	−1.51	KPNO
9402652	55815.8236	0.839	131.60	2.58	−4.85	−108.36	2.31	−0.97	KPNO
9402652	55815.8822	0.893	102.24	3.57	−1.47	−69.27	3.21	5.32	KPNO
9592855	55369.8005	0.031	−25.16	2.29	−4.58	53.32	3.10	17.35	KPNO
9592855	56078.8302	0.525	36.12	2.31	5.95	−31.75	3.12	−16.80	KPNO
9592855	56081.8543	0.005	4.23	1.86	1.19	11.14	2.52	−1.11	KPNO
9592855	56486.7320	0.056	−43.49	4.72	−1.59	75.97	6.10	18.59	KPNO
9592855	56486.8808	0.178	−121.23	3.12	0.86	138.56	4.02	0.62	KPNO
9592855	56488.7212	0.687	141.97	2.37	1.09	−121.57	3.15	4.59	KPNO
9592855	56488.8381	0.783	146.83	2.28	−2.06	−128.01	3.00	6.21	KPNO
9602595	55367.6794	0.795	19.02	0.82	−1.07	−185.04	7.37	−0.91	KPNO
9602595	55431.7621	0.813	22.26	0.81	3.55	−181.41	7.50	−3.99	KPNO
9602595	55431.8984	0.852	18.37	1.33	3.91	−202.87	9.16	···	KPNO
9602595	55733.7205	0.716	21.42	0.85	0.71	−190.98	7.29	−4.28	KPNO
9602595	55733.8419	0.750	24.96	0.78	3.45	−183.68	6.99	7.18	KPNO
9602595	55733.9739	0.788	20.02	0.80	−0.49	−187.18	7.14	−0.97	KPNO
9602595	55735.8491	0.315	−47.38	0.82	−0.38	137.43	7.44	−10.98	KPNO
9602595	55815.7715	0.787	19.20	0.76	−1.35	−201.03	7.14	−14.67	KPNO
9602595	56077.8246	0.470	−18.68	1.09	2.30	43.59	8.72	23.11	KPNO

Continued on Next Page...

Table 3.4: Radial Velocity Measurements

Object (KIC)	Date (HJD−2,400,000)	Orbital Phase[a]	V_1 (km s^{-1})	σ_1 (km s^{-1})	$(O-C)_1$ (km s^{-1})[b]	V_2 (km s^{-1})	σ_2 (km s^{-1})	$(O-C)_2$ (km s^{-1})[b]	Source (Obs.)
9602595	56077.9122	0.494	−18.94	0.97	−3.44	24.05	7.95	30.68	KPNO
9602595	56078.7239	0.722	17.92	1.07	−3.05	−181.66	8.31	6.36	KPNO
9602595	56078.8197	0.749	17.88	0.80	−3.63	−184.16	7.45	6.69	KPNO
9602595	56521.9758	0.354	−40.94	1.27	1.68	24.61	···	···	KPNO
9851944	55367.6938	0.318	−117.36	2.36	0.10	102.52	2.04	−2.46	KPNO
9851944	55368.6869	0.776	119.45	2.20	−0.43	−117.70	1.89	−1.60	KPNO
9851944	55368.7235	0.793	117.46	2.31	0.47	−110.14	2.00	3.26	KPNO
9851944	55368.7705	0.815	113.54	2.42	2.25	−107.04	2.09	1.05	KPNO
9851944	55368.8208	0.838	96.91	2.27	−5.92	−102.74	1.96	−2.53	KPNO
9851944	55369.6816	0.236	−130.78	2.27	−2.70	112.84	1.97	−2.03	KPNO
9851944	55369.7259	0.257	−126.56	2.39	1.88	118.03	2.08	2.82	KPNO
9851944	55369.7869	0.285	−122.38	2.34	3.19	115.63	2.03	3.09	KPNO
9851944	55369.8234	0.302	−121.19	2.24	0.83	108.25	1.94	−0.97	KPNO
9851944	55434.8181	0.338	−113.02	2.33	−2.92	97.98	2.01	−0.14	KPNO
9851944	55449.9141	0.314	−104.95	2.45	13.68	134.64	2.13	···	Lowell
9851944	55463.8100	0.736	133.77	2.55	12.68	−104.76	2.23	12.47	Lowell
9851944	55755.9599	0.746	114.08	2.47	−7.49	−128.96	2.14	−11.29	Lowell
9899416	55367.7426	0.193	−116.90	1.15	0.43	172.96	8.56	−8.13	KPNO
9899416	55367.8219	0.253	−128.10	1.18	−3.98	192.63	8.61	−1.53	KPNO
9899416	55401.8241	0.769	89.29	6.66	−2.19	−249.49	29.72	−25.74	DAO
9899416	55401.8949	0.822	84.40	5.77	3.10	−205.00	26.00	−1.06	DAO
9899416	55402.8665	0.551	14.81	6.01	−3.58	−121.31	27.28	−38.99	DAO
9899416	55403.8122	0.261	−126.75	7.52	−2.87	191.28	33.54	−2.40	DAO
9899416	55403.8575	0.295	−121.90	7.08	−2.07	213.61	31.76	27.83	DAO
9899416	55403.9098	0.334	−104.07	7.13	5.24	166.85	31.92	1.52	DAO
9899416	55404.9541	0.118	−89.07	6.94	−0.07	120.45	31.03	−5.81	DAO
9899416	55405.8040	0.756	88.18	6.68	−4.01	−234.75	29.84	−9.60	DAO
9899416	55406.7954	0.500	−17.43	6.30	−1.33	−10.42	28.46	5.05	DAO
9899416	55431.7022	0.191	−110.96	1.93	5.74	176.69	10.71	−3.18	KPNO
9899416	55431.7559	0.231	−119.18	1.52	4.18	194.72	9.62	1.99	KPNO
9899416	55463.8754	0.334	−99.69	3.43	9.56	228.02	16.43	···	Lowell

Continued on Next Page...

Table 3.4: Radial Velocity Measurements

Object (KIC)	Date (HJD−2,400,000)	Orbital Phase[a]	V_1 (km s^{-1})	σ_1 (km s^{-1})	$(O-C)_1$ (km s^{-1})[b]	V_2 (km s^{-1})	σ_2 (km s^{-1})	$(O-C)_2$ (km s^{-1})[b]	Source (Obs.)
9899416	55463.9425	0.385	−84.16	1.90	3.42	176.02	11.11	···	Lowell
9899416	55716.9386	0.241	−137.19	2.98	−13.21	181.72	13.91	−12.19	Lowell
9899416	55718.9411	0.744	96.91	2.54	4.72	−217.14	12.58	8.02	Lowell
9899416	55720.9233	0.232	−126.27	3.76	−2.85	200.67	16.93	7.83	Lowell
9899416	55730.8765	0.701	88.52	1.51	1.36	−197.68	9.33	17.79	KPNO
9899416	55734.8575	0.688	84.62	1.56	0.37	−206.75	9.39	3.11	KPNO
9899416	55754.9232	0.746	144.74	6.74	52.51	−214.71	29.76	10.53	Lowell
10156064	55369.8314	0.539	19.45	1.12	−2.82	−31.14	5.99	−5.99	KPNO
10156064	55731.7920	0.079	−23.59	1.16	9.22	70.93	6.15	14.17	KPNO
10156064	55733.8698	0.507	5.13	1.00	−1.77	37.34	···	···	KPNO
10156064	55751.9310	0.226	−60.50	1.27	11.68	105.65	6.37	−9.79	Lowell
10156064	55814.7987	0.173	−66.28	1.13	−2.11	105.65	5.95	2.16	KPNO
10156064	56078.8130	0.542	18.20	1.21	−5.50	−36.11	6.58	−8.82	KPNO
10156064	56078.9811	0.577	34.99	1.24	−4.21	−60.92	6.76	−10.54	KPNO
10156064	56081.7235	0.141	−58.81	1.97	−2.92	92.63	8.45	1.48	KPNO
10156064	56081.8969	0.177	−65.01	1.49	0.14	83.35	7.17	−21.60	KPNO
10156064	56082.8570	0.375	−50.29	1.17	0.32	76.65	6.23	−6.72	KPNO
10156064	56234.5997	0.624	59.56	1.36	2.09	−66.29	6.91	11.30	Lowell
10156064	56235.6362	0.837	69.15	1.40	0.06	−113.76	6.79	−18.78	Lowell
10156064	56487.8960	0.786	85.86	1.35	7.49	−102.83	6.79	5.96	KPNO
10191056	55367.8272	0.050	−53.55	1.86	−2.69	15.81	3.09	−1.19	KPNO
10191056	55369.6535	0.802	77.14	1.82	2.93	−136.62	2.91	−3.94	KPNO
10191056	55369.7182	0.829	67.75	1.85	0.22	−127.12	3.01	−2.39	KPNO
10191056	55404.7418	0.257	−119.37	3.68	0.24	97.24	6.17	−2.59	DAO
10191056	55404.8035	0.282	−107.75	3.72	9.91	94.84	6.23	−2.72	DAO
10191056	55404.8843	0.316	−102.28	3.94	9.09	85.14	6.64	−4.96	DAO
10191056	55405.8834	0.727	80.67	3.86	2.15	−122.36	6.53	15.29	DAO
10191056	55405.9557	0.757	74.28	4.25	−5.17	−131.60	7.07	7.25	DAO
10191056	55432.8041	0.817	74.21	1.57	3.37	−136.59	2.64	−7.92	KPNO
10191056	55717.8019	0.221	−115.89	2.06	2.18	104.71	3.23	6.82	Lowell
10191056	55733.6676	0.757	81.70	1.57	2.25	−140.85	2.58	−2.00	KPNO

Continued on Next Page...

Table 3.4: Radial Velocity Measurements

Object (KIC)	Date (HJD−2,400,000)	Orbital Phase[a]	V_1 (km s^{-1})	σ_1 (km s^{-1})	$(O-C)_1$ (km s^{-1})[b]	V_2 (km s^{-1})	σ_2 (km s^{-1})	$(O-C)_2$ (km s^{-1})[b]	Source (Obs.)
10191056	55734.6699	0.170	−122.62	1.71	−15.28	94.25	2.78	9.35	KPNO
10191056	56077.7444	0.498	−25.91	1.64	−4.87	−21.01	2.65	−3.07	KPNO
10191056	56077.8710	0.551	4.41	1.96	−6.67	−60.89	3.22	−4.43	KPNO
10206340	55366.6695	0.760	17.11	1.35	2.58	−160.77	6.28	4.03	KPNO
10206340	55366.7134	0.770	21.77	1.30	7.48	−154.67	6.14	9.33	KPNO
10206340	55368.8540	0.239	−68.49	1.30	−0.01	112.26	6.15	2.97	KPNO
10206340	55368.9108	0.252	−67.63	1.50	0.95	108.94	6.67	−0.67	KPNO
10206340	55402.8063	0.678	9.53	2.89	−0.85	−145.94	11.62	5.14	DAO
10206340	55403.9029	0.918	−20.40	1.39	−13.96	−110.81	6.29	−15.20	Lowell
10206340	55403.9348	0.925	−8.60	2.96	−0.55	−97.99	12.12	−7.69	DAO
10206340	55404.9061	0.138	−50.47	3.06	8.16	72.79	12.03	−3.93	DAO
10206340	55405.8383	0.342	−54.51	3.28	7.33	87.10	12.80	−0.31	DAO
10206340	55406.8371	0.561	−15.09	2.97	−3.58	−89.61	11.78	−10.84	DAO
10206340	55432.7658	0.241	−67.75	1.19	0.77	118.67	5.70	9.27	KPNO
10206340	55432.8145	0.252	−67.06	1.13	1.52	116.87	5.59	7.27	KPNO
10206340	55432.8620	0.262	−71.66	1.18	−3.21	97.69	5.69	−11.51	KPNO
10206340	55731.7078	0.736	17.85	1.37	3.40	−166.20	6.22	−1.69	KPNO
10206340	55733.6955	0.171	−61.45	1.28	2.11	89.82	6.01	−3.14	KPNO
10206340	55754.7615	0.786	6.81	1.75	−6.73	−159.65	7.08	1.92	Lowell
10486425	55369.8616	0.861	67.22	1.54	1.32	−77.12	4.97	4.04	KPNO
10486425	55730.7617	0.280	−58.16	1.75	−0.28	88.55	5.41	−2.19	KPNO
10486425	55730.9522	0.317	−54.17	1.63	−1.10	93.73	5.08	9.65	KPNO
10486425	55735.7825	0.232	−58.10	1.61	0.63	90.43	5.04	−1.47	KPNO
10486425	55814.8837	0.228	−58.36	1.51	0.15	87.06	4.81	−4.54	KPNO
10486425	56081.7320	0.817	72.68	1.35	−3.50	−88.22	4.47	7.19	KPNO
10486425	56081.9505	0.859	68.91	1.38	2.39	−93.48	4.56	−11.46	KPNO
10486425	56486.7817	0.607	61.50	4.31	5.86	−69.28	12.57	−2.50	KPNO
10581918	55368.8052	0.336	−85.29	1.00	−1.34	65.41	18.18	−21.59	KPNO
10581918	55730.8061	0.239	−86.84	1.14	0.28	113.78	18.39	2.63	KPNO
10581918	55730.9330	0.310	−85.65	1.03	−0.06	94.81	17.28	−4.77	KPNO
10581918	55731.7281	0.751	−38.62	1.04	2.91	−263.01	17.53	−22.72	KPNO

Continued on Next Page...

Table 3.4: Radial Velocity Measurements

Object (KIC)	Date (HJD−2,400,000)	Orbital Phase[a]	V_1 (km s^{-1})	σ_1 (km s^{-1})	$(O-C)_1$ (km s^{-1})[b]	V_2 (km s^{-1})	σ_2 (km s^{-1})	$(O-C)_2$ (km s^{-1})[b]	Source (Obs.)
10581918	55731.8407	0.813	−43.85	0.96	−0.54	−235.29	16.82	−8.57	KPNO
10581918	55733.6766	0.832	−46.94	0.97	−2.43	−221.73	17.02	−4.17	KPNO
10581918	55813.6510	0.216	−84.27	1.19	2.40	103.50	18.22	−4.11	KPNO
10581918	56077.6931	0.755	−44.33	1.17	−2.79	−239.75	18.44	0.47	KPNO
10581918	56077.7844	0.805	−39.48	1.05	3.42	−228.73	18.41	1.14	KPNO
10581918	56077.8760	0.856	−46.22	1.05	0.21	−187.21	18.82	15.56	KPNO
10581918	56082.6870	0.526	−63.15	1.42	−2.55	−138.48	21.19	···	KPNO
10619109	55369.8955	0.798	8.58	0.91	−0.24	−175.37	15.75	2.98	KPNO
10619109	55735.6859	0.654	3.66	1.17	−0.88	−164.13	16.48	−7.66	KPNO
10619109	56078.8792	0.462	−30.97	0.85	−0.30	69.88	15.10	52.57	KPNO
10619109	56079.9679	0.994	−21.96	1.08	−0.46	20.64	15.64	50.82	KPNO
10619109	56081.8864	0.932	−7.17	1.04	1.88	−67.87	16.68	23.45	KPNO
10661783	55366.6888	0.372	−52.25	1.00	2.99	49.19	18.66	···	KPNO
10661783	55367.7378	0.224	−62.41	1.01	−1.69	183.41	18.70	−20.29	KPNO
10661783	55402.7936	0.693	−20.23	3.76	0.96	−287.20	41.10	−14.98	DAO
10661783	55402.8543	0.742	−20.25	3.95	−0.34	−484.18	···	···	DAO
10661783	55402.8773	0.761	−23.37	4.07	−3.43	−519.73	···	···	DAO
10661783	55402.9264	0.801	−19.69	3.89	1.24	−295.27	42.40	−19.93	DAO
10661783	55403.8815	0.577	−38.56	1.26	−7.63	−115.94	19.64	38.98	Lowell
10661783	55403.8971	0.589	−24.14	3.83	5.37	−17.12	···	···	DAO
10661783	55404.7169	0.255	−65.40	3.92	−4.42	185.33	42.79	−21.56	DAO
10661783	55404.7804	0.307	−65.47	3.84	−5.76	181.53	41.97	−10.02	DAO
10661783	55404.8468	0.360	−51.02	3.89	5.22	172.40	42.36	22.65	DAO
10661783	55405.9783	0.279	−67.25	3.92	−6.61	216.17	42.76	13.37	DAO
10661783	55406.7834	0.933	−29.76	3.92	2.30	−50.80	···	···	DAO
10661783	55431.7377	0.199	−56.54	0.97	3.40	187.45	18.00	−6.87	KPNO
10661783	55431.8157	0.262	−62.90	1.09	−1.97	180.02	18.71	−26.27	KPNO
10661783	55463.7831	0.223	−51.27	1.18	9.43	206.48	19.04	2.99	Lowell
10661783	55753.8456	0.785	−22.34	1.37	−1.95	−285.25	20.70	−3.41	Lowell
10686876	55369.9024	0.855	46.86	1.10	1.63	···	···	···	KPNO
10686876	55731.7582	0.052	−26.41	0.97	2.07	···	···	···	KPNO

Continued on Next Page...

Table 3.4: Radial Velocity Measurements

Object (KIC)	Date (HJD−2,400,000)	Orbital Phase[a]	V_1 (km s^{-1})	σ_1 (km s^{-1})	$(O-C)_1$ (km s^{-1})[b]	V_2 (km s^{-1})	σ_2 (km s^{-1})	$(O-C)_2$ (km s^{-1})[b]	Source (Obs.)
10686876	55732.8200	0.457	−22.79	0.99	2.15	···	···	···	KPNO
10686876	55732.9675	0.514	−2.61	1.00	−0.99	···	···	···	KPNO
10686876	56078.7500	0.571	18.63	1.17	−2.95	···	···	···	KPNO
10686876	56079.7413	0.950	10.60	1.92	−2.69	···	···	···	KPNO
10686876	56079.8231	0.981	4.08	1.11	3.52	···	···	···	KPNO
10686876	56079.9108	0.015	−19.53	1.14	−6.12	···	···	···	KPNO
10686876	56079.9596	0.033	−19.99	1.10	1.12	···	···	···	KPNO
10686876	56488.8977	0.211	−72.83	1.97	−1.04	···	···	···	KPNO
10686876	56521.9353	0.828	81.77	1.24	···	···	···	···	KPNO
10686876	56522.9367	0.211	−72.95	1.35	−1.18	···	···	···	KPNO
10736223	55367.9337	0.121	−35.18	1.42	−0.93	144.66	23.48	2.20	KPNO
10736223	56077.8457	0.521	3.63	1.30	0.03	−40.08	22.52	−11.05	KPNO
10736223	56081.8318	0.128	−34.96	1.23	0.67	145.13	21.82	−3.63	KPNO
10858720	55367.8833	0.677	105.21	2.29	2.21	−177.36	2.47	−5.36	KPNO
10858720	55368.8993	0.744	118.12	2.45	−0.37	−187.33	2.63	0.88	KPNO
10858720	55369.9149	0.810	106.15	2.32	−1.79	−176.76	2.49	0.31	KPNO
10858720	55400.8167	0.257	−184.38	5.83	−1.19	120.40	6.18	−8.21	DAO
10858720	55401.7965	0.286	−182.94	5.96	−3.44	118.72	6.32	−6.00	DAO
10858720	55402.8081	0.348	−148.92	3.61	6.61	58.41	3.86	−41.08	Lowell
10858720	55431.7241	0.710	117.18	2.58	3.31	−182.84	2.77	0.55	KPNO
10858720	55718.8795	0.224	−166.66	3.71	14.69	133.98	3.94	7.26	Lowell
10858720	55720.8708	0.315	−294.39	21.78	−123.48	−86.57	23.01	···	Lowell
10858720	55735.8420	0.035	−82.95	3.54	−17.80	31.13	3.79	26.34	KPNO
12071006	55730.9073	0.143	−53.01	0.67	3.54	76.52	18.07	−8.77	KPNO
12071006	55733.8159	0.620	−30.86	0.91	3.11	−137.42	20.53	20.80	KPNO
12071006	55815.7185	0.056	−51.14	0.76	−1.37	54.11	19.17	41.77	KPNO
12071006	55815.8549	0.078	−55.20	0.77	−3.45	38.52	19.28	4.93	KPNO
12071006	56077.7586	0.041	−54.02	0.80	−5.60	−2.64	19.94	−0.36	KPNO
12071006	56077.9201	0.067	−47.24	0.82	3.59	32.84	19.50	9.15	KPNO

[a] Relative to T_0 at primary eclipse.

[b] No data in $O-C$ columns indicates RV measurement was excluded from the orbital fit.

3.3.2 Comparison with TODCOR

To confirm the accuracy and reliability of our double cross-correlation scheme we compared our derived radial velocities with those from TODCOR, which represents a reliable standard for velocity measurements. We used a version of TODCOR written in IDL by James Davenport[3]. This code produces the $R(s_1, s_2, \alpha)$ matrix for a given value of α, then determines the radial velocities using the IDL DERIV procedure to find the local maximum position of $R(s_1, s_2, \alpha)$. We found that the local maximum may sit on a sloping background in some cases where the companion is faint, so we added an option to remove the background before finding the position of the maximum.

We first applied the IDL version of TODCOR to synthetic spectra formed by co-adding templates with known Doppler shifts and flux ratio. In every test case, TODCOR recovered correctly the adopted radial velocities of the primary and secondary within the uncertainties, and our own double cross-correlation scheme also produced velocities that matched the known model values. Next we compared radial velocities derived from both TODCOR and our double cross-correlation method for KIC 5738698, and found that both sets agreed within the mutual uncertainties. Similar good agreement was found with other systems. Thus, we are confident that the radial velocities we measured using our double cross-correlation method are reliable and unhampered by systematic errors.

[3]`https://github.com/jradavenport/jradavenport_idl/blob/master/todcor.pro`

3.3.3 Orbital Solutions

Orbital elements for each star were determined using a nonlinear, least-squares fitting routine (Morbey & Brosterhus 1974). The periods (P) and epochs (T_0) were fixed to the values obtained from the eclipse timings of Gies et al. (2015, see Section 2.4), with the epoch corresponding to the time of primary eclipse. The radial velocities were weighted by the inverse square of the uncertainties divided by the mean uncertainty for each star, while those with anomalous measurements were zero weighted and omitted from the fitting process (radial velocities without $O - C$ values in Table 3.4).

In order to derive orbital parameters and optimize our observing time we concentrated on obtaining spectra during velocity extrema or quadrature phases to best constrain the orbits using fewer velocity measurements. Because of the resulting partial orbital coverage for many of the systems and the nature of short-period binaries, we used circular orbits to fit the velocities, with three exceptions: KIC 4544587, 4851217, and 8196180. The first system is a known 2.18 d period eccentric binary ($e = 0.275$) with tidally induced pulsations, strong apsidal motion, and self-excited pressure and gravity modes studied in detail by Hambleton et al. (2013). We therefore use the eccentricity (e) and argument of periastron (ω) determined by Hambleton et al. when fitting the spectroscopic orbit of KIC 4544587. KIC 4851217 and 8196180 were identified as eccentric in Gies et al. (2015) and have separations between their primary and secondary eclipses that deviate from one-half the period (as in a circular system) by more than ± 0.005 (Kirk et al. 2016). We use $e \sin \omega$ and $e \cos \omega$ as reported by Slawson et al. (2011) to determine e and ω for KIC 4851217 and hold them fixed when determining

the orbital solution, as they are not well constrained by our radial velocities. However, the values of e and ω given in Slawson et al. for KIC 8196180 did not agree with our derived radial velocities. We therefore fit for e and ω based on the offset between ($e\cos\omega$) and duration ($e\sin\omega$) of the two eclipses in the *Kepler* light curve using the method outlined in Appendix A (also see Section 4.4.3.1), obtaining values of $e = 0.18$ and $\omega = 145\,\mathrm{deg}$, which were then fixed to derive the spectroscopic orbital elements.

The primary and secondary radial velocities for each system were fit separately, providing consistency checks of the fits as well as our derived radial velocities. While the systemic velocities for the primary (γ_1) and secondary (γ_2) agree within uncertainties for most systems, mismatches highlight large uncertainties in the secondary velocities and/or orbits that are not well constrained. For systems with highly discrepant systemic velocities, especially those with small mass and/or flux ratios where the secondary radial velocities were not as well constrained, the systemic velocities of the secondary (γ_2) were fixed to the value derived from the primary as noted in Table 3.5.

Orbital parameters for each system, including the period (P), time of primary eclipse (T_0), velocity semi-amplitudes of the primary (K_1) and secondary (K_2), systemic velocities of the primary (γ_1) and secondary (γ_2), eccentricity (e), argument of periastron (ω), root mean square of the primary (rms_1) and secondary (rms_2) velocity fits, the derived mass ratio ($q = M_2/M_1$), inclination (i), semi-major axis (a), and derived masses of the primary (M_1) and secondary (M_2) are given in Table 3.5. The inclination values are taken from Slawson et al. (2011) and were used to determine the semi-major axis (a), mass of the primary

Table 3.5. Orbital Solutions

KIC	P (d)	T_0 (HJD−2, 400, 000)	K_1 (km s^{-1})	K_2 (km s^{-1})	γ_1 (km s^{-1})	γ_2 (km s^{-1})	e	ω (deg)	rms$_1$ (km s^{-1})	rms$_2$ (km s^{-1})	M_2/M_1	i (deg)	a ($R_\odot$)	M_1 ($M_\odot$)	M_2 ($M_\odot$)
2305372	1.40469145	55693.58496	80 ± 2	152 ± 7	−14 ± 1	−14[a]	0.0	···	2.3	14.7	0.52 ± 0.03	90[g]	6.4 ± 0.2	1.2 ± 0.1	0.62 ± 0.04
2708156	1.89126932	55690.03950	54 ± 2	238 ± 8	−25 ± 2	−25[a]	0.0	···	8.3	25.3	0.23 ± 0.01	84.2	11.0 ± 0.3	4.05 ± 0.3	0.92 ± 0.07
3241619	1.70334707	55694.50030	92.5 ± 0.5	135 ± 3	−47.1 ± 0.4	−47[a]	0.0	···	1.2	7.7	0.69 ± 0.02	84.0	7.7 ± 0.1	1.24 ± 0.04	0.86 ± 0.02
3327980	4.23102194	55699.074202	89 ± 2	102 ± 3	10 ± 2	10 ± 2	0.0	···	4.6	5.8	0.87 ± 0.03	85.1	16.0 ± 0.3	1.66 ± 0.07	1.44 ± 0.06
3440230	2.88110031	55690.39643	38 ± 1	151 ± 6	−5.4 ± 0.9	−5.4[a]	0.0	···	2.8	14.2	0.25 ± 0.01	86.8	10.7 ± 0.3	1.6 ± 0.1	0.40 ± 0.03
4544587	2.18911430	55689.673044	114 ± 4	135 ± 5	−24 ± 4	−19 ± 5	0.28[b]	329[b]	12.8	16.0	0.84 ± 0.04	87.9[b]	10.4 ± 0.3	1.69 ± 0.1	1.42 ± 0.09
4574310	1.30622004	55644.346499	42.6 ± 0.6	188 ± 4	−44.2 ± 0.6	−44.2[a]	0.0	···	1.6	11.4	0.227 ± 0.006	82.5	6.0 ± 0.1	1.38 ± 0.06	0.31 ± 0.01
4660997	0.56256070	55654.43913	139 ± 7	184 ± 5	−32 ± 5	−32[a]	0.0	···	13.5	12.2	0.76 ± 0.05	80.5	3.6 ± 0.1	1.16 ± 0.07	0.88 ± 0.07
4665989	2.248067589	55646.917282	100.2 ± 0.4	134 ± 4	−26.8 ± 0.4	−26.8[a]	0.0	···	1.3	13.1	0.75 ± 0.02	82.5	10.5 ± 0.2	1.77 ± 0.09	1.32 ± 0.05
4848423	3.0036461	55928.7090	91 ± 2	103 ± 2	18 ± 2	17 ± 2	0.0	···	6.0	7.4	0.88 ± 0.03	87.3[f]	11.6 ± 0.2	1.22 ± 0.05	1.08 ± 0.04
4851217	2.47028283	55643.10900	115 ± 2	107 ± 2	−26 ± 2	−24 ± 2	0.03[c]	211[c]	7.0	7.2	1.08 ± 0.03	77.8	11.1 ± 0.2	1.43 ± 0.05	1.55 ± 0.05
5444392	1.51952889	55688.84830	123.8 ± 0.7	122.3 ± 0.8	−13.1 ± 0.6	−12.9 ± 0.7	0.0	···	2.0	2.3	1.013 ± 0.008	86.3	7.41 ± 0.03	1.17 ± 0.01	1.19 ± 0.1
5513861	1.51020825	55625.52615	121 ± 1	138 ± 2	9 ± 1	9[a]	0.0	···	4.2	7.8	0.88 ± 0.02	80.9	7.82 ± 0.08	1.50 ± 0.04	1.32 ± 0.03
5621294	0.938905233	55693.432093	57 ± 3	238 ± 20	19 ± 3	19[a]	0.0	···	5.0	37.1	0.24 ± 0.02	75.3	5.7 ± 0.4	2.2 ± 0.4	0.54 ± 0.08
5738698	4.80877396	55692.334870	88.1 ± 0.6	92.8 ± 1	8.0 ± 0.6	8 ± 1	0.0	···	2.3	3.6	0.95 ± 0.01	86.3[d]	17.2 ± 0.1	1.52 ± 0.03	1.44 ± 0.02
6206751	1.24534281	55683.783072	26.8 ± 0.5	203 ± 3	−50.4 ± 0.4	−56 ± 3	0.0	···	1.2	8.0	0.132 ± 0.003	76.3	5.81 ± 0.08	1.50 ± 0.05	0.198 ± 0.007
7368103	2.18251508	55698.67906	21 ± 1	···	−21.8 ± 0.7	···	0.0	···	2.0	···	···	78.0	···	···	···
8196180	3.67165963	55695.751468	67 ± 2	···	−11.7 ± 0.8	···	0.18	145	2.0	···	···	82.4	···	···	···
8262223	1.61301473	55692.217903	21.8 ± 0.5	203 ± 2	23.1 ± 0.4	21 ± 1	0.0	···	1.5	4.8	0.107 ± 0.002	75.2	7.42 ± 0.05	1.91 ± 0.03	0.205 ± 0.005
8552540	1.06193426	55692.5027	121 ± 1	153 ± 2	−12 ± 1	−12 ± 2	0.0	···	4.1	6.3	0.79 ± 0.01	80.7	5.83 ± 0.05	1.32 ± 0.03	1.04 ± 0.02
8553788	1.60616365	55690.62207	8.6 ± 0.7	···	27.9 ± 0.6	···	0.0	···	1.7	···	···	69.9	···	···	···
8823397	1.506503700	55686.100164	22.4 ± 0.9	221 ± 10	−21.9 ± 0.7	−23 ± 7	0.0	···	2.2	21.9	0.101 ± 0.006	82.1	7.3 ± 0.3	2.1 ± 0.2	0.21 ± 0.02
9159301	3.04477215	55693.13726	36 ± 1	147 ± 4	1.5 ± 0.9	1.5[a]	0.0	···	3.3	11.0	0.25 ± 0.01	81.1	11.2 ± 0.2	1.61 ± 0.08	0.40 ± 0.02
9357275	1.588298214	55643.386640	81.4 ± 0.9	···	−10.1 ± 0.8	···	0.0	···	2.5	···	···	74.9	···	···	···
9402652	1.07310422	55689.37059	144 ± 2	144 ± 1	14 ± 1	15 ± 1	0.0	···	4.5	3.9	1.0 ± 0.01	80.7	6.19 ± 0.04	1.39 ± 0.02	1.39 ± 0.03
9592855	1.21932483	55691.664073	144 ± 2	145 ± 7	8 ± 1	8[a]	0.0	···	3.4	12.5	0.99 ± 0.05	74.1	7.3 ± 0.2	1.7 ± 0.1	1.72 ± 0.08
9602595	3.5565129	55642.26003	36 ± 1	177 ± 4	−14 ± 1	−14[a]	0.0	···	2.7	13.2	0.202 ± 0.008	86.5	15.0 ± 0.3	3.0 ± 0.1	0.60 ± 0.03
9851944	2.16390178	55646.150110	125 ± 1	117 ± 2	−3 ± 1	−1 ± 1	0.0	···	5.1	5.4	1.07 ± 0.02	74.5[e]	10.7 ± 0.1	1.70 ± 0.04	1.83 ± 0.04
9899416	1.332564228	55689.965570	108 ± 1	210 ± 3	−15.9 ± 0.9	−16 ± 3	0.0	···	3.9	12.0	0.516 ± 0.009	82.8	8.44 ± 0.08	3.00 ± 0.07	1.55 ± 0.03
10156064	4.85593645	55648.858147	77 ± 2	114 ± 4	4 ± 1	3 ± 3	0.0	···	4.8	9.4	0.67 ± 0.03	82.8	18.5 ± 0.4	2.1 ± 0.1	1.44 ± 0.08
10191056	2.42749484	55688.135138	100 ± 2	119 ± 2	−20 ± 2	−20 ± 2	0.0	···	6.8	6.9	0.83 ± 0.02	80.5	10.7 ± 0.2	1.50 ± 0.05	1.25 ± 0.04
10206340	4.564405	55710.0929	42 ± 2	137 ± 2	−27 ± 1	−28 ± 2	0.0	···	5.5	8.2	0.30 ± 0.01	82.0	16.3 ± 0.3	2.14 ± 0.07	0.65 ± 0.03
10486425[h]	5.2748181	55681.8090	70.8 ± 0.9	98 ± 3	11.6 ± 0.8	−6 ± 3	0.0	···	2.4	8.0	0.72 ± 0.03	82.7	17.8 ± 0.3	1.57 ± 0.08	1.13 ± 0.05
10581918	1.80186369	55744.790056	23.4 ± 0.8	191 ± 7	−64.1 ± 0.7	−64.1[a]	0.0	···	2.3	19.4	0.130 ± 0.005	88.1	7.1 ± 0.1	1.30 ± 0.06	0.169 ± 0.009
10619109	2.04516645	55642.31502	33 ± 1	163 ± 22	−22.8 ± 0.7	−22.8[a]	0.0	···	1.2	33.1	0.20 ± 0.03	73.4	8.3 ± 0.9	1.50 ± 0.4	0.31 ± 0.07
10661783	1.23136328	55692.541890	21 ± 1	247 ± 4	−40 ± 1	−40[a]	0.0	···	4.7	17.5	0.083 ± 0.006	82.4	6.6 ± 0.1	2.33 ± 0.09	0.19 ± 0.01
10686876	2.61841548	55632.12313	67 ± 2	···	−7.3 ± 0.9	···	0.0	···	3.0	···	···	79.9	···	···	···
10736223	1.105094315	55692.697641	46 ± 2	211 ± 8	−2.4 ± 0.9	−2.4[a]	0.0	···	1.1	8.4	0.22 ± 0.01	89.2	5.6 ± 0.2	1.6 ± 0.1	0.35 ± 0.03
10858720	0.952377618	55692.951773	151 ± 3	159 ± 6	−32 ± 3	−30 ± 5	0.0	···	7.3	13.3	0.95 ± 0.04	90[g]	5.8 ± 0.1	1.50 ± 0.08	1.43 ± 0.07
12071006	6.0960363	55693.45930	15 ± 4	166 ± 17	−44 ± 2	−44[a]	0.0	···	4.5	21.7	0.09 ± 0.03	90[g]	22 ± 2	3.4 ± 0.7	0.3 ± 0.1

[a] Fixed to systemic value of the primary.
[b] Fixed to value derived by Hambleton et al. 2013.
[c] Fixed to value derived by Slawson et al. 2011.
[d] Fixed to value derived by Matson et al. 2016.
[e] Fixed to value derived by Guo et al. 2016.
[f] Fixed to value obtained from preliminary light curve fit.
[g] Inclination set to 90°as $\sin i > 1$ in Slawson et al. 2011.
[h] Possible triple system (see §3.4.3.1).

Note. — The period (P) and epoch (T_0 at primary eclipse) were fixed to values from Gies et al. (2015). Inclination values are from Slawson et al. (2011) and were used to determine the semi-major axis (a), mass of the primary (M_1) and mass of the secondary (M_2) unless otherwise noted.

(M_1) and mass of the secondary (M_2) from our derived $a \sin i$ and $m \sin^3 i$ products, unless otherwise noted in the table.

As noted in Section 2.3, the variations in the *Kepler* light curve of KIC 4678873 are due to a neighboring eclipsing binary, KIC 4678875. The spectroscopic observations of KIC 4678873 show it to be a constant velocity star, and we therefore present the radial velocities we measured in Table 3.4 but omit the system from Table 3.5.

3.4 Discussion of RV results

3.4.1 Single-Lined Spectroscopic Binaries

In five of the systems only the primary member of the binary was definitively detected in our spectra. In these cases the correlation peaks for the velocity separations were not prominent enough to yield reliable measurements of the secondary velocities. Small flux ratios and differences between the component spectra and their corresponding templates, as well as small velocity differences between the components and varying S/N of the observed spectra, can all contribute to difficulty in measuring the secondary velocities. The last two factors can even vary from one observation to another, resulting in reliable secondary velocities from one spectrum of an object but not from another (Mazeh et al. 2003).

In general, these five single-lined systems have late-A/early-F type primaries ($7000 - 8000\,\mathrm{K}$) with weak eclipses in the *Kepler* light curves, especially the secondary eclipses, and flux ratios $f_2/f_1 < 5\%$. We therefore present these systems as single-lined spectroscopic binaries (SB1), measuring orbital parameters based on the primary component. The velocity

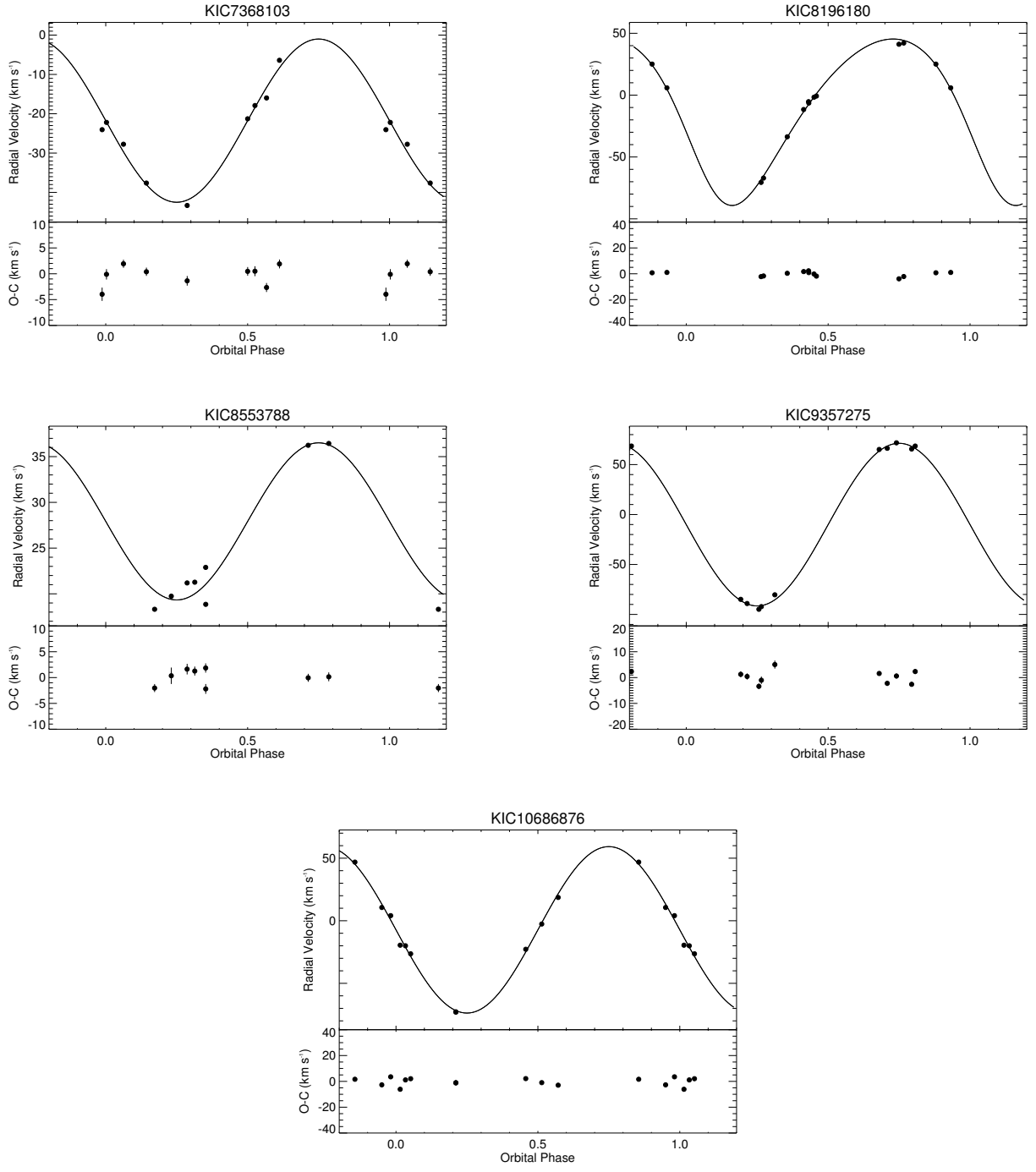

Figure 3.2: Radial velocities, spectroscopic orbits, and observed minus calculated $(O - C)$ values of SB1 systems.

semi-amplitude of the primary (K_1), systemic velocity (γ_1), eccentricity (e), and longitude of periastron for the primary (ω) are reproduced in Table 3.6 with the projected semi-major axis of the primary, $a_1 \sin i$, and the mass function, $f(m)$. The radial velocities, orbital solutions, and residuals of the SB1 systems are plotted in Figure 3.2.

Table 3.6: Single-Lined Binary Orbital Parameters

KIC	K_1 (km s^{-1})	γ_1 (km s^{-1})	e	ω (deg)	$a_1 \sin i$ ($R_\odot$)	$f(m)/\sin^3 i$ ($M_\odot$)
7368103	21 ± 1	-21.8 ± 0.7	0.0	$\cdots$	0.89±0.05	0.0020 ± 0.0004
8196180	67 ± 2	-11.7 ± 0.8	0.18	145	4.8±0.1	0.110±0.008
8553788	8.6 ± 0.7	27.9 ± 0.6	0.0	$\cdots$	0.27±0.02	0.00011±0.00002
9357275	81.4 ± 0.9	-10.1 ± 0.8	0.0	$\cdots$	2.55±0.03	0.089±0.003
10686876	67 ± 2	-7.3 ± 0.9	0.0	$\cdots$	3.4±0.1	0.080±0.007

3.4.2 Double-Lined Spectroscopic Binaries

Thirty-four of the remaining systems in our sample exhibited double lines in their spectra and/or were detected via cross-correlation allowing us to derive mass ratios ($q = M_2/M_1$) from the velocity semi-amplitudes of both stars. The mass ratio distribution of binaries provides one of the few diagnostics for testing models of binary formation. While mass ratios are often determined for SB1 systems based on statistical techniques, the resolution ability of such techniques is limited and are most useful for examining general trends of the distribution (Mazeh et al. 2003). Therefore, dynamically determined mass ratios from double-lined spectroscopic binaries are valuable for deriving true mass ratio distributions and validating binary star formation scenarios. The characteristics of our sample, including limited magnitudes, the brightness ratios imposed by the presence of eclipses, and using

visual band spectra in which the luminosity of stars less than $1\,M_{\odot}$ depends strongly on mass (impacting the detectability of companions), result in severe selection effects that do not provide a uniform sample for statistical analysis. Having said that, the sample does allow us to examine trends in the derived mass ratios and compare them to previous results. Figure 3.3 shows the distribution of mass ratios in our sample in six bins of width $\Delta\, q = 0.17$. The distribution is bimodal with a strong peak at $q = 0.17 - 0.33$ and a second peak at $q = 0.84 - 1.0$. The region with diagonal stripes represents systems with $q = M_2/M_1 > 1.0$, but are included in the plot as $q = M_1/M_2$. See Section 3.4.2.3 for more details.

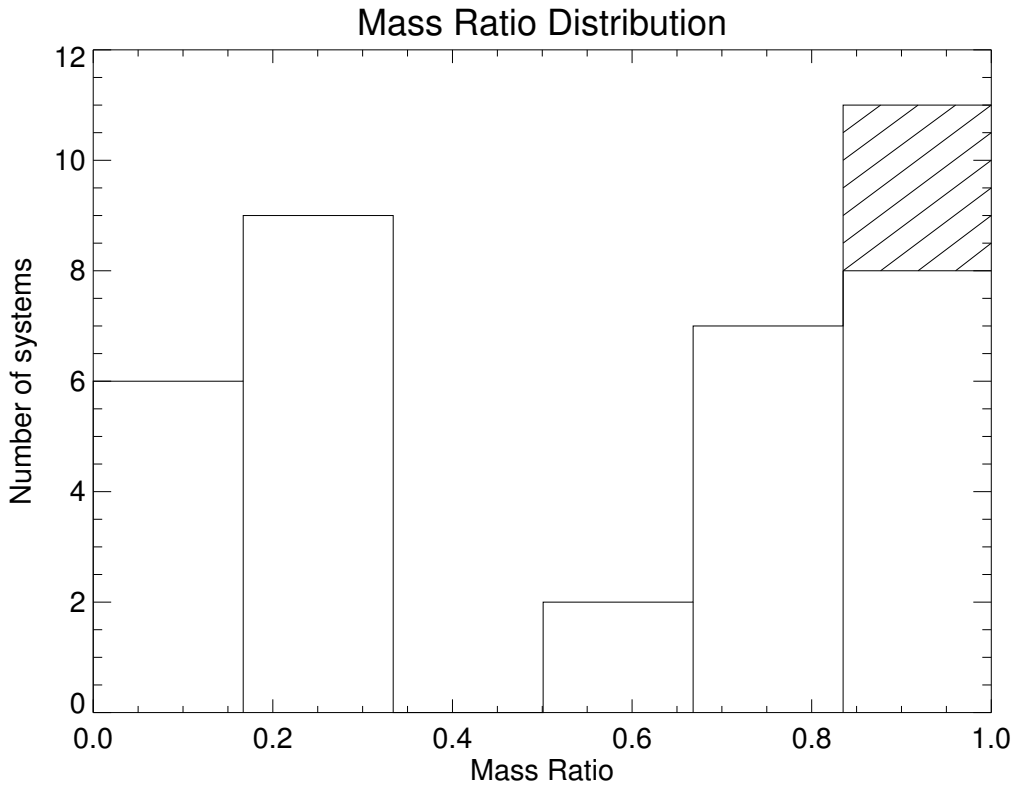

Figure 3.3: Mass ratio distribution for 34 double-lined spectroscopic binaries and the possible triple KIC 10486425 (see §3.4.3.1). The region with diagonal stripes represents systems with $q = M_2/M_1 > 1.0$, but are included in the plot as $q = M_1/M_2$ (see §3.4.2.3).

Studies of mass ratio distributions of spectroscopic binaries thus far have produced conflicting results with no consensus on the true mass ratio distribution. For example, Goldberg et al. (2003) examined 129 binaries (25 SB2s) with K-type primaries and periods between $1 - 2500$ days, finding a bimodal distribution similar to ours with a peak at $q \sim 0.2$ and a smaller peak at $q \sim 0.8$. However, both Raghavan et al. (2010), who performed a comprehensive survey of companions to nearby solar-type stars, and Mazeh et al. (2003), who examined 62 (43 SB2s) main sequence and pre-MS binaries in the infrared to detect cooler companions, found relatively flat mass ratio distributions. Raghavan et al. reported a nearly flat distribution between $0.2 < q < 0.95$ with a strong peak at $q \sim 1$, demonstrating binaries, and in particular short-period systems, prefer like-mass pairs. Similarly, Mazeh et al. (2003) showed a flat distribution for $q > 0.3$, with an increase below $q = 0.3$ due to primarily long period systems. While such analyses have not produced a universal mass ratio distribution, several suggest separate distributions for long and short-period binaries (Duchêne & Kraus 2013) and a dependence on the mass of the primary, as massive binaries are known to favor companions of comparable mass while low-mass systems are more consistent with a flat mass-ratio distribution (Podsiadlowski 2014).

3.4.2.1 Similar Mass Binaries: $0.84 \leq q \leq 1.0$

The peak at $0.84 \leq q \leq 1.0$ in our mass ratio distribution is roughly consistent with the studies of Goldberg et al. (2003) and Raghavan et al. (2010), which both found peaks for approximately like-mass binaries. There is ongoing debate about the existence of a population of 'twin' binaries based on an excess of systems with mass ratios from 0.95 to 1.

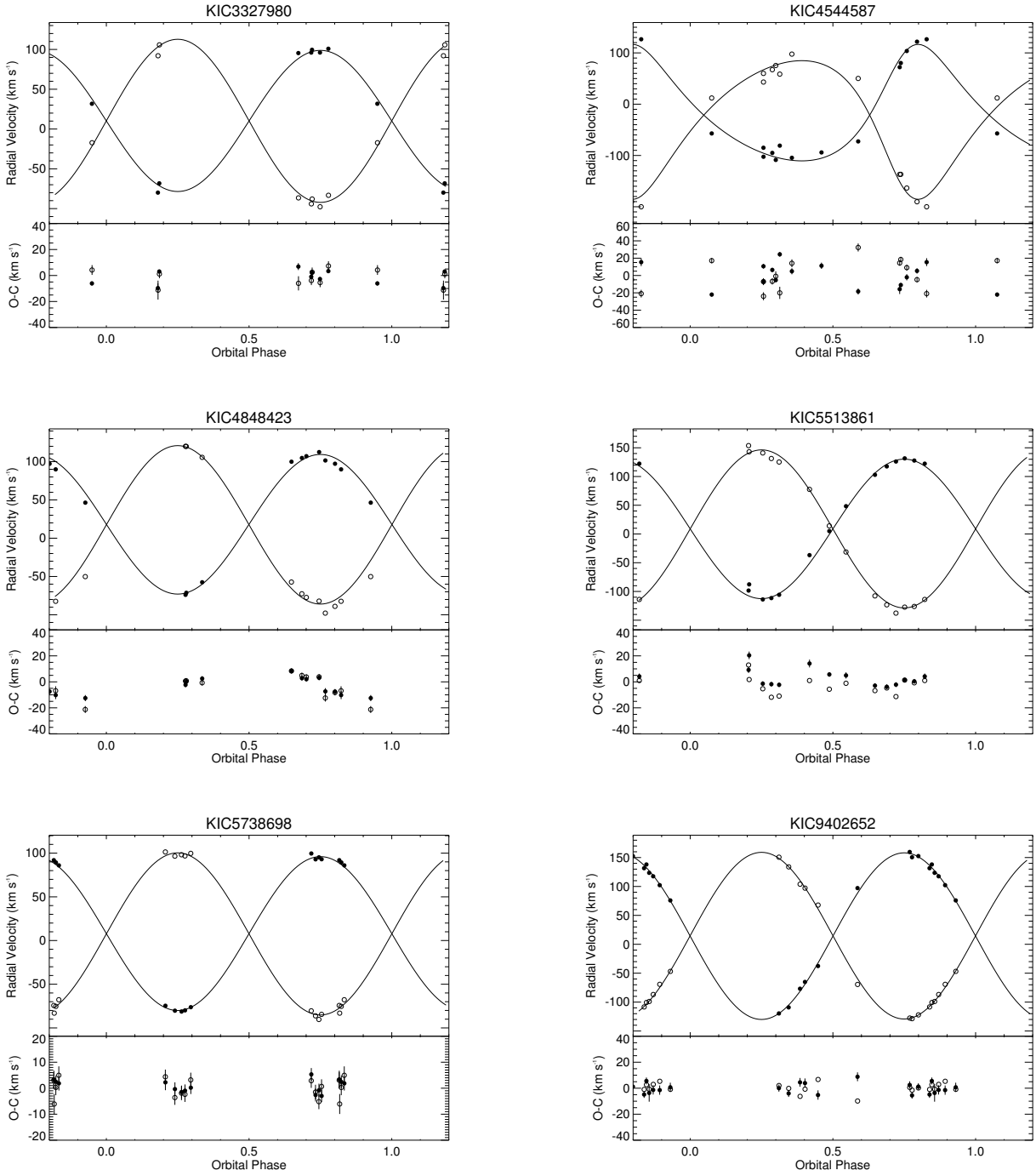

Figure 3.4: Radial velocities, spectroscopic orbits, and observed minus calculated $(O - C)$ values for SB2 systems with similar mass components $(0.84 \leq q \leq 1.0)$.

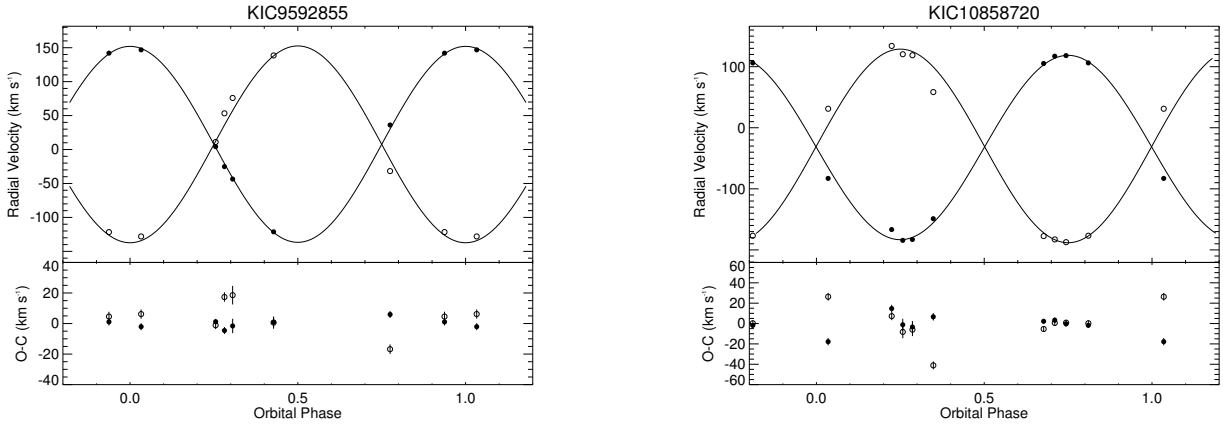

Figure 3.5: Radial velocities, spectroscopic orbits, and observed minus calculated $(O - C)$ values for SB2 systems with similar mass components ($0.84 \leq q \leq 1.0$).

While spectroscopic binaries with nearly identical components are found among all spectral types and in both long and short-period systems, a peak at $q \sim 1$ for solar-type short-period systems ($\sim 2 - 30$ d) has been found to be significant in some studies (e.g. Tokovinin 2000). Such like-mass pairs agree with theoretical simulations that show gas around proto-binaries preferentially accretes onto the secondary component, accumulating more mass until the components are roughly equal (Bate 1997).

In our sample of double-lined binaries only four systems have $0.95 \leq q \leq 1.0$ (KIC 5738698, 9402652, 9592855, and 10858720), not enough to affirm the 'twin' binary excess. However, there is a trend toward similar mass components, as nearly 25% of the SB2s have mass ratios between $0.84-1.0$, which increases to more than 30% when the $q = M_2/M_1 > 1.0$ systems (diagonal striped region of Fig. 3.3) are included. The radial velocities, orbital solutions, and residuals of the eight binary systems with similar mass components are plotted in Figure 3.5.

3.4.2.2 Intermediate mass secondaries: $0.50 < q < 0.84$

Below the peak at $0.84 \leq q \leq 1.0$, the mass ratio distribution of our sample trails off until reaching the peak between $0.17 < q < 0.33$. The decreasing number of systems with lower mass ratios is consistent with the results of Goldberg et al. (2003), which show a decrease through $q = 0.5$ before increasing toward the peak at $q = 0.2$. The fewer systems observed with mass ratios between $0.50 - 0.84$ is also likely due to the increasing difficulty in detecting lower mass companions and more extreme flux ratios as well as the lack of any longer period systems ($P > 100\,\mathrm{d}$) that peak at lower mass ratios ($q \sim 0.2 - 0.3$) in the sample of Mazeh et al. (2003). The radial velocities, orbital solutions, and residuals of systems with mass ratios between $0.50 < q < 0.84$ are plotted in Figure 3.6. Note that KIC 10486425 has $q = 0.72$ but may be a triple system so it is discussed separately in Section 3.4.3.1.

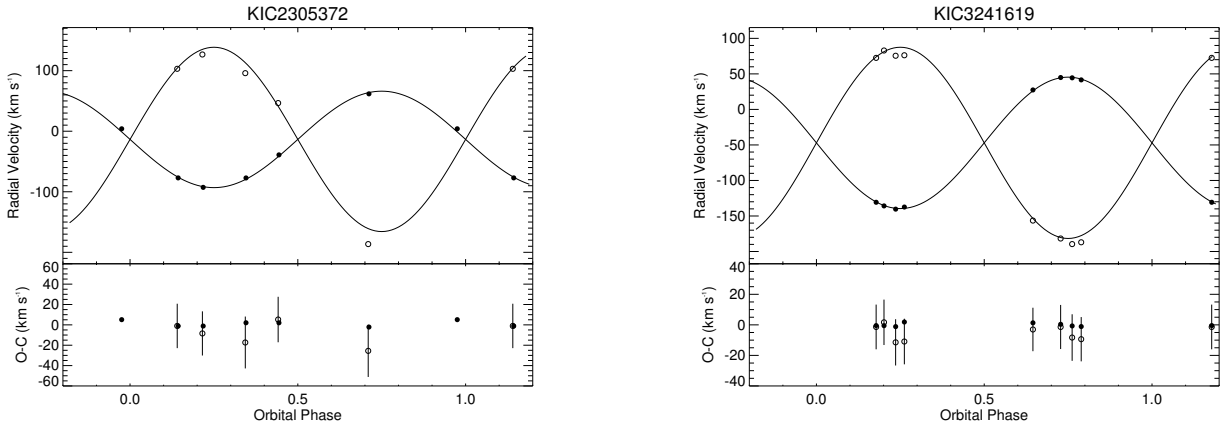

Figure 3.6: Radial velocities, spectroscopic orbits, and observed minus calculated ($O - C$) values for SB2 systems with intermediate mass ratios ($0.5 < q < 0.84$).

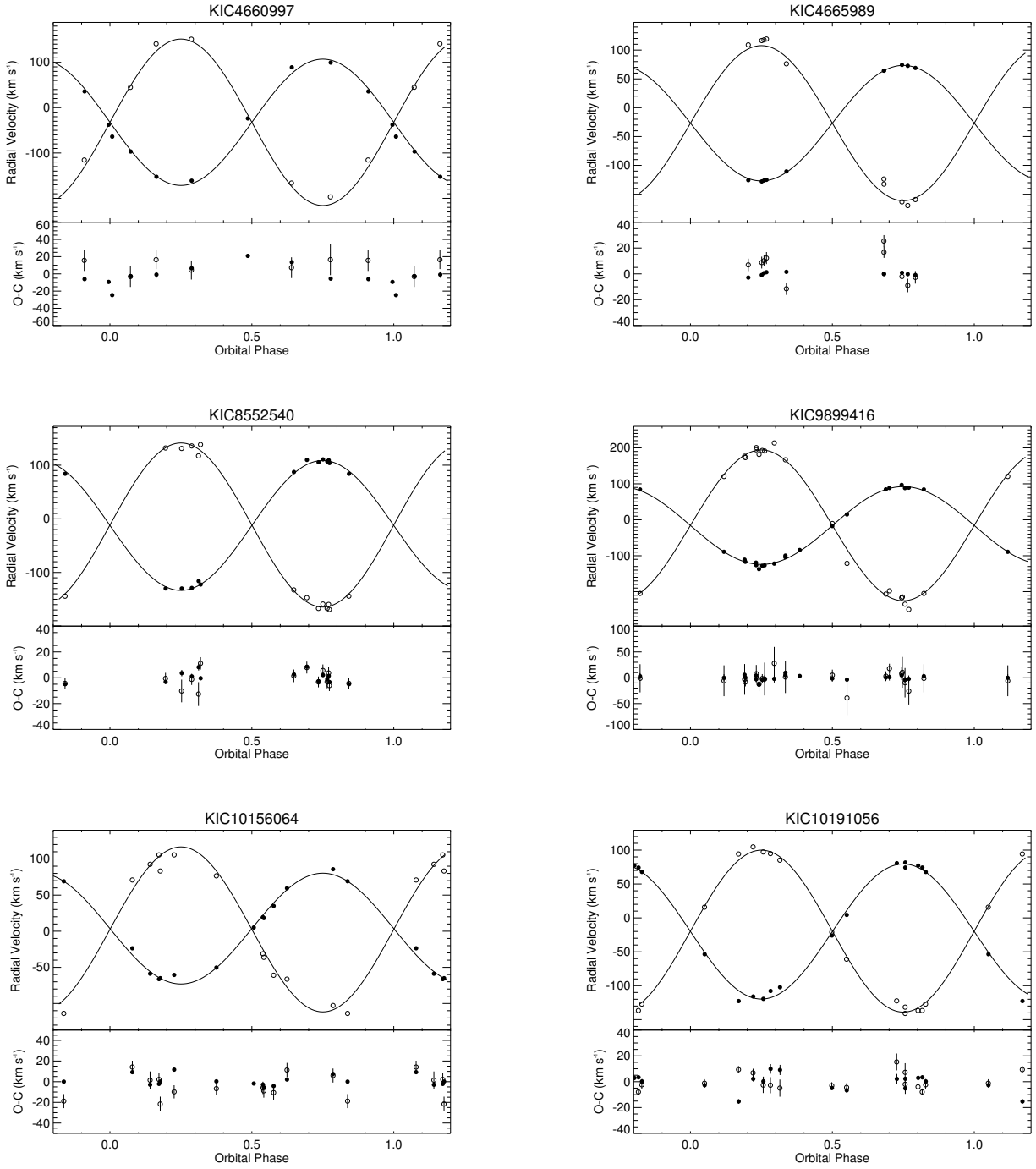

Figure 3.6: Radial velocities, spectroscopic orbits, and observed minus calculated $(O - C)$ values for SB2 systems with intermediate mass ratios ($0.5 < q < 0.84$).

3.4.2.3 More massive secondaries: $q > 1.0$

Three of the SB2 binaries have mass ratios greater than unity, in which the secondary component (the cooler star based on the weaker eclipse in the *Kepler* light curve) is more massive than the primary. Such systems are usually excluded from mass ratio distributions as they are typically evolved systems that have one or more components that differ from normal dwarf stars and, especially in short-period binaries, have experienced mass transfer that modifies the original mass ratio and no longer provides information about formation mechanisms. The radial velocities, orbital solutions, and residuals of the three systems where the secondary component is more massive than the primary are plotted in Figure 3.7.

KIC 9851944 ($q = 1.07 \pm 0.02$) was analyzed by Guo et al. (2016), who found that the components have very different radii (2.27 $R_\odot$, 3.19 $R_\odot$) despite their similar masses (1.76$M_\odot$, 1.79$M_\odot$) and temperatures (7026, 6920 K), indicating the hotter primary is still on the main sequence (MS) while the larger, cooler secondary has evolved to post-MS hydrogen shell burning. Using the more rigorous method described in Section 3.3.1 to derive updated radial velocities we find masses of 1.70 and 1.83$M_\odot$, which provide an even better match to the best-fit coeval MESA evolutionary models in Guo et al. (2016), confirming the evolutionary status of KIC 9851944.

KIC 5444392 was similarly found to have a mass ratio greater than one ($q = 1.013 \pm 0.008$). While the light curve shows minimal ellipsoidal variations, the larger mass and lower temperature of the secondary suggests it may have evolved off the main sequence. The primary temperature (5965 K) is consistent with the derived mass of 1.17$M_\odot$ for a G0 main

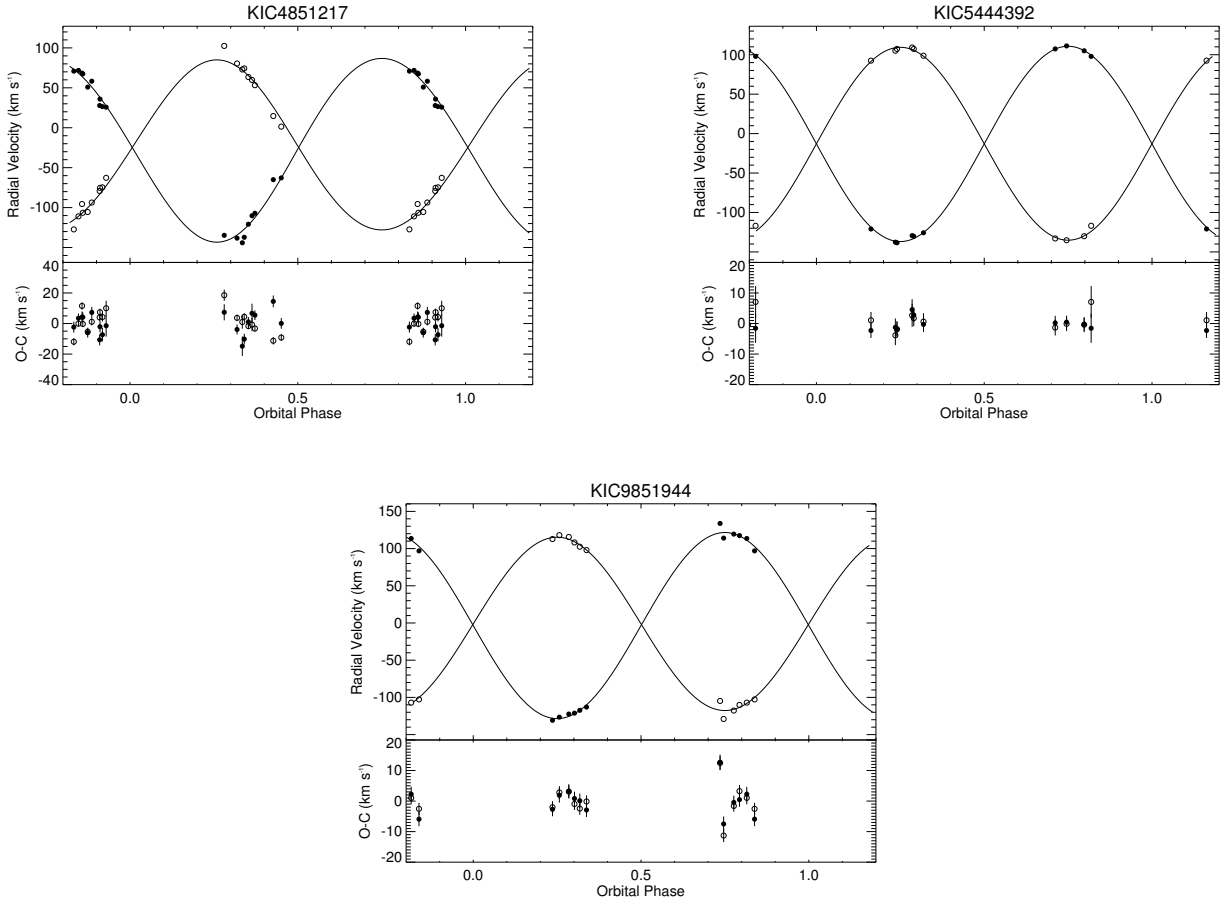

Figure 3.7: Radial velocities, spectroscopic orbits, and observed minus calculated $(O - C)$ values for SB2 systems with mass ratios greater than 1.0.

sequence star while $T_2 = 5725\,\mathrm{K}$ is slightly too cool for $M_2 = 1.19\ M_\odot$ (Gray 2008), though this could be due to uncertainties in the temperature of the secondary. Further analysis of the light curve, specifically derivation of the component radii, is needed to confirm the evolutionary status of the system.

The final system with a mass ratio greater than unity is KIC 4851217, which has $q = 1.08 \pm 0.03$ and masses (1.43 and $1.55 M_\odot$) and temperatures consistent with mid F-type MS stars. However, the best-fit flux ratio determined by maximizing the correlation functions

is $f_2/f_1 = 2.0$ indicating the secondary star gives off twice as much flux in the blue as the primary, while the light curve indicates the primary star is hotter. Thus, the cooler star has likely evolved within its Roche lobe to greater luminosity but a cooler temperature.

3.4.2.4 Algol-Type Binaries: $q < 0.33$

The most dominant feature in the mass ratio distribution for the eclipsing and spectroscopic binaries we observed is the peak at $0.17 < q < 0.33$. While such a peak is seen in Goldberg et al. (2003), the other studies discussed previously have reported a flat distribution or even a deficiency of low-mass companions. As we have focused on short-period systems that are known to prefer like-mass companions, the presence of a low q peak seems at odds with our expectations. However, when the secondary masses for systems with $q < 0.33$ are compared to the adopted temperatures, nearly all of the stars are hotter than expected for main sequence stars. This is highlighted in the plot of $\log M$ vs. $\log T_{\rm eff}$ in Figure 3.8, where plus signs represent the primary components and asterisks the secondary components in our sample. Yonsei-Yale isochrones (Demarque et al. 2004) for 0.1, 0.4, and 1.0 Gyr show the expected relationship between the mass and temperature of stars on the main sequence. Stars in detached binary (DB) systems that have not yet evolved or interacted should lie along the main sequence, and a significant portion of our sample do (approximately). However, a subset of binaries display different $\log M - \log T$ relations for the primary and secondary components, with the secondaries having lower then expected masses for a given temperature. These systems are known as Algol-type binaries and are semi-detached interacting binary (SDB) systems in which the less massive cool secondary stars have expanded to fill their

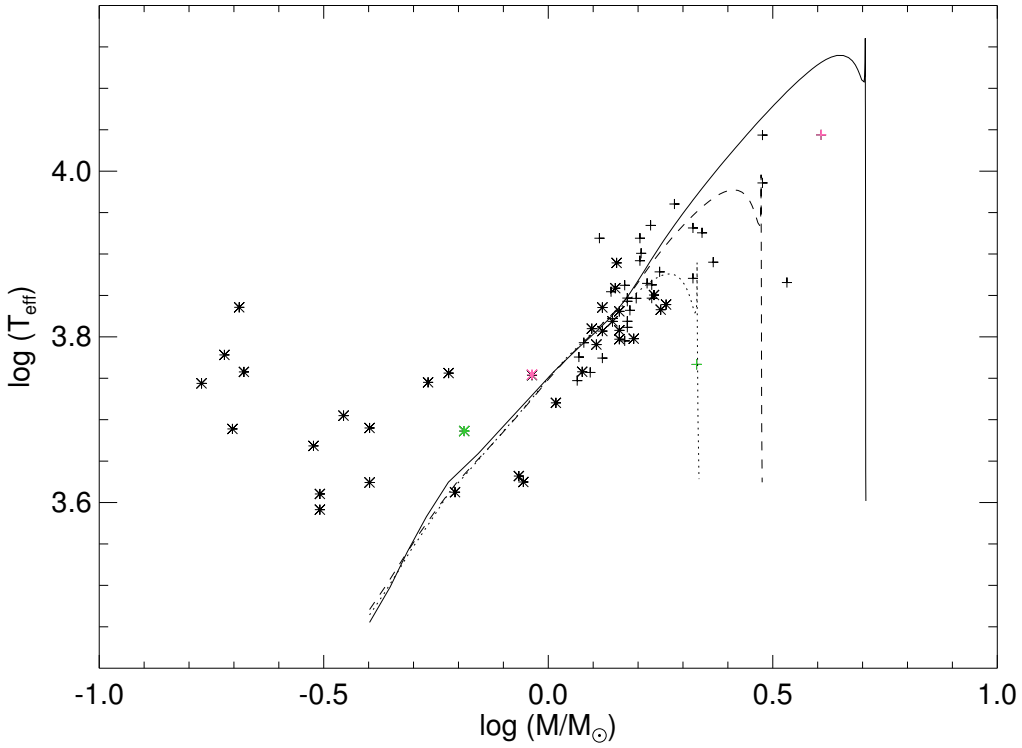

Figure 3.8: Locations of the primary (plus signs) and secondary (asterisks) components of the double-lined spectroscopic binaries in the $\log M - \log T$ plane. Yonsei-Yale (Y^2) Isochrones are plotted for 0.1 Gyr (solid line), 0.4 Gyr (dashed line), and 1.0 Gyr (dotted line). Pink and green symbols represent the components of KIC 2708156 and KIC 10206340, respectively; see text for more details.

Roche lobes. In general, the secondary components of SDBs have larger radii and luminosities with respect to the corresponding mass of main sequence stars (Ibanoğlu et al. 2006).

Algol-type binaries were originally defined in terms of their light curves, which show nearly constant brightness outside of eclipse and clearly defined eclipses, indicative of what were believed to be relatively straightforward systems with approximately spherical stars. Both detached and semi-detached eclipsing binaries exhibit Algol-type light curves; however, classical Algol-type systems refer to a sub-group of semi-detached binaries in which the

originally more massive component evolved to fill its Roche lobe before transferring mass to its companion, making it the currently more massive primary. These systems are categorized based on the prototype member of the class, β Persei or Algol (see also Section 1.1.1). Algols are produced when the originally more massive component (mass loser) fills its Roche lobe and begins transferring mass to the less massive component (mass gainer) during central hydrogen burning (Case A) or after hydrogen in the core has been exhausted and shell hydrogen burning has begun (Case B). These systems typically consist of an A or F-type primary with G or K-type subgiant or giant secondaries with masses of $0.2 - 0.4\ M_{\odot}$.

The Algol candidates in our sample ($q < 0.33$) consist of primaries with masses between 1.3 and 4.05 $M_{\odot}$ corresponding to B, A, and F spectral types, with secondaries ranging from $0.169 - 0.92 M_{\odot}$ and a mean mass of $0.37 M_{\odot}$. All of the secondary components appear to the left of the main sequence in the $\log M - \log T$ plot (Fig. 3.8), with most significantly less massive then expected for main sequence stars. The two systems whose secondaries do not differ from the main sequence $\log M - \log T$ relation as much as the others and lie closest to the plotted main sequence are KIC 2708156 (pink symbols in Fig. 3.8), the most massive of the Algol systems in our sample ($M_1 = 4.05 M_{\odot}$, $M_2 = 0.92 M_{\odot}$), and KIC 10206340 (green symbols), which has the largest mass ratio ($q = 0.3$). However, as the primaries for both systems are notably to the right of the plotted main sequence, the temperatures may be underestimated for all components, in which case shifting the temperatures to higher values may place the secondaries more distinctly in the subgiant/giant region of the $\log M - \log T$ plane.

One of the systems, KIC 10661783, has been previously studied by Southworth et al. (2011) and Lehmann et al. (2013). Analysis of the *Kepler* light curve and spectroscopic observations revealed it to be a detached post-Algol binary system with δ Scuti pulsations in the primary. Lehmann et al. (2013) derived parameters of $M_1 = 2.10 \pm 0.03$, $R_1 = 2.58 \pm 0.02$, $T_1 = 7764 \pm 54$ for the primary and $M_2 = 0.191 \pm 0.003$, $R_2 = 1.12 \pm 0.02$, $T_2 = 6001 \pm 100$ for the secondary, with a slightly smaller primary mass then what we derive (2.33 ± 0.09) but an equivalent secondary mass. The values for the secondary clearly confirm it has undergone mass loss in the past, though it has a short orbital period (1.23 d) and very low mass ratio ($q \sim 0.09$) compared to typical Algol systems. Based on comparisons with known Algol-type systems, Lehmann et al. (2013) determined KIC 10661783 to be a R CMa object, a small subgroup of stars that is characterized by the combination of a short period, low mass ratio, oversized secondary, and overluminous components. However, these systems are semi-detached binaries whereas Lehmann et al. (2013) were only able to fit the light curve and radial velocities of KIC 10661783 as a detached binary. In our sample, KIC 12071006 has similar temperatures and an equally small mass ratio ($q = 0.09$) but a longer period ($P = 6.10$ d). Further analysis of this system will provide an interesting comparison to KIC 10661783 and help inform our understanding of mass transfer and angular momentum redistribution in evolving binaries.

We have shown the $0.17 < q < 0.33$ peak in our mass ratio distribution is due to semi-detached Algol-type binaries, which are easier to detect due to their higher temperatures and increased luminosity, and not a reflection of the true/original mass ratios of our sample. In

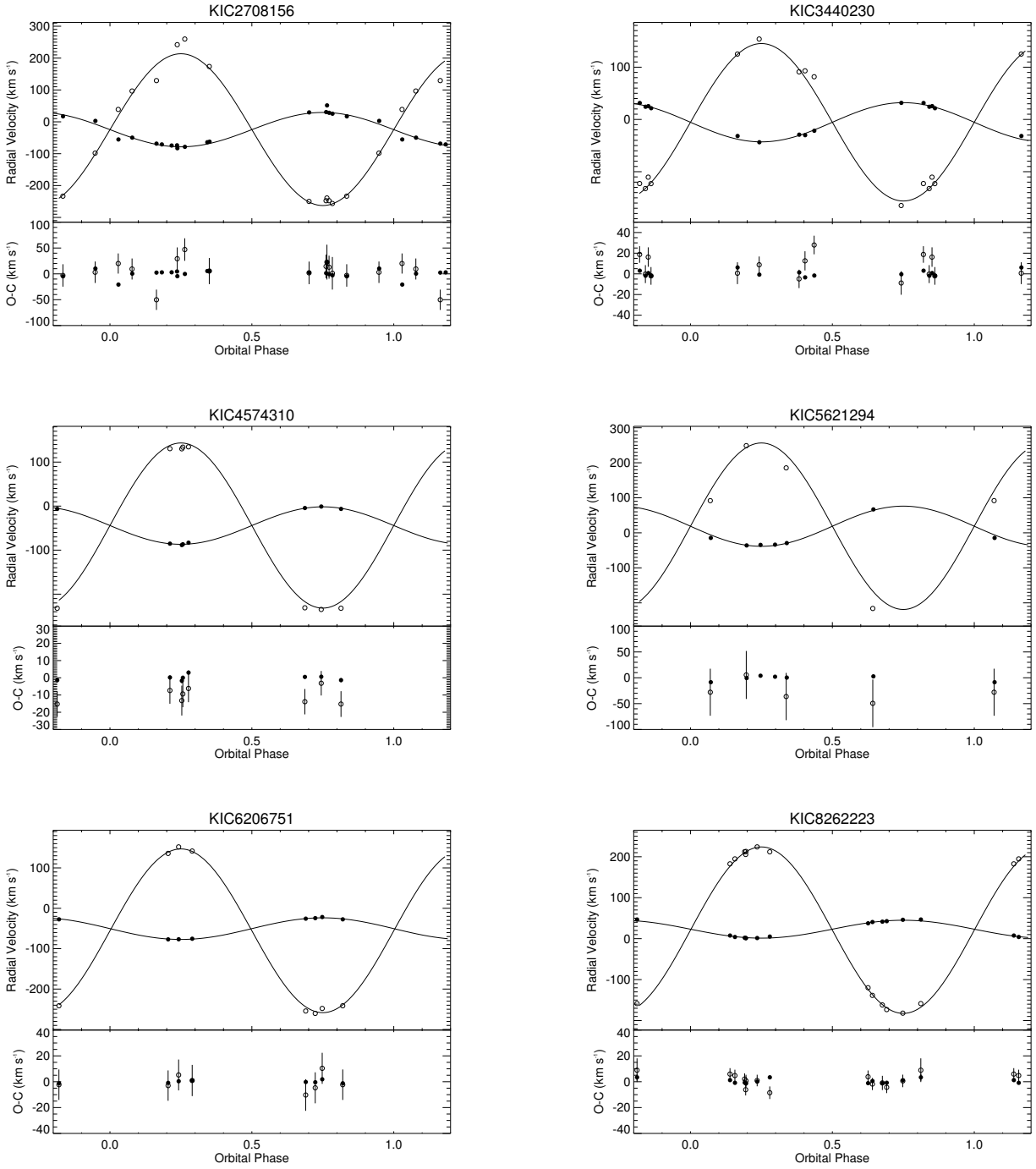

Figure 3.9: Radial velocities, spectroscopic orbits, and observed minus calculated $(O - C)$ values for candidate Algol systems ($q < 0.33$).

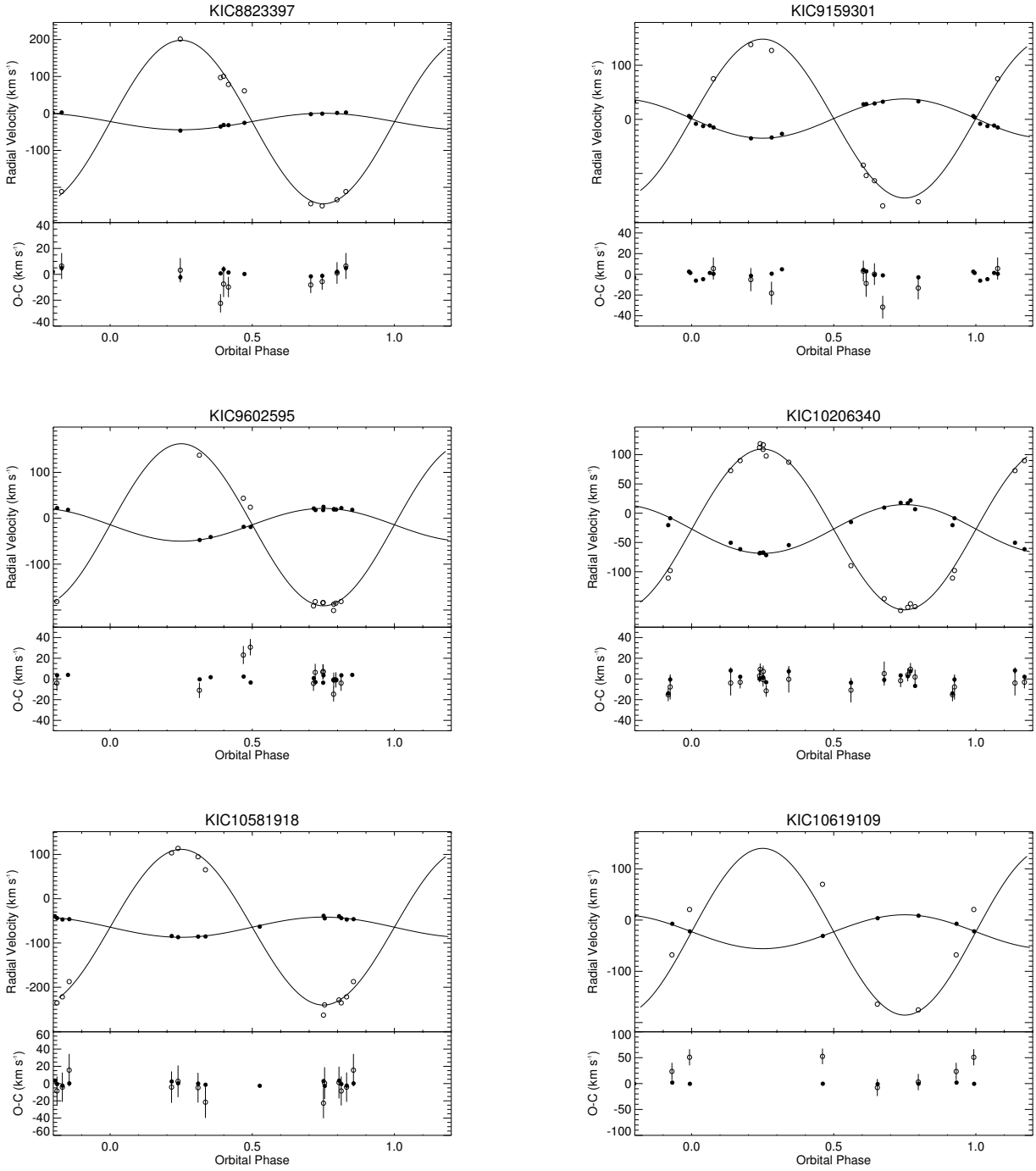

Figure 3.9: Radial velocities, spectroscopic orbits, and observed minus calculated $(O - C)$ values for candidate Algol systems ($q < 0.33$).

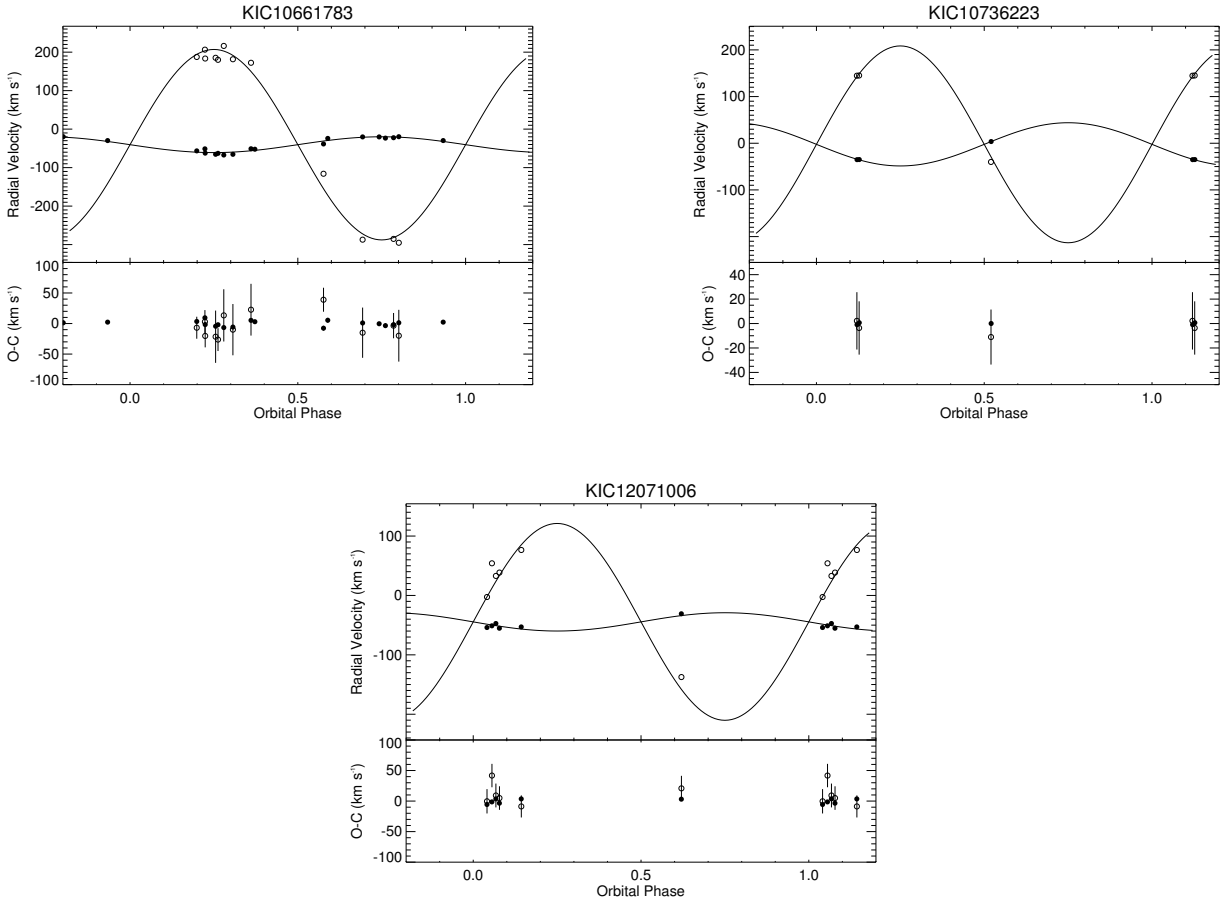

Figure 3.9: Radial velocities, spectroscopic orbits, and observed minus calculated ($O - C$) values for candidate Algol systems ($q < 0.33$).

a sample of 135 Algol-type eclipsing binaries with well determined parameters (74 detached (DB), 61 semi-detached (SDB) close binaries), Ibanoğlu et al. (2006) found more than 73% of the DBs had mass ratios larger than 0.80, with a mean value of $q = 0.88 \pm 0.14$, while the mass ratios of short-period ($< 5\,\mathrm{d}$) SDBs ranged from 0.11 to 0.57 with a mean of $q = 0.30$. This closely matches the mass ratio distribution of our sample, demonstrating the differences between evolved and unevolved systems and supporting the conjecture that unevolved systems have a preference for like-mass components. The radial velocities, orbital

solutions, and residuals for the 15 candidate Algol systems are plotted in Figure 3.9.

3.4.3 Triple Star Systems

Eclipse timing analysis of all 41 binaries in Gies et al. (2012, 2015, see Section 2.4) detected seven probable triple systems and long term trends indicative of a tertiary companion in seven additional systems. For the seven systems that showed two inflection points in the $O-C$ changes for both the primary and secondary eclipses they determined preliminary orbital elements including mass functions for the third star via

$$f(m_3) = \frac{(m_3 \sin i)^3}{(m_1 + m_2 + m_3)^2} = \frac{1}{P_3^2} \left(\frac{173.15\, A}{\sqrt{1 - e^2 \cos^2 \omega}} \right)^3, \tag{3.1}$$

where the semi-major axis A and period P_3 of the outer system are given in units of days and years, respectively. While we do not know the mass of the tertiary star nor the inclination of its orbit, we can further constrain its mass using the individual masses we derived for the primary and secondary components of the inner binary. The lower bound on the third star, $m_3 \sin i$, is calculated from the mass function for five systems with probable tertiaries in double-lined spectroscopic binaries. The primary and secondary masses derived from the spectroscopic orbits (M_1, M_2), the mass function $(f(m))$ of Gies et al. (2015), and $m_3 \sin i$ are shown in Table 3.7. The two additional systems with probable third components for which we were unable to detect confidently the secondary are listed for completeness.

Based on the $m_3 \sin i$ value calculated for KIC 2305372, the tertiary component is likely similar in mass or larger than the secondary component. We performed a three-star Doppler tomography reconstruction (Penny et al. 2001) in an attempt to detect the spectrum of the

third star, but were unable to do so with any reliability. This is likely due to the extreme flux ratio of cool stars in the blue as well as uncertainty in the mass of the third star (Borkovits et al. 2016, determine $m_3 \sin i = 0.41\,\mathrm{M}_\odot$). This system, however, would be an ideal target for high resolution spectroscopy, which may enable spectral reconstruction of all three stars in the future.

Table 3.7: Mass Constraints for Systems with Tertiaries

KIC	M_1 $(M_\odot)$	M_2 $(M_\odot)$	$f(m_3)$ $(M_\odot)$	$m_3 \sin i$ $(M_\odot)$
2305372	1.2 ± 0.1	0.62 ± 0.04	0.25 ± 0.12	0.9 ± 0.2
4574310	1.38 ± 0.06	0.31 ± 0.01	0.000032 ± 0.000003	0.045 ± 0.002
4848423	1.22 ± 0.05	1.08 ± 0.04	0.076 ± 0.011	0.74 ± 0.04
5513861	1.50 ± 0.04	1.32 ± 0.03	0.081 ± 0.006	0.86 ± 0.02
8553788	$\cdots$	$\cdots$	0.035 ± 0.005	$\cdots$
9402652	1.39 ± 0.02	1.39 ± 0.03	0.0259 ± 0.0006	0.585 ± 0.005
10686876	$\cdots$	$\cdots$	0.019 ± 0.005	$\cdots$

3.4.3.1 KIC 10486425

In addition to the known and suspected triples found via eclipse timing, we think one additional binary is a triple system because initial measurements of the radial velocities of KIC 10486425 led to unrealistically small estimates of the semi-amplitudes. Inspection of several deep and isolated spectral lines showed that the profiles at Doppler shift maxima had extensions towards zero velocity indicating the presence of a non-shifted spectral component. We subsequently performed a three-star Doppler tomography (see Section 4.3.3 for more information on Doppler tomography) reconstruction (Penny et al. 2001) of the individual spectrum of each star that revealed a mid F-type spectrum for the stationary component

(and F0 V and G0 V types for the primary and secondary, respectively). Consequently, it appears that this is a spectroscopic triple system in which blending with the stationary lines of the tertiary reduces the absolute value of the velocity measurements of the primary and secondary components. We dealt with this by subtracting a model tertiary spectrum from the observed ones. The model was derived from the UVBLUE grid for $T_{\rm eff} = 6510$ K and $\log g = 4.3$ (representative main sequence values) that was shifted to the velocity of the tertiary in the reconstructed spectrum, 4.7 ± 2.0 km s^{-1}, and was rescaled to the expected flux contribution of the tertiary. We can only make a rough estimate of the tertiary's flux contribution in the observed spectral range, and unfortunately, this parameter has a large influence on the measured velocities. Subtracting the expected tertiary component removes absorption from the center of the observed profiles in such a way that the more that is removed, the weaker and more well separated the residual components from the primary and secondary appear. Thus, the larger the assumed tertiary contribution, the greater the absolute radial velocity measurements and the derived semi-amplitudes. We present here velocities for the primary and secondary (see Table 3.4) measured in difference spectra for a tertiary that contributes 40% of the total flux in the B-band covered by our spectra, but this is just one solution in a family based upon the adopted tertiary flux ratio. We encourage future higher resolving power spectroscopy of this system to resolve fully the three components and derive reliable semi-amplitudes. The radial velocities, orbital solution, and residuals for KIC 10486425 are plotted in Figure 3.10.

The *Kepler* light curve of KIC 10486425 was analyzed by Aliçavuş & Soydugan (2014),

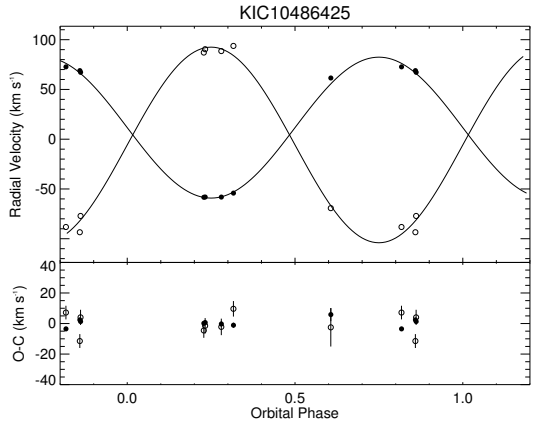

Figure 3.10: Radial velocities, spectroscopic orbits, and observed minus calculated $(O - C)$ values for the suspected triple KIC 10486425.

who used the first two quarters of data to obtain binary parameters and perform a frequency analysis. They derived two solutions, one with the eccentricity and third-light contribution fixed at zero and a second where these were left as free parameters. The second solution has larger values of T_2 (5727 vs. 5210 in the first solution) and q (0.59 vs. 0.40), which are (slightly) more consistent with our derived parameters, but the third light contribution was still found to be zero. This disagreement with our results will only be resolved through future high angular resolution and high spectral resolving power observations.

3.5 Summary

Spectroscopic observations of the 41 eclipsing binaries in our sample have resulted in 454 spectra that were used to measure radial velocities through cross-correlation with template spectra. One of the stars, KIC 4678873, is shown to be a single star. Radial velocities were measured for only the primary component in five of the systems, resulting in orbital parameters based on the primary, including $a_1 \sin i$ and the mass function $f(m)$. In systems

where velocities were measured for the primary and secondary we derived orbital elements for both components and values of $m_1 \sin^3 i$, $m_2 \sin^3 i$, and $a \sin i$. Using inclinations from light curve fits by Slawson et al. (2011), we determine masses and semi-major axis values for 34 double-lined spectroscopic binaries. We analyze the resulting mass ratio distribution, identifying 15 semi-detached Algol systems that have undergone Roche lobe overflow and mass transfer. Three additional systems show evolved secondaries, while the remaining systems appear to be unevolved. The mass ratio distribution also demonstrates the tendency for short-period binaries to have similar mass components, likely a result of gas preferentially accreting onto the lower-mass component until reaching comparable masses during formation Bate (1997).

For five of the seven systems with eclipse timing variations indicative of a third body we use our derived masses for the primary and secondary to determine minimum masses of the tertiary. Four of the distant companions may be K-type stars with $0.5\,M_\odot < M_3 < 0.9\,M_\odot$, while the fifth may be substellar ($M_3 \geq 0.045\,M_\odot$). We detect what is likely another triple system via spectroscopy, as KIC 10486425 had unrealistically small semi-amplitudes and indications of unshifted spectral features during Doppler shift maxima. We derive masses of $1.57\,M_\odot$ and $1.13\,M_\odot$ for the primary and secondary stars by subtracting a mid F-type model tertiary spectra shifted to the velocity of the third star.

CHAPTER 4
FUNDAMENTAL PARAMETERS OF KIC 5738698

This dissertation has demonstrated that eclipsing binaries serve as valuable sources of stellar masses and radii and presented both photometric and spectroscopic data for a subset of eclipsing binaries in the *Kepler* field of view. The information gleaned from these data sets is now combined to determine masses and radii for KIC 5738698, a detached eclipsing binary consisting of two nearly identical F-type stars orbiting with a period of 4.8 days, via binary modeling techniques discussed in Chapter 1. The observations and analysis presented here were previously published in Matson et al. (2016).

4.1 Introduction

KIC 5738698 was detected as an eclipsing binary in the HATNet (199-19185; Hartman et al. 2004) and ASAS (J195853+4054.2; Pigulski et al. 2009) surveys ahead of *Kepler*. It is listed in the *Kepler* Input Catalog (KIC)/*Kepler* Target Catalog (KTC) as having $K_p = 11.941$, $T_{\rm eff} = 6210\,{\rm K}$, $\log g = 4.259$, $\log[{\rm Fe/H}] = -0.490$, and $R = 1.317 R_\odot$, while Armstrong et al. (2014) derived $T_{\rm eff,1} = 6578 \pm 358\,{\rm K}$, $T_{\rm eff,2} = 6519 \pm 555\,{\rm K}$, $R_2/R_1 = 0.83 \pm 0.32$ and $T_2/T_1 = 0.9905$ in their catalog of temperatures for *Kepler* eclipsing binary stars.

Though the eclipse timing measurements of KIC 5738698 (Gies et al. 2015) do not show any evidence of a third star, this analysis highlights the methods and additional considerations that arise when modeling *Kepler* photometry. The exquisite *Kepler* data and optical spectroscopy are further used to measure accurately the masses and radii of KIC 5738698, contributing to knowledge of detached systems with accurately known fundamental parame-

ters in the mass/temperature regime where convective cores begin to develop and affect the observational properties of the stars (Clausen et al. 2008).

The observations of KIC 5738698 are discussed in Section 4.2, followed by the determination of radial velocities and atmospheric parameters from reconstructed spectra in Section 4.3. In Section 4.4 the binary modeling method is described, including details of a circular baseline model, efforts to minimize the residuals, and parameter uncertainties. Section 4.5 compares the results to theoretical predictions of several evolutionary models, followed by a short summary in Section 4.6.

4.2 Observations

4.2.1 Kepler Photometry and Orbital Ephemeris

KIC 5738698 was observed in long cadence mode during all 18 quarters the *Kepler* mission was in operation (Q0-17; 2009 May 2 – 2013 May 8) and one month in short cadence mode (Q4.1; 2009 Dec 19 – 2010 January 19). We again used the Simple Aperture Photomtery (SAP) light curves output by the *Kepler* data processing pipeline, correcting for varying flux levels within quarters by binning the data to give a minimum scatter in out-of-eclipse phases and fitting a cubic spline through the mean of the upper 50% of each section. Each quarter was then divided by the spline fit before being combined into a single light curve as described in Section 2.2. Again, this method of detrending does not fully account for some of the jumps, drifts, and outliers present in the *Kepler* data, but does minimize their effects while preserving the eclipses. In addition, any remaining artifacts should be randomized

and merely add to the overall scatter of the residuals as we phase fold the light curve for all subsequent analysis.

An updated ephemeris for KIC 5738698 was determined from eclipse templates made with the binned and folded *Kepler* light curve in Gies et al. (2015). A period of $4.80877396 \pm 0.000000035$ days was adopted from the average of the individual periods of the primary and secondary eclipses. The epoch of mid-eclipse of the primary is $2455692.3348702 \pm 0.000002$ (BJD).

4.2.2 Ground-based Spectroscopy

Thirteen moderate resolution spectra of KIC 5738698, shown in Figure 4.1, were obtained between 2010 June and 2011 September at Kitt Peak National Observatory (KPNO; 12 spectra) and the Anderson Mesa Station of Lowell Observatory (1 spectrum). As detailed in Chapter 3, observations at KPNO provided wavelength coverage of $3930 - 4610$Å with an average resolving power of $R = \lambda/\delta\lambda \approx 6200$, while Lowell spectra had a resolving power of $R = \lambda/\delta\lambda \approx 6000$ over the wavelength range $4000 - 4530$Å. Calibration exposures at KPNO and Lowell used HeNeAr and HgNeArCd Pen-Ray lamps, respectively, and were taken either immediately before or after each science exposure. Bias and flat-field spectra were also obtained nightly.

All spectra were reduced, extracted, and wavelength calibrated using the corresponding comparison lamp spectra and standard IRAF routines as noted in Section 3.2, with the Lowell spectra wavelength calibrated using observations of standard velocity stars cross-correlated with appropriate UVBLUE models (Rodríguez-Merino et al. 2005). After wavelength calibra-

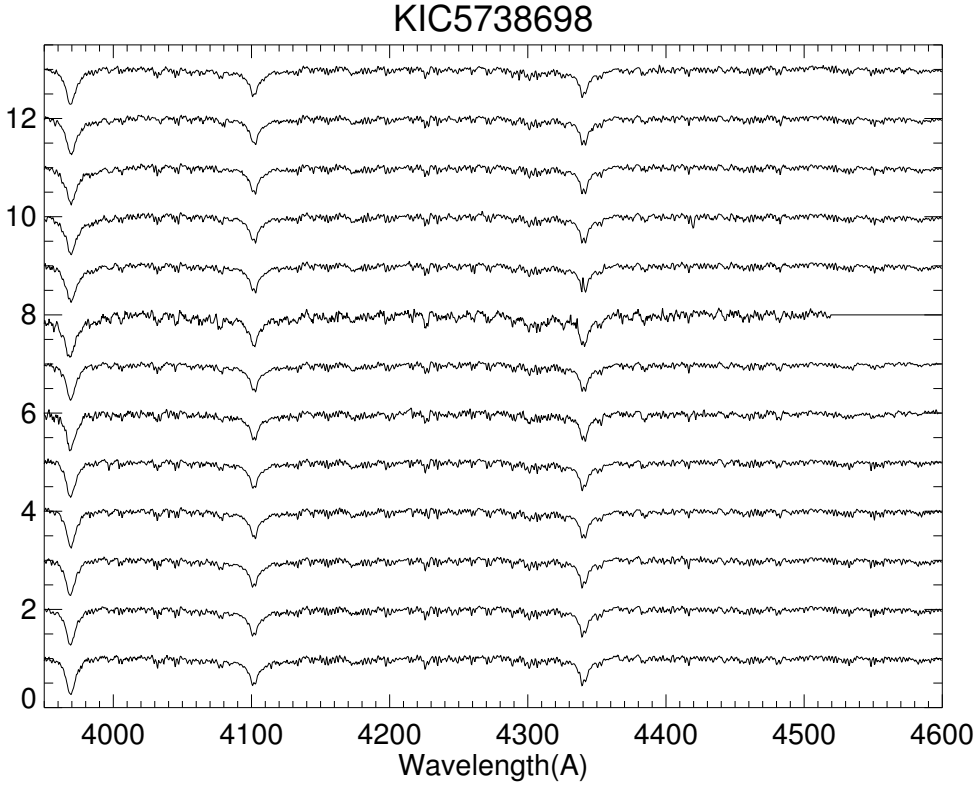

Figure 4.1: Reduced and normalized spectra of KIC 5738698, offset for clarity. The spectrum with the flat region beyond 4530Å is from Lowell Observatory.

tion, all spectra were rectified to a unit continuum and transformed to a common heliocentric wavelength grid in log λ increments.

4.3 Spectral Analysis

4.3.1 Radial Velocities

Radial velocities were measured using a previous version of the two-dimensional cross-correlation technique outlined in Section 3.3.1 prior to the improved treatment of edge effects in the spectra, background subtraction for blended cross-correlation peaks, and a more con-

sistent determination of uncertainties. More than half of the radial velocities presented here are the same as the updated values within the measured uncertainties, with the remaining values roughly $4 - 5$ km s^{-1} larger. Thus, the orbital elements and masses derived here are slightly smaller than the updated versions in Chapter 3, the effects of which are summarized in Section 4.5.5.

Template spectra from the UVBLUE grid of high resolution model spectra with parameters $T_1 = 6210\,\mathrm{K}$, $\log g_1 = 4.43$, $v_1 \sin i = 11.6\,\mathrm{km\ s^{-1}}$ and $T_2 = 6141\,\mathrm{K}$, $\log g_2 = 4.44$, $v_2 \sin i = 11.3\,\mathrm{km\ s^{-1}}$ (based on Slawson et al. 2011) were used to form composite spectra for cross-correlation with the observed spectra. After deriving atmospheric parameters from the tomographically reconstructed spectra (§ 4.3.3), the templates were updated and radial velocities re-derived. The radial velocities for KIC 5738698 are listed in Table 4.1, along with the date of observation in Heliocentric Julian days, orbital phase, uncertainty σ, and observed minus calculated $(O - C)$ residuals from the spectroscopic fit (§ 4.3.2). Orbital phase is determined relative to T_0, taken to be the epoch of primary eclipse.

4.3.2 Orbital Solution

We determined orbital elements for KIC 5738698 using the method outlined in Section 3.3. The orbital period was held fixed to the value obtained from the eclipse timings, while the epoch was allowed to vary. The radial velocities were weighted by the inverse square of the uncertainties, with the exception of an anomalous measurement of the primary component from Lowell Observatory which was zero weighted and therefore omitted from the fitting process. While we would expect the radial velocity measurement of the secondary component

Table 4.1. KIC 5738698 Radial Velocity Measurements

Date (HJD−2,400,000)	Orbital Phase[a]	V_1 (km s^{-1})	σ_1 (km s^{-1})	$(O-C)_1$ (km s^{-1})	V_2 (km s^{-1})	σ_2 (km s^{-1})	$(O-C)_2$ (km s^{-1})
55366.7614	0.297	−74.32	1.18	0.78	94.93	1.79	0.70
55368.7913	0.719	98.39	1.23	6.30	−74.10	1.68	5.53
55368.8630	0.734	88.86	1.30	−4.42	−86.03	2.03	−5.06
55368.9200	0.746	95.19	1.35	1.51	−82.23	1.76	−0.75
55368.9649	0.755	89.37	1.16	−4.29	−83.57	1.77	−2.04
55402.9316	0.819	···	···	···	−78.10	3.91	−4.29
55431.7764	0.817	87.15	1.27	1.00	−72.22	1.80	1.96
55431.8614	0.835	82.60	1.44	0.85	−68.73	2.04	0.99
55731.8001	0.208	−73.96	1.15	1.89	96.83	1.70	2.48
55734.7638	0.824	84.21	1.10	−0.26	−73.35	1.50	−0.87
55813.7096	0.241	−80.02	1.22	−1.31	95.82	1.62	−1.75
55813.8211	0.265	−79.34	1.15	−0.86	97.61	1.50	0.11
55813.8798	0.277	−78.44	1.28	−0.82	95.34	1.73	−1.37

[a]Relative to T_0 at primary eclipse.

to be similarly affected, it appears comparable to the other measurements near the same phase and we therefore chose to include it after verifying that doing so did not alter the orbital solution. Although initial fits indicated that the orbit of KIC 5738698 is circular, as expected for short period systems, we fit the radial velocities with both circular and eccentric orbits. The statistical significance of each fit was evaluated according to the tests of Lucy & Sweeney (1971) and Lucy (2013), but the eccentric orbit failed to improve the fit in both cases and we therefore adopt the circular orbit for now (see §4.4.3.1).

Parameters for the circular fit to the orbit of KIC 5738698, including the period (P), time of primary eclipse (T_0), systemic velocity (γ), and velocity semi-amplitude of the primary (K_1) and secondary (K_2) are given in Table 4.2 as well as the derived mass ratio ($q = M_2/M_1$) and $a \sin i$. The primary and secondary radial velocities were fit separately, which allows us

Table 4.2. Orbital Solutions for KIC 5738698

Element	Spectroscopic Solution	ELC Solution
P (days)	4.80877396[a]	4.80877396[a]
T_0 (HJD−2,400,000)[b]	55692.33 ± 0.03	55692.3348[a]
e	0[a]	0.0006[a]
ω (deg)	...	52[a]
K_1 (km s^{-1})	86.3 ± 0.9	86.2±0.6
K_2 (km s^{-1})	89.7 ± 0.9	89.7±0.9
γ (km s^{-1})	7.8 ± 0.6	7.6 ± 0.5
M_2/M_1	0.96 ± 0.01	0.96 ± 0.01
$a \sin i$ ($R_\odot$)	16.7 ± 0.1	16.7 ± 0.1

[a]Fixed.

[b]Time of primary eclipse.

to check the consistency of the fits as well as our derived radial velocities. The epochs determined from both components agree within uncertainties ($T_{0_1} = 55692.330 \pm 0.032$, $T_{0_2} + \frac{P}{2} = 55692.340 \pm 0.028$) and are consistent with the epoch from the eclipse timings, though less precise. Similarly, the systemic velocities from each fit ($\gamma_1 = 7.4 \pm 0.9$ km s^{-1}, $\gamma_2 = 8.1 \pm 0.8$ km s^{-1}) are consistent within the uncertainties and we adopt the weighted mean for the spectroscopic solution (see Table 4.2). The radial velocities, residuals, and an updated orbital solution (via ELC, as described in § 4.4.1) are plotted in Figure 4.2.

4.3.3 Spectral Reconstruction and Atmospheric Parameters

We used the Doppler tomography algorithm of Bagnuolo et al. (1994) to reconstruct the primary and secondary spectra of KIC 5738698. Using the composite spectra, radial velocities, and flux ratio of the primary and secondary, this method iteratively shifts and adds flux from each component in proportion while making small corrections via a least-squares

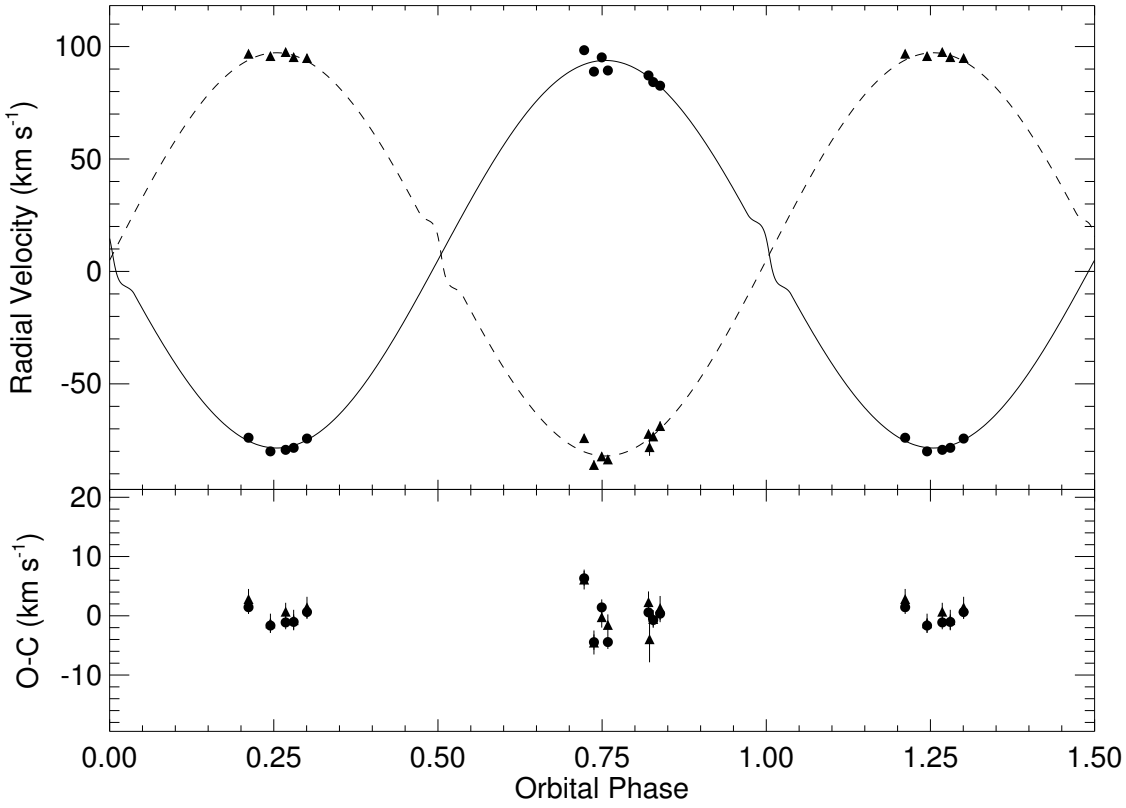

Figure 4.2: Top: radial velocity curves of the primary (filled circles) and secondary (filled triangles) of KIC 5738698 and the best fitting ELC model. Phase zero corresponds to the time of primary eclipse. Bottom: residuals for the fits to the primary and secondary velocities.

technique. Reconstructed spectra of the primary and secondary are shown in Figure 4.3 along with model spectra as described below.

We begin by comparing the reconstructed spectra with UVBLUE models based on initial parameter estimates from the *Kepler* Eclipsing Binary Catalog (as in our radial velocity determination) over a range of rotational broadenings to determine v sin i for the primary and secondary. By minimizing a chi-squared goodness-of-fit statistic for metallic lines in the reconstructed spectrum and a grid of models spanning a range of rotational broadenings, we

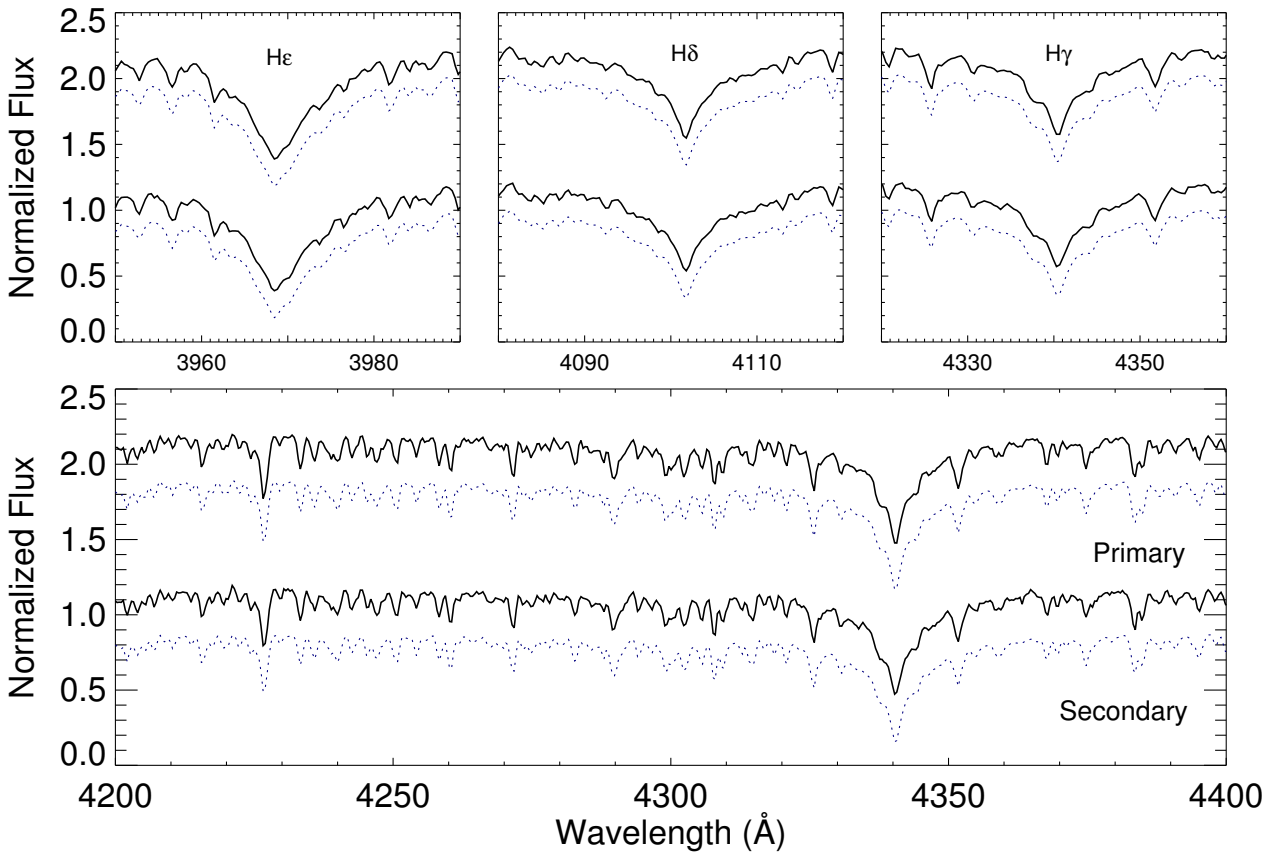

Figure 4.3: A portion of the reconstructed spectra of the primary (upper) and secondary (lower) components of KIC 5738698 based on 13 moderate resolution optical spectra. Corresponding model spectra from the UVBLUE grid are shown as (blue) dashed lines (offset by -0.3 normalized flux units). The upper (3) panels depict the reconstructions of the individual hydrogen Balmer lines, which are particularly sensitive to temperature in this spectral region and (Hδ and Hγ) were used to constrain the effective temperatures of each component.

find projected rotational velocities of 18 ± 16 km s^{-1} for the primary and 21 ± 10 km s^{-1} for the secondary. While these errors indicate large uncertainties in our derived rotational velocities, they are expected as the $v \sin i$ values are at the limits of our spectral resolution. Based on our resolving power of $\lambda/\Delta\lambda \sim 6200$, we can only reliably measure $v \sin i$ as small as $c/2R \sim 24$ km s^{-1}. However, as the $v \sin i$ values are consistent with the estimated

Table 4.3. Atmospheric Parameters of KIC 5738698

Parameter	Primary	Secondary
$T_{\rm eff}$ (K)	6792 ± 50	6773 ± 50
$\log g$ (cgs)	4.05[a]	4.09[a]
$V \sin i$ (km s^{-1}) .	18 ± 16	21 ± 10
F_2/F_1 (~ 4275Å)	0.82 ± 0.06	
$\log Z$ (cgs)	-0.4 ± 0.1	

[a]Fixed from light curve solution.

synchronous rate of 18.6 km s^{-1}, we adopt them and fix $\log g$ (initially to the values from the second release of the *Kepler* Eclipsing Binary Catalog, then according to our light curve solution § 4.4.2) for the model comparisons. Fixing $\log g$ in this way helps mitigate the known degeneracies between $\log g$, $T_{\rm eff}$, and $\log Z$ (where Z is the metallicity or mass fraction of elements other than hydrogen and helium in a star; Torres et al. 2012).

Because the properties of the tomographic reconstruction depend upon the assumed flux ratio r and (slightly) on the metallicity, to determine the best solution and remaining stellar parameters we make separate fits to the primary and secondary over a grid of $r = F_2/F_1$ and $\log Z/Z_\odot$ values. Tomography is repeated at each grid point and best-fit temperatures are determined via a least-squares fitting routine (using lines most sensitive to temperature, specifically Hδ and Hγ for KIC 5738698). The best $\log Z/Z_\odot$ and $r = F_2/F_1$ fits for the primary and secondary individually form two 'valleys' of minimum chi-squared as a function of $\log Z/Z_\odot$ and r, and we select the intersection of these two valleys so that the metallicity and flux ratio are the same for both stars. The final temperatures are then derived for each component using the $\log Z/Z_\odot$ and r at this consistent minimum. Table 4.3 gives the

stellar parameters derived from the best-fit models to the tomographic reconstructions of the primary and secondary.

As seen in Figure 4.3, the line depths and overall appearance of the model spectra are in very good agreement with the reconstructed spectra. The Balmer lines are the most temperature sensitive features in our wavelength range and are extremely well fit in both depth and width. Other lines sensitive to temperature and metallicity such as Ca I λ4226, Fe I $\lambda\lambda$4046, 4271, 4383 (Gray & Corbally 2009) also show consistent fits.

Uncertainties were computed via bootstrapping, in which we randomly resampled the input spectra for the tomography grids and used the standard deviation of 500 resampled solutions as the uncertainty. In addition, we also created a simulated stack of model spectra with the same Doppler shift sampling as the observations based on the derived stellar parameters and characteristic signal-to-noise levels. We then performed tomography and the grid search on the simulated spectra to determine how much the derived parameters differ from those used to create the model. Quoted parameter uncertainties (see Table 4.3) were adopted from the technique that gave the larger estimated uncertainty or one-tenth the UVBLUE grid step size of $\Delta T_{\rm eff} = 500\,{\rm K}$ and $\Delta \log Z = 0.5\,{\rm dex}$.

4.4 Binary Star Modeling

The light curve and radial velocities of KIC 5738698 were modeled using the Eclipsing Light Curve (ELC) code of Orosz & Hauschildt (2000). The code fits for a variety of binary star parameters using optimizers, such as the genetic algorithm employed in this work, to

determine a best-fit model based on an overall chi-squared goodness-of-fit. ELC uses Roche geometry and specific intensities computed from PHOENIX model atmospheres (Hauschildt et al. 1997) to determine the flux by numerically integrating over surface tiles.

4.4.1 Radial Velocity Modeling

ELC is designed to model simultaneously radial velocities and photometric data in multiple bandpasses; however when fitting data with the precision of *Kepler* the combined solutions converge where the radial velocities are not well fit due to the mismatch in the relative weights of the spectroscopic and photometric data (Bass et al. 2012). Because of this issue with the relative weights and the fact that KIC 5738698 is a well detached (nearly) circular system, we chose to fit the light curve and radial velocities separately (as done by Bass et al. 2012, Sandquist et al. 2013a, Jeffries et al. 2013). While information on the eccentricity (e) and longitude of periastron (ω) is contained in both the radial velocity and light curves and they should usually be modeled simultaneously, the very small eccentricity we detect in the light curve (§ 4.4.3.1) cannot be constrained by the radial velocity curves to the precision at which we detect it in the light curve, so a constrained fit was made.

Although the relative weights of the radial velocities and *Kepler* data prevent a simultaneous solution, we did fit the radial velocities with ELC using the results of our previous spectroscopic orbit, tomographic reconstruction, and initial parameter estimates from the *Kepler* Eclipsing Binary Catalog. This second spectroscopic fit not only verifies the consistency of the two methods but also employs the more complete physical descriptions of the two stars in ELC, which can account for offsets between the center of light and center of mass

of each component as in the Rossiter-McLaughlin and reflection effects. For the ELC model we allowed the mass ratio (q), velocity semi-amplitude of the primary (K_1), and velocity zero point (γ) to vary. The period was again fixed to the value derived from eclipse timings in Gies et al. (2015) and a circular orbit was assumed initially. A revised (eccentric) radial velocity model was determined once the light curve parameters were derived (§ 4.4.3.4) and can be seen in Figure 4.2. The associated orbital parameters are given in Table 4.2, which shows that the results of this model agree quite well with our previous spectroscopic orbital solution. A slight discrepancy, though still within the uncertainties, occurs in the systemic or zero point velocity, which is not surprising as the spectroscopic solution determined γ separately for each star, and we report the weighted mean of the two values (§ 4.3.2). One sigma uncertainties were determined by collapsing the n-dimensional χ^2 function from ELC onto each parameter and determining where the lower envelope is equal to $\chi^2_{min} + 1$ (see § 4.4.4).

4.4.2 Light Curve Modeling

4.4.2.1 Circular Orbit Model Parameters

Light curve models of KIC 5738698 were computed with ELC using all 18 quarters of *Kepler* long cadence data. We began by fixing the orbital period to 4.80877396 d from the eclipse timing results (Gies et al. 2015) and assuming a circular orbit. The value of T_0 from the eclipse timings was initially used as the time of primary eclipse ($T_{\rm conj}$ in ELC), but better convergence was reached when it was allowed to vary slightly. The primary effective tem-

perature was fixed according to the tomography results (§ 4.3.3), while the parameters from the ELC radial velocity fit (q, K_1, and γ) were held constant as they have little influence on the light curve solution.

Our baseline model had five free parameters: inclination (i), temperature ratio (T_2/T_1), fractional radii (R_1/a and R_2/a), and time of primary eclipse (T_0). We set ELC to use the included model atmosphere table to describe the variation of local intensities with emergent angle in the *Kepler* bandpass. This negates the need for limb darkening coefficients, except in the computation of the reflection effect, for which we used a logarithmic law (which provides a better match in the optical for stars cooler than 9000 K; Prša & Zwitter 2005) and coefficients from Howarth (2011). The bolometric albedo was set to 0.5 for convective envelopes (Ruciński 1969) and the gravity darkening exponents were set internally, based on the input effective temperatures, according to Claret (2000). The model intensity is integrated over a grid of equal angle increments corresponding to 60 points in latitude and 80 points in longitude on the surface of the star. For more details on running ELC, see Appendix C.

4.4.2.2 Features of Kepler Data

In order to produce the best fit to the *Kepler* long cadence data, the model light curve is computed approximately every 10 minutes then binned to 29.4244 minute intervals using simple numerical integration. This ensures the model eclipse profiles are smoothed in a manner similar to the effective exposure time of *Kepler* long cadence data while maintaining feasible computation times.

Another consideration when using *Kepler* data is the aperture contamination from other stars due to the large pixels and apertures used. KIC 5738698 has several nearby stars that, though fainter, often contribute excess light. ELC attempts to account for this by using the contamination parameter (fraction of total flux contributed by nearby stars based on the final photometric aperture) reported by the Data Search database at MAST[1] to apply an offset to the model, given by $y_{\rm off} = (k * y_{\rm med})/(1 - k)$, where k is the value of the contamination parameter and $y_{\rm med}$ is the median value of the normalized flux light curve. The contamination parameter varies each quarter (between 0.010 and 0.021 for KIC 5738698) based on the orientation of the telescope, so we use the mean value of 0.015 when fitting the combined long cadence data. Quarter-to-quarter variations likely caused by the varying contamination values are discussed in § 4.4.4.2.

4.4.2.3 Baseline Model

The best-fit model, as described above, for the long cadence light curve of KIC 5738698 is shown in Figure 4.4. The *Kepler* photometry (black dots) and model (solid green line) are shown as well as the $(O - C)$ residuals. Parameters used in the fit and their statistical uncertainties (see §4.4.4) are summarized in the first column of Table 4.4. While the model approximates the overall light curve and eclipse shapes quite well, there is distinct structure in the residuals implying the fit is insufficient. In the next section we discuss several adjustments made to the model to minimize the residuals, including fitting for an eccentric orbit, examining the family of possible solutions over a range of inclinations and fractional radii,

[1] `http://archive.stsci.edu/kepler/data_search/search.php`

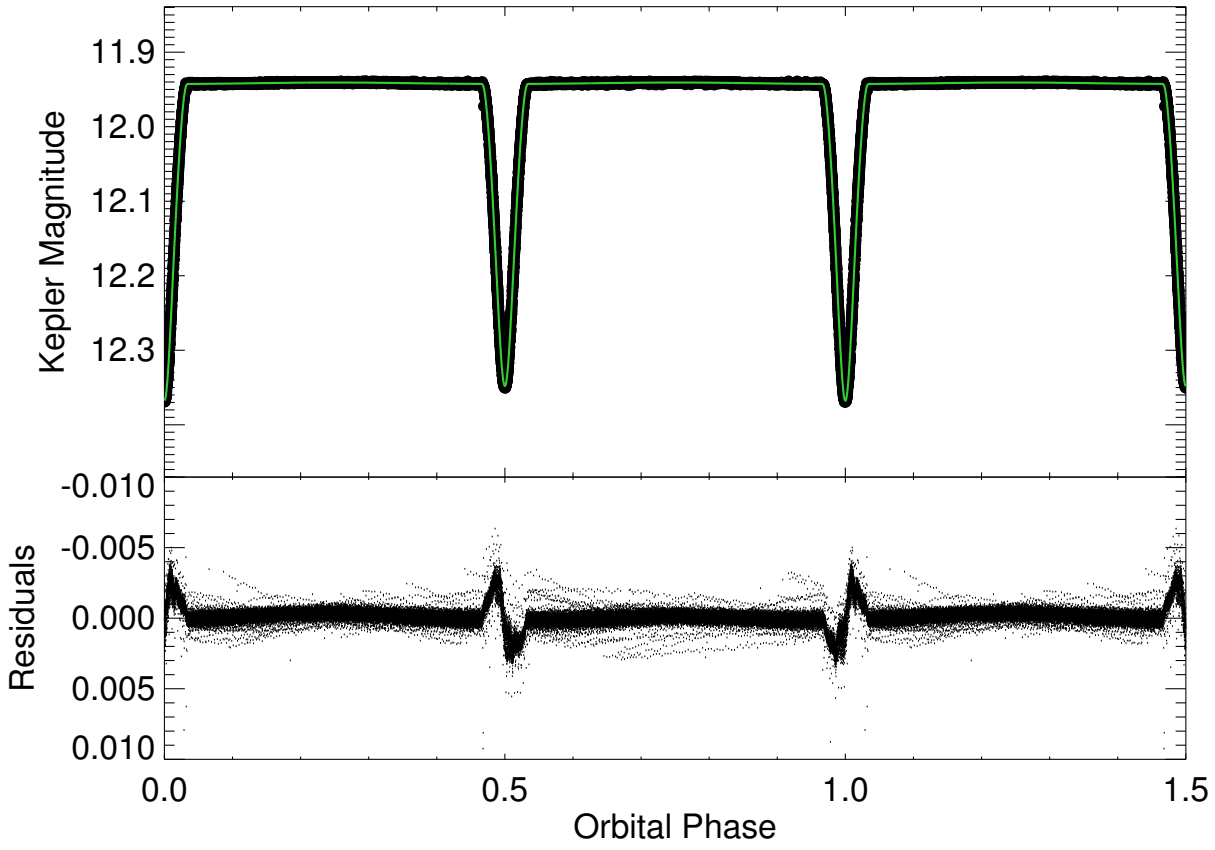

Figure 4.4: Top: the phased, long cadence *Kepler* light curve of KIC 5738698 (black points) with the best-fit circular baseline model from ELC (solid green line). A randomly selected 20% of the more than 65,000 data points are shown here. Bottom: residuals from the ELC fit to the *Kepler* light curve. See text for a discussion of the specific features and trends.

and considering the radiative properties of the stars.

4.4.3 Improving the Fit/Minimizing Residuals

4.4.3.1 In-Eclipse Residuals - Eccentric Solution

The circular baseline model for KIC 5738698 shows distinct features in the eclipse phase residuals, specifically a sine wave shaped component (see Fig. 4.4), that indicate the po-

Table 4.4. Combined Long Cadence Light Curve Fitting Parameters

Parameter	Circular Solution	Eccentric Solution
T_0 (HJD−2,400,000) .	55692.335 ± 0.003	55692.3348 ± 0.0004
e	0[a]	0.0006 ± 0.0003
ω (deg)	···	52 ± 23
i (deg)	86.32 ± 0.03	86.33 ± 0.03
R_1/a	0.1105 ± 0.0001	0.1097 ± 0.0007
R_2/a	0.1023 ± 0.0001	0.1027 ± 0.0008
T_2/T_1	0.9922 ± 0.0002	0.9920 ± 0.0003
Kepler contamination	0.015[a]	0.015[a]
Albedo (star 1)	0.5[a]	0.33
Albedo (star 2)	0.5[a]	0.33
$T_{\rm grav}$ (star 1)	0.068	0.068
$T_{\rm grav}$ (star 2)	0.068	0.068
T_1 (K)	6792[a]	6792[a]
T_2 (K)	6739 ± 51	6740 ± 52
M_1 ($M_\odot$)	1.39 ± 0.04	1.39 ± 0.04
M_2 ($M_\odot$)	1.34 ± 0.06	1.34 ± 0.06
R_1 ($R_\odot$)	1.85 ± 0.02	1.84 ± 0.03
R_2 ($R_\odot$)	1.71 ± 0.02	1.72 ± 0.03
a ($R_\odot$)	16.8 ± 0.1	16.8 ± 0.1
$\log g_1$ (cgs)	4.0462 ± 0.0004	4.0525 ± 0.0004
$\log g_2$ (cgs)	4.0963 ± 0.0006	4.0933 ± 0.0006

[a]Fixed.

sitions and durations of the eclipses are not well fit. This implies that KIC 5738698 has a small, distinctly non-zero, eccentricity. In order to speed up convergence of an eccentric solution with ELC we derived initial estimates of the eccentricity (e) and longitude of periastron (ω) from the light curve based on the offset between ($e\cos\omega$) and duration ($e\sin\omega$) of the two eclipses. The details of the approximations can be found in Appendix A, but the process is summarized here. We began by determining the time of mid-eclipse for the primary and secondary by fitting a line through bisectors at different depths along each eclipse

and extrapolating to the eclipse minimum. The phase difference between the primary and secondary is then used to determine $e\cos\omega$ according to the following relation (eq. A.12):

$$e\cos\omega = \pi\frac{(\phi_s - \phi_p - 0.5)}{(1+\csc i)} \tag{4.1}$$

where ϕ_p, ϕ_s are the phases of the primary and secondary eclipses, respectively, and the denominator $(1+\csc i)$ is used to approximate the effects of inclination when $i < 90°$ (see Appendix A.1). For KIC 5738698 we find $e\cos\omega$ to be 0.00035, which is consistent with the value 0.000357 derived from the eclipse timing results (Gies et al. 2015).

We then measure eclipse durations ($d = t_{\rm last} - t_{\rm first}$) using a fit to the eclipse bisector widths extrapolated to the out-of-eclipse continuum. The ratio of the difference in eclipse times over their sum is then related to $e\sin\omega$ by (eq. A.18)

$$e\sin\omega = \frac{(d_s - d_p)}{(d_s + d_p)}\frac{1}{m}. \tag{4.2}$$

Here d_p and d_s are the durations of the primary and secondary eclipses, respectively, while m represents the slope of the linear relation between the ratio of the difference and sum of the eclipse durations and $e\sin\omega$ when the eccentricity is small. We use a grid of $(R_1+R_2)/a$ and inclination i values to derive the slope m from linear fits to the ratio $(d_s - d_p)/(d_s + d_p) = m \times e\sin\omega$ (see Fig. A.2). This enables us to estimate m from the values of $(R_1 + R_2)/a$ and i derived from our circular ELC model. We can then estimate $e\sin\omega$ from the observed ratio $(d_s - d_p)/(d_s + d_p)$ (see eqs. A.19 and A.20 in Appendix A.2) divided by this value of m. For the circular model of KIC 5738698, $i = 86.32°$ and $(R_1 + R_2)/a = 0.2128$, which gives us a value of $m = 0.884$. We then determine $e\sin\omega$ to be 0.0017.

These approximations ($e\cos\omega = 0.00035$, $e\sin\omega = 0.0017$) provide starting values of $e = 0.0017$ and $\omega = 78°$ that we use to define regions of parameter space to explore with ELC. Using the genetic optimizer, ELC converged to values of $e = 0.0006$ and $\omega \sim 50°$. However, because the durations of the primary and secondary eclipses are nearly identical and our measurement of the durations is only approximate, $e\sin\omega$ is not well constrained and slightly different estimations can lead to a range of $e\sin\omega$ values where $0° < \omega < 90°$ or $270° < \omega < 360°$. To account for this we also allowed ω to vary between 270 and 360°, which resulted in solutions where $e = 0.0004$ and $\omega \sim 300°$ with approximately the same chi-squared. Fitting for $e\cos\omega$ and $e\sin\omega$ directly led to $e\cos\omega = 0.00034$ and $e\sin\omega = -0.00122$, corresponding to $e = 0.0016$ and $\omega \sim 280°$ but the chi-squared was higher than solutions fitting for e and ω directly. Based on the slightly lower chi-squared and better fit to the light curve we adopt $e = 0.0006$ and $\omega = 52°$. The fitted and derived parameters from the eccentric model are listed in Table 4.4 and the model fit and residuals are shown in Figure 4.6. Given the ambiguity in the longitude of periastron and range of possible eccentricities for the system, however, it might be more appropriate to establish an upper limit (as advocated for spectroscopic binaries by Lucy 2013) of $e \lesssim 0.0017$ for KIC 5738698.

Given the precision of *Kepler* light curves and the delay in the secondary eclipse, another factor that has to be considered is the light travel time across the binary orbit. Bass et al. (2012) found approximately one-third of the delay in the secondary eclipse relative to phase 0.5 of KIC 6131659 was due to light travel time. We determine the delay using (eq. A13)

$$\Delta t_{LT} = \frac{PK_2}{\pi c}(1 - q) \tag{4.3}$$

where Δt_{LT} is the time difference between eclipses due to light travel time, P is the period, K_2 is the velocity semi-amplitude of the secondary, q is the mass ratio, and c is the speed of light. We can then compare this to the relative times of the primary and secondary eclipses in an eccentric orbit (Δt_e) using

$$\Delta t_e \approx \frac{2Pe}{\pi} \cos \omega \tag{4.4}$$

(see eq. A.9), where P is the period, e is the eccentricity, and ω is the longitude of periastron of the binary. With the appropriate values from Table 4.2 and our adopted eccentric ELC model, we calculate the light travel time delay in KIC 5738698 to be 1.5 sec compared with the total observed delay between the primary and secondary eclipses of 98.8 s. Even if we consider the range of possible e and ω values from different ELC models, the light travel time delay is at most 3% of the total delay and we therefore do not attempt to make any corrections in our models, but are aware it may be a source of additional uncertainty in our measurements of e and ω.

4.4.3.2 Out-of-Eclipse Residuals - Stellar shapes and sizes

In addition to the signature of an eccentric orbit, the light curve residuals demonstrate a slight ellipsoidal variation outside of eclipse which was not well fit with the circular model. Figure 4.4 shows that the residuals appear slightly brighter at quadrature relative to eclipse phases. We attempted to fit this modulation by adjusting the rotational distortion of the stars incrementally over a range of sizes and inclinations. To find combinations of fractional radii and inclination that would fit the observed light curve, we used a simple analytical

model (employing linear limb darkening and *Kepler* contamination) to find values of r_1, r_2, and i that were capable of reproducing the depths and widths of the primary eclipse. We then used the gridELC optimizer package, which uses a grid search routine to adjust a given set of parameters and find the minimum chi-squared, to find the model with the best fit to the observed light curve. The grid search produced two models with similar chi-squared values where the primary was larger in the first ($r_1 = 0.110$, $r_2 = 0.101$, $i = 86.47°$) and smaller in the second ($r_1 = 0.103$, $r_2 = 0.109$, $i = 86.47°$). We then produced model light curves using combinations of r_1 and r_2 spanning these values ($r_{1,2} = 0.095$ - 0.12 with $\Delta r = 0.0025$) using our best-fit inclination ($i = 86.33°$, §4.4.3.4). The chi-squared surface contours from these ELC models are plotted in Figure 4.5 as a function of the primary and secondary fractional radii.

As demonstrated in the contour plot, for eclipsing binaries with partial, moderately deep, and nearly equal eclipses there exists a range of equally good fits due to a degeneracy among the inclination, radii, and secondary temperature (Rozyczka et al. 2014). In order to remove the degeneracy and determine the best solution along the 'valley' of fractional radii values, we use our spectroscopic flux ratio ($F_2/F_1 = 0.82 \pm 0.06$; §4.3.3) and surface flux models from ATLAS9 to calculate the ratio of the radii (R_2/R_1). The observed flux ratio is proportional to the projected areas and surface fluxes ($f_2/f_1 = 0.98$) of the stars, such that

$$\frac{R_2}{R_1} = \sqrt{\frac{F_2/F_1}{f_2/f_1}}. \tag{4.5}$$

Thus, the spectroscopic data impose the condition $R_2/R_1 = 0.91 \pm 0.04$, shown by the dashed line and gray region in Figure 4.5. We therefore adopt solutions to the light curve in this

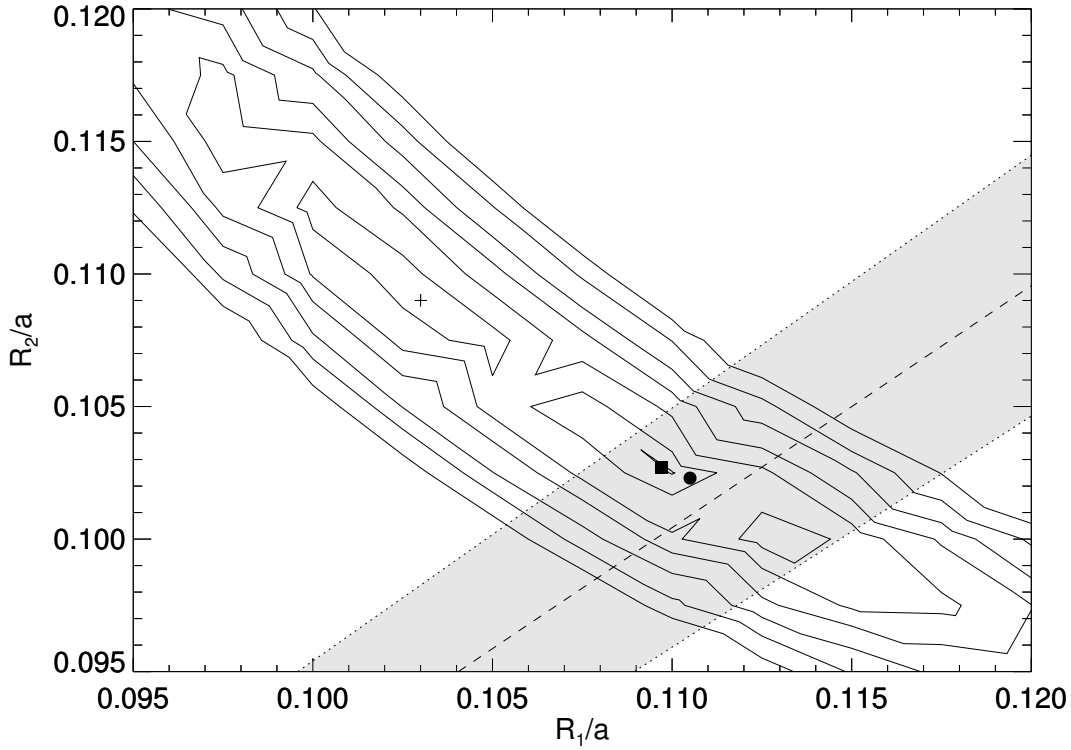

Figure 4.5: Plot of chi-squared surface contours as a function of the fractional radii of the primary and secondary from a grid of values spanning $r_{1,2} = 0.095$ - 0.12 with $\Delta r = 0.0025$. The contours represent regions 1 (behind square), 4, 9, 16, 25, 36, and 49 times the minimum chi-squared (arbitrarily chosen to highlight the topography), increasing outward from the valley through the center of the plot. The ratio of the radii, $R_2/R_1 = 0.91 \pm 0.04$, as derived from the spectroscopic flux ratio (§4.3.3) is shown by the dashed line with the gray stripe representing the uncertainty. The filled circle and square show the fractional radii of our best-fit circular and eccentric ELC solutions, respectively. The plus sign gives the location of a solution where the primary star is smaller then the secondary; see text for details.

region of the valley where the primary is larger than the secondary. The filled circle and square show the fractional radii of our best-fit circular (§ 4.4.2.3) and eccentric ELC solutions (§ 4.4.3.4), respectively. The plus sign gives the location of the minimum gridELC model where the primary star is smaller than the secondary for comparison.

While solutions in this region are mutually consistent with the light curve and spectro-

scopic data, the associated best-fit fractional radii do not account for the apparent ellipsoidal variation seen in the light curve.

4.4.3.3 Out-of-Eclipse Residuals - Radiative Effects

In an effort to understand the out-of-eclipse modulation in our light curve residuals we next examined various radiative properties associated with binary modeling. As mentioned previously, we used the model atmospheres contained in ELC to compute surface intensities and thus account for the stellar limb darkening. In order to test whether this had any affect on the remaining residuals we produced ELC model light curves using linear and logarithmic limb darkening laws with coefficients from Howarth (2011), Claret & Bloemen (2011), and the internal limb darkening tables (2011 version) of PHOEBE (Prša & Zwitter 2005). When using the ELC atmospheres to set the intensity at the surface normal and the logarithmic limb darkening law for all other angles, the eclipse depth is most affected. Similar changes in eclipse depth and very slight changes in eclipse widths occurred when local intensities were computed using a blackbody approximation with a linear or logarithmic limb darkening law. However, while the slight changes in eclipse depths and durations from the different parameterizations of limb darkening account for some of the modulation and scatter in the eclipse residuals, as expected they have no impact on the out-of-eclipse residuals.

Similarly, changing the gravity darkening exponents between the canonical value of 0.08 (Lucy 1967) for stars with convective envelopes and that derived from Claret (2000) (see Table 4.4) did not influence the residuals.

As adjustments to the limb darkening and gravity brightening did not significantly im-

prove the model fits to the out-of-eclipse variations, we included the bolometric albedo A of each star as fitted parameters in ELC. In the circular model of KIC 5738698 we fixed the albedo to 0.5, the canonical value for a star with a convective envelope. While Claret (2001) determined that the upper limit for convective envelopes should be 6300 K, using 1.0 (the theoretical value of albedo for stars with radiative envelopes) greatly over estimated the out-of-eclipse flux. However, allowing the albedo to vary freely resulted in even lower values, with a best-fit solution of $A_1 = 0.336$ and $A_2 = 0.334$. This suggests that the baseline model overestimated the flux around the eclipse times (when the illuminated hemispheres are directed our way), and thus the model residuals appeared somewhat fainter (Fig. 4.4).

Using photometry from the WIRE satellite, Southworth et al. (2007) similarly found better fits to the amplitude of the light variation outside eclipse for the detached eclipsing binary β Aurigae by including the bolometric albedos as fitting parameters. While the albedos they derived were similar to the theoretical value of 0.5 for convective atmospheres (0.59 and 0.56), the stellar temperatures (9350 and 9200 K) suggest radiative atmospheres, indicating a lower then expected albedo. Southworth et al. (2011) and Hambleton (2011) also found unrealistic values (>1) of albedo when fitting eclipsing binaries using *Kepler* data.

While a lower albedo implies the stars re-radiate a smaller fraction of incident light then expected from theory, several past studies have found evidence for a broad range of albedo values. Initially Ruciński (1969) estimated the albedo for stars with convective envelopes to be between 0.4 and 0.5, and Rafert & Twigg (1980) observationally determined a value slightly greater than 0.3 for two stars with temperatures similar to KIC 5738698. Fur-

thermore, Sipahi et al. (2013) derive b and v-band albedos between 0.2 and 0.3 for three near contact binaries with convective secondaries ($T_{\rm eff} \sim 5500\,{\rm K}$). This discrepancy between theory and observation revealed by the *Kepler* data serves to highlight our lack of understanding concerning the physical processes in the photospheres of stars near the transition zone between radiative and convective envelopes.

4.4.3.4 Final LC Model

Initial results from our baseline light curve model, updated radial velocity fit, and the values of r_1, r_2, i, e, and ω as derived above were then used as constraints for final models with ELC. The values of i, r_1, r_2, T_2/T_1, e, ω, and T_0 were allowed to vary and the genetic algorithm was used to determine the best-fit model. Our adopted ELC model light curve is shown in Figure 4.6 with the *Kepler* data (black dots), model (solid green line), and $(O-C)$ residuals shown at bottom. The fitted and calculated parameters are listed in Table 4.4.

As can be seen in Figure 4.6, the residuals still show some structure, especially during eclipse. These likely reflect a combination of imperfect light curve normalization and quarterly changes in contamination values. In addition, Hambleton et al. (2013) point out that small model discrepancies during light curve minima are common in the case of very accurate satellite light curves due to the incomplete physics in presently available models, while Sandquist et al. (2013b) cite differences in the vertical structure of the ELC atmosphere models and observations as potential causes of systematic uncertainties in the derived parameters, which can be seen as mismatches between the model and observations.

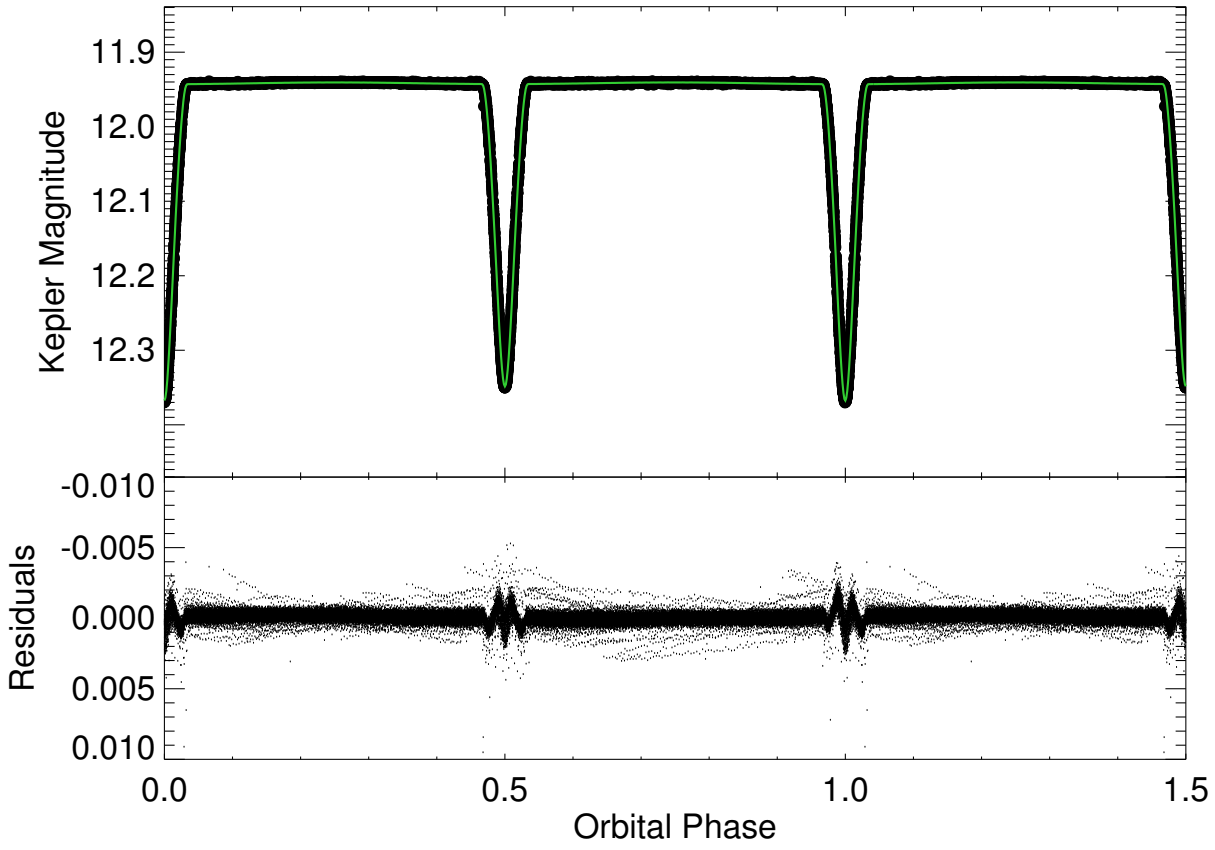

Figure 4.6: Top: the phased, long cadence *Kepler* light curve of KIC 5738698 (black points) with the best-fit eccentric model from ELC (solid green line), as described in §4.4.3. A randomly selected 20% of the more than 65,000 data points are shown here. Phase zero is set as the time of primary eclipse. Bottom: residuals from the ELC fit to the *Kepler* light curve.

4.4.4 Parameter Uncertainties

In order to estimate the statistical uncertainties on the fitted and derived astrophysical parameters we collapse the n-dimensional χ^2 function from ELC onto each parameter of interest as done by Orosz et al. (2002). We scale the chi-squared values such that $\chi^2_{min}/\nu \approx 1$ and plot the lower envelope of each parameter by determining the minimum chi-squared in

Table 4.5. Long Cadence Segments & Short Cadence Parameters

Parameter	Q0-Q2	Q3-Q4	Q5-Q6	Q7-Q8	Q9-Q10	Q11-Q12	Q13-Q14	Q15-Q17	Short Cad.	Mean	Std Dev
T_0[a]	0.3347	0.3349	0.3348	0.3349	0.3336	0.3349	0.3348	0.3347	0.3348	0.3347	0.0004
e	0.0009	0.0006	0.0005	0.0004	0.0008	0.0010	0.0011	0.0009	0.0005	0.0007	0.0003
ω (deg) ..	301	54	46	17	340	69	288	62	325	314/50	23/20
i (deg) ...	86.26	86.36	86.33	86.31	86.29	86.32	86.33	86.34	86.33	86.32	0.03
R_1/a	0.1099	0.1116	0.1108	0.1095	0.1102	0.1100	0.1109	0.1106	0.1099	0.1104	0.0007
R_2/a	0.1030	0.1006	0.1018	0.1035	0.1027	0.1027	0.1016	0.1019	0.1027	0.1023	0.0008
T_2/T_1	0.9920	0.9923	0.9925	0.9919	0.9927	0.9921	0.9921	0.9923	0.9920	0.9923	0.0003

[a]HJD−2,455,692

small bins across the whole range. The 1 and 2 σ confidence intervals are the parameter values where the lower envelope of the χ^2 function is equal to $\chi^2_{min} + 1$ and $\chi^2_{min} + 4$, respectively.

4.4.4.1 Long Cadence Segments and Short Cadence Data

As a check on systematic uncertainties in the light curve modeling and to examine any parameter variations over time, we divided our 18 quarters of long cadence data into eight individual segments. Each segment spanned two quarters (except the first and last groups which spanned three quarters; Q0-2 and Q15-17) with an average of ∼8000 data points. ELC models were run on each segment individually using the same input and fitting parameters as the 'final' eccentric fit to the combined long cadence data. Table 4.5 shows the free parameters for each segment as well as the mean and standard deviation. In each segment the longitude of periastron was allowed to vary between $0° < \omega < 90°$ and $270° < \omega < 360°$, resulting in two distinct clusters of ω as seen in Table 4.5. The values of ω oscillate in every other segment between mean values of $314 \pm 23°$ and $50 \pm 20°$. This highlights that while the tiny eccentricity is detectable in the light curve residuals, ω is not well constrained by the ELC models.

We also fit the single month of short cadence data for KIC 5738698 collected in Q4 (∼45,000 data points). Because of the different 'exposure times' of the long and short cadence data they cannot be modeled together, so we treated the short cadence data as a ninth segment and determined an optimized ELC model for the light curve. All of the inputs and model constraints were the same as those of the other segments except the model was not binned and the contamination parameter of 0.017 associated with the short cadence data was used. The parameters from the short cadence model are given in Table 4.5 and agree very well with the other segments.

Because the spread of derived parameter values obtained in the segments should give us an independent measure of the systematic uncertainties, we adopt the standard deviations as our uncertainties in Table 4.4.

4.4.4.2 Aperture Contamination

Our adopted value of the contamination factor, the fraction of flux from other stars in the *Kepler* pixel aperture, presents another possible source of systematic uncertainty in our parameter estimates. Changes in the pixel aperture used in successive observing quarters can lead to changes in the contamination factor as faint nearby stars are included or excluded from the photometric summation over the aperture. Figure 2.1 demonstrates how the raw counts vary between observing quarters due to contamination and other factors. We checked for varying contamination by forming phase binned light curves for each observing quarter and comparing the eclipse depths to those in a global average, phase binned light curve. We find that there is a small variation in eclipse depth that repeats over a four quarter

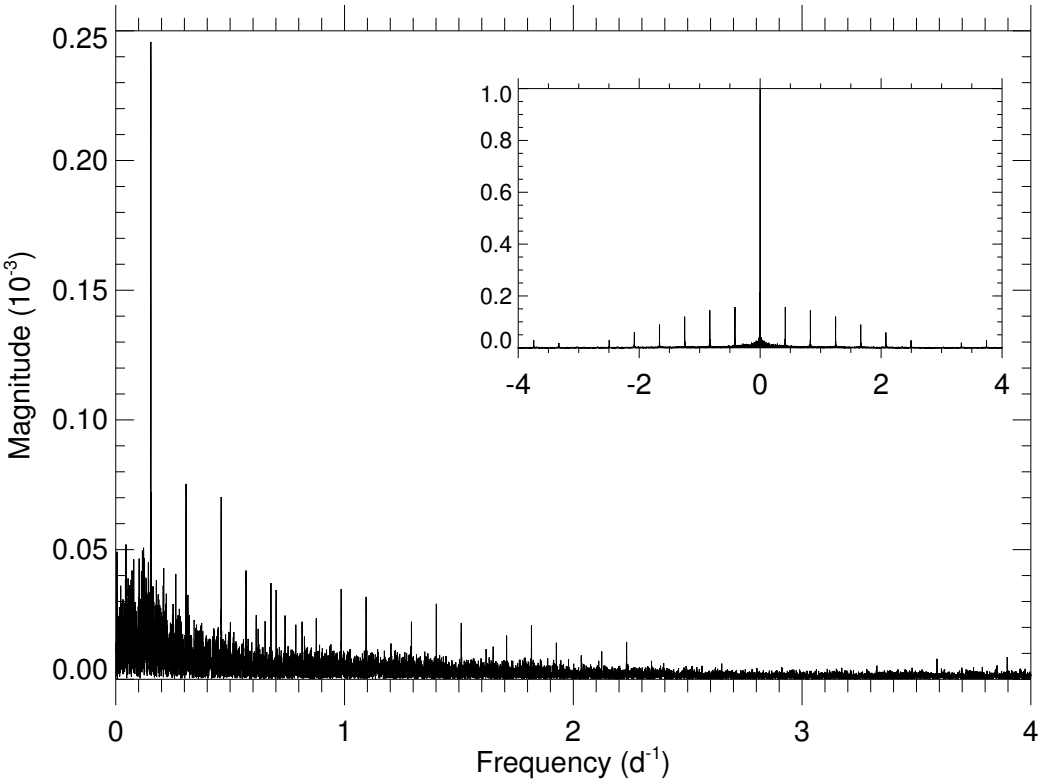

Figure 4.7: The Fourier spectrum of the long cadence light curve residuals for KIC 5738698. The dominant frequencies are $f_1 = 0.15347$, $f_2 = 0.30725$, and $f_3 = 0.46067$ d^{-1}. The inset shows the spectral window function, which indicates the locations of the alias peaks introduced by removing the eclipse portion of the light curve resulting in gaps equal to twice the orbital frequency.

cycle with a total amplitude of 0.5% and which appears to correspond to maximum depth when the pixel aperture largely excludes three faint nearby stars (KIC 5738680, 5738689, and 5738720). We therefore think that the changes in the derived binary inclination with samples from different quarters (Table 4.5) is the result of the changing contamination factor.

4.4.5 Non-Orbital Frequencies

Gies et al. (2012) detected a hint of pulsation in the gray-scale diagram that depicts the difference from the mean light curve for each photometric measurement through Quarter 9 of KIC 5738698. We therefore calculated the Fourier transform of the long cadence residuals to detect any pulsational frequencies. The Fourier spectrum, shown in Figure 4.7, has a dominant peak at $f_1 = 0.15347 \pm 0.00002$ d^{-1} (period of 6.51593 days) with two harmonics, $f_2 = 0.30725 \pm 0.00002$ d^{-1} and $f_3 = 0.46067 \pm 0.00002$ d^{-1}. The observed frequencies appear similar to those generally found for high order-g modes and both components of KIC 5738698 do fall inside the γ Doradus instability strip when placed on the $T_{\rm eff} - L$ plane (Dupret et al. 2005), making it possible one of the components is a γ Doradus variable. We note, however, the period of f_1 is longer than the expected range for γ Doradus stars ($0.3-3$ d; Bradley et al. 2015) and it is also possible the frequency is due to rotational modulation. Nevertheless, the frequencies differ from the orbital period of the binary and should not affect our analysis of the light curve but will add to the residual scatter.

4.5 Comparison with Evolutionary Models

In the following, we compare the newly derived parameters of KIC 5738698 with those predicted by stellar evolutionary models. As masses and radii are the most directly testable parameters from eclipsing binaries, we compare our results with isochrones from a selection of evolutionary models in the $M - R$ plane through a chi-squared goodness-of-fit statistic. We determine the best fitting metallicity and age for our derived parameters by forming a

grid of isochrones over a range of precomputed $\log Z/Z_{\odot}$ values and ages. The masses, radii, temperatures, and metallicities of the isochrones at each grid point are compared to our derived values using the following chi-squared criterion:

$$\chi^2 = \left[\sum_{i=1}^{2}\left(\frac{M-M_i}{\Delta M_i}\right)^2 + \left(\frac{R-R_i}{\Delta R_i}\right)^2 + \left(\frac{T-T_i}{\Delta T_i}\right)^2\right] + \left(\frac{\log\frac{Z_m}{Z_{\odot}} - \log\frac{Z_o}{Z_{\odot}}}{\Delta\log\frac{Z_o}{Z_{\odot}}}\right)^2 \quad (4.6)$$

where $M_{1,2}$, $R_{1,2}$, and $T_{1,2}$ are the masses, radii, and temperatures determined via ELC for the primary and secondary components (see Table 4.4); M, R, and T are the corresponding values for the selected model isochrone; Z_m is the metallicity of the selected isochrone; and Z_o is the observed metallicity derived from spectroscopy (-0.4 ± 0.1; §4.3.3). We find the minimum chi-squared for each $\log Z/Z_{\odot}$ and age, then use a spline fit to interpolate to the global minimum and determine the corresponding best-fit metallicity and age. To compare the metallicity with our spectroscopic results, we transform $\log Z/Z_{\odot}$ in terms of the solar metallicity used by each individual model (see Table 4.6) to the solar metallicity used in the UVBLUE spectral grids ($Z_{UV_{\odot}} = 0.01886$). Uncertainties are found by using the degrees of freedom (5) to scale the chi-squared values and selecting the 1σ confidence interval where $\chi^2 = \chi^2_{min} + 1$. The best-fit values and corresponding (unscaled) minimum chi-squared are given in the last three columns of Table 4.6. The unscaled minimum chi-squared for most of the models is well below the number of degrees of freedom indicating the parameter uncertainties are overestimated, however we use it as a means to intercompare the various models examined here.

Table 4.6. Evolutionary Model Details

Model	Enrichment Law (Y=)	Solar Composition (X)	(Y)	(Z)	Mixing Length (l/H_p)	Helium Diffusion	Best-fit $\log Z/Z_{UV_\odot}$	Best-fit Age (Gyr)	Unscaled Chi-Squared
Yonsei-Yale[a]	$0.23 + 2Z$	0.7156	0.2662	0.0181	1.7432	Y	-0.31 ± 0.08	2.32 ± 0.02	0.5
Victoria-Regina[b]	$0.2354 + 2.2Z$	0.7044	0.2768	0.0188	1.90	N	-0.30 ± 0.02	2.16 ± 0.01	1.8
PARSEC[c]	$0.2485 + 1.78Z$	0.7343	0.2756	0.0152	1.7	Y[e]	-0.23 ± 0.04	2.18 ± 0.01	3.6
Geneva[d]	$0.248 + 1.2857Z$	0.7200	0.2660	0.0140	1.6467	Y[f]	-0.37 ± 0.07	2.3 ± 0.1	22.3

[a] Solar Mixture Source: Grevesse et al. 1996.
[b] Solar Mixture Source: Grevesse & Noels 1993.
[c] Solar Mixture Source: Grevesse & Sauval 1999.
[d] Solar Mixture Source: Asplund et al. 2005.
[e] For $M_{conv} > 0.05 M_{tot}$
[e] For $M < 1.1 M_\odot$

4.5.1 Yonsei-Yale

The Yonsei-Yale (Y^2) isochrones[2] by Demarque et al. (2004) provide the best fit to the parameters of KIC 5738698. These models include an updated treatment of convective core overshoot in which the overshooting parameter Λ_{OS} 'ramps up' depending on the mass of the star and the metallicity, affecting the critical mass above which stars have a substantial convective core on the main sequence ($M_{\rm crit}^{\rm conv}$). More details of the input physics in the Y^2 models can be found in Table 4.6. Isochrones and evolutionary tracks for $X = 0.749$ and $Z = 0.007$ (corresponding to $\log Z/Z_{UV_\odot} = -0.43$; solid black lines) and $X = 0.740$ and $Z = 0.010$ (corresponding to $\log Z/Z_{UV_\odot} = -0.28$; dashed red lines) are shown in Figure 4.8. While the uncertainties in the parameters allow for a range of possible ages, the best fit occurs at 2.32 Gyr with a metallicity of $\log Z/Z_{UV_\odot} = -0.31$. As seen in the $M - R$ plane, the isochrones have a steeper slope then that of a line connecting the primary (diamond) and secondary (square) suggesting the primary is younger. Similar age discrepancies have been observed in other F-type eclipsing binaries by Clausen et al. (2010b, see their Figures 9 and

[2] `http://www.astro.yale.edu/demarque/yystar.html`

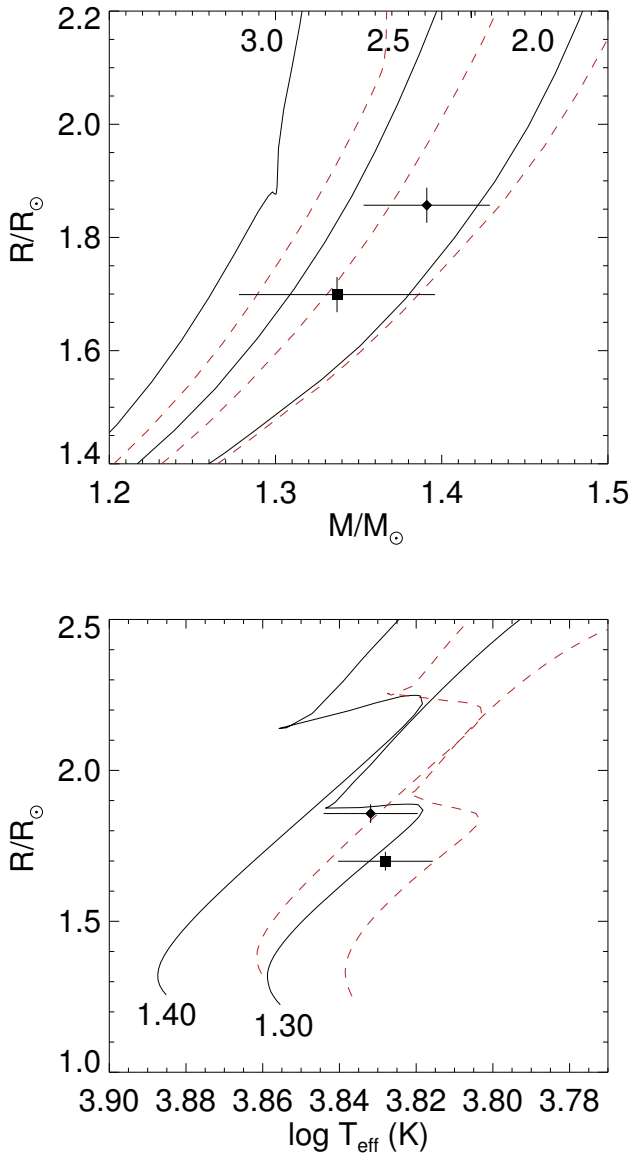

Figure 4.8: Yonsei-Yale isochrones and evolutionary tracks plotted against the primary (diamond) and secondary (square) of KIC 5738698. Top: isochrones for $\log Z/Z_{UV_\odot} = -0.43$ (solid black lines) and $\log Z/Z_{UV_\odot} = -0.28$ (dashed red lines) with ages of (right to left) 2.0, 2.5, and 3.0 Gyr, as marked to the left of the isochrones. The metallicities have been scaled to the solar metal mass fraction used in the UVBLUE models, see §4.5.1 for details. Bottom: evolutionary tracks for $\log Z/Z_{UV_\odot} = -0.43$ (solid black lines) and $\log Z/Z_{UV_\odot} = -0.28$ (dashed red lines) at (right to left) 1.3 and $1.4 M_\odot$.

10) and Torres et al. (2014b), although they concentrate on systems with unequal masses in the range $1.15-1.70 M_{\odot}$. Both papers conclude that the age disparity in this particular mass range is likely due to the calibration of convective overshooting, though Torres et al. suggest it may arise from a more complex relationship between overshooting, mass, and metallicity, possibly involving the evolutionary state as well. The evolutionary tracks plotted in the $T_{\rm eff} - R$ plane of Figure 4.8 show an offset between the derived masses and Y^2 theoretical tracks, such that both stars are undersized and/or cooler at our spectroscopically derived metallicity. When compared with the $\log Z/Z_{UV_{\odot}} = -0.28$ tracks (most similar to the best-fit metallicity of -0.31), however, both components fall along the corresponding mass track within the uncertainties. While this slightly higher metallicity appears to bring our observations in line with the models, we note that Clausen et al. (2010b) similarly found the components of V1130 Tau ($1.31 M_{\odot}$ and $1.39 M_{\odot}$, $1.49 R_{\odot}$ and $1.78 R_{\odot}$, 6650 K and 6625 K, P = 0.8 d) approximately 200 K cooler then the corresponding Y^2 models (see their Figure 6) at their observed metallicity of $\log Z = -0.24$ which may indicate a discrepancy with theory, although (like us) their abundances have not been derived in detail.

4.5.2 Victoria-Regina

We also compare our results to the Victoria-Regina Stellar Models[3] from VandenBerg et al. (2006). These models determine the convective core boundary using integral equations for the maximum size of the central convective zone based on the luminosity from radiative processes and nuclear reactions using the free parameter $F_{\rm over}$, calibrated via open cluster

[3] `http://www.cadc-ccda.hia-iha.nrc-cnrc.gc.ca/community/VictoriaReginaModels/`

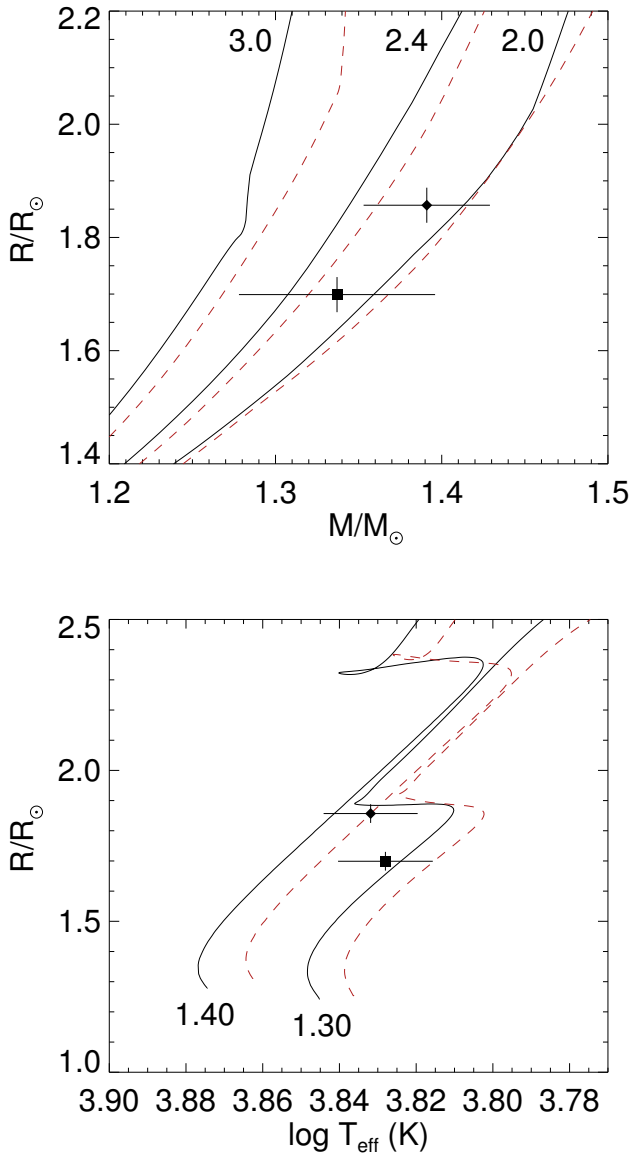

Figure 4.9: Victoria-Regina isochrones and evolutionary tracks plotted against the primary (diamond) and secondary (square) of KIC 5738698. Top: isochrones for $\log Z/Z_{UV_\odot} = -0.37$ (solid black lines) and $\log Z/Z_{UV_\odot} = -0.27$ (dashed red lines) with ages of (right to left) 2.0, 2.4, and 3.0 Gyr, as marked to the left of the isochrones. The metallicities have been scaled to the solar metal mass fraction used in the UVBLUE models, see §4.5.2 for details. Bottom: evolutionary tracks for $\log Z/Z_{UV_\odot} = -0.37$ (solid black lines) and $\log Z/Z_{UV_\odot} = -0.27$ (dashed red lines) at (right to left) 1.3 and $1.4 M_\odot$.

color-mass diagrams. $F_{\rm over}$ is treated as a continuously increasing function between 1 and $2M_{\odot}$, with the transition mass range adjusted for varying metallicities. In the $M-R$ plane of Figure 4.9 the best-fit isochrones correspond to a younger age of 2.16 Gyr but nearly the same metallicity, -0.30, as the Y^2 models. In the $T_{\rm eff}-R$ plane the Victoria-Regina evolutionary tracks are very similar to the Y^2 models, although the $1.4M_{\odot}$ tracks turn off at slightly cooler temperatures and larger radii.

4.5.3 PARSEC

Next we consider the PARSEC Stellar Evolution Code[4] of Bressan et al. (2012) (v1.2s). Similar to the previously discussed models, PARSEC adopts a variable overshoot parameter that linearly increases throughout a transition region dependent on the metallicity. However, they define overshooting based on the mean free path of convective bubbles *across* the border of the convective region, with a maximum $\Lambda_{\rm C}$ of 0.5 which roughly coincides with $\Lambda_{\rm OS}=0.25$ above the convective border as in other parameterizations (Bressan et al. 2012). The best-fit isochrones in the $M-R$ plane (Figure 4.10) indicate an age of 2.18 Gyr, consistent with the Victoria-Regina models, but less metal-poor with $\log Z/Z_{UV_{\odot}}=-0.23$. In the $T_{\rm eff}-R$ plane the tracks are slightly warmer then those of the Y^2 and Victoria-Regina models and the components of KIC 5738698 are further from the 'blue hook' than in any of the other models.

[4] `http://people.sissa.it/~sbressan/parsec.html`

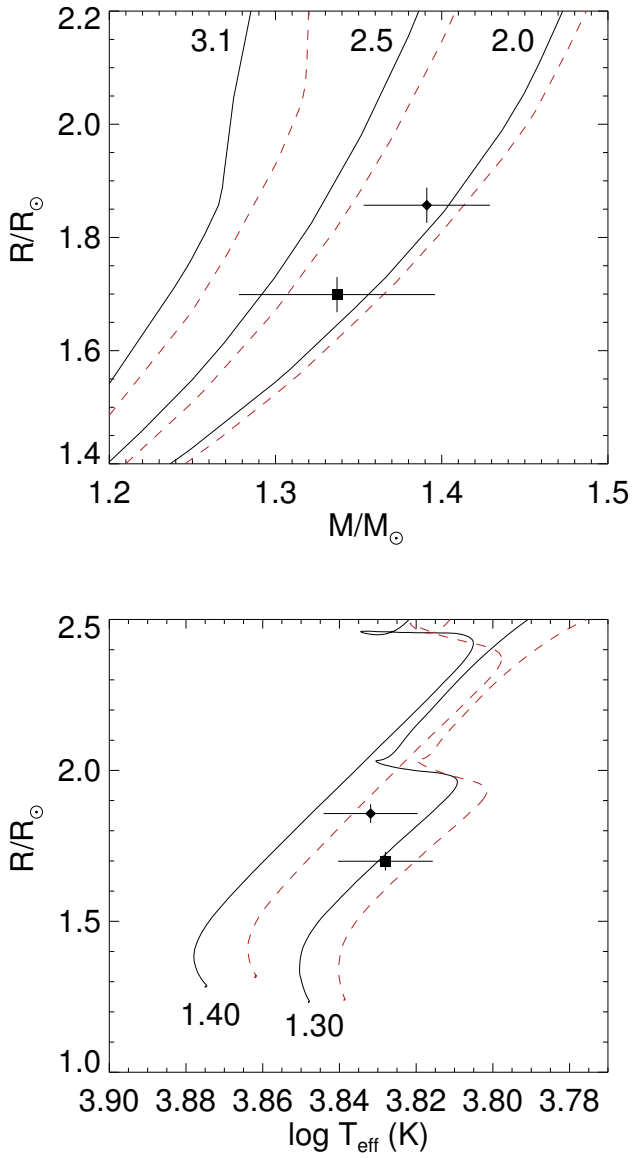

Figure 4.10: PARSEC isochrones and evolutionary tracks plotted against the primary (diamond) and secondary (square) of KIC 5738698. Top: isochrones for $\log Z/Z_{UV_\odot} = -0.37$ (solid black lines) and $\log Z/Z_{UV_\odot} = -0.28$ (dashed red lines) with ages of (right to left) 2.0, 2.5, and 3.0 Gyr, as marked to the left of the isochrones. The metallicities have been scaled to the solar metal mass fraction used in the UVBLUE models, see §4.5.3 for details. Bottom: evolutionary tracks for $\log Z/Z_{UV_\odot} = -0.37$ (solid black lines) and $\log Z/Z_{UV_\odot} = -0.28$ (dashed red lines) at (right to left) 1.3 and $1.4 M_\odot$.

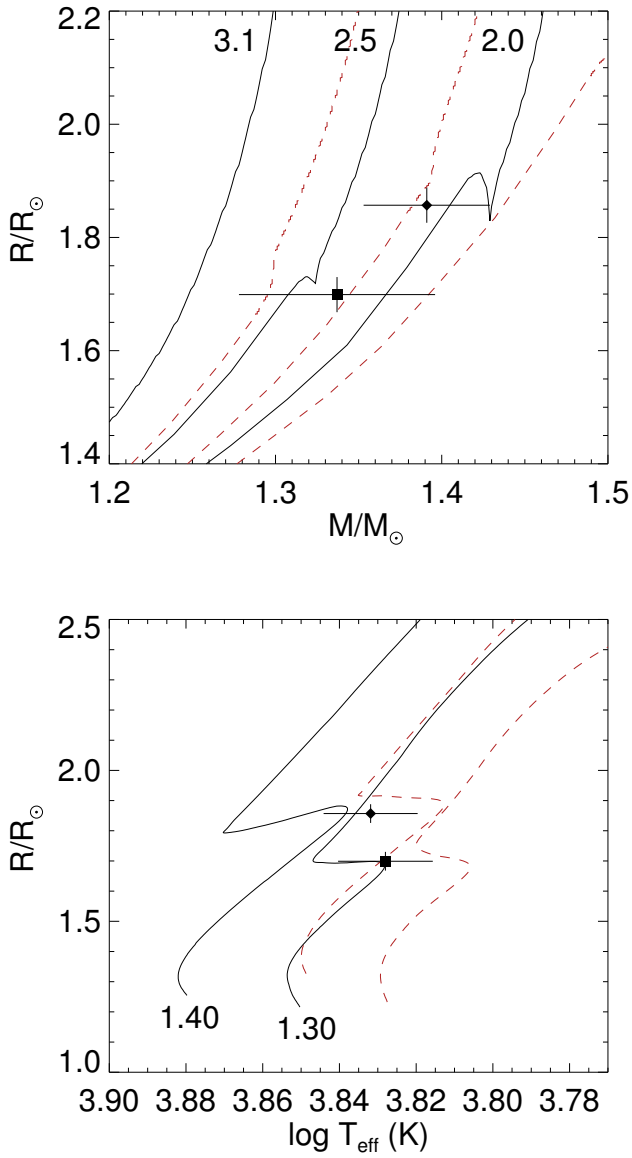

Figure 4.11: Geneva isochrones and evolutionary tracks plotted against the primary (diamond) and secondary (square) of KIC 5738698. Top: isochrones for $\log Z/Z_{UV_\odot} = -0.50$ (solid black lines) and $\log Z/Z_{UV_\odot} = -0.28$ (dashed red lines) with ages of (right to left) 2.0, 2.5, and 3.1 Gyr, as marked to the left of the isochrones. The metallicities have been scaled to the solar metal mass fraction used in the UVBLUE models, see §4.5.4 for details. Bottom: evolutionary tracks for $\log Z/Z_{UV_\odot} = -0.50$ (solid black lines) and $\log Z/Z_{UV_\odot} = -0.28$ (dashed red lines) at (right to left) 1.3 and $1.4 M_\odot$.

4.5.4 Geneva

Finally, we compare our derived parameters with the Geneva[5] stellar evolution code of Mowlavi et al. (2012). Here, the adopted overshoot treatment involves applying an overshoot parameter of $\Lambda_{\rm OS} = 0.10$ for $M > 1.7 M_{\odot}$, and half that between 1.25 and $1.7 M_{\odot}$. The chi-squared from the isochrones indicates an age of 2.26 Gyr, midway between the other age estimates, and $\log Z/Z_{UV_{\odot}} = -0.37$. This metallicity is the most metal-poor result from among the models examined here, but is the most consistent with our spectroscopic results. In the $T_{\rm eff} - R$ plane (Figure 4.11), however, the Geneva models place the primary and secondary components very near to or even in the contraction phase of the 'blue hook'. As this evolutionary stage is unlikely due to the short timescales involved, and overshooting results in extra hydrogen fuel in the core that lengthens the main sequence lifetimes of stars (Lacy et al. 2008), we speculate that the amount of overshooting applied in the Geneva models may be underestimated. For stars with our derived masses, the Geneva overshooting parameter is $\Lambda_{\rm OS} = 0.05$, compared to $\Lambda_{\rm OS} = 0.10$ at $1.3 M_{\odot}$ and $\Lambda_{\rm OS} = 0.15$ at $1.4 M_{\odot}$ in the $\rm Y^2$ models.

4.5.5 Implications of the Revised Radial Velocity Solution

The updated radial velocity method described in Section 3.3.1, which includes improved treatments of edge effects in the spectra, blended correlation functions, and uncertainty estimates, resulted in slightly larger masses of $1.52\,M_{\odot}$ and $1.44\,M_{\odot}$ for KIC 5738698. When compared to the $\rm Y^2$ models (see Figure 4.12), these larger masses yield an age between $1.6 - 1.8$ Gyr for metallicities between $-0.43 < \log Z/Z_{\odot} < -0.28$. However, the revised positions

[5] `http://obswww.unige.ch/Recherche/evol/-Database-`

of the stars in the $T_{\rm eff} - R$ plane due to the larger masses and correspondingly (slightly) larger radii, calculated from R/a values derived by ELC and the updated semi-major axis a, are even more undersized and/or cooler then before. In both cases the derived radii are larger than expected for main sequence stars at our measured masses and temperatures, however, even larger radii or hotter temperatures are needed to agree with the evolutionary tracks at $\log Z/Z_{\odot} = -0.31$. A higher (less negative) metallicity can again provide an improved match to our observations, however, additional observations with high resolution spectra may resolve this issue and better constrain the degeneracy between temperature and metallicity.

4.6 Summary

We have analyzed ∼3.5 years of *Kepler* photometric data along with supporting ground-based optical spectra to solve for the orbital and physical properties of the eclipsing binary KIC 5738698. Through radial velocity measurements and reconstruction of the individual spectra we find effective temperatures of 6790 and 6740 K for the primary and secondary, respectively. In modeling the light curve we have highlighted the detail probed by *Kepler* that allows us to consider a tiny orbital eccentricity and the lower than expected value of albedo. The parameters derived from the radial velocity and light curves indicate the binary consists of two very similar stars ($1.39 M_{\odot}$, $1.34 M_{\odot}$; $1.84 R_{\odot}$, $1.72 R_{\odot}$). Comparisons with stellar evolutionary models suggest the components are slightly less metal-poor than we estimated from spectroscopy, though still within our uncertainty. This minor discrepancy may indicate we underestimated the flux contamination from nearby stars, as extra light in

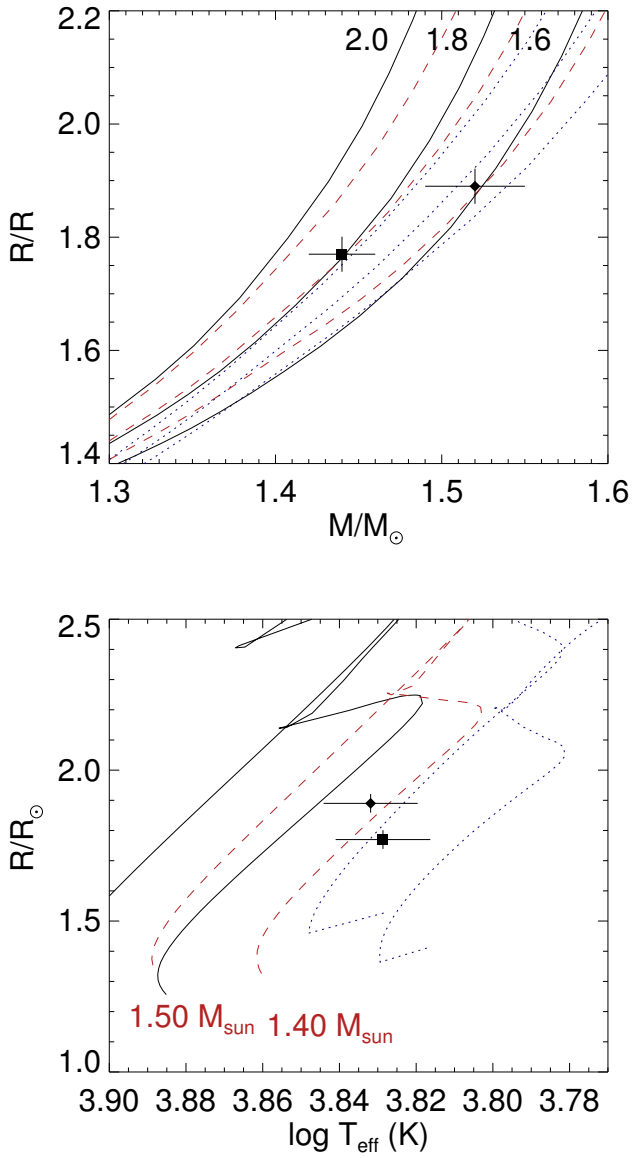

Figure 4.12: Yonsei-Yale isochrones and evolutionary tracks plotted against the updated masses for the primary (diamond) and secondary (square) of KIC 5738698 (see Table 3.5). Top: isochrones for $\log Z/Z_{UV_\odot} = -0.43$ (solid black lines), $\log Z/Z_{UV_\odot} = -0.28$ (dashed red lines), and $\log Z/Z_{UV_\odot} = 0.04$ (dotted blue lines) with ages of (right to left) 1.6, 1.8, and 2.0 Gyr, as marked to the left of the isochrones. The metallicities have been scaled to the solar metal mass fraction used in the UVBLUE models, see Section 4.5.1 for details. Bottom: evolutionary tracks for $\log Z/Z_{UV_\odot} = -0.43$ (solid black lines), $\log Z/Z_{UV_\odot} = -0.28$ (dashed red lines), and $\log Z/Z_{UV_\odot} = 0.04$ (dotted blue lines) at (right to left) 1.4 and $1.5 M_\odot$.

the spectra would result in weaker lines that can mimic the effects of a smaller $\log Z/Z_{\odot}$. At this time, however, we find the best agreement with the Y^2 models for $\log Z/Z_{\odot} = -0.31$ and an age of 2.3 Gyr (or less if the revised radial velocity solution is adopted).

This work exploits the precise photometry and long time baseline of *Kepler* to add to the known eclipsing binaries with accurate masses and radii (within 4% and 2%, respectively), adding to a small sample of stars located at the end of the core hydrogen burning phase which are sensitive to the amount of convective overshooting adopted in models. However, further benefit would come from high resolution spectra of KIC 5738698 in order to derive detailed abundances that could either reinforce the abundances suggested by the evolutionary models or indicate the presence of a companion. Such spectra would also result in tighter constraints on the effective temperatures and masses (through more RV measurements) of the stellar components.

CHAPTER 5

HST/COS DETECTION OF THE SPECTRUM OF THE SUBDWARF COMPANION OF KOI-81

Thus far we have used radial velocities and spectroscopic orbital elements to derive masses and examine the evolutionary states of detached and semi-detached binaries, as well as to obtain fundamental parameters of a detached eclipsing binary through light curve synthesis. We now apply such techniques to the analysis of KOI-81 (*Kepler* Object of Interest), a totally eclipsing binary that represents a possible future state for close binaries that undergo mass transfer.

Avenues of evolution for close binary systems depend on the initial orbital period, the two stellar masses, the presence of additional companions, spin and tidal interactions, and the consequent mass transfer details. Depending largely on the mass ratio and initial orbital period, mass transfer can be stable and mostly conservative, stable and mostly non-conservative, or dynamically unstable (Rappaport et al. 2015). Such evolution can lead to Algol systems where the mass transfer is stable and the envelope of the primary has not yet been exhausted. These include: helium-core-burning objects with very thin hydrogen-rich envelopes, known as hot subdwarfs, likely formed by common envelope ejection and/or stable, non-conservative RLOF (Han et al. 2002, 2003); double-degenerate binaries (Brown et al. 2013; Hermes et al. 2014); or the newly discovered hot, bloated, low-mass white dwarfs where the envelope of the primary has been lost (e.g., van Kerkwijk et al. 2010; Rappaport et al. 2015; Faigler et al. 2015). KOI-81 was identified as an eclipsing binary with a small hot companion by the *Kepler* mission due to its unusual light curve, and found to be one of

the first examples of such hot, bloated, low-mass white dwarfs orbiting main-sequence stars. This work represents a collaboration by many people, including significant contributions by Douglas Gies and Zhao Guo, which was previously published as Matson et al. (2015).

5.1 Introduction

Observations of a stellar system with a smaller companion that orbits along our line of sight will be seen to move in front (transit) and behind (occultation) the host star. Rowe et al. (2010) reported *Kepler* observations of two transiting systems dubbed KOI-74 ($P = 5.2$ d) and KOI-81 ($P = 23.9$ d) that display light curves with minima that were deeper during occultation than during transit, implying that the planetary size companions are hotter than their A or B-type host stars. Rowe et al. proposed that these companions were actually very low mass white dwarf (WD) stars, the remnants of more massive progenitors in an interacting binary. The light curves of both systems were further analyzed by van Kerkwijk et al. (2010), who found that both appear more luminous during orbital phases where the bright star is approaching due to relativistic Doppler boosting ("beaming binaries"; Zucker et al. 2007). van Kerkwijk et al. used the radial velocity semi-amplitude implied by Doppler boosting to estimate that the white dwarf stars had masses of $\approx 0.2 - 0.3 M_{\odot}$.

Kepler observations eventually led to the discovery of other similar eclipsing binary systems. Carter et al. (2011a) found that KIC 10657664 consists of a hot WD orbiting an A-type star ($P = 3.3$ d), and Breton et al. (2012) discovered a WD and F-star binary system, KOI-1224 ($P = 2.7$ d). Two more systems orbiting A-type stars were recently dis-

covered by Rappaport et al. (2015), KIC 9164561 ($P = 1.3$ d) and KIC 10727668 ($P = 2.3$ d). Maxted et al. (2011, 2014) also reported on the detection of 18 similar short-period systems ($P = 0.7 - 2.2$ d) in photometric time series from the ground-based *Wide Angle Search for Planets* (WASP; Pollacco et al. 2006) survey program. Photometric detection of longer period systems is less probable because the orbital inclination must be extremely close to 90° for transits to occur. However, longer period systems can be found through extensive, time series, radial velocity measurements from spectroscopy. For example, Gies et al. (2008) used radial velocity measurements to show that the nearby star Regulus is a spectroscopic binary ($P = 40.1$ d) consisting of a B-star with a probable WD companion. These hot companions of main sequence stars are probably related to the subdwarf companions of rapidly rotating Be stars that are detected through ultraviolet spectroscopy (Peters et al. 2013).

Close binaries are common among intermediate mass stars, and many of these will experience large scale mass transfer (Rappaport et al. 2009; van Kerkwijk et al. 2010; Di Stefano 2011; Clausen et al. 2012). As the initially more massive star grows in radius, this donor star will begin Roche lobe overflow (RLOF) and transfer mass and angular momentum to the companion (the mass gainer). The orbit will shrink until the masses are equal, and if contact can be avoided, then additional mass transfer will cause an expansion of the orbit that ceases once the donor has lost its envelope. The resulting system will consist of a stripped-down and hot donor star in orbit around a rapidly rotating and more massive gainer star.

Detecting binaries in this stage of evolution is difficult because the small donor stars are relatively faint and lost in the glare of the brighter companions. Furthermore, the donors

are now low mass objects that create only small reflex orbital motions in the gainer stars, so detection through spectroscopy is challenging. Thus, the *Kepler* discoveries offer us a remarkable opportunity to investigate the properties of stars that are known examples of this post-mass transfer state. However, the hot companions will contribute a larger fraction of the total flux at shorter wavelengths, so a direct search for the flux and spectral features associated with the hot companion is best done in the ultraviolet. For example, it was through UV spectroscopy from the *International Ultraviolet Explorer* satellite (Thaller et al. 1995) and from the *Hubble Space Telescope* (Gies et al. 1998) that the hot subdwarf companion of the Be star ϕ Per was first detected.

Here we report on an UV spectroscopic investigation of KOI-81 (KIC 8823868; TYC 3556-3094-1; 2MASS J19350857+4501065) made possible with the *HST* Cosmic Origins Spectrograph (COS) that has revealed the spectral features of the hot companion for the first time. We describe the COS observations and supporting ground-based spectroscopy in Section 5.2. We present radial velocity measurements and a double-lined orbital solution in Section 5.3 to obtain mass estimates. We then use the derived radial velocity curves to perform a Doppler tomographic reconstruction of the component spectra, and we compare the reconstructed spectra to model spectra to derive effective temperatures and projected rotational velocities (Section 5.4). The *Kepler* light curve outside eclipses shows evidence of pulsational and rotational frequency signals that we discuss in Section 5.5. The transit light curve is analyzed in Section 5.6 using a model for the rotationally distorted B-star. We then summarize and consider some consequences of the results in Section 5.7.

5.2 Spectroscopic Observations

The Cosmic Origins Spectrograph (COS) is a high dispersion instrument designed to record the UV spectra of point sources (Osterman et al. 2011; Green et al. 2012). The *HST*/COS observations of KOI-81 were obtained over five visits between 2011 June and 2011 October. These were scheduled so that two occurred during each of the quadrature phases near the Doppler shift extrema, and the fifth observation was made during the hot star occultation phase in order to isolate the flux of the B-star alone. The UV spectra were made with the G130M grating to record the spectrum over the range from 1150 to 1450 Å with a spectral resolving power of $R = \lambda/\triangle\lambda = 18000$. There are two COS detectors that are separated by a small gap, so the spectra were made at slightly different central wavelengths in order to fill in the missing flux: 1300 Å (four exposures of 447 s), 1309 Å (three exposures of 399 s), and 1318 Å (three exposures of 399 s). This sequence required an allocation of two orbits for each visit. The observations were processed with the standard COS pipeline to create wavelength and flux calibrated spectra as `x1d.fits` files for each central wavelength arrangement (Massa et al. 2013). These ten sub-exposures were subsequently merged onto a single barycentric wavelength grid using the IDL procedure `coadd_x1d.pro`[1] (Danforth et al. 2010). We created a list of the sharp interstellar lines in the spectrum, and we cross-correlated each of these spectral regions with those in the average spectrum in order to make small corrections to the wavelength calibration. Then the interstellar lines were removed in each spectrum by linear interpolation across their profiles. Finally, all five spectra were transformed to a uniform

[1] `http://casa.colorado.edu/~danforth/science/cos/coadd_x1d.pro`

grid with a $\log \lambda$ pixel spacing equivalent to a Doppler shift step size of 2.60 km s^{-1} over the range from 1150 to 1440 Å. The co-added spectra have a signal-to-noise ratio of S/N = 110 in the central, best exposed parts.

We also obtained three sets of complementary ground-based spectra of KOI-81. The first set consists of 19 high dispersion spectra made with Tillinghast Reflector Echelle Spectrograph (TRES[2]) mounted on the 1.5 m Tillinghast telescope at the Fred Lawrence Whipple Observatory at Mount Hopkins, Arizona. These spectra cover the optical range from 3850 to 9100 Å with a resolving power of $R = \lambda/\triangle\lambda = 48000$. The spectra were processed and rectified to intensity versus wavelength using standard procedures (Buchhave et al. 2010), and they are available at the *Kepler* Community Follow-up Observing Program (CFOP) website[3]. A second set of six moderate resolution spectra were made in 2010 and 2012 with the Kitt Peak National Observatory (KPNO) 4 m Mayall telescope and the Ritchey-Chretien (RC) Focus Spectrograph. These were made with the BL 380 grating (1200 grooves mm^{-1}) to record the spectrum between 3950 to 4600 Å with a resolving power of $R = 6300$. Finally a third set of five, lower resolution, and flux calibrated spectra were obtained in 2010 with the Mayall telescope and RC spectrograph using the KPC-22B grating (632 grooves mm^{-1}) to cover the region from 3577 to 5058 Å with a resolving power of $R = 2500$. This third set is also available at the CFOP website.

[2] `http://tdc-www.harvard.edu/instruments/tres/`
[3] `https://cfop.ipac.caltech.edu/home/`

5.3 Radial Velocities and Orbital Elements

Our first goal was to measure the orbital motion of the primary star using the COS UV spectra. Direct inspection of the spectra showed that the main features were very broadened and blended due to large rotational broadening (Section 5.4). Consequently, we decided to measure the individual spectrum velocities by cross-correlating them with a spectral template. We formed cross-correlation functions (CCFs) using the hot star occultation phase spectrum (made on HJD 2455775.9626) as the CCF template. The calculation was made using only the regions from 1270 to 1300 Å and from 1314 to 1437 Å (see Fig. 4 below) in order to avoid the low wavelength region where the secondary's flux becomes larger and to remove the Si II $\lambda\lambda 1260, 1264, 1304, 1309$ features that may be affected by incomplete removal of the interstellar components. The resulting CCFs are extremely broad, therefore we found the center of each CCF by measuring the wing bisector position by convolving the CCF wings with oppositely signed Gaussian functions (Shafter et al. 1986). We similarly measured the center of the CCF of the hot star occultation phase spectrum with a model spectrum for the B-star (Section 5.4) from the UVBLUE library (Rodríguez-Merino et al. 2005). This offset was then added to the relative velocities to transform them to an absolute scale. The resulting radial velocities are collected in Table 5.1 that lists a leading P or S for primary B-star or secondary hot star (see below), the heliocentric Julian date of mid-observation, the orbital phase based upon the *Kepler* solution for the time of mid-transit (B-star superior conjunction), the radial velocity, the difference between the radial velocity and the systemic velocity for the specific observation set (see below), the uncertainty σ, the

Table 5.1. Radial Velocity Measurements

Primary / Secondary	Date (HJD–2,400,000)	Orbital Phase	V_r (km s^{-1})	$V_r - \gamma_i$ (km s^{-1})	σ (km s^{-1})	$(O-C)$ (km s^{-1})	Observation Source
P	55136.6338	0.7248	0.77	4.31	1.57	−2.34	TRES
P	55139.6337	0.8504	2.03	5.57	0.85	0.13	TRES
P	55143.5776	0.0156	−5.33	−1.79	0.84	−1.13	TRES
P	55344.8716	0.4464	−3.46	0.08	3.70	2.30	TRES
P	55347.8033	0.5692	−6.76	−3.22	1.43	−6.05	TRES
P	55350.7684	0.6934	3.63	7.17	1.62	0.86	TRES
P	55366.7730	0.3637	−8.98	−7.52	1.60	−2.43	KPNO
P	55366.8595	0.3673	−11.00	−7.46	3.13	−2.47	TRES
P	55367.8714	0.4097	−3.93	−2.47	1.59	1.15	KPNO
P	55369.7871	0.4899	−3.17	0.38	3.69	0.80	TRES
P	55374.7716	0.6987	2.49	6.03	3.23	−0.36	TRES
P	55375.8748	0.7449	6.08	9.62	3.44	2.88	TRES
P	55376.7460	0.7814	10.38	13.92	2.65	7.31	TRES
P	55377.8023	0.8256	3.48	7.02	6.23	1.03	TRES
P	55380.8825	0.9546	−0.89	2.66	2.53	0.76	TRES
P	55401.7202	0.8274	5.38	8.92	1.86	2.97	TRES
P	55458.7261	0.2150	−7.64	−4.10	3.15	2.47	TRES
P	55459.6061	0.2518	−0.91	2.64	2.08	9.37	TRES
P	55469.6640	0.6731	4.14	7.68	3.54	1.72	TRES
P	55483.5960	0.2566	−16.32	−12.78	4.97	−6.05	TRES
P	55495.5829	0.7586	13.85	17.39	4.43	10.67	TRES
P	55734.3079	0.7571	−0.33	8.00	1.09	1.27	HST/COS
P	55734.4731	0.7640	−1.81	6.52	1.09	−0.19	HST/COS
P	55775.9626	0.5017	−9.31	−0.98	1.09	−1.05	HST/COS
P	55841.5269	0.2478	−14.29	−5.96	1.09	0.78	HST/COS
P	55841.6811	0.2542	−15.88	−7.55	1.09	−0.81	HST/COS
P	56077.7512	0.1415	−10.35	−8.88	1.84	−3.65	KPNO
P	56081.7577	0.3093	−2.55	−1.08	1.87	5.19	KPNO
P	56082.7568	0.3512	−3.22	−1.76	2.45	3.66	KPNO
P	56486.7101	0.2699	−17.15	−15.68	4.03	−9.00	KPNO
S	55734.3079	0.7571	−102.81	···	2.08	−1.54	HST/COS
S	55734.4731	0.7640	−99.37	···	2.12	1.61	HST/COS
S	55841.5269	0.2478	101.12	···	2.42	0.15	HST/COS
S	55841.6811	0.2542	100.74	···	2.81	−0.21	HST/COS

observed minus calculated $(O-C)$ velocity residual from the fit (Section 5.4), and the source (HST/COS in this case). Both pairs of quadrature observations were separated in time by only a few hours and are expected to have almost the same orbital velocity, so we used the absolute differences of the measured velocities of these pairs to estimate $\sqrt{2}\sigma$.

We realized at the outset that finding and measuring the spectral lines of the companion would be challenging because of its relative faintness. However, detection is favored at

the shorter wavelength part of the UV spectrum because the hotter companion contributes relatively more flux there. An inspection of the spectra in the region with $\lambda < 1200$ Å did indeed hint at the presence of a velocity variable, narrow-lined component. We needed to isolate the flux contribution from the bright B-star in this region in order to remove its flux from each spectrum and reveal the secondary's spectral lines in the flux difference. This was accomplished using the hot star occultation phase spectrum to represent the flux of the B-star alone. This spectrum was smoothed by convolution with a Gaussian function of FHWM = 133 km s^{-1} in order to increase the S/N ratio without unduly altering the spectral shape. The smoothed version was then shifted in velocity according to the predicted orbital motion of the primary star and a difference spectrum was formed for each of the four quadrature phase observations. Renormalized and averaged versions of these quadrature phase spectra are illustrated in Figure 5.1, and these show a host of weak and narrow lines that are Doppler shifted as expected for the orbital motion of the hot secondary. The flux scaling for the hot companion is not accurate because of the rudimentary means of the B-star's flux removal, but it is sufficient to reveal the lines of the hot component so that its radial velocity can be measured. We did so by calculating the CCF of each quadrature spectrum using a hot model spectrum (Section 5.4) for the template, and the center of the narrow signal in the resulting CCF was estimated by fitting a parabola to its peak (with uncertainties determined using the method of Zucker 2003). The derived radial velocities of the secondary are listed at bottom of Table 5.1 in rows with a leading column marked S. No measurement is given for the occultation phase spectrum because the flux of the hot component is totally blocked

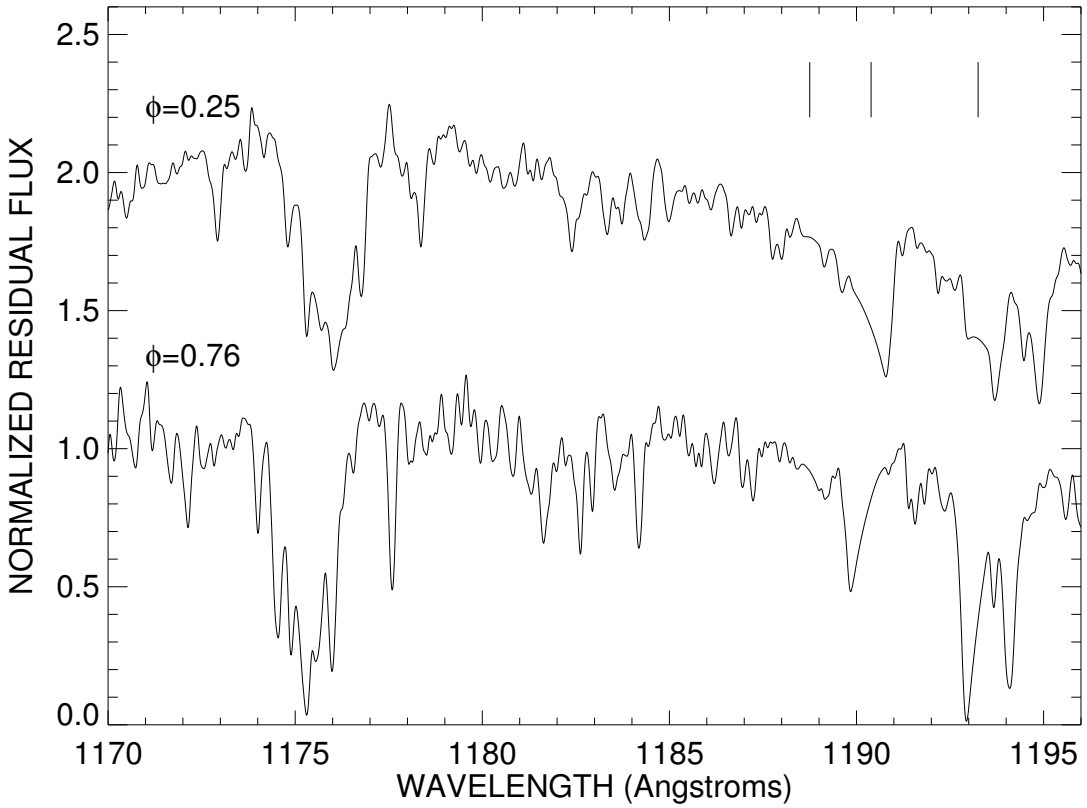

Figure 5.1: Difference spectra of KOI-81 formed by subtracting the occultation phase spectrum of the primary alone. The sharp absorption lines from the subdwarf star appear near maximum redshift (blueshift) at orbital phase $\phi = 0.25$ ($\phi = 0.76$). The vertical line segments indicate the positions where interstellar lines were removed from the spectrum.

then (Rowe et al. 2010).

We also measured radial velocities for the primary B-star using the higher resolution, ground-based spectra. The 19 TRES spectra have a S/N that is too low for measurement of the weak and broadened He and metallic lines, but they are sufficient to measure the Doppler shifts in the strong and broad, H Balmer lines. We formed CCFs of each of Hα, Hβ, Hγ, Hδ, and Hϵ with model template spectra from the BLUERED[4] grid (Bertone et al.

[4]`http://www.inaoep.mx/~modelos/bluered/go.html`

2008). The radial velocity was estimated by fitting a parabola to the peak of the CCF for each line. The quality of the measurement varies depending on the position of the feature relative to the echelle blaze function (best for Hα and Hγ, which fall close to the blaze maximum), so we formed weights for each of the Balmer lines proportional to the inverse square of the standard deviation of the velocity measurements. We then determined the weighted mean and standard deviation of the mean from the set of five line measurements for each observation, and these are listed in Table 5.1 (noted by TRES in the final column).

We followed a similar procedure to measure radial velocities for the six KPNO moderate resolution spectra. We calculated CCFs using a model B-star template (from the UVBLUE grid) and including all the lines in the region from 4050 to 4520 Å (dominated by Hγ and Hδ), and we fit a parabola to the CCF peak to estimate radial velocities. These are identified in Table 5.1 by KPNO in the final column.

We fit orbital elements for each of the primary and secondary velocity sets using the program described by Morbey & Brosterhus (1974). We fixed the orbital period and epoch of mid-transit to those derived by the *Kepler* project (dated 2014 November 24) that are posted at the CFOP website. Because the transit and occultation light curves have the same duration and are separated by half of the orbital period, we assumed that the orbit is circular. We set the fitting weights to the inverse square of the uncertainties. Because the COS, TRES, and KPNO measurements are derived from differing spectral ranges and instruments, we might expect that there will be systematic differences in the velocities for each set. The upper panel of Figure 5.2 shows the measured radial velocities from Table 5.1,

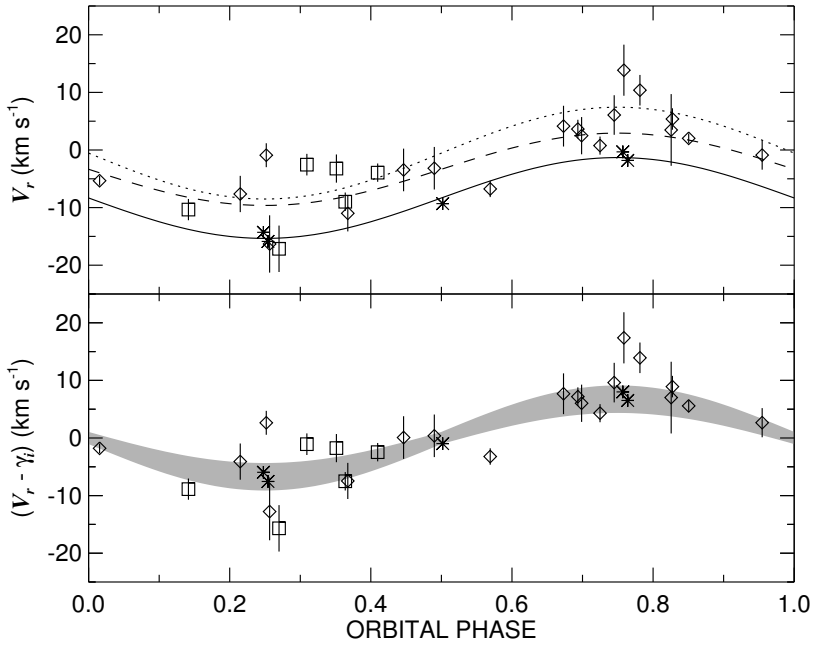

Figure 5.2: Top panel: The radial velocity data from Table 5.1 for the primary star plotted as a function of orbital phase. Phase 0.0 corresponds to the time of central transit of the hot subdwarf across the face of the brighter B-type star. The asterisk, diamond, and square symbols represent measurements from COS, TRES, and KPNO, respectively, and the solid, dashed, and dotted lines show preliminary circular fits for the same three sets (with $K_1 = 7.0$, 6.3, and 8.0 km s^{-1} and $\gamma_i = -8.3$, -3.4, and -0.5 km s^{-1}, respectively). Lower panel: The radial velocity differences (formed by subtracting the systemic velocities for each set reported in Table 5.2) as a function of phase. The shaded region indicates the $\pm 2\sigma$ range in the velocity curve for the adopted fit of the combined measurements.

using different symbols for each set of spectra, as well as preliminary fits of each set, and there do indeed appear to be constant offsets between the sets. We found independent estimates for the systemic velocity γ_i of each set by iterating between global (all data) and individual sets of velocities for the orbital fits. This was done by fixing the semi-amplitude K_1 from the global fit to find estimates of γ_i for solutions to each set. Then a new global fit was made using velocity differences (subtracting the γ_i value associated with each set) to

Table 5.2. Orbital Elements for KOI-81

Element	Value
P (days)	23.8760923[a]
T_t (HJD–2,400,000)	54976.07186[a]
K_1 (km s^{-1})	6.74 ± 0.67
K_2 (km s^{-1})	101.18 ± 0.73
γ_1[TRES] (km s^{-1})	-3.54 ± 0.62
γ_1[KPNO] (km s^{-1})	-1.47 ± 0.68
γ_1[COS] (km s^{-1}) ..	-8.33 ± 0.17
γ_2[COS] (km s^{-1}) ..	-0.19 ± 0.72
M_2/M_1	0.0666 ± 0.0066
$a \sin i$ ($R_\odot$)	50.91 ± 0.47
rms$_1$ (km s^{-1})	2.9
rms$_2$ (km s^{-1})	1.6

[a]Fixed.

find a revised K_1. This procedure converged after a few iterations to the final adopted fit presented in Table 5.2. The γ_i-corrected velocities (listed under column $V_r - \gamma_i$ in Table 5.1) and 2σ range of the fitted velocity of the primary are shown in the lower panel of Figure 5.2, and the combined velocity curves of the primary and secondary are illustrated in Figure 5.3. We also made a fit of the γ_i-corrected velocities of the primary using a Markov Chain Monte Carlo algorithm that led to almost the same result, $K_1 = 6.75^{+0.43}_{-0.44}$ km s^{-1}. However, we conservatively adopt the somewhat larger uncertainty estimates from the non-linear least squares program in what follows. van Kerkwijk et al. (2010) estimated $K_1 \approx 7$ km s^{-1} from the Doppler boosting in the light curve of KOI-81, and their result is verified through our direct Doppler shift measurement of $K_1 = 6.7 \pm 0.7$ km s^{-1}.

The orbital inclination is very close to $i = 90°$. We derive a value from the transit

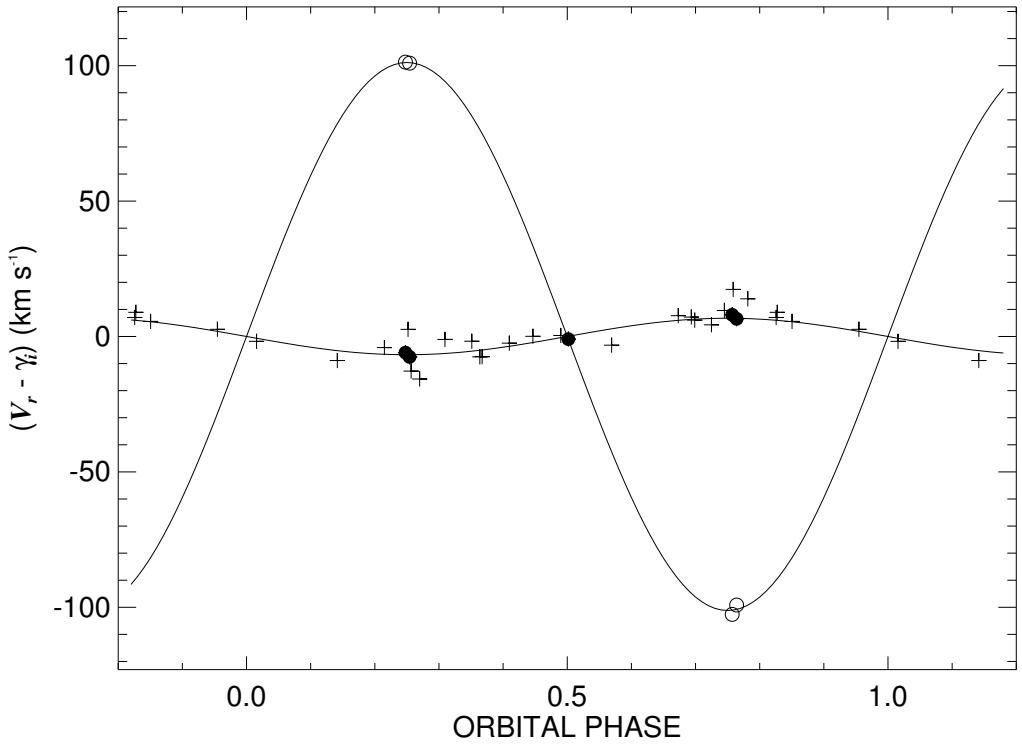

Figure 5.3: Radial velocity curves for KOI-81 and its companion. The solid circles and open circles represent the radial velocities derived from COS spectra for the B-star and hot subdwarf, respectively. Plus signs represent the measurements of the B-star velocity from ground-based spectroscopy (see Fig. 5.2).

light curve (Section 5.6) of $i = 88\overset{\circ}{.}97 \pm 0\overset{\circ}{.}04$, which is intermediate between the estimates from Rowe et al. (2010) of $i = 88\overset{\circ}{.}2 \pm 0\overset{\circ}{.}3$ and from the *Kepler* project posted at CFOP of $i = 89\overset{\circ}{.}95$. Thus, we can use our estimate to derive the physical masses from the $M_1 \sin^3 i$, $M_2 \sin^3 i$ products, and these are given in Table 5.3. Furthermore, the average density ρ of the B-star can be directly estimated from the transit light curve (provided the star is spherical; see Section 5.6), and the *Kepler* project finds $\rho = 0.280 \pm 0.005$ g cm^{-3} for KOI-81 (reported at the CFOP website). We used this value together with the mass estimate M_1 to

Table 5.3. Stellar Parameters for KOI-81

Parameter	Primary	Secondary
$M/M_\odot$	2.916 ± 0.057	0.194 ± 0.020
$R/R_\odot$	2.447 ± 0.022[a]	0.0911 ± 0.0025[a]
$\log g$ (cgs)	4.13[b]	5.81[b]
$T_{\rm eff}$ (kK)	11.7 ± 1.5	$> 19.4 \pm 2.5$
$V \sin i$ (km s^{-1})	296 ± 5	< 10

[a]Assuming a spherical shape for the primary.

[b]Calculated from $M/M_\odot$ and $R/R_\odot$.

arrive at the radius R_1 reported in Table 5.3. Finally, the CFOP website gives the ratio of the radii derived from the transit light curve, $R_2/R_1 = 0.03725 \pm 0.00026$, and we used this ratio to find R_2. Table 5.3 also presents the gravitational acceleration $\log g$ derived from the mass and radius information. We must examine the spectrum of the system to derive the remaining stellar parameters.

5.4 Tomographic Reconstruction of the UV Spectra

We used the Doppler tomography algorithm of Bagnuolo et al. (1994) to extract individual UV spectra of the primary and secondary stars. We initially assumed featureless continua as the starting approximation for the spectra of both stars, but after comparison with model spectra, we ran the algorithm again using the models as starting values which helped to limit the continuum wander in the resulting spectral reconstructions. In Figures 5.4 and 5.5 we present the reconstructed UV spectra derived from the four COS spectra obtained at the quadrature phases. Figure 5.4 also shows the excellent agreement between the reconstructed

spectrum of the primary and the hot star occultation phase spectrum that represents the flux of the primary alone. Figures 5.4 and 5.5 indicate some of the principal lines as well as the locations of the interstellar lines, where their removal by interpolation may have interfered with the accurate reconstruction of the spectra. All spectra in Figures 5.4 and 5.5 are smoothed by convolution with a boxcar function of width 133 km s^{-1} in order to reduce the noise and facilitate intercomparison of the line features.

We compared the reconstructed spectra with model spectra from the UVBLUE grid of high resolution spectra, using the solar metallicity models that incorporate a microturbulent velocity of 2 km s^{-1}. We then made simple bilinear interpolations of flux in the $(T_{\rm eff}, \log g)$ plane to derive the model spectra. We adopted $\log g_1 = 4.13$ for the primary (Table 5.3), but set $\log g_2 = 5.0$ for the secondary as this value is the largest available in the UVBLUE grid. The model spectra were rebinned onto the observed wavelength grid and convolved with the instrumental broadening function (from the COS line spread function[5] for a central wavelength of 1300 Å) and with a rotational broadening function (using linear limb darkening coefficients from Wade & Rucinski 1985).

To estimate the projected rotational velocity $V \sin i$ of each star we formed a χ^2 goodness-of-fit statistic between the observed and model spectra over a test grid of $V \sin i$ values, then found the $V \sin i$ corresponding to the minimum χ^2. This was repeated for a series of wavelength regions that contained well defined absorption lines or line blends, and the mean and standard deviation of the derived $V \sin i$ for the primary is presented in Table 5.3. The primary B-star is indeed a very rapidly rotating star, a property noted first by van Kerkwijk

[5] `http://www.stsci.edu/hst/cos/performance/spectral_resolution/fuv_130M_lsf_empir.html`

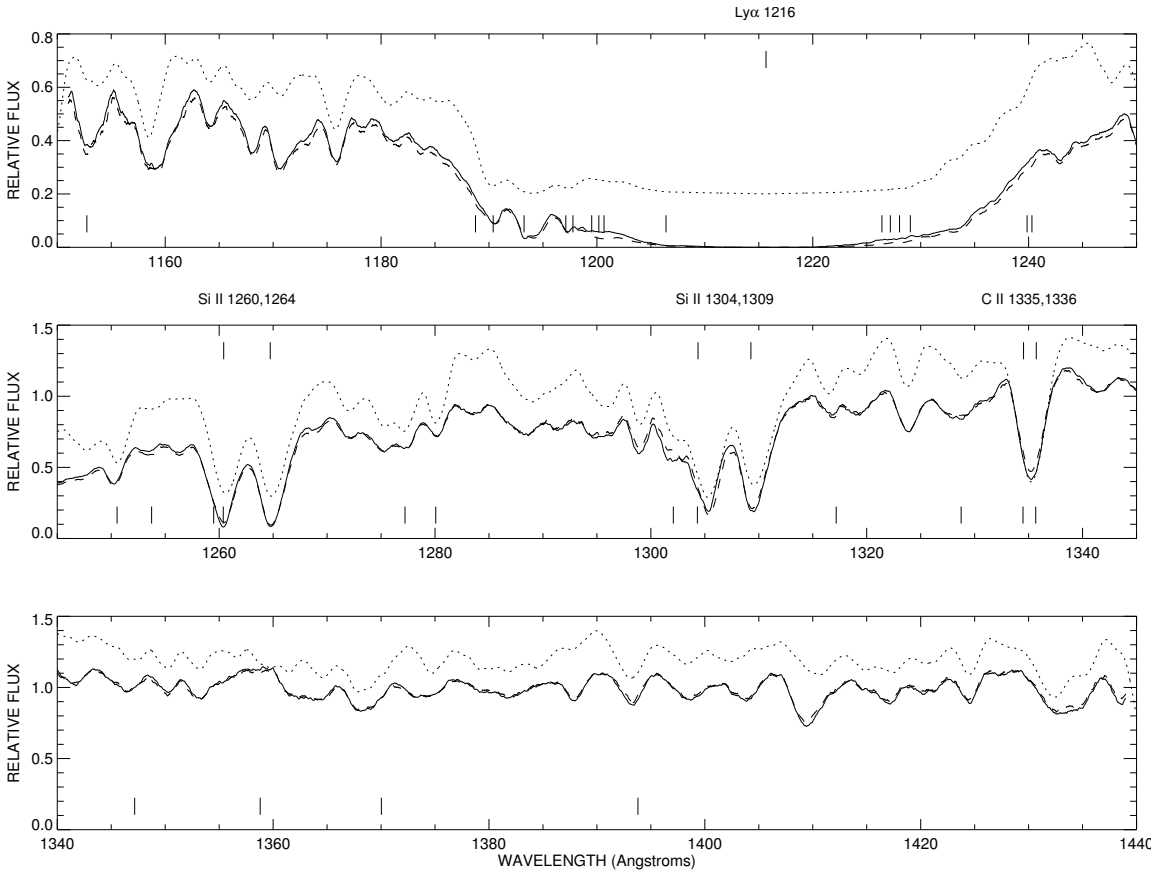

Figure 5.4: The reconstructed UV spectrum of the B-star (solid line) depicted in three successive wavelength panels. The dashed line shows the COS spectrum obtained when the subdwarf was occulted, and it is identical within uncertainties with the reconstructed spectrum. A model spectrum constructed from the UVBLUE grid appears as a dotted line above the reconstructed spectrum (offset by +0.2 in units of normalized flux). Several strong absorption lines are identified and marked by the upper vertical line segments, while the lower line segments indicate the locations where interstellar lines were removed from the spectrum.

et al. (2010). The lines of the hot secondary companion, on the other hand, appear very sharp and any rotational broadening is unresolved in the COS spectra, so we present only an upper limit in Table 5.3.

Next we adjusted the model spectra for the variable interstellar extinction across the

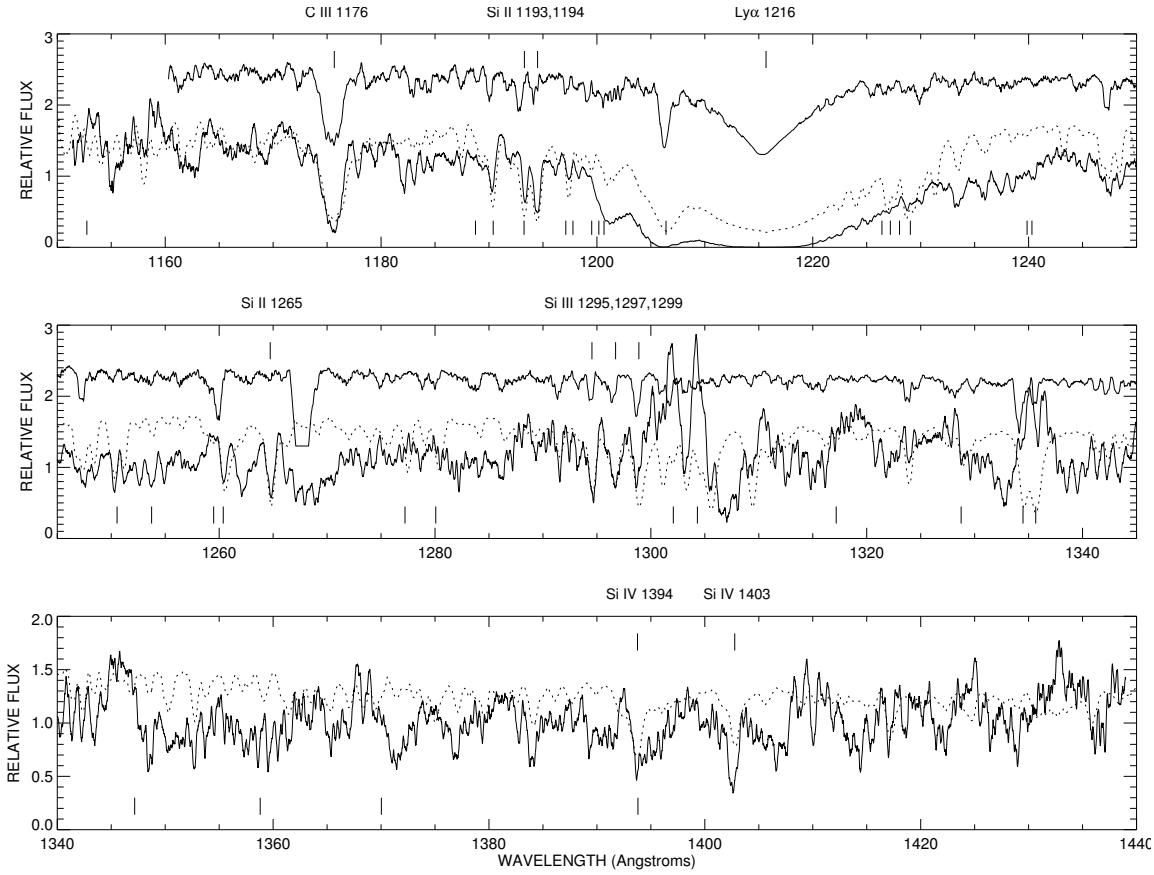

Figure 5.5: The reconstructed UV spectrum of the subdwarf star depicted in three successive wavelength panels (in the same format as Fig. 5.4, excluding the occultation spectrum). The top two panels also show for comparison the spectrum of the hot subdwarf CPD−64°481 (solid line offset by +1.3 in normalized flux).

COS wavelength band. We derived the interstellar reddening by comparing the available observed fluxes with a model flux distribution for the binary transformed using the extinction law presented by Fitzpatrick (1999). The observed fluxes are shown in a spectral energy distribution (SED) plot in Figure 5.6, including rebinned COS measurements, a GALEX[6] NUV measurement[7], rebinned KPNO low dispersion spectrophotometry, and 2MASS and

[6] `http://galex.stsci.edu/GR6/`

[7] KOI-81 appears as two sources in GALEX, but we simply summed the fluxes of what appears to be the trailed image of a single object.

WISE photometric fluxes. The model fluxes were a sum of Kurucz models for the primary and secondary that were attenuated according to the extinction law for a ratio of total-to-selective extinction of $R = 3.1$. The fit shown in Figure 5.6 was made with a reddening of $E(B-V) = 0.169 \pm 0.008$ mag and a limb darkened angular diameter of the primary of $\theta = 0.0182 \pm 0.0005$ milliarcsec. The former agrees with prior estimates ($E(B-V) = 0.175$ and 0.193 mag in the *Kepler* Input Catalog and the GALEX Catalog, respectively), and the latter indicates a distance of 1.25 kpc (using $R_1/R_\odot$ from Table 5.3). The extinction in the COS band was calculated for the derived value of $E(B-V)$, and each model was multiplied by this extinction curve to account for the greater interstellar attenuation at lower wavelength.

With the gravity, projected rotational velocity, and interstellar extinction set, we calculated model spectra over a grid of effective temperatures and determined a χ^2 goodness-of-fit as a function of $T_{\rm eff}$. The best fit temperatures and their estimated uncertainties from this comparison of the reconstructed and model spectra are listed in Table 5.3. These uncertainties do not account for possible differences from the assumed microturbulent velocity and abundance. Nevertheless, these models offer a framework to interpret the appearance of the UV spectra.

Figure 5.4 shows the derived model spectrum offset above the reconstructed spectrum of the primary star. The overall agreement is very good in both the appearance of the lines and line blends. The C II $\lambda\lambda 1335, 1336$ feature is weaker than predicted, but this may result from our means of removal of interstellar line components in this feature. The flux in the optical

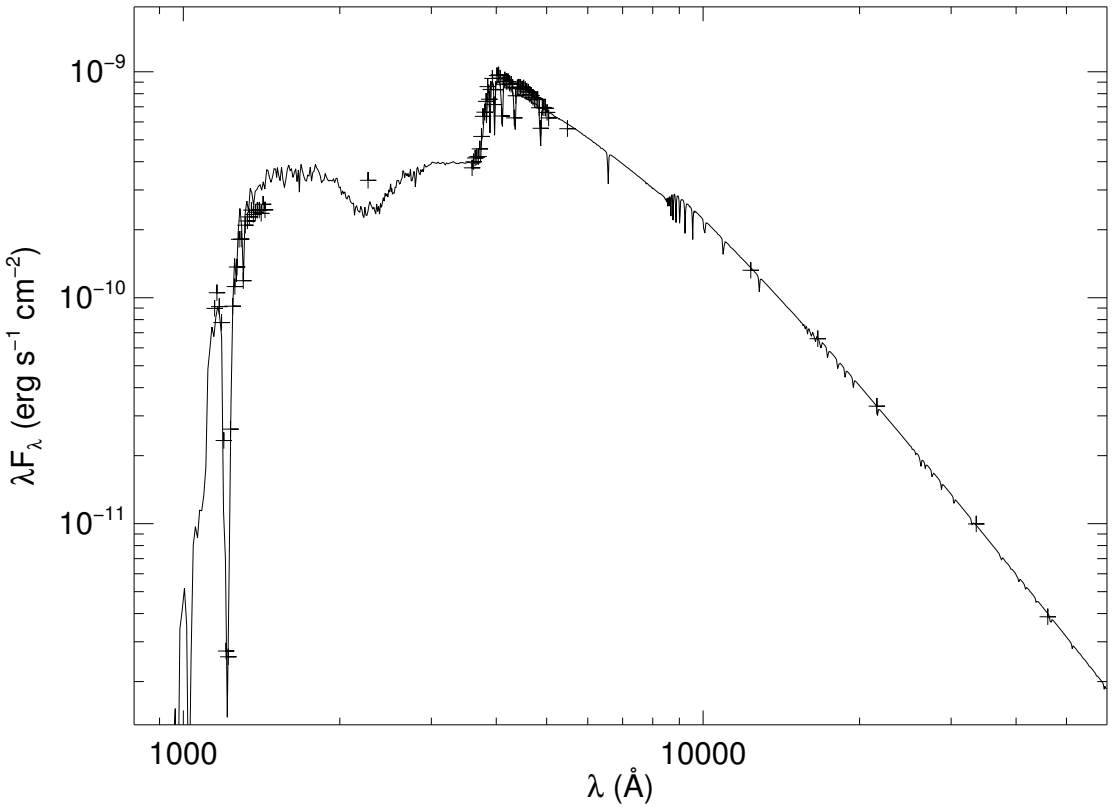

Figure 5.6: The spectral energy distribution of the KOI-81 binary including (from short to long wavelength) fluxes from COS (UV), GALEX (NUV), the KPNO 4 m (optical, low resolution spectroscopy), 2MASS (near-IR), and WISE (mid-IR). The solid line depicts a Kurucz atmosphere flux model for the combined system that is based upon a fit of the reddening and the B-star angular diameter.

wavelength range is totally dominated by the light from the B-star primary (Section 5.6), so we did not attempt Doppler tomography reconstructions of the optical spectrum. However, we show in Figure 5.7 two optical lines of special interest. The most temperature sensitive feature in the optical spectrum at $T_{\rm eff} \approx 10$ kK is the Ca II λ3933 K line that grows rapidly in strength with decreasing temperature (Gray & Corbally 2009). The average TRES spectrum of this feature is shown in Figure 5.7 (*left*) together with model spectra for $T_{\rm eff} = 11.7$ kK and

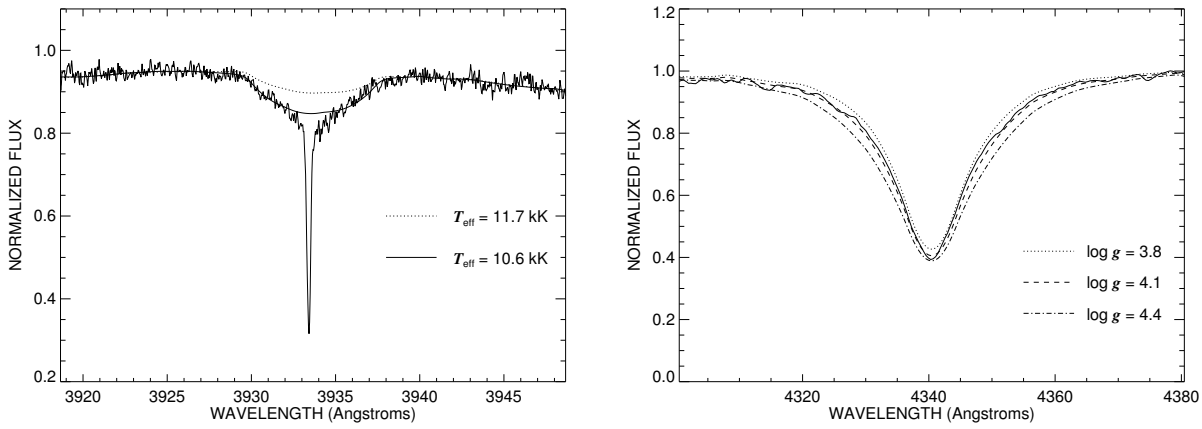

Figure 5.7: *Left:* The Ca II λ3933 feature (structured solid line) from the average of the TRES high resolution spectra. A sharp, interstellar component (with a radial velocity of $V_r = -19.2 \pm 0.9$ km s^{-1}) is situated near the center of the broad photospheric component. The solid and dotted lines show UVBLUE model profiles for $T_{\rm eff}$ = 10.6 and 11.7 kK, respectively. *Right:* The Hγ line profile (solid line) from an average of the KPNO 4 m moderate resolution spectra. The other lines represent UVBLUE model spectra for three choices of surface gravity.

10.6 kK, and a comparison with the observed K-line suggests that the effective temperature may be somewhat lower than that derived from the ultraviolet spectrum (but still within the uncertainties). On the other hand, the difference may result from gravity darkening in the rapidly rotating B-star that creates a cooler equatorial region (Section 5.6) that would promote the appearance of lines favored in cooler atmospheres. Figure 5.7 also illustrates the average observed and model profiles of the gravity sensitive Hγ line (*right*), and the observed profile has a shape that is approximately consistent with predictions for the adopted gravity of the primary.

The reconstructed secondary spectrum shown in Figure 5.5 is quite noisy because this component is relatively faint (see below), but there is satisfactory agreement between the

reconstructed and model spectra in the vicinity of some features. For example, the reconstructed and model spectra of the secondary appear similar in the lines of C III λ1176, Si II $\lambda\lambda$1193, 1194, Si III $\lambda\lambda$1295, 1297, 1299, and Si IIII $\lambda\lambda$1394, 1403. The latter are only seen in the spectrum of the hotter secondary. However, the agreement is less satisfactory in the regions where interstellar lines were removed (near 1229, 1251, 1303, 1335, and 1347 Å). The model spectra were formed using UVBLUE models with $\log g = 5.0$, the largest value in the grid, which is smaller than the estimated gravity, $\log g = 5.8$. This has two important consequences. First, the model Lyα line is narrower than observed because the linear Stark broadening associated with the lower gravity model is insufficient to match the observed broadening. Second, the effective temperature estimation is based upon the relative strengths of transitions corresponding to different ionization states, and according to the Saha equation, line formation in a denser medium (at higher gravity) will shift the ionization balance to less ionized states. Consequently, a good fit of the spectrum would also be possible with a higher gravity and higher temperature model, so our derived effective temperature should be regarded as a lower limit. In Figure 5.5 we also show an example spectrum of the B-subdwarf CPD$-64°481$ that was made with the Space Telescope Imaging Spectrograph and E140H grating. O'Toole & Heber (2006) used this and other spectra to estimate $T_{\rm eff} = 27.5$ kK and $\log g = 5.6$, a value of gravity that is close to that of the secondary in KOI-81. Comparing these similar gravity stellar spectra, we see that transitions of Si II are almost absent in the spectrum of CPD$-64°481$, whereas they are quite strong in the spectrum of the KOI-81 secondary, so the KOI-81 secondary must be cooler than

CPD$-64°481$. Thus, we can place lower and upper limits on the effective temperature of the secondary of $19 < T_{\rm eff} < 27$ kK.

All the spectra in Figures 5.4 and 5.5 were normalized in flux by dividing by the mean flux over the range between 1340 and 1400 Å. We set the monochromatic flux ratio from this normalization to $F_2(1370)/F_1(1370) = 0.05 \pm 0.02$ based upon a comparison of the line depths in the reconstructed and model spectra of the secondary. This comparison was made using relative line depths in the vicinity of the lines that matched reasonably well, because there is too much wander in the continuum of the reconstructed spectrum of the secondary for a reliable global fit. We caution that the model line depths are sensitive to the adopted values of temperature, gravity, and especially microturbulence, so the flux ratio may need revision if different assumptions are made.

5.5 Non-orbital Frequencies in the Light Curve

Both Rowe et al. (2010) and van Kerkwijk et al. (2010) noted that the light curve of KOI-81 shows evidence of pulsations, and it is interesting to consider the pulsational frequencies and their relation to the rotational frequency of the B-star primary. We calculated the Fourier transform amplitude of the detrended, long cadence *Kepler* observations from quarters 0 to 17 using the package Period04 (Lenz & Breger 2005). The portions of the light curve covering the transit and occultation of the secondary were removed from the time series in order to focus on non-orbital timescales of variation. We adopted an empirical noise level by smoothing the envelope of the residual spectrum after pre-whitening all significant

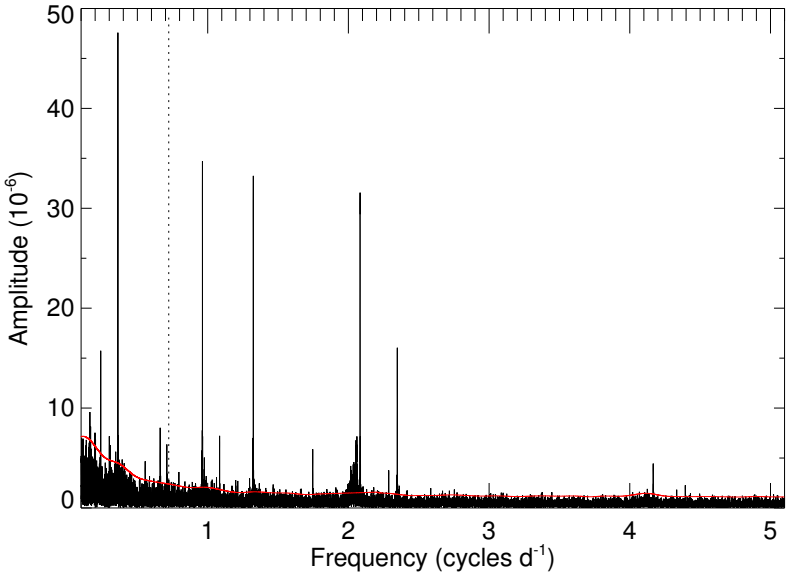

Figure 5.8: The Fourier amplitude spectrum of *Kepler* short cadence photometry after prewhitening the dominant peak at 0.72297 d^{-1} indicated by the dotted line. The empirical noise level is indicated by the red solid line.

frequencies with $S/N > 3$ (except for the broad rotational feature; see below). Uncertainties were calculated following Kallinger et al. (2008). The Fourier spectrum is dominated by a very strong signal with a frequency of $f_1 = 0.722974$ cycles d^{-1} (period of 1.38318 d), so we removed this signal by pre-whitening to uncover the remaining periodic signals that are plotted in Figure 5.8. There are a number of strong signals that appear well above the noise level, and the frequencies, amplitudes, sinusoidal phases (relative to the epoch of central transit), and peak signal-to-noise ratio are listed in Table 5.4. The final column of Table 5.4 lists several numerical relations among these frequencies, and identifies one frequency f_{12} that corresponds to the ellipsoidal (tidal) variation with half the orbital period (discussed by van Kerkwijk et al. 2010).

Table 5.4. Significant Photometric Frequencies

	Frequency (d^{-1})	Amplitude (10^{-6})	Phase (rad/2π)	S/N	Comment
f_1	0.722974 ± 0.000002	257.6 ± 4.1	0.822 ± 0.001	107.4	
f_2	1.32403 ± 0.00001	33.4 ± 2.8	0.34 ± 0.006	20.6	$f_4 + f_6$
f_3	1.08445 ± 0.00002	22.1 ± 3.2	0.98 ± 0.01	20.5	$f_1 + f_6$
f_4	0.96250 ± 0.00001	34.6 ± 3.6	0.22 ± 0.008	16.7	
f_5	2.08287 ± 0.00001	31.4 ± 2.6	0.77 ± 0.006	11.4	f_{rot}
f_6	0.36148 ± 0.00002	47.5 ± 7.7	0.28 ± 0.01	10.6	$0.5 f_1$
f_7	2.34753 ± 0.00002	15.7 ± 2.3	0.36 ± 0.01	8.0	
f_8	0.70933 ± 0.00009	6.3 ± 4.2	0.96 ± 0.04	6.9	
f_9	1.74647 ± 0.00006	5.8 ± 2.3	0.15 ± 0.03	6.8	
f_{10}	2.08357 ± 0.00003	12.3 ± 2.6	0.37 ± 0.05	4.5	f_{rot}
f_{11}	4.16643 ± 0.00008	4.4 ± 2.4	0.08 ± 0.04	4.3	$2f_{rot}$
f_{12}	0.0837 ± 0.0002	10.9 ± 4.0	0.25 ± 0.02	3.2	$2f_{orb}$
f_{13}	2.08216 ± 0.00003	10.4 ± 2.6	0.09 ± 0.04	3.1	f_{rot}

The dominant periodicity (1.38 d) is unrelated to the orbital period, and it probably represents a strong and long-lived pulsational mode. This and the other low frequency pulsation signals may be of two possible kinds. First, the B-star primary of KOI-81 has a temperature and radius that are similar to those of the slowly pulsating B-type (SPB) stars (Pamyatnykh 1999), and these stars display relatively long period g-mode oscillations. Second, the B-star is a rapid rotator, and both Townsend (2005) and Savonije (2013) argue that rapidly rotating, late-type B-stars can experience retrograde mixed modes of low azimuthal order m. The rotational frequency of the B-star is probably ≈ 2 cycles d^{-1} (see below), so the smaller frequency of the dominant signal is consistent with retrograde non-radial pulsation.

There is a broad distribution of peaks just above 2 cycles d^{-1}, and we show an enlarged version of the Fourier amplitude in this vicinity in the top panel of Figure 5.9. A wide distri-

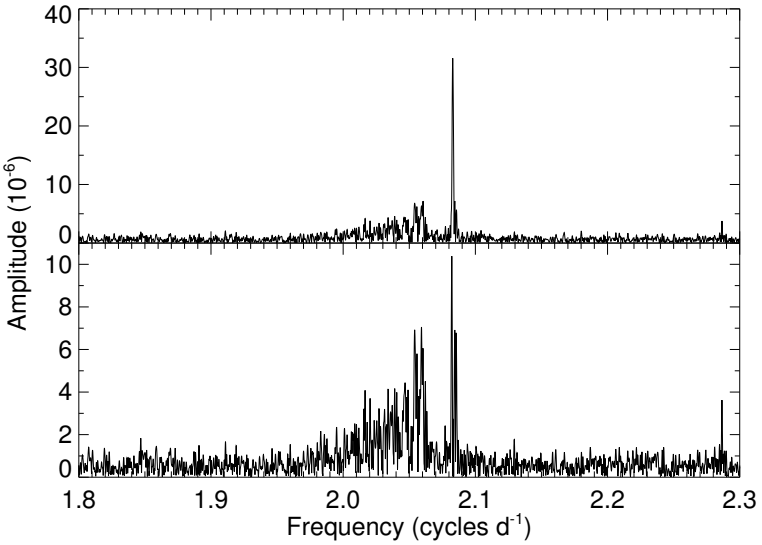

Figure 5.9: Top: The broad differential rotation feature at a frequency of about $1.96 \sim 2.06$ d^{-1} and the adjacent sharp peak $f_5 = 2.08287$ d^{-1}. Bottom: the same diagram but with the sharp f_5 peak prewhitened.

bution appears around 2.04 cycles d^{-1} that is accompanied by a strong peak at $f_5 = 2.08287$ cycles d^{-1}. The lower panel shows the residual peaks after pre-whitening and removal of the strong f_5 signal, revealing the presence of several other significant peaks near f_5. This kind of broad feature with a stronger single peak at slightly higher frequency has been detected by Balona (2013, 2014) in the *Kepler* light curves of some 19% of A-type stars. Balona argues persuasively that this feature probably corresponds to the stellar rotational frequency. In his interpretation, the single strong peak corresponds to the equatorial rotational frequency and the wider peak samples the rotational frequencies at different latitudes in stars with differential rotation. Following this line of argument, we may tentatively identify f_5 as the equatorial rotational frequency of the B-star in KOI-81, and thus, the rotational period is 0.48 d at the

equator. Balona (2014) considers several explanations for the origin of the photometric variation including pulsation, rotational modulation by starspots, and tidal variations induced by a co-orbiting exoplanet. We suspect that in the case of KOI-81, any co-orbiting planet would have a short period and an orbital plane similar to that of the stellar companion so that we might expect to observe a transit signal in the f_5 folded light curve, but instead the folded light curve is approximately sinusoidal in shape. We speculate that the rotational signals in the light curve of KOI-81 and similar stars may result from long-lived vortices (Kitchatinov & Rüdiger 2009) that develop in the outer atmospheres of rotating stars due to differential rotation (similarly to the spots in the atmosphere of Jupiter).

5.6 Transit Light Curve

The B-star we observe was spun up during the mass transfer process to produce a very rapidly rotating star with a rotationally broadened spectrum. It is important to consider how this rapid rotation influences our interpretation of the light curve. We expect that the spun up star will have a rotational axis parallel to the orbital angular momentum vector, so that the star's spin axis also has an inclination of $i \approx 90°$. We argued in Section 5.5 that the photometric signal f_5 is the rotational frequency of the B-star. Then we may estimate the star's equatorial radius from $R_{1\ \mathrm{equator}} = (V \sin i)/(2\pi f_5 \sin i) = (2.81 \pm 0.05) R_\odot$. This is somewhat larger than what we derived from the mass and mean stellar density (Table 5.3), but is not unexpected for a rotationally distorted star in which the equatorial radius will be larger (and the polar radius smaller) than the mean radius.

We can model the predicted appearance of the B-star based upon our estimates of stellar mass, equatorial radius, rotational period, and average effective temperature. We created a model image of the specific intensity at a wavelength of 6430 Å, which is the centroid of the *Kepler* instrument response function, using the same methods applied in a study of the rapidly rotating B-star Regulus (McAlister et al. 2005). The star is assumed to have a shape that follows the Roche potential for rotation about a point mass, and each surface element has a specific intensity defined by limb and gravity darkening. The specific intensity of a surface element is set by interpolation in a set of Kurucz model values defined by the local temperature, gravity, and orientation of the surface normal to the line of sight. We found values of the polar radius and temperature that led to our derived equatorial radius and surface average temperature, a physical average based on the luminosity of a sphere with surface area equivalent to that of the star. An image of the rotationally distorted star appears in Figure 5.10. The resulting model has a ratio of equatorial to critical velocity (where the gravitational and centrifugal accelerations are equal) of 0.74, and the radius varies from $2.30 R_\odot$ at the poles to $2.81 R_\odot$ at the equator (18% flattened). The temperature in this model varies between 13.8 kK and 10.8 kK from pole to equator, and gravity likewise varies from $\log g = 4.18$ to 3.75. The flux weighted, disk integrated value of gravity is $\log g = 3.9$, and this appears to be approximately consistent with the appearance of the Hγ profile (Fig. 5.7).

We used this model image to calculate transit light curves. We assumed that the apparent transit path follows a trajectory parallel to the stellar equator with a relative velocity

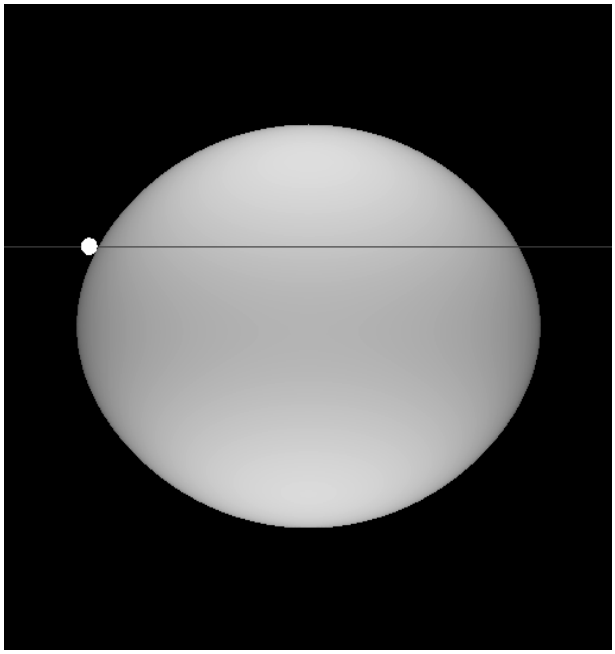

Figure 5.10: A model representation of the monochromatic intensity in the *Kepler* bandpass of the rotationally distorted B-star and the small, hot companion star (shown at first contact). The horizontal gray line shows the derived transit path.

given by $2\pi a/P$. During phases when the disk of the companion is seen projected against the background B-star, we took the flux removed as the product of the companion area and the specific intensity at the projected position of the center of companion (Mandel & Agol 2002; Barnes 2009). For the phases between first and second contact, we assumed that the companion occults a locally linear stellar limb of the B-star with a slope given by the Roche model shown in Figure 5.10, and the specific intensity was estimated at test positions perpendicular to the local limb to make a numerical calculation of the occulted flux. This constrained model has only two free parameters: the ratio of secondary to primary polar radius $R_2/R_{1\ \mathrm{polar}}$ and the ratio $z_0/R_{1\ \mathrm{polar}}$ of the smallest distance z_0 from the transit trajec-

tory to the center of the B-star relative to the primary polar radius. The value of $R_2/R_{1\ \mathrm{polar}}$ sets the amount of light removed and hence the depth of the transit light curve, while the value of $z_0/R_{1\ \mathrm{polar}}$ sets the duration of the transit (longer for transits near the equator with smaller z_0).

We show in Figure 5.11 the occultation and transit light curves of KOI-81 from nine months of *Kepler* short cadence observations. These plots show the photometric fluxes normalized to unity outside of eclipses that we calculated by rebinning and averaging all the available measurements in orbital phase bins equivalent to 3 minutes duration. The *Kepler* photometry was detrended and pre-whitened for the primary oscillation frequency f_1 (Section 5.5) before rebinning. The upper plot of the total occultation of the hot companion by the B-star indicates that the companion contributes a flux fraction of $F_2/F_1 = 0.00501 \pm 0.00006$ in the *Kepler* band-pass, and we renormalized the model for this extra flux in calculating the model transit curves. The model curves were also convolved with a temporal box function to represent the bin size applied to the observations. Our best fit (shown in Fig. 5.10 and Fig. 5.11) was obtained with $R_2/R_{1\ \mathrm{polar}} = 0.0426 \pm 0.0003$ and $z_0/R_{1\ \mathrm{polar}} = 0.396 \pm 0.011$ (equivalent to an orbital inclination of $i = 88\overset{\circ}{.}97 \pm 0\overset{\circ}{.}04$). The individual transits display asymmetries that appear to be related to the pulsational phases at the times of transit, and because the mean transit curve shown in Figure 5.11 represents data from only 12 transits, we do not attribute any significance to the trends in the residuals from the fitted transit light curve. We caution that the quoted uncertainties in the fitting parameters do not account for the range in the possible values for the rotation rate

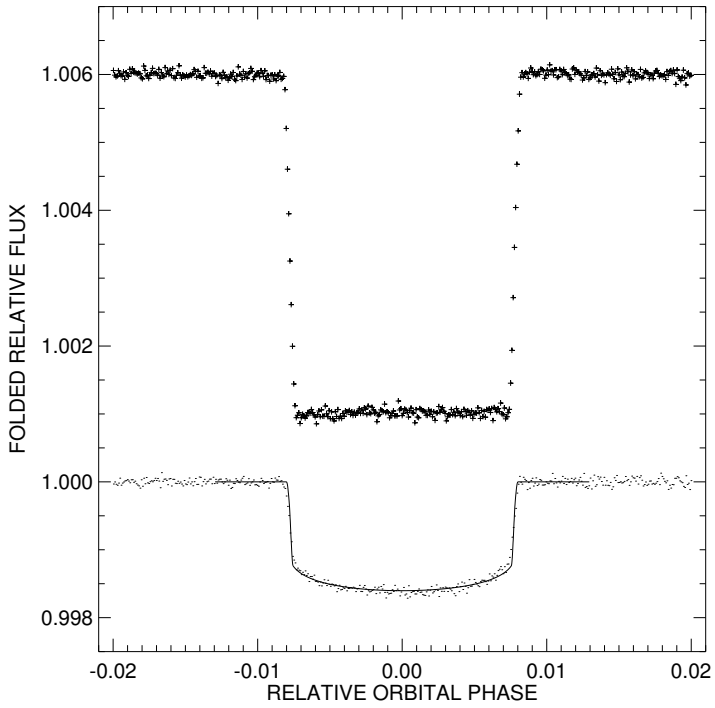

Figure 5.11: The phase-folded light curve of KOI-81 for the occultation of the companion (plus signs, shifted by half an orbit and offset by +0.006 for clarity) and the transit of the companion (dots). The model transit light curve is shown by the solid line.

we adopted. Nevertheless, it is interesting to note that the derived radius of the companion $R_2/R_\odot = 0.0979 \pm 0.0019$ is close to what we list in Table 5.3 based upon the spherical approximation, mean density, and radius ratio from the *Kepler* project, and the primary radius given in Table 5.3 falls comfortably between the polar and equatorial radii of the rotating model.

In Section 5.4 we compared the observed and model spectral line depths of the secondary to estimate that the total flux ratio at 1370 Å is $F_2/F_1 = 0.05 \pm 0.02$, and using the temperatures we derived, we predict that this flux ratio will vary from $F_2/F_1 = 0.14$ at 1150 Å to $F_2/F_1 = 0.0076$ in the *Kepler* optical band. The observed flux ratio is approximately

related to radius ratio by

$$\frac{F_2}{F_1} = \frac{f_2}{f_1}\left(\frac{R_2}{R_1}\right)^2 \tag{5.1}$$

where f_2/f_1 is the ratio of monochromatic flux per unit area. According to the Kurucz flux models for our stellar parameters, $f_2/f_1 = 14.5 \pm 0.5$ at 1370 Å, so the observed flux ratio would then imply a radius ratio of $R_2/R_1 = 0.059 \pm 0.012$. Both the flux and radius ratio estimates from spectroscopy are somewhat larger than the corresponding estimates from the *Kepler* transit analysis, but the differences are not surprising given the large uncertainties associated with the flux ratio from spectroscopy.

We can also use equation 5.1 to infer the temperature ratio from the observed flux ratio in the *Kepler* band. The Kurucz flux models vary as $f \propto T_{\rm eff}^a$ with $a = 1.58$ for $\log g = 5$, $\lambda = 6430$ Å, and $T_{\rm eff}$ in the range 10 to 25 kK. Thus, if we set the radius of the primary as $(R_{1\ \rm equator} + R_{1\ \rm polar})/2 = 1.11 R_{1\ \rm polar}$, then we can use the values of F_2/F_1 and $R_2/R_{1\ \rm polar}$ from above to find a temperature ratio of $T_{2\ \rm eff}/T_{1\ \rm eff} = 2.2$. This is broadly consistent with the temperature estimates from spectroscopy (Section 5.4), $T_{2\ \rm eff}/T_{1\ \rm eff} = 1.7 - 2.3$.

5.7 Discussion

The *HST*/COS observations of KOI-81 have revealed the spectrum of the hot companion, the stripped down remains of the originally more massive star in the binary. Our derived mass, radius, and temperature values for KOI-81 are consistent with previous results. The mass estimate of the hot, compact companion is slightly lower than earlier estimates ($\sim 0.3 M_\odot$; van Kerkwijk et al. 2010), solidifying its place among low mass He WDs and their

immediate progenitors (with masses below $0.3M_{\odot}$ where WDs have helium cores that are too small to sustain He burning; Silvotti et al. 2012). The radius derived for the subdwarf remains essentially unchanged from earlier estimates, and our analysis confirms that it is larger than typical for He WDs (see Fig. 15 of Panei et al. 2007) like the other thermally bloated WDs found by *Kepler* (Rappaport et al. 2015). The effective temperature range for the hot companion determined through spectral reconstruction is higher than the previous estimate of Rowe et al. (2010), placing it in the hot subdwarf (sdB) and WD regime. Of the known main sequence (MS) + sdB/He WD binaries, KOI-81 has the hottest, low mass WD (the others range between 9 – 15 kK), although several of the sdB/He WD stars in double degenerate systems have similar effective temperatures (Brown et al. 2013; Hermes et al. 2014).

The relatively long orbital period of KOI-81 suggests that the system widened as the result of conservative mass transfer following the mass ratio reversal. The binary probably began as a relatively close binary, so that mass transfer was initiated as the donor grew in size after concluding core H burning (designated channel 1 in the evolutionary schemes presented by Willems & Kolb 2004). Population synthesis models by Willems & Kolb (2004) show that the post-RLOF systems may frequently have a remnant mass and orbital period like those we find for KOI-81 (see their Fig. 2). The progenitor binaries of such systems typically have similar and low component masses and initial orbital periods somewhat larger than 1 d (see Fig. 2 in Willems & Kolb 2004). For example, van Kerkwijk et al. (2010) present an evolutionary scenario for KOI-81 that begins with a 1.8 and $1.3M_{\odot}$ pair with an

orbital period of 1.3 d. It is curious that the dominant pulsation period is similar to this. It may simply be a coincidence, but an alternative possibility is that this pulsation period represents the rotational period of the mass gainer in synchronous rotation before the onset of RLOF. Mass transfer from the donor would subsequently spin up the gainer, but it might take a long time for the angular momentum to be effectively redistributed into the core of the gainer star. We speculate that a slower rotating core may be the source of pulsational wave generation in the envelope of the gainer B-star.

The mass donor remnant may have retained enough of its H-envelope to maintain shell H-burning longer, so that it evolves to hotter temperature before cooling begins (Maxted et al. 2014; Rappaport et al. 2015). Based on the evolutionary scenarios presented by Silvotti et al. (2012) and Rappaport et al. (2015), our derived mass of $0.194 \pm 0.020 M_{\odot}$ for the hot companion of KOI-81 is consistent with a low mass, pre-He WD that has not yet reached the cooling branch, or a He core WD that is already on the cooling branch after experiencing episodes of shell H-burning in CNO flashes. However, when plotted in the $(\log T_{\rm eff}, \log g)$ plane with the evolutionary sequences for low mass white dwarfs of Althaus et al. (2013), KOI-81 appears to be in an early cooling phase of He core WD evolution. A specific age estimate is difficult to pin down because the star is located in a mass regime that experiences multiple CNO flashes that cause multiple loops in the $(\log T_{\rm eff}, \log g)$ diagram. Althaus et al. present a grid of masses and cooling ages weighted by the amount of time spent in specific regions of the cooling tracks and the range of masses found in each region. Using the values of $\log T_{\rm eff}$ and $\log g$ derived by van Kerkwijk et al. (2010), they find a mass of

$0.196 \pm 0.007 M_{\odot}$ and cooling age of 372 ± 186 Myr for KOI-81 (see their Table 2). Our higher values of $\log T_{\rm eff} \approx 4.3$ and $\log g = 5.8$ correspond to a mean evolutionary track mass of $0.202 \pm 0.015 M_{\odot}$ and a cooling age 356 ± 187 Myr, so our derived stellar parameters are broadly consistent with the evolutionary model predictions.

The evolutionary path of KOI-81 is one of many that create binary systems with low mass WDs. The MS + sdB binaries discovered by *Kepler* (Rappaport et al. 2015) and *WASP* (Maxted et al. 2014) represent those systems with stripped-down remnants formed during the first RLOF phase. These occur during the faster part of the pre-He WD evolutionary tracks, but it is easier to detect the low mass WDs at this stage because of their relatively large luminosities (Istrate et al. 2014). In fact, most of the known low mass He WDs are those fainter WDs on the long-lived part of the cooling tracks that are members of binaries with even fainter companions. These are often the remnants of a second mass exchange that involves a common envelope stage. They are generally short period systems that are sdB + WD binaries (Heber et al. 2003; Silvotti et al. 2012), but also include sdB + sdB systems (Ahmad et al. 2004; Kupfer et al. 2015), sdB + neutron star companion (Geier et al. 2009; Istrate et al. 2014), and sdB + substellar companion (Geier et al. 2009; Geier 2015).

The detection of the hot companion in KOI-81 provides us with the means to determine the stellar parameters in one example of what must be a large population of undetected binaries with faint, hot companions (Willems & Kolb 2004; Di Stefano 2011). The fact that the B-star component is also a pulsator opens up the possibility to study the stellar interior of a star that has been radically changed through mass transfer. Furthermore, an analysis

of the transit shapes at different phases in the pulsational and rotational cycles may help elucidate the nature of the pulsation modes and source of the rotational modulation (Bíró & Nuspl 2011). The serendipitous discovery of KOI-81 by *Kepler* has given us the opportunity to explore the properties of stars that have survived transformative mass exchange.

CHAPTER 6
SUMMARY AND FUTURE WORK

6.1 Summary

Throughout this dissertation we have focused on obtaining well-defined stellar parameters in order to gain more accurate knowledge of stellar and binary evolution. Both spectroscopic and photometric observations of binaries are vital for determining fundamental parameters such as mass and radius. The potent combination of *Kepler* light curves and complementary spectroscopy of a (relatively) large sample of exemplary eclipsing binaries has enabled detailed analyses of the physical attributes of systems in different evolutionary stages, providing constraints on the evolution of close binary systems.

The precision and nearly continuous coverage provided by *Kepler* paved the way for detecting eclipse timing variations in thousands of eclipsing binaries. The subsample of 41 systems analyzed by Gies et al. (2012, 2015) focused on short-period detached and semi-detached systems, nearly all of which are expected to have companions (Tokovinin et al. 2006). Probable third bodies were detected in seven systems, with $O-C$ variations in seven additional systems that may indicate a distant companion, leading to a detection rate of $7/41 = 17\%$, or possibly as high as $14/41 = 34\%$. Both rates are consistent with other, larger surveys, e.g., Borkovits et al. (2016). Preliminary orbital elements for the seven probable triples combined with spectroscopic mass determinations for the components of the inner binary in five of the systems (KIC 2305372, 4574310, 4848423, 5513861, 9402652) provided minimum masses for the third bodies, indicating that four of the distant companions are likely

K-type stars ($M_3 \geq 0.5 - 0.9\,M_\odot$) while the fifth may be a brown dwarf ($M_3 \geq 0.045\,M_\odot$). These results are also consistent with those from Borkovits et al. (2016), who find that the mass distribution for tertiary components is well populated up to $1.0\,M_\odot$, with a propensity for low mass tertiaries that is, at least in part, due to *Kepler* selection effects and using lower limits for many of the masses. Both ours and the sample of Borkovits et al. also show an absence of third bodies with $P_3 < 200\,\mathrm{d}$. Planets orbiting eclipsing binaries have similarly only been detected in systems with $P > 7\,\mathrm{d}$, perhaps indicating the Kozai cycles thought to drive the inner binary to shorter periods may clear away lower mass components (Martin et al. 2015; Domingos et al. 2015).

To complement the *Kepler* light curves we performed a spectroscopic survey of all 41 eclipsing binaries, deriving spectroscopic orbits and component masses. We collected 454 moderate resolution ground-based spectra, balancing the large number of observations required for spectroscopic orbits of 41 systems with finite telescope time. Radial velocities for each system were measured by combining template spectra for the primary and secondary components over a range of velocity separations and cross-correlating them with the observed spectra. Once the velocity separation of the two components was determined, a final cross-correlation was used to find the velocity of the primary. The resulting radial velocities have typical uncertainties of $1 - 3\,\mathrm{km\ s^{-1}}$ for the primary and $\lesssim 20\ \mathrm{km\ s^{-1}}$ for the secondary stars (due to extreme flux ratios), respectively. In 34 of the 41 systems we measured radial velocities for both the primary and secondary components, allowing us to derive spectroscopic orbital elements and individual masses. One system, KIC 10486425, was found to

be a triple system consisting of an F0 V ($1.57\,M_{\odot}$) and G0 V ($1.13\,M_{\odot}$) type primary and secondary stars, respectively, with a mid F-type tertiary component. Five of the remaining systems are presented as single-lined spectroscopic binaries, as we were only able to measure radial velocities of the primaries. The final system, KIC 4678873, is a constant velocity star whose neighbor KIC 4678875 is the eclipsing binary causing variation in the *Kepler* light curve.

For the double-lined systems, we derived the velocity semi-amplitude of the primary, the velocity semi-amplitude of the secondary, systemic velocities, the mass ratio, $m_1 \sin^3 i$, $m_2 \sin^3 i$, and $a \sin i$. Using inclination values from Slawson et al. (2011), we then calculated the semi-major axis and individual stellar masses for each system. The primary masses ranged from $1.16 - 4.05\,M_{\odot}$, with two-thirds having masses between $1 - 2\,M_{\odot}$, while the secondaries spanned the mass range $0.17{-}1.83\,M_{\odot}$. The mass ratio ($q = M_2/M_1$) distribution shows a preference for similar mass companions ($0.84 \leq q \leq 1.0$) and companions less than $\sim$30% of the primary mass. While the expected mass ratio distribution for binaries is still debated, short-period binaries have been shown to prefer like-mass pairs (Tokovinin 2000; Raghavan et al. 2010). This is reflected in our sample, as the detached binaries have mass ratios of $0.5 < q < 1.0$, with nearly half occurring in the range $0.84 < q < 1.0$. The lower end of the mass ratio distribution is dominated by semi-detached classical Algol systems whose secondaries have larger radii and therefore higher luminosities than stars on the main sequence with similar masses. These systems have undergone mass transfer as the originally more massive star evolved, filling its Roche lobe and transferring mass to the companion,

resulting in the present-day mass ratio. In addition, three systems (KIC 4851217, 5444392, and 9899416) have mass ratios greater than unity (where the primary star is the hotter star as defined by the light curve), indicating the more massive secondary components have evolved to cooler temperatures. Thus, the stars in our sample demonstrate different stages of binary evolution, with nearly half of the double-lined binaries consisting of normal main sequence stars in detached systems, a few where one component has started evolving off the main sequence, and the remaining systems in which Roche lobe overflow and mass transfer have resulted in mass ratio reversal.

Detailed studies of both detached and semi-detached binaries are extremely important for a global understanding of the formation and evolution of binary systems as well as single stars. While stellar evolution is chiefly governed by a star's mass and chemical composition, if the star is gravitationally bound to another star the total mass of the system, mass ratio, and orbital period/separation may play important roles in its evolution if the two stars are close to one another. In particular, as a star in a binary evolves and expands, the expansion is controlled by the presence of the companion star since the expanding star cannot exceed its Roche lobe. Once the star fills its Roche lobe, it begins to transfer mass and angular momentum to its companion. Theoretical models describing the evolution of Algols using conservative mass and angular momentum transfer have proven relatively successful at reproducing the observed characteristics of semi-detached system with B−F spectral types in both components, however, this does not extend to binaries with later spectral types (Eggleton 2001). In fact, growing evidence indicates non-conservative mass transfer/loss is

necessary to reproduce the observed mass ratios of classical Algols (van Rensbergen et al. 2011). Angular momentum loss via mass loss from the system, in particular, is not well understood and may play an even larger role in the evolution of close binaries as semi-detached binaries with orbital periods less than 5 days show more angular momentum loss than those with longer periods (Ibanoğlu et al. 2006).

While mass ratio and period distributions inform binary evolution outcomes, we have shown that the most stringent constraints on binary star formation theories come from detailed radial velocity and light curve modeling. The derivation of fundamental parameters for the detached binary KIC 5738698 demonstrates the utility of model-independent measurements and how these accurate measurements can be used to test stellar theories. For this system, we used our radial velocity measurements to fit a double-lined spectroscopic orbit and determined orbital elements for both stars. Spectra of the primary and secondary components were then reconstructed via Doppler tomography and compared to synthetic spectra to obtain effective temperatures and projected rotational velocities for each star, as well as the flux ratio and metallicity. These parameters were then used as constraints on the light curve model constructed with ELC, in which we determined the inclination, temperature ratio, and relative radii for KIC 5738698. We attempted to solve our difficulties in fitting both the eclipses and outside of eclipse variations simultaneously by fitting for an eccentric orbit, rotational distortions, and gravity brightening exponents. A small eccentricity of $e = 0.0006$ improved the fit marginally, but we ultimately obtained a normal distribution of residuals by including the stellar albedos as fitted parameters. Ultimately, we find KIC 5738698 consists

of two very similar F-type stars with masses and radii of $M_1 = 1.39 M_\odot$, $R_1 = 1.84 R_\odot$ and $M_2 = 1.34 M_\odot$, $R_2 = 1.72 R_\odot$ for the primary and secondary, respectively. Comparison with four widely adopted evolutionary grids found ages of approximately $2.2 - 2.3$ Gyr and generally slightly higher metallicities than our observed value of $\log Z/Z_\odot = -0.4 \pm 0.1$, though most agree within the uncertainty. The best agreement is found with models in which the parameterization of convective core overshooting incrementally increases in the transition region where stars begin to develop convective cores ($M \sim 1.1 - 1.7\, M_\odot$). The overall best match for both components is the Yonsei-Yale (Y^2) evolutionary tracks and isochrones at a metallicity of $\log Z/Z_\odot = -0.31$ and an age of 2.3 Gyr. The updated masses derived in Section 3.3.1, however, yield younger ages ($1.6 - 1.8$ Gyr) in the $M - R$ plane and are even more undersized and/or cooler compared to Y^2 evolutionary tracks in the $T_{\rm eff} - R$ plane, indicating that larger radii, hotter temperatures, or a less negative metallicity is needed to match the models.

Finally, we used the combination of *Kepler* photometry and spectroscopically derived radial velocities to determine stellar parameters for one system in a growing sample of post mass-transfer binaries with a low-mass, thermally bloated, hot white dwarf (WD). The totally eclipsing binary KOI-81, discovered by the *Kepler* mission, is in a stage of evolution usually difficult to observe because the faint, low mass companion creates little reflex orbital motion and is lost in the glare of the brighter star. However, using *HST/COS* we obtained UV spectra of the spun up B-star and hot companion and measured radial velocities to derive a double-lined spectroscopic orbit. Using an inclination of $i = 88.^\circ97$, estimated from

the transit light curve, we derive masses of $2.92 M_{\odot}$ and $0.19 M_{\odot}$ for the B-star and hot WD, respectively. Reconstructions of the UV spectra from Doppler tomography yielded an effective temperature of $12,000$ K for the B-star and $19,000-27,000$ K for the hot companion. We also identified a number of peaks in the Fourier transform of the light curve of the pulsating B-star, including one that may indicate an equatorial rotation period of 11.5 hours. A rotationally distorted model of the B-star was used to fit the transit light curve with $R_2/R_{1\ \mathrm{polar}} = 0.0426$ and $z_0/R_{1\ \mathrm{polar}} = 0.396$ (where z_0 is the smallest distance from the transit trajectory to the center of the B-star relative to the primary polar radius), allowing us to derive an equatorial velocity 74% of the critical velocity where centrifugal and gravitational accelerations balance at the equator.

The evolutionary path of KOI-81, with Roche lobe overflow causing large scale mass-transfer that stripped the mass donor of its envelope and spun up the mass gainer, is one of several that create binary systems with low mass WDs. In recent years a number of detached WD main-sequence binaries have been detected in various large-scale surveys. However, a majority of these systems have low-mass main-sequence components ($\lesssim 0.3\, M_{\odot}$) due to the difficulty of detecting faint companions of more massive stars because of the large luminosity difference between components (Willems & Kolb 2004). The precise photometry and long time span of *Kepler* has since enabled the identification of ten short-period binaries with F/A-type primaries and pre-Helium WD secondaries having radii of $0.04 - 0.28\, R_{\odot}$ (Rowe et al. 2010; van Kerkwijk et al. 2010; Bloemen et al. 2012; Carter et al. 2011a; Breton et al. 2012; Rappaport et al. 2015; Faigler et al. 2015), with an additional 17 systems discovered

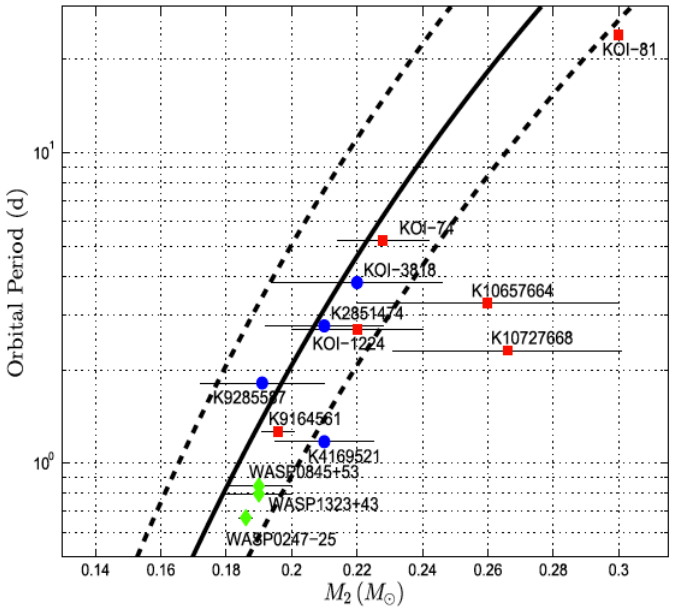

Figure 6.1: WD mass-period relation of Lin et al. (2011, solid curve) with ±10% uncertainties in the model (dashed lines). Red squares and blue circles are ten of the known Kepler systems with derived masses, while green diamonds are three of the known WASP systems. From Faigler et al. (2015).

in the WASP database by Maxted et al. (2014). Such systems are produced by long-term stable mass transfer between low-mass stars in close binary systems, with the stripped down remnants formed during the first Roche lobe oveflow phase (Faigler et al. 2015). They represent a rarely seen evolutionary stage, as the WD is evolving to higher temperatures at a nearly constant luminosity or, having just departed this stage, are experiencing hydrogen shell flashes before settling on the He WD cooling track (Chen et al. 2016). Mass-transfer models predict a direct dependence between the final orbital period and the WD mass if the WD evolves from stable mass transfer and its progenitor has a degenerate core. Using the expected mass-period relation (Lin et al. 2011; Rappaport et al. 1995), Faigler et al. (2015)

plotted the current orbital period as a function of WD mass for 13 of the known main-sequence pre-Helium WD binaries, including KOI-81. The correlation with the expected mass-period relationship seen in Figure 6.1 supports the stable mass-transfer evolutionary mechanism for these systems. Thus, main-sequence stars with compact companions open a unique window into the end products of close binaries.

6.2 Directions for Future Work

While significant work has been put into this project through both data collection and analysis, much more can be gleaned from continued efforts. With the data already in hand, there are two main avenues in which additional system parameters can be determined: reconstruction of the individual component spectra for all SB2 systems, and deriving temperature ratios, radii, and inclinations for the rest of the eclipsing binary sample. Such work would complete the full vision of this dissertation by deriving fundamental parameters for all double-lined spectroscopic binaries in this sample, enabling tests of stellar evolution for single stars via the detached binaries and close binary evolution via Algols. Additional observations, both spectroscopic and photometric, could enhance this data set and begin to characterize the orbits and stellar parameters of third bodies. Finally, this work can be extended to the thousands of eclipsing binaries that have already and will be detected in large scale photometric surveys.

6.2.1 Doppler Tomography

The technique of Doppler tomography is a valuable tool in spectral analysis and vital for determining atmospheric parameters of binary stars that constrain light curve models, enabling more rigorous comparisons between fundamental parameters and evolutionary models. In particular, well defined effective temperatures, metallicities and rotation rates are critical for informing our understanding of the evolutionary processes of stars. The analyses of KIC 5738698 and KOI-81 demonstrate the capabilities of Doppler tomography for separating binary spectra and the derivation of stellar parameters through comparisons with models. Reconstruction of the component spectra for all of the SB2 systems in our sample will enable us to measure the effective temperature, metallicity, rotation, and flux ratios for these stars, which will further our knowledge of each system and constrain light curve solutions to develop full binary models. This work has commenced for some systems, but was largely based on earlier radial velocity results without the aid of improved temperature and flux ratio estimates.

Thus far, tomography has been performed for 16 SB2 systems, representing all of the binaries with estimated flux ratios larger than $F_2/F_1 = 0.10$ (excluding KIC 4544587, previously analyzed by Hambleton et al. 2013) and one additional system, KIC 3440230, with $F_2/F_1 = 0.05$. These systems also have roughly equal mass components and more than eight RV observations each, conditions that increase the reliability of the reconstructions. Preliminary results for 15 systems are given in Table 6.1 ($\log g$ held fixed based on the stellar temperatures as described in Section 3.3), and tomographically reconstructed spectra (solid

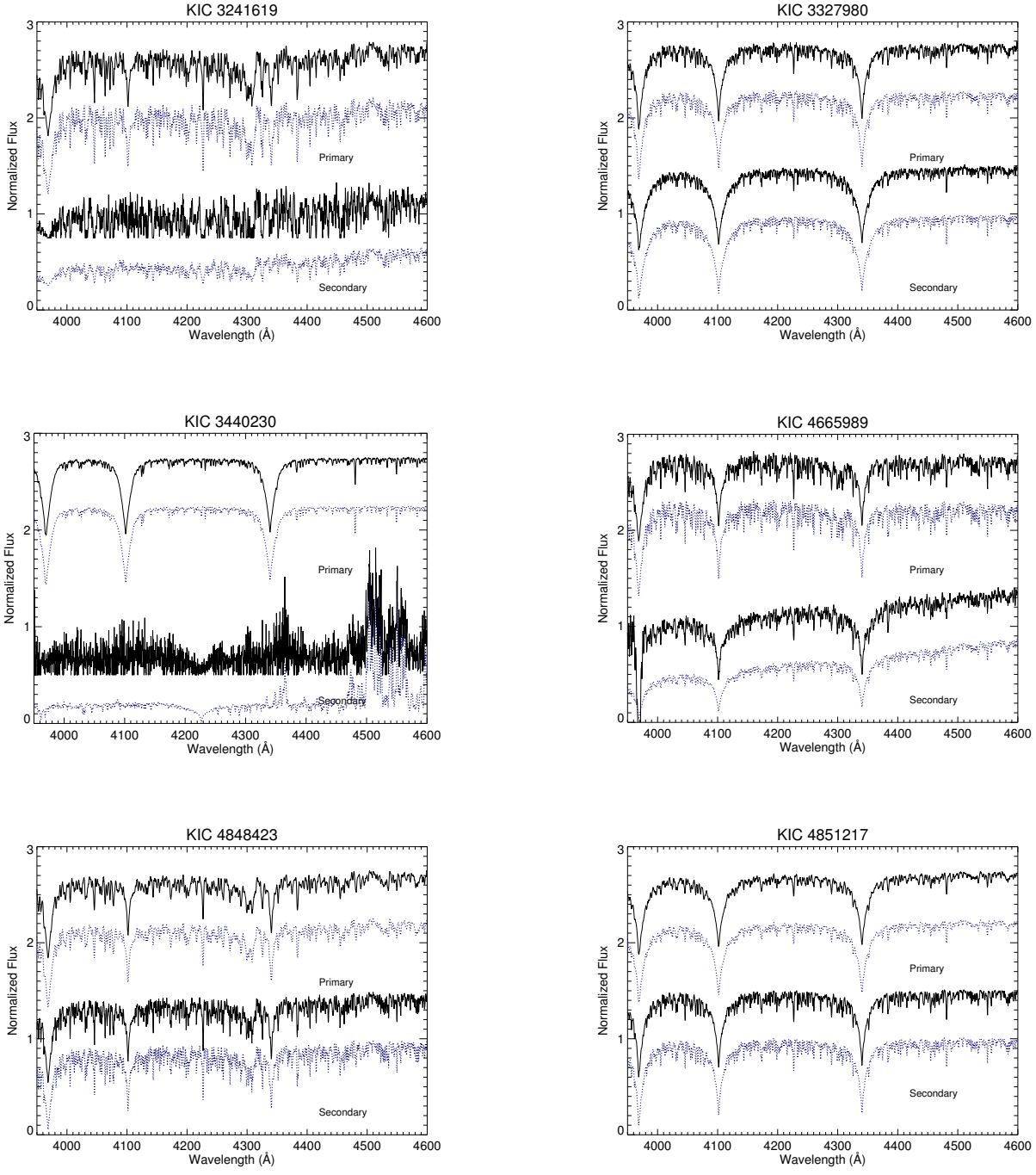

Figure 6.2: Preliminary spectral reconstructions for 14 SB2 systems via Doppler tomography. Solid black lines show the reconstructed primary (top) and secondary (bottom) spectral components for each system, with synthetic spectra (blue dotted lines) shown for comparison. All spectra have been flux normalized and offset for clarity.

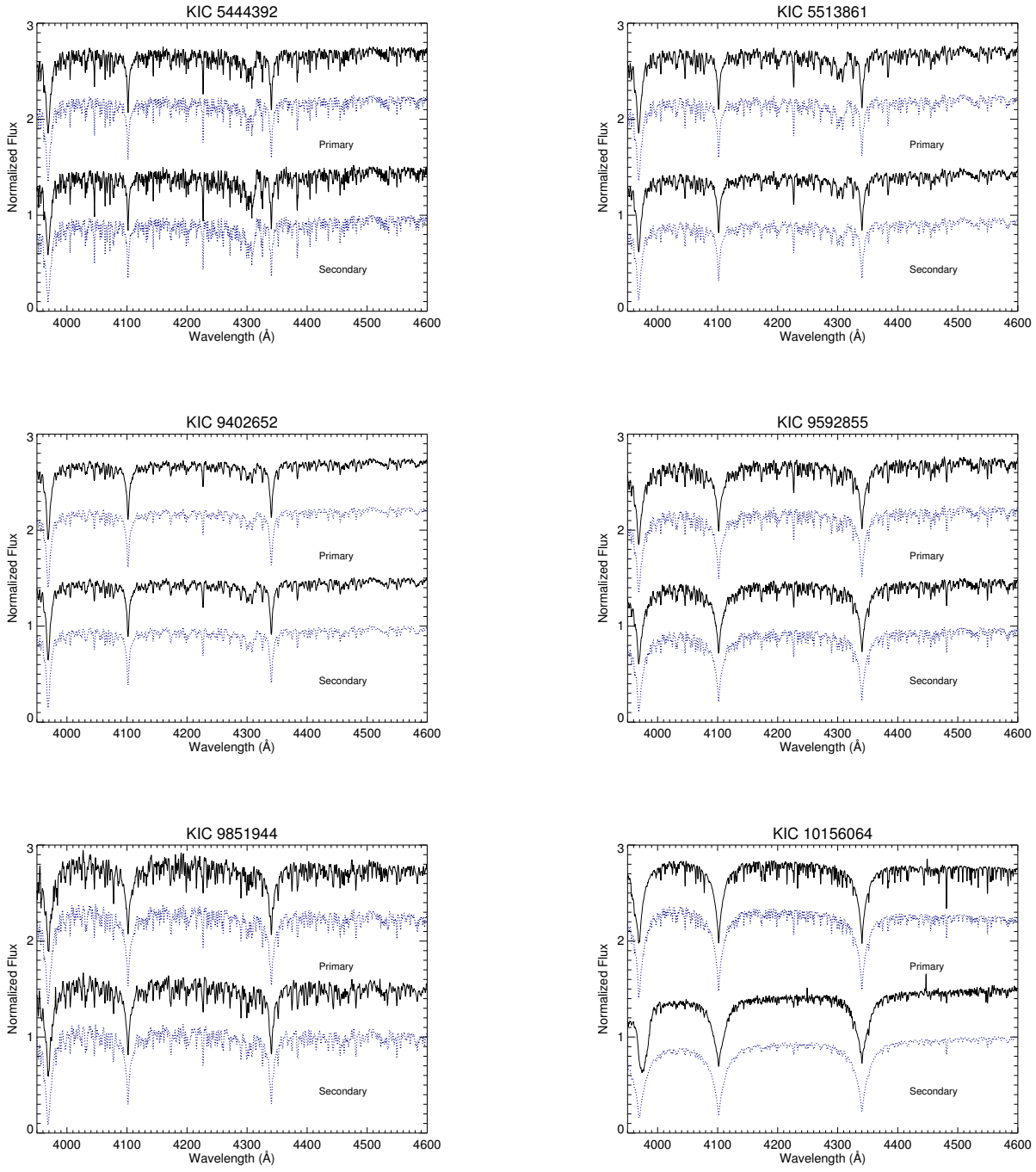

Figure 6.2: Preliminary spectral reconstructions for 14 SB2 systems via Doppler tomography. Solid black lines show the reconstructed primary (top) and secondary (bottom) spectral components for each system, with synthetic spectra (blue dotted lines) shown for comparison. All spectra have been flux normalized and offset for clarity.

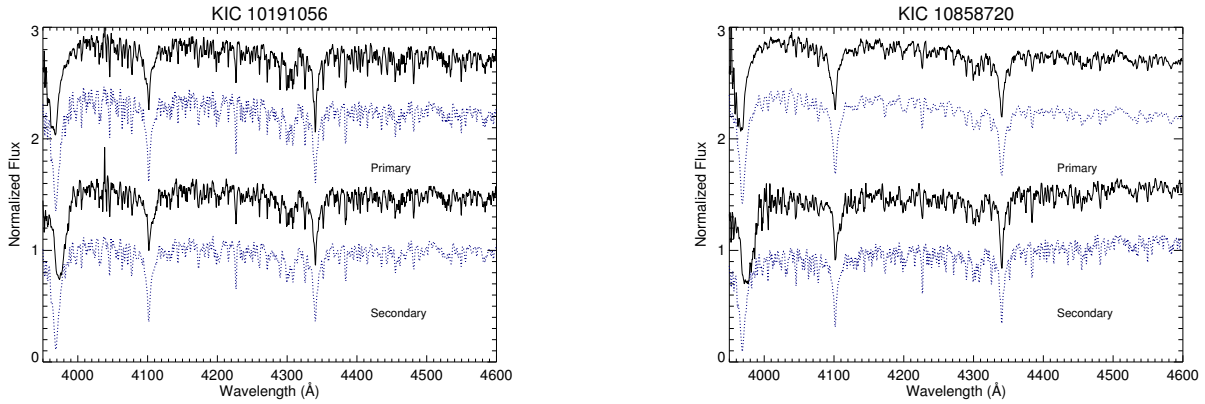

Figure 6.2: Preliminary spectral reconstructions for 14 SB2 systems via Doppler tomography. Solid black lines show the reconstructed primary (top) and secondary (bottom) spectral components for each system, with synthetic spectra (blue dotted lines) shown for comparison. All spectra have been flux normalized and offset for clarity.

black lines) are shown for 14 systems with synthetic spectra (blue dotted lines) for comparison in Figure 6.2. Doppler tomography of KIC 5738698 was already presented and is not repeated here. The difficulty reconstructing spectra for systems with faint companions is illustrated in the case of KIC 3440230, in which the reconstructed spectrum of the secondary has the same general trends as the model spectrum but is much noisier and is artificially cut off when the flux goes below zero. Similarly, several artifacts appear in the reconstructions of KIC 8552540 ($F_2/F_1 = 0.17$; not shown in Fig. 6.2), and more work is needed for reliable results.

Future tomography efforts will include using updated temperature and flux ratio determinations from our radial velocity measurements, as well as the application of the technique to more systems. Tomography of binaries with similar companions is the most successful due to the presence of double-lines that result in well-measured radial velocities and similar fluxes.

Table 6.1: Preliminary Atmospheric Parameters from Doppler Tomography

KIC	$T_{\rm eff,1}$ (K)	$T_{\rm eff,2}$ (K)	$v_1 \sin i$ (km s^{-1})	$v_2 \sin i$ (km s^{-1})	F_2/F_1 (~ 4275Å)	$\log Z/Z_\odot$
3241619	6153 ± 93	4684 ± 400	51 ± 14	24[a]	0.09 ± 1.50	0.01 ± 0.32
3327980	7699 ± 114	8248 ± 250	44 ± 18	23 ± 20	0.60 ± 0.01	-0.20 ± 0.29
3440230	8698 ± 116	4095 ± 200	75 ± 15	12[a]	0.10 ± 0.06	0.01 ± 0.26
4665989	7305 ± 140	7054 ± 877	23 ± 7	54 ± 15	0.30 ± 0.01	0.30 ± 0.16
4848423	6529 ± 50	6577 ± 50	83 ± 8	12[a]	0.74 ± 0.08	0.03 ± 0.16
4851217	7963 ± 117	7800 ± 112	77 ± 10	27 ± 13	1.34 ± 0.14	0.02 ± 0.07
5444392	6418 ± 974	6158 ± 500	29[a]	24[a]	0.85 ± 0.30	-0.63 ± 0.88
5513861	6501 ± 50	6694 ± 50	70 ± 8	76 ± 5	0.75 ± 0.05	-0.41 ± 0.06
8552540	6435 ± 276	4245 ± 444	162 ± 70	30[a]	0.20 ± 0.03	0.20 ± 0.50
9402652	6617 ± 50	6501 ± 50	90 ± 4	90 ± 8	1.15 ± 0.03	-0.77 ± 0.05
9592855	7256 ± 78	7811 ± 90	61 ± 3	25 ± 3	0.93 ± 0.04	0.04 ± 0.15
9851217	7112 ± 87	6993 ± 81	54 ± 4	66 ± 7	1.28 ± 0.07	0.12 ± 0.12
10156064	8051 ± 235	8762 ± 526	35 ± 12	86 ± 19	0.41 ± 0.15	-0.34 ± 0.11
10191056	6764 ± 203	6837 ± 224	63 ± 17	86 ± 15	0.72 ± 0.21	0.10 ± 0.54
10858720	6969 ± 253	6822 ± 878	154 ± 20	63 ± 18	0.62 ± 0.08	-0.02 ± 0.32

[a] $v \sin i$ fixed to synchronous value.

However, many of the binaries in our sample have small flux ratios and secondary components that were barely detected via cross-correlation. Accurate Doppler tomography for such cases is challenging, and the signal-to-noise of the reconstructed secondary spectrum deteriorates rapidly for faint secondaries (as shown in Figure 6.2). The small number of spectra and incomplete orbital coverage also impact the reliability of some reconstructions. However, spectral reconstructions of systems with faint companions will offer additional insight into stellar evolution, because tests of evolutionary tracks are more stringent for binaries with unequal companions and advanced evolutionary states such as Algols. Abundance determinations for systems that have undergone mass transfer can also constrain nucleosynthesis processes, chemical mixing, and mass loss/transfer during binary interactions.

6.2.2 Light Curve Modeling

In this dissertation we have presented the results of eclipse timing analysis of the *Kepler* light curves and examined them for general system characteristics. However, to take full advantage of the information contained in the light curves of such exquisite systems requires light curve modeling. Determining the stellar sizes, temperature ratios, and orbital inclinations will complement the spectroscopic orbital parameters already derived from the radial velocities, while results from Doppler tomography will further constrain the solutions allowing us to calculate fundamental parameters for each system.

Light curve modeling with ELC has resulted in preliminary results for five systems, including KIC 3327980, 5513861, 9402652, 10156064, and 10191056. These efforts make use of spectroscopic orbits and tomographic reconstructions based on preliminary measured radial velocities, but give us solid estimates of the system parameters. Preliminary light curve fitting parameters and calculated system parameters are shown in Table 6.2. The phased, long cadence *Kepler* light curve (black points), light curve (solid green line), and residuals from the ELC model are shown in Figure 6.3 for these five systems.

Future work will include updating the radial velocity results and tomographic reconstructions to constrain more accurately the light curves of these and other systems. The role of second order effects and *Kepler* data characteristics will also be explored, as KIC 3327980 shows residuals similar to KIC 5738698 that may require adjustments to the eccentricity and albedo, while the residuals of KIC 10156064 indicate an overestimate of the reflection effect. Further exploration of how the presence of a tertiary companion affects the light curve flux,

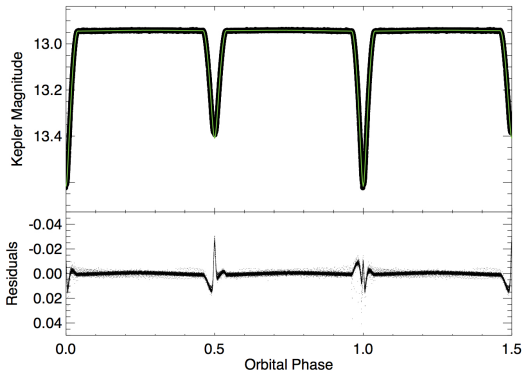

(a) KIC 3327980

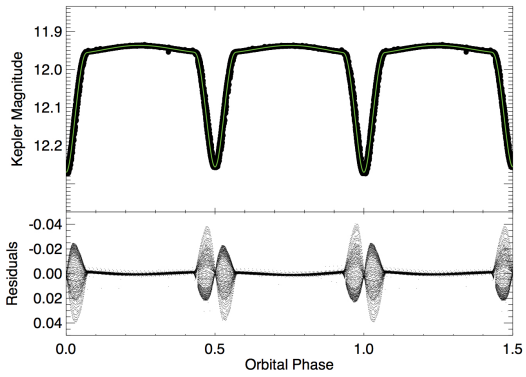

(b) KIC 5513861

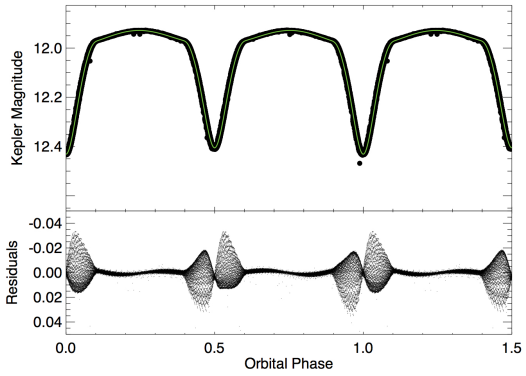

(c) KIC 9402652

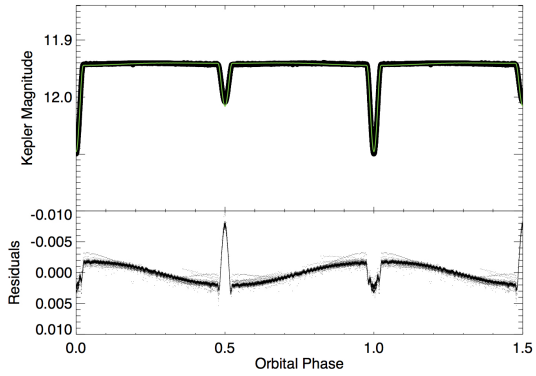

(d) KIC 10156064

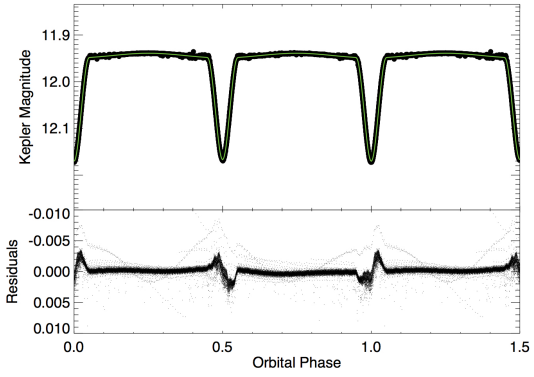

(e) KIC 10191056

Figure 6.3: Top: phased, long cadence *Kepler* light curves (black points) for KIC 3327980, 5513861, 9402652, 10156063, and 10191056 with the preliminary circular models from ELC (solid green line). A randomly selected 20% of the more than 65,000 data points for each system are shown here. Bottom: residuals from the ELC fit to the *Kepler* light curves.

Table 6.2. Preliminary Long Cadence Light Curve Fitting Parameters

Parameter	KIC 3327980	KIC 5513861	KIC 9402652	KIC 10156064	KIC 10191056
P (days)[a]	4.23102194	1.51020825	1.07310422	4.85593645	2.42749484
T_0 (HJD−2,400,000)	55701.1891	55626.2860	55689.9022	556751.2859	55689.3495
i (deg)	87.86	79.64	80.23	82.67	79.49
R_1/a	0.1175	0.2020	0.2796	0.1225	0.1791
R_2/a	0.1198	0.2295	0.3125	0.0662	0.1698
T_2/T_1	1.084	1.0113	1.014	1.2407	1.0019
T_1 (K)[b]	7582	6500	6617	8050	6561
T_2 (K)	8229	6573	6711	9987	6573
M_1 ($M_\odot$)	1.30	1.71	1.31	1.67	1.28
M_2 ($M_\odot$)	1.21	1.55	1.29	1.22	1.17
R_1 ($R_\odot$)	1.76	1.66	1.70	2.11	1.85
R_2 ($R_\odot$)	1.79	1.88	1.90	1.14	1.74
a ($R_\odot$)	15.0	8.2	6.1	17.2	10.2
$\log g_1$ (cgs)	4.06	4.23	4.09	4.01	4.02
$\log g_2$ (cgs)	4.01	4.08	3.99	4.41	4.02

[a]Fixed to value from Gies et al. (2015).

[b]Fixed from preliminary tomography.

and potential eclipse timing variations, will also be necessary to constrain fully systems such as KIC 5513861 and 9402652. Future improvements in light curve models will improve the treatment of such effects, in addition to the Doppler boosting effect, time delays, and gravitational lensing, enabling better constraints on the physical processes in stellar photospheres and proximity effects in close binaries. Computational challenges also need to be addressed in working with such large and precise data sets. ELC now includes an analytic fitting routine that speeds up the modeling process if the stars are well approximated as spheres, as well as parallelized versions of the genetic and MCMC optimizer packages that will aid in reducing the nearly month long computations times necessary to model KIC 5738698.

Results from the light curve analysis of the detached and semi-detached binaries in this

sample will provide continued constraints on evolutionary models of detached binaries and single stars. Moreover, fundamental parameters for systems having undergone large scale mass transfer will add valuable new insights into the outcomes of close binary evolution, as we are detecting Algols with low mass companions and low mass precursors to helium WDs that will provide benchmarks for comparison to evolutionary models and answer open questions regarding the redistribution of mass and angular momentum in interacting binaries.

6.2.3 Distances from Eclipsing Binaries

The accurate stellar temperatures and radii determined via light curve and radial velocity analysis of detached eclipsing binaries (EBs) can also be used to determine bolometric luminosities, which allow the distance to the eclipsing binary to be determined to high precision (Taylor & Southworth 2006). Various applications of this method have been used to determine distances to nearby star clusters and external galaxies, including the Pleiades (Southworth et al. 2005), Cygnus OB2 association (Kiminki et al. 2015), Large Magellanic Cloud (Pietrzyński et al. 2009), and M31 (Ribas 2004). In addition, distances determined using eclipsing binaries can also serve as independent benchmarks for stellar distances obtained by other methods. For example, trigonometric parallax, the most fundamental way to measure stellar distances, uses the difference in the apparent position of a star viewed along two different lines of sight to measure the distance. *Gaia*, an European Space Agency (ESA) mission to map the position and motion of a billion objects in the Galaxy, will provide parallaxes with eventual precisions of $\approx 20\mu as$, 100 times better than its predecessor *Hipparcos*. Distances determined via EBs, however, can provide independent confirmation of

Table 6.3: Preliminary Gaia Parallax Data

KIC	TYC	Parallax (mas)	Distance (pc)
2708156	3134-1093-1	1.1 ± 0.3	884 ± 236
4544587	3124-1348-1	1.4 ± 0.4	736 ± 220
4678873	3140-587-1	1.5 ± 0.3	652 ± 146
4848423	3140-2904-1	1.8 ± 0.3	546 ± 83
5444392	3138-829-1	1.7 ± 0.3	595 ± 120
5513861	3123-2012-1	1.2 ± 0.2	817 ± 166
6206751	3142-1295-1	2.2 ± 0.3	452 ± 71
8262223	3162-1562-1	1.9 ± 0.6	518 ± 157
8552540	3133-1149-1	4.4 ± 0.3	227 ± 16
8553788	3133-360-1	1.0 ± 0.6	1013 ± 615
9159301	3556-2697-1	0.7 ± 0.3	1360 ± 604
9402652	3542-1026-1	1.3 ± 0.3	781 ± 202
9592855	3556-1944-1	1.0 ± 0.4	1039 ± 386
9851944	3558-939-1	0.4 ± 0.4	2451 ± 2302
9899416	3556-3214-1	1.1 ± 0.3	901 ± 217
10156064	3561-1283-1	1.3 ± 0.3	782 ± 187
10191056	3544-1392-1	1.8 ± 0.4	561 ± 120
10206340	3547-2762-1	0.6 ± 0.4	1624 ± 1148
10661783	3547-2135-1	1.9 ± 0.3	517 ± 70
10686876	3562-961-1	1.1 ± 0.3	908 ± 248
10858720	3547-1131-1	1.8 ± 0.3	561 ± 88
KOI-81	3556-3094-1	0.4 ± 0.5	2357 ± 3049

distances from *Gaia* parallaxes and identify systematics in the data, especially since they do not deteriorate with increasing distance or magnitude (Stassun & Torres 2016a). The first *Gaia* data release (Gaia Collaboration et al. 2016) provides parallaxes for approximately two million stars using external information in the form of previous position measurements from the *Hipparcos* (Perryman et al. 1997; van Leeuwen 2007) and *TYCHO-2* (Høg et al. 2000) Catalogs. Distance measurements from eclipsing binaries appearing in the *Gaia* data release can therefore be used to asses the quality of this and future data releases (e.g. Stassun &

Torres 2016b). As the data improves with continued observations, parallax measurements from *Gaia* can also be used to augment the existing eclipsing binary data, allowing for the derivation of individual masses for single-lined systems (see §1.3).

Table 6.3 gives the *Kepler* (KIC) and *TYCHO* (TYC) numbers, as well as preliminary parallaxes and distances for 21 of the 41 eclipsing binaries studied in this dissertation, plus KOI-81, based on the *Gaia* first data release. The average percent error for the systems in Table 6.3 is 35%, with several much larger errors. Determining the distances of these systems from binary modeling could therefore provide more accurate distances for comparison with the *Gaia* results and be used to verify the systematic offset as a function of ecliptic latitude found by Stassun & Torres (2016b). Note the distance given for KOI-81 (2.4 ± 3.0 kpc) is nearly double the value found in this work (1.25 kpc, see Section 5.4), however, the value does agree within the *Gaia* uncertainty as it is so large.

6.2.4 New Observing Initiatives

In addition to the work in progress and future analysis of existing data, more information can be gleaned from this sample of close binaries with new observations. High resolution spectroscopy would be valuable in determining more detailed abundances to minimize the degeneracy with temperature for stricter comparisons with evolutionary models, as well as to study the effects of mass loss on surface abundances as mentioned previously. Such observations may also be used to detect directly tertiaries in the spectra, as in the case of KIC 10486425, while long term RV monitoring could enable mass determinations of the third body. UV spectroscopy of additional objects like KOI-81 would also allow us to separate the

spectra of hot companions to main sequence stars, resulting in masses and temperatures that will provide clues to their evolutionary pathways and further characterize this new sample of post mass-transfer binaries. The prototype for these systems, EL CVn, the brightest and only one previously identified as a variable star, is in fact the subject of a recently accepted *HST/COS* proposal to obtain such UV spectroscopy.

Further efforts to detect and characterize tertiaries in close binaries will also benefit from additional photometric observations which, despite the lower precision, will allow continued monitoring of eclipse timing variations for those systems already showing long term changes and enable the determination of the outer orbital parameters. Measuring the orbits of especially long period tertiaries may also be determined through direct detection via high angular resolution imaging. The separations, relative brightnesses, and colors of detected companions can provide information on the distribution of periods and mass ratios in multiple star systems as well as their stellar properties. The arrangements and orbital characteristics of very wide systems help to constrain formation scenarios and determine the role of dynamical interactions such as scattering events and the eccentric Kozai-Lidov mechanism, responsible for shrinking the orbits of close binaries and extrasolar planets.

Thus, the work begun here demonstrates the abundance of information that can be gleaned from eclipsing binaries detected in large-scale photometric surveys and observed with moderate resolution spectroscopy. Characteristics of the stars contained in close binaries as well as their orbital parameters augment our understanding of single star and binary star evolution as well as how interactions between the stars and any additional companions affect

both the stars and the system as a whole. Future surveys will only increase the sample of binaries we can employ to expand our knowledge of the physical processes of stars and the various stages and pathways of binary evolution.

REFERENCES

Ahmad, A., Jeffery, C. S., & Fullerton, A. W. 2004, A&A, 418, 275

Aliçavuş, F. K., & Soydugan, E. 2014, in IAU Symposium, Vol. 301, Precision Asteroseismology, ed. J. A. Guzik, W. J. Chaplin, G. Handler, & A. Pigulski (Cambridge, UK: Cambridge University Press), 433

Alonso, R., Deeg, H. J., Hoyer, S., et al. 2015, A&A, 584, L8

Althaus, L. G., Miller Bertolami, M. M., & Córsico, A. H. 2013, A&A, 557, A19

Andersen, J. 1991, A&A Rev., 3, 91

Armstrong, D. J., Gómez Maqueo Chew, Y., Faedi, F., & Pollacco, D. 2014, MNRAS, 437, 3473

Asplund, M., Grevesse, N., & Sauval, A. J. 2005, in ASP Conf., Vol. 336, Cosmic Abundances as Records of Stellar Evolution and Nucleosynthesis, ed. T. G. Barnes, III & F. N. Bash (San Francisco: ASP), 25

Bagnuolo, Jr., W. G., Gies, D. R., Hahula, M. E., Wiemker, R., & Wiggs, M. S. 1994, ApJ, 423, 446

Baines, E. K., Döllinger, M. P., Guenther, E. W., et al. 2016, AJ, 152, 66

Balona, L. A. 2013, MNRAS, 431, 2240

—. 2014, MNRAS, 441, 3543

Barnes, J. W. 2009, ApJ, 705, 683

Bass, G., Orosz, J. A., Welsh, W. F., et al. 2012, ApJ, 761, 157

Batalha, N. M., Borucki, W. J., Koch, D. G., et al. 2010, ApJ, 713, L109

Bate, M. R. 1997, MNRAS, 285, 16

Bate, M. R. 2015, in Astronomical Society of the Pacific Conference Series, Vol. 496, Living Together: Planets, Host Stars and Binaries, ed. S. M. Rucinski, G. Torres, & M. Zejda, 37

Bate, M. R., & Bonnell, I. A. 1997, MNRAS, 285, 33

Bate, M. R., Bonnell, I. A., & Bromm, V. 2002, MNRAS, 336, 705

Beck, P. G., Hambleton, K., Vos, J., et al. 2014, A&A, 564, A36

Berger, D. H., Gies, D. R., McAlister, H. A., et al. 2006, ApJ, 644, 475

Bertone, E., Buzzoni, A., Chávez, M., & Rodríguez-Merino, L. H. 2008, A&A, 485, 823

Binnendijk, L. 1960, Properties of double stars; a survey of parallaxes and orbits (Philadelphia, PA: University of Pennsylvania Press)

Bíró, I. B., & Nuspl, J. 2011, MNRAS, 416, 1601

Bloemen, S., Marsh, T. R., Degroote, P., et al. 2012, MNRAS, 422, 2600

Boden, A. F., Torres, G., & Latham, D. W. 2006, ApJ, 644, 1193

Borkovits, T., Hajdu, T., Sztakovics, J., et al. 2016, MNRAS, 455, 4136

Borucki, W. J., Caldwell, D., Koch, D. G., et al. 2001, PASP, 113, 439

Borucki, W. J., Koch, D., Basri, G., et al. 2010, Science, 327, 977

Boyajian, T. S., von Braun, K., van Belle, G., et al. 2012, ApJ, 757, 112

Bradley, P. A., Guzik, J. A., Miles, L. F., et al. 2015, AJ, 149, 68

Bressan, A., Marigo, P., Girardi, L., et al. 2012, MNRAS, 427, 127

Breton, R. P., Rappaport, S. A., van Kerkwijk, M. H., & Carter, J. A. 2012, ApJ, 748, 115

Brogaard, K., Bruntt, H., Grundahl, F., et al. 2011, A&A, 525, A2

Brown, T. M., Latham, D. W., Everett, M. E., & Esquerdo, G. A. 2011, AJ, 142, 112

Brown, W. R., Kilic, M., Allende Prieto, C., Gianninas, A., & Kenyon, S. J. 2013, ApJ, 769, 66

Buchhave, L. A., Bakos, G. Á., Hartman, J. D., et al. 2010, ApJ, 720, 1118

Carter, J. A., Rappaport, S., & Fabrycky, D. 2011a, ApJ, 728, 139

Carter, J. A., Fabrycky, D. C., Ragozzine, D., et al. 2011b, Science, 331, 562

Cenarro, A. J., Peletier, R. F., Sánchez-Blázquez, P., et al. 2007, MNRAS, 374, 664

Chaplin, W. J., & Miglio, A. 2013, ARA&A, 51, 353

Chen, X., Maxted P. F., L., Jiao, L., & Zhanwen, H. 2016, ArXiv e-prints, arXiv:1604.01956

Claret, A. 2000, A&A, 359, 289

—. 2001, MNRAS, 327, 989

Claret, A., & Bloemen, S. 2011, A&A, 529, A75

Clausen, D., Wade, R. A., Kopparapu, R. K., & O'Shaughnessy, R. 2012, ApJ, 746, 186

Clausen, J. V., Frandsen, S., Bruntt, H., et al. 2010a, A&A, 516, A42

Clausen, J. V., Olsen, E. H., Helt, B. E., & Claret, A. 2010b, A&A, 510, A91

Clausen, J. V., Torres, G., Bruntt, H., et al. 2008, A&A, 487, 1095

Conroy, K. E., Prša, A., Stassun, K. G., et al. 2014, AJ, 147, 45

Danforth, C. W., Keeney, B. A., Stocke, J. T., Shull, J. M., & Yao, Y. 2010, ApJ, 720, 976

Demarque, P., Woo, J.-H., Kim, Y.-C., & Yi, S. K. 2004, ApJS, 155, 667

Di Stefano, R. 2011, AJ, 141, 142

Domingos, R. C., Winter, O. C., & Izidoro, A. 2015, International Journal of Astrobiology, 14, 153

Doyle, L. R., Carter, J. A., Fabrycky, D. C., et al. 2011, Science, 333, 1602

Duchêne, G., & Kraus, A. 2013, ARA&A, 51, 269

Dupret, M.-A., Grigahcène, A., Garrido, R., Gabriel, M., & Scuflaire, R. 2005, A&A, 435, 927

Eggleton, P. P. 2001, in Astrophysics and Space Science Library, Vol. 264, The Influence of Binaries on Stellar Population Studies, ed. D. Vanbeveren (Dordrecht: Kluwer Academic Publishers), 299

Epstein, C. R., Elsworth, Y. P., Johnson, J. A., et al. 2014, ApJ, 785, L28

Fabrycky, D., & Tremaine, S. 2007, ApJ, 669, 1298

Fabrycky, D. C. 2010, Non-Keplerian Dynamics of Exoplanets, ed. S. Seager (Tucson, AZ: University of Arizona Press), 217

Faigler, S., Kull, I., Mazeh, T., et al. 2015, ApJ, 815, 26

Famaey, B., Jorissen, A., Luri, X., et al. 2005, A&A, 430, 165

Fitzpatrick, E. L. 1999, PASP, 111, 63

Gaia Collaboration, Brown, A. G. A., Vallenari, A., et al. 2016, A&A, 595, A2

Garcia, E. V., Stassun, K. G., Pavlovski, K., et al. 2014, AJ, 148, 39

Gaulme, P., McKeever, J., Rawls, M. L., et al. 2013, ApJ, 767, 82

Geier, S. 2015, Astronomische Nachrichten, 336, 437

Geier, S., Heber, U., Edelmann, H., et al. 2009, Journal of Physics Conference Series, 172, 012008

Gies, D. R., Bagnuolo, Jr., W. G., Ferrara, E. C., et al. 1998, ApJ, 493, 440

Gies, D. R., & Bolton, C. T. 1986, ApJS, 61, 419

Gies, D. R., Matson, R. A., Guo, Z., et al. 2015, AJ, 150, 178

Gies, D. R., Williams, S. J., Matson, R. A., et al. 2012, AJ, 143, 137

Gies, D. R., Dieterich, S., Richardson, N. D., et al. 2008, ApJ, 682, L117

Gilliland, R. L., Jenkins, J. M., Borucki, W. J., et al. 2010, ApJ, 713, L160

Giménez, A. 2006, A&A, 450, 1231

Giuricin, G., Mardirossian, F., & Mezzetti, M. 1983, ApJS, 52, 35

Goldberg, D., Mazeh, T., & Latham, D. W. 2003, ApJ, 591, 397

Gray, D. F. 2008, The Observation and Analysis of Stellar Photospheres (Cambridge, UK: Cambridge University Press)

Gray, R. O., & Corbally, J., C. 2009, Stellar Spectral Classification (Princeton, NJ: Princeton University Press)

Green, J. C., Froning, C. S., Osterman, S., et al. 2012, ApJ, 744, 60

Grevesse, N., & Noels, A. 1993, Physica Scripta Volume T, 47, 133

Grevesse, N., Noels, A., & Sauval, A. J. 1996, in ASP Conf., Vol. 99, Cosmic Abundances, ed. S. S. Holt & G. Sonneborn (San Francisco, CA: ASP), 117

Grevesse, N., & Sauval, A. J. 1999, A&A, 347, 348

Guo, Z., Gies, D. R., Matson, R. A., & García Hernández, A. 2016, ApJ, 826, 69

Haas, M. R., Batalha, N. M., Bryson, S. T., et al. 2010, ApJ, 713, L115

Hambleton, K. M. 2011, Master's thesis, University of Central Lancashire

Hambleton, K. M., Kurtz, D. W., Prša, A., et al. 2013, MNRAS, 434, 925

Han, Z., Podsiadlowski, P., Maxted, P. F. L., & Marsh, T. R. 2003, MNRAS, 341, 669

Han, Z., Podsiadlowski, P., Maxted, P. F. L., Marsh, T. R., & Ivanova, N. 2002, MNRAS, 336, 449

Hartman, J. D., Bakos, G., Stanek, K. Z., & Noyes, R. W. 2004, AJ, 128, 1761

Hauschildt, P. H., Baron, E., & Allard, F. 1997, ApJ, 483, 390

Heber, U., Edelmann, H., Lisker, T., & Napiwotzki, R. 2003, A&A, 411, L477

Hełminiak, K. G., Graczyk, D., Konacki, M., et al. 2015, MNRAS, 448, 1945

Hermes, J. J., Gänsicke, B. T., Koester, D., et al. 2014, MNRAS, 444, 1674

Hilditch, R. W. 2001, An Introduction to Close Binary Stars (Cambridge, UK: Cambridge University Press), 392

Høg, E., Fabricius, C., Makarov, V. V., et al. 2000, A&A, 355, L27

Howarth, I. D. 2011, MNRAS, 413, 1515

Ibanoğlu, C., Soydugan, F., Soydugan, E., & Dervişoğlu, A. 2006, MNRAS, 373, 435

Iben, Jr., I., & Livio, M. 1993, PASP, 105, 1373

Istrate, A. G., Tauris, T. M., Langer, N., & Antoniadis, J. 2014, A&A, 571, L3

Jeffries, Jr., M. W., Sandquist, E. L., Mathieu, R. D., et al. 2013, AJ, 146, 58

Kallinger, T., Reegen, P., & Weiss, W. W. 2008, A&A, 481, 571

Kaplan, D. L. 2010, ApJ, 717, L108

Kim, D.-W., Protopapas, P., Bailer-Jones, C. A. L., et al. 2014, A&A, 566, A43

Kiminki, D. C., Kobulnicky, H. A., Vargas Álvarez, C. A., Alexander, M. J., & Lundquist, M. J. 2015, ApJ, 811, 85

Kipping, D. M. 2010, MNRAS, 407, 301

Kirk, B., Conroy, K., Prša, A., et al. 2016, AJ, 151, 68

Kitchatinov, L. L., & Rüdiger, G. 2009, A&A, 504, 303

Kopal, Z. 1959, International Astrophysics Series, Vol. 5, Close binary systems (New York, NY: Wiley)

Kostov, V. B., Orosz, J. A., Welsh, W. F., et al. 2016, ApJ, 827, 86

Kupfer, T., Geier, S., Heber, U., et al. 2015, A&A, 576, A44

Kurtz, M. J., Mink, D. J., Wyatt, W. F., et al. 1992, in ASP Conf., Vol. 25, Astronomical Data Analysis Software and Systems I, ed. D. M. Worrall, C. Biemesderfer, & J. Barnes (San Francisco, CA: ASP), 432

Lacy, C. H. S., Torres, G., & Claret, A. 2008, AJ, 135, 1757

Latham, D. W., & Stefanik, R. P. 1992, in IAU Transactions, Vol. XXI B, XXIst General Assembly - Transactions of the IAU, ed. E. J. Bergeron (Dordrecht: Kluwer Academic Publishers), 269

Lehmann, H., Southworth, J., Tkachenko, A., & Pavlovski, K. 2013, A&A, 557, A79

Lenz, P., & Breger, M. 2005, Communications in Asteroseismology, 146, 53

Lin, J., Rappaport, S., Podsiadlowski, P., et al. 2011, ApJ, 732, 70

Luck, R. E., & Heiter, U. 2006, AJ, 131, 3069

Lucy, L. B. 1967, ZAp, 65, 89

—. 1968, ApJ, 153, 877

—. 2013, A&A, 551, A47

Lucy, L. B., & Sweeney, M. A. 1971, AJ, 76, 544

Maceroni, C., Gandolfi, D., Montalbán, J., & Aerts, C. 2012, in IAU Symposium, Vol. 282, From Interacting Binaries to Exoplanets: Essential Modeling Tools, ed. M. T. Richards & I. Hubeny (Cambridge, UK: Cambridge University Press), 41

Maceroni, C., Montalbán, J., Michel, E., et al. 2009, A&A, 508, 1375

Maceroni, C., Lehmann, H., da Silva, R., et al. 2014, A&A, 563, A59

Mandel, K., & Agol, E. 2002, ApJ, 580, L171

Martin, D. V., Mazeh, T., & Fabrycky, D. C. 2015, MNRAS, 453, 3554

Massa, D., York, B., & Hernandez, S. e. 2013, COS Data Handbook v. 2.0 (Baltimore, MD: STScI)

Massarotti, A., Latham, D. W., Stefanik, R. P., & Fogel, J. 2008, AJ, 135, 209

Matson, R. A., Gies, D. R., Guo, Z., & Orosz, J. A. 2016, AJ, 151, 139

Matson, R. A., Gies, D. R., Guo, Z., et al. 2015, ApJ, 806, 155

Maxted, P. F. L., Anderson, D. R., Burleigh, M. R., et al. 2011, MNRAS, 418, 1156

Maxted, P. F. L., Bloemen, S., Heber, U., et al. 2014, MNRAS, 437, 1681

Mazeh, T., Simon, M., Prato, L., Markus, B., & Zucker, S. 2003, ApJ, 599, 1344

McAlister, H. A., ten Brummelaar, T. A., Gies, D. R., et al. 2005, ApJ, 628, 439

Mjaseth, K., Batalha, N., Borucki, W., et al. 2007, in Bulletin of the American Astronomical

Society, Vol. 39, American Astronomical Society Meeting Abstracts #210, 98

Molenda-Zakowicz, J., Frasca, A., Latham, D. W., & Jerzykiewicz, M. 2007, Acta Astron., 57, 301

Morbey, C. L., & Brosterhus, E. B. 1974, PASP, 86, 455

Mowlavi, N., Eggenberger, P., Meynet, G., et al. 2012, A&A, 541, A41

Muraveva, T., Clementini, G., Maceroni, C., et al. 2014, MNRAS, 443, 432

Naoz, S. 2016, ARA&A, in press, (arXiv:1601.07175)

Nidever, D. L., Marcy, G. W., Butler, R. P., Fischer, D. A., & Vogt, S. S. 2002, ApJS, 141, 503

Ofir, A., Gandolfi, D., Buchhave, L., et al. 2012, MNRAS, 423, L1

Orosz, J. A., & Hauschildt, P. H. 2000, A&A, 364, 265

Orosz, J. A., Groot, P. J., van der Klis, M., et al. 2002, ApJ, 568, 845

Orosz, J. A., Welsh, W. F., Carter, J. A., et al. 2012, Science, 337, 1511

Osterman, S., Green, J., Froning, C., et al. 2011, Ap&SS, 335, 257

O'Toole, S. J., & Heber, U. 2006, A&A, 452, 579

Pamyatnykh, A. A. 1999, Acta Astron., 49, 119

Panei, J. A., Althaus, L. G., Chen, X., & Han, Z. 2007, MNRAS, 382, 779

Penny, L. R., Seyle, D., Gies, D. R., et al. 2001, ApJ, 548, 889

Perryman, M. A. C., Lindegren, L., Kovalevsky, J., et al. 1997, A&A, 323, L49

Peters, G. J., Pewett, T. D., Gies, D. R., Touhami, Y. N., & Grundstrom, E. D. 2013, ApJ, 765, 2

Petrie, R. M., Andrews, D. H., & Scarfe, C. D. 1967, in IAU Symposium, Vol. 30, Determination of Radial Velocities and their Applications, ed. A. H. Batten & J. F. Heard (London, UK: Academic Press), 221

Pietrukowicz, P., Mróz, P., Soszyński, I., et al. 2013, Acta Astron., 63, 115

Pietrzyński, G., Thompson, I. B., Graczyk, D., et al. 2009, ApJ, 697, 862

Pigulski, A., Pojmański, G., Pilecki, B., & Szczygieł, D. M. 2009, Acta Astron., 59, 33

Podsiadlowski, P. 2014, in Accretion Processes in Astrophysics, ed. I. González Martínez-País, T. Shahbaz, & J. Casares Velázquez, XXI Canary Islands Winter School of Astrophysics (Cambridge, UK: Cambridge University Press), 45

Pollacco, D. L., Skillen, I., Collier Cameron, A., et al. 2006, PASP, 118, 1407

Popper, D. M. 1967, ARA&A, 5, 85

—. 1980, ARA&A, 18, 115

Pribulla, T., & Rucinski, S. M. 2006, AJ, 131, 2986

Prša, A., Guinan, E. F., Devinney, E. J., et al. 2012, in IAU Symposium, Vol. 282, From Interacting Binaries to Exoplanets: Essential Modeling Tools, ed. M. T. Richards & I. Hubeny (Cambridge, UK: Cambridge University Press), 271–278

Prša, A., & Zwitter, T. 2005, ApJ, 628, 426

Prša, A., Batalha, N., Slawson, R. W., et al. 2011, AJ, 141, 83

Rafert, J. B., & Twigg, L. W. 1980, MNRAS, 193, 79

Raghavan, D., McAlister, H. A., Henry, T. J., et al. 2010, ApJS, 190, 1

Rappaport, S., Deck, K., Levine, A., et al. 2013, ApJ, 768, 33

Rappaport, S., Nelson, L., Levine, A., et al. 2015, ApJ, 803, 82

Rappaport, S., Podsiadlowski, P., & Horev, I. 2009, ApJ, 698, 666

Rappaport, S., Podsiadlowski, P., Joss, P. C., Di Stefano, R., & Han, Z. 1995, MNRAS, 273, 731

Rawls, M. L., Gaulme, P., McKeever, J., et al. 2016, ApJ, 818, 108

Ribas, I. 2004, in Astronomical Society of the Pacific Conference Series, Vol. 318, Spectroscopically and Spatially Resolving the Components of the Close Binary Stars, ed. R. W. Hilditch, H. Hensberge, & K. Pavlovski, 261–269

Rodríguez-Merino, L. H., Chavez, M., Bertone, E., & Buzzoni, A. 2005, ApJ, 626, 411

Rowe, J. F., Borucki, W. J., Koch, D., et al. 2010, ApJ, 713, L150

Rowe, J. F., Coughlin, J. L., Antoci, V., et al. 2015, ApJS, 217, 16

Rozyczka, M., Kaluzny, J., Thompson, I. B., et al. 2014, Acta Astron., 64, 233

Ruciński, S. M. 1969, Acta Astron., 19, 245

Sandquist, E. L., Shetrone, M., Serio, A. W., & Orosz, J. 2013a, AJ, 146, 40

Sandquist, E. L., Mathieu, R. D., Brogaard, K., et al. 2013b, ApJ, 762, 58

Savonije, G. J. 2013, A&A, 559, A25

Shafter, A. W., Szkody, P., & Thorstensen, J. R. 1986, ApJ, 308, 765

Silvotti, R., Østensen, R. H., Bloemen, S., et al. 2012, MNRAS, 424, 1752

Sipahi, E., Çakirli, Ö., & Ibanoglu, C. 2013, Rev. Mexicana Astron. Astrofis., 49, 25

Slawson, R. W., Prša, A., Welsh, W. F., et al. 2011, AJ, 142, 160

Smullen, R. A., & Kobulnicky, H. A. 2015, ApJ, 808, 166

Soszyński, I., Stępień, K., Pilecki, B., et al. 2015, Acta Astron., 65, 39

Southworth, J., Bruntt, H., & Buzasi, D. L. 2007, A&A, 467, 1215

Southworth, J., Maxted, P. F. L., & Smalley, B. 2005, A&A, 429, 645

Southworth, J., Zima, W., Aerts, C., et al. 2011, MNRAS, 414, 2413

Stassun, K. G., & Torres, G. 2016a, AJ, 152, 180

—. 2016b, ApJ, 831, L6

Taylor, J., & Southworth, J. 2006, PhD thesis, Keele University, Staffordshire, ST5 5BG, UK

Thaller, M. L., Bagnuolo, Jr., W. G., Gies, D. R., & Penny, L. R. 1995, ApJ, 448, 878

Thompson, S. E., Everett, M., Mullally, F., et al. 2012, ApJ, 753, 86

Tobin, J. J., Kratter, K. M., Persson, M. V., et al. 2016, Nature, 538, 483

Tokovinin, A., Thomas, S., Sterzik, M., & Udry, S. 2006, A&A, 450, 681

Tokovinin, A. A. 2000, A&A, 360, 997

Torres, G. 2014, in Astronomical Society of the Pacific Conference Series, Vol. 487, Resolving The Future Of Astronomy With Long-Baseline Interferometry, ed. M. J. Creech-Eakman, J. A. Guzik, & R. E. Stencel, 21

Torres, G., Andersen, J., & Giménez, A. 2010, A&A Rev., 18, 67

Torres, G., Fischer, D. A., Sozzetti, A., et al. 2012, ApJ, 757, 161

Torres, G., Sandberg Lacy, C. H., Pavlovski, K., et al. 2014a, ApJ, 797, 31

Torres, G., Sandberg Lacy, C. H., Pavlovski, K., Fekel, F. C., & Muterspaugh, M. W. 2015, AJ, 150, 154

Torres, G., Vaz, L. P. R., Sandberg Lacy, C. H., & Claret, A. 2014b, AJ, 147, 36

Townsend, R. H. D. 2005, MNRAS, 364, 573

Valenti, J. A., & Fischer, D. A. 2005, ApJS, 159, 141

van Kerkwijk, M. H., Rappaport, S. A., Breton, R. P., et al. 2010, ApJ, 715, 51

van Leeuwen, F. 2007, A&A, 474, 653

van Rensbergen, W., de Greve, J. P., Mennekens, N., Jansen, K., & de Loore, C. 2011, A&A, 528, A16

VandenBerg, D. A., Bergbusch, P. A., & Dowler, P. D. 2006, ApJS, 162, 375

Wade, R. A., & Rucinski, S. M. 1985, A&AS, 60, 471

Welsh, W. F., Orosz, J. A., Carter, J. A., et al. 2012, Nature, 481, 475

Willems, B., & Kolb, U. 2004, A&A, 419, 1057

Wilson, R. E., & Devinney, E. J. 1971, ApJ, 166, 605

Yakut, K., Eggleton, P. P., Kalomeni, B., Tout, C. A., & Eldridge, J. J. 2015, MNRAS, 453, 2937

Zakirov, M. M. 2010, Kinematics and Physics of Celestial Bodies, 26, 269

Zasche, P., Wolf, M., Kučáková, H., et al. 2015, AJ, 149, 197

Zucker, S. 2003, MNRAS, 342, 1291

Zucker, S. 2012, in IAU Symposium, Vol. 282, From Interacting Binaries to Exoplanets: Essential Modeling Tools, ed. M. T. Richards & I. Hubeny (Cambridge, UK: Cambridge University Press), 371

Zucker, S., & Mazeh, T. 1994, ApJ, 420, 806

Zucker, S., Mazeh, T., & Alexander, T. 2007, ApJ, 670, 1326

APPENDIX A

Estimating $e\cos\omega$ and $e\sin\omega$ from an Eclipsing Binary Light Curve

This appendix contains the methods and IDL code `findecc.pro` used to determine estimates of the eccentricity (e) and longitude of periastron (ω) from *Kepler* light curves based on the offset between ($e\cos\omega$) and duration ($e\sin\omega$) of the two eclipses. This method was used to derive initial estimates of e and ω to narrow the parameter range searched by ELC when fitting for an eccentric orbit for KIC 5738698 in Section 4.4.3.1. We also used this method to obtain e and ω for KIC 8196190 when fitting the spectroscopic orbit to the radial velocities measured from the primary star (Section 3.3.3). The following first appeared in the appendices given in Matson et al. (2016).

A.1 Eclipse Timings and $e\cos\omega$

The time between primary and secondary eclipse will generally differ from half the orbital period P for binary systems with a non-zero eccentricity. Kopal (1959), Binnendijk (1960), and Hilditch (2001) present an analytical solution for this difference for the case of inclination $i = 90°$ that we summarize here. Figure A.1 illustrates the orbital geometry for the elliptical orbit of the primary star. This star orbits the center of mass attaining periastron at the right hand side of the diagram. Suppose we observe the binary along a line of sight from the lower left, so that primary eclipse (primary superior conjunction) occurs when the primary is at the location marked by a square and secondary eclipse occurs at the point indicated by a diamond. The true anomaly ν measures the angle from periastron to the eclipse position, and given a longitude of periastron for the primary ω, then $\nu = \pi/2 - \omega$ at primary eclipse

and $\nu = 3\pi/2 - \omega$ at secondary eclipse. The relation between orbital phase and position is given by the Kepler equation

$$\frac{2\pi(t-T)}{P} = E - e\sin E \tag{A.1}$$

where T is the epoch of periastron, e is the eccentricity, and E is the eccentric anomaly. The angle E is measured from periastron through the center of the ellipse to the stellar position projected onto the auxiliary circle. Then the time between eclipses is given by

$$\frac{2\pi(t_s - t_p)}{P} = E_s - E_p - e(\sin E_s - \sin E_p) \tag{A.2}$$

where E_p and E_s are the values of the eccentric anomaly at the primary and secondary eclipses, respectively.

The true and eccentric anomalies are related through the expression for the ratio of binary separation r to semimajor axis a,

$$\frac{r}{a} = \frac{(1-e^2)}{(1+e\cos\nu)} = 1 - e\cos E. \tag{A.3}$$

We can determine $\cos E_p$ from the above as

$$\cos E_p = (1 - \frac{r_p}{a})/e \tag{A.4}$$

where r_p is the center of mass to primary distance at primary eclipse (and similarly for the secondary eclipse). From inspection of Figure A.1, we can derive an expression for $\sin E_p$,

$$\sin E_p = \frac{r_p}{a}\frac{\sin\nu}{b/a} = \frac{r_p}{a}\frac{\cos\omega}{b/a} \tag{A.5}$$

where the ratio of minor to major axis is $b/a = (1-e^2)^{1/2}$. The comparable expression for

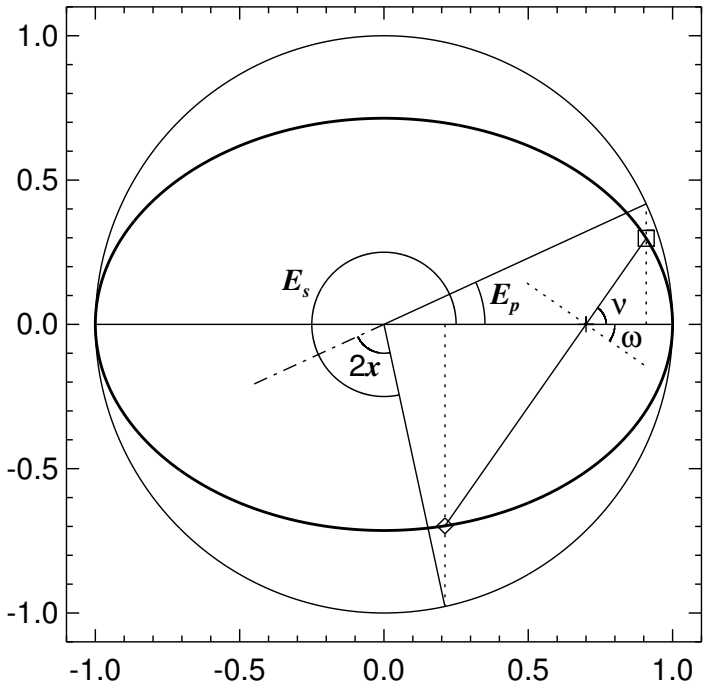

Figure A.1: A diagram of an elliptical orbit and eclipse geometry as seen from above the orbit. The thick solid ellipse shows the elliptical orbit of the primary star with a semimajor axis shown by the horizontal line and focus (center of mass) shown by a plus sign. The primary (secondary) eclipses occur when the primary is located at the position marked by a square (diamond). The observer views these from a line of sight from the lower left (along the conjunction line from diamond to square). The longitude of periastron ω is measured from the ascending node crossing the plane of the sky (dotted line through center of mass position) to the periastron position at right. The true anomaly ν at primary eclipse is indicated as the angle from periastron to stellar position. Dotted lines show normals from the semimajor axis drawn through the eclipse positions out to the auxiliary circle inscribing the ellipse. The angle from periastron through ellipse center to the position on the auxiliary circle is the eccentric anomaly E, which is indicated for both eclipses. The solution for angle $2x$ is derived in the text.

the secondary eclipse is

$$\sin E_s = -\frac{r_s}{a}\frac{\cos\omega}{b/a}. \tag{A.6}$$

We need to solve for the angle $2x \equiv y \equiv E_s - E_p - \pi$ shown in Figure A.1. The analytical solution is obtained by using the identity relation for the tangent of a half angle

$$\tan\frac{y}{2} = \sqrt{\frac{1-\cos y}{1+\cos y}} = \sqrt{\frac{1+\cos E_s\cos E_p+\sin E_s\sin E_p}{1-\cos E_s\cos E_p-\sin E_s\sin E_p}} = \frac{e\cos\omega}{(1-e^2)^{1/2}}. \tag{A.7}$$

Then we arrive at the final expression for the observed phase difference between eclipses,

$$\frac{2\pi(t_s-t_p)}{P} = \pi + 2\arctan\frac{e\cos\omega}{(1-e^2)^{1/2}} + \frac{2(1-e^2)^{1/2}\ e\cos\omega}{(1-e^2\sin^2\omega)}. \tag{A.8}$$

A Taylor series expansion for small e of the right hand side of equation A.8 yields

$$\frac{2\pi(t_s-t_p)}{P} = \pi + 4e\cos\omega \tag{A.9}$$

or in terms of the orbital phase difference

$$e\cos\omega = \frac{\pi}{2}(\phi_s - \phi_p - 0.5). \tag{A.10}$$

This approximation for $e\cos\omega$ differs from the actual value by less than $10^{-3.8}$, $10^{-6.8}$, and $10^{-9.7}$ for $e = 0.1$, 0.01, and 0.001, respectively, so use of this approximation will introduce negligible errors in cases of small eccentricity and $i = 90°$.

The relationship will change somewhat for $i < 90°$. The projected separation in the sky δ in units of the semimajor axis will vary as (see eq. 9 from Giménez 2006)

$$\delta^2 = \left[\frac{1-e^2}{1-e\sin(\theta-\omega)}\right]^2 (1-\cos^2\theta\sin^2 i) \tag{A.11}$$

where $\theta = \nu + \omega - \pi/2$. The central times of the eclipses correspond to the two minima

of this function. We made a numerical solution to the eclipse time difference as a function of inclination, eccentricity, and longitude of periastron. Once again we find that the eclipse time difference is mainly related to the parameter $e\cos\omega$. However, direct use of equation A.10 may lead to small overestimates of $e\cos\omega$ for $i < 90°$, and a good approximation for the effects of inclination (better than 0.5% for $i > 60°$) is given by

$$e\cos\omega = \pi\ \frac{\phi_s - \phi_p - 0.5}{1 + \csc i}. \tag{A.12}$$

Finally, we note that light travel time differences between eclipses may also cause a small difference in eclipse times given by (Kaplan 2010; Fabrycky 2010)

$$\triangle t = t_s - t_p - \frac{P}{2} = \frac{PK_2}{\pi c}\left(1 - \frac{M_2}{M_1}\right)\frac{(1-e^2)^{3/2}}{1 - e^2\sin^2\omega} \tag{A.13}$$

where K_2 is the orbital semiamplitude of the secondary, c is the speed of light, and M_2/M_1 is the mass ratio. The last factor relating to the eccentricity is of order $1 - e^2$ and can be ignored for the small e case. If radial velocity solutions are available for both components and $\triangle t$ is found to be significant, then the numerator factor in equation A.12 should be replaced with $\phi_s - \phi_p - 0.5 - \triangle t/P$ in order to estimate $e\cos\omega$.

A.2 Eclipse Durations and $e\sin\omega$

Kopal (1959), Binnendijk (1960), and Hilditch (2001) discuss how the eclipse durations are closely related to the product $e\sin\omega$. Figure A.2 shows the geometry for the eclipse as viewed in the sky. Suppose that first contact occurs on the left side when the stellar limbs first meet and that final contact occurs on the right side as the limbs last coincide. In the frame of

reference of the primary star, the secondary moves a distance $2x$ where $x^2 = (R_p + R_s)^2 - \delta^2$ and $\delta = r\cos i$ (minimum separation). The relative projected velocity of secondary at the eclipse time is $v = \frac{2\pi a}{P}\frac{a}{r}$ according to Kepler's Second Law (ignoring minor non-tangential motions). Then using the relations for the separation r/a at both eclipses, the duration of the primary and secondary eclipses are, respectively,

$$d_p = \frac{P}{\pi}\frac{1-e^2}{1+e\sin\omega}\sqrt{\left(\frac{R_p+R_s}{a}\right)^2 - \left(\frac{1-e^2}{1+e\sin\omega}\right)^2\cos^2 i} \tag{A.14}$$

and

$$d_s = \frac{P}{\pi}\frac{1-e^2}{1-e\sin\omega}\sqrt{\left(\frac{R_p+R_s}{a}\right)^2 - \left(\frac{1-e^2}{1-e\sin\omega}\right)^2\cos^2 i}. \tag{A.15}$$

Note that if eclipses do occur, then the arguments of the square root will be positively valued.

It is helpful to consider a specific case to understand the dependencies in the above equations. Suppose $\omega = 90^\circ$ so that primary eclipse occurs when the primary reaches periastron at its superior conjunction. At this instance the separation is a minimum $(1-e)\,a$, so the Keplerian velocity reaches a maximum to cause a shorter duration eclipse. This part of the variation is given by the leading term $(1-e^2)/(1+e\sin\omega) = (1-e)$ in the expression for d_p. However, if the eclipse is viewed with an inclination different from $i = 90^\circ$, then the reduced separation between the stars will result in a proportional decrease in the impact parameter δ (Fig. A.2) and hence an increase in the eclipse crossing distance $2x$. This change appears in the square root term in the expressions above. Thus, the change in eclipse duration depends on the relative sizes of the competing terms of changing velocity (shorter eclipse in this case) and eclipse path length (longer eclipse in this case). While both terms depend on

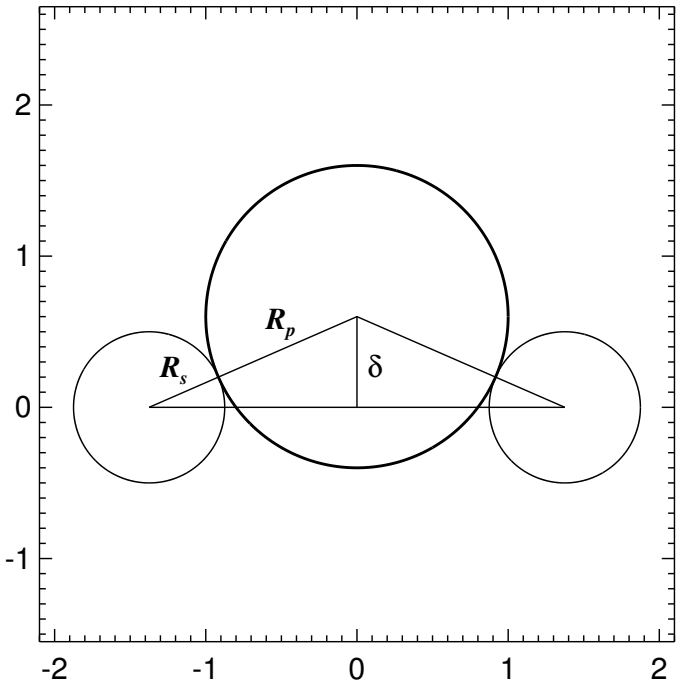

Figure A.2: A depiction of the appearance of an eclipse in the plane of the sky in the frame of the primary star. The smaller secondary star moves from left to right attaining a minimum separation of projected centers indicated by $\delta = r\cos i$. The horizontal line connecting the center of the secondary at the start and end of the eclipse marks the projected distance of secondary motion.

$e\sin\omega$, the latter one also depends upon the sum of the stellar radii and inclination.

We may then form an expression for the ratio of the difference in eclipse durations over their sum,

$$\frac{d_s - d_p}{d_s + d_p} = \frac{(1+e\sin\omega)\sqrt{1-\left(\frac{1-e^2}{1-e\sin\omega}\right)^2\epsilon^2} - (1-e\sin\omega)\sqrt{1-\left(\frac{1-e^2}{1+e\sin\omega}\right)^2\epsilon^2}}{(1+e\sin\omega)\sqrt{1-\left(\frac{1-e^2}{1-e\sin\omega}\right)^2\epsilon^2} + (1-e\sin\omega)\sqrt{1-\left(\frac{1-e^2}{1+e\sin\omega}\right)^2\epsilon^2}} \tag{A.16}$$

where $\epsilon = \frac{a\cos i}{R_p+R_s}$. For most eclipsing systems, $i \approx 90^\circ$ and $\epsilon^2 << 1$, and, therefore, we

may use the Taylor series expansion for the square root terms, $\sqrt{1-x^2} \approx 1 - x^2/2$. Then, ignoring terms of e^2 and higher order, the above ratio simplifies to

$$\frac{d_s - d_p}{d_s + d_p} = \frac{2 - 3\epsilon^2}{2 - \epsilon^2}\, e \sin\omega \equiv m\, e \sin\omega \tag{A.17}$$

which yields the estimator

$$e \sin\omega = \frac{(d_s - d_p)}{(d_s + d_p)} \frac{1}{m}. \tag{A.18}$$

It is usually possible to make a preliminary fit of an eclipsing light curve assuming a circular orbit for small eccentricity systems, and $m(\epsilon)$ may be estimated from the inclination and fractional radius sum associated with the circular fit.

The simple rectilinear approximation above does not account fully for the three dimensional projection of the orbit during the eclipse, and a better approximation of the eclipse duration is given by Kipping (2010, see his eq. 15)

$$d_p = \frac{P}{\pi} \frac{(1-e^2)^{3/2}}{(1 + e\sin\omega)^2} \arcsin\left[\frac{\sqrt{\left(\frac{R_p+R_s}{a}\right)^2 - \left(\frac{1-e^2}{1+e\sin\omega}\right)^2 \cos^2 i}}{\left(\frac{1-e^2}{1+e\sin\omega}\right)\sin i} \right] \tag{A.19}$$

and

$$d_s = \frac{P}{\pi} \frac{(1-e^2)^{3/2}}{(1 - e\sin\omega)^2} \arcsin\left[\frac{\sqrt{\left(\frac{R_p+R_s}{a}\right)^2 - \left(\frac{1-e^2}{1-e\sin\omega}\right)^2 \cos^2 i}}{\left(\frac{1-e^2}{1-e\sin\omega}\right)\sin i} \right]. \tag{A.20}$$

This approximation assumes that the separation at mideclipse is constant throughout the eclipse. In the limit when $i \approx 90^\circ$ and the sum of the radii is small, these expressions attain the same form as in equations A.14 and A.15. However, equations A.19 and A.20 show more clearly that eclipse durations are really functions of two variables, the inclination and the

sum of the relative radii, rather than a ratio of these parameters.

The ratio of the difference and sum of equations A.19 and A.20 forms an expression like equation A.18 that is also linear in $e \sin \omega$ for small eccentricity. We show in Figure A.3 the derived slope m from linear fits of the ratio $(d_s - d_p)/(d_s + d_p) = m \times (e \sin \omega)$ for a grid of summed radii $(R_1 + R_2)/a$ and inclinations i. This graph can be used to estimate m from the preliminary values of $(R_1 + R_2)/a$ and i derived using a circular fit to the light curve. Then $e \sin \omega$ may be estimated from the observed ratio $(d_s - d_p)/(d_s + d_p)$ divided by the slope m from Figure A.3. Note that as the radius sum and inclination decline the slope changes from a positive to negative sign as the relative sizes of the terms for changes in velocity and eclipse path length reverse. Thus, at some point along a constant i curve there occurs $m = 0$, meaning that small changes in $e \sin \omega$ result in no change in eclipse duration. In such a situation $e \sin \omega$ cannot be determined from the equal eclipse durations. We also show as a thin dashed line in Figure A.3 the estimate of m derived from the first order expression (eq. A.17) for the case of $i = 85°$. Comparing this to the more accurate calculation (solid line indicated by $i = 85°$), we see that the first order expression is only adequate over a small range in $(R_1 + R_2)/a$ and can even have the wrong sign in some cases (small $(R_1 + R_2)/a$). Consequently, we recommend the use in practice of the calculations for m shown in Figure A.3 rather than the approximation given in equation A.17.

Listed below is the IDL code `findecc.pro` that may be used to determine estimates of $e \cos \omega$ and $e \sin \omega$ as described above. A subroutine `tkmod.pro` is included therein that calculates the slope term m as a function of $(R_1 + R_2)/a$ and i using equations A.19 and

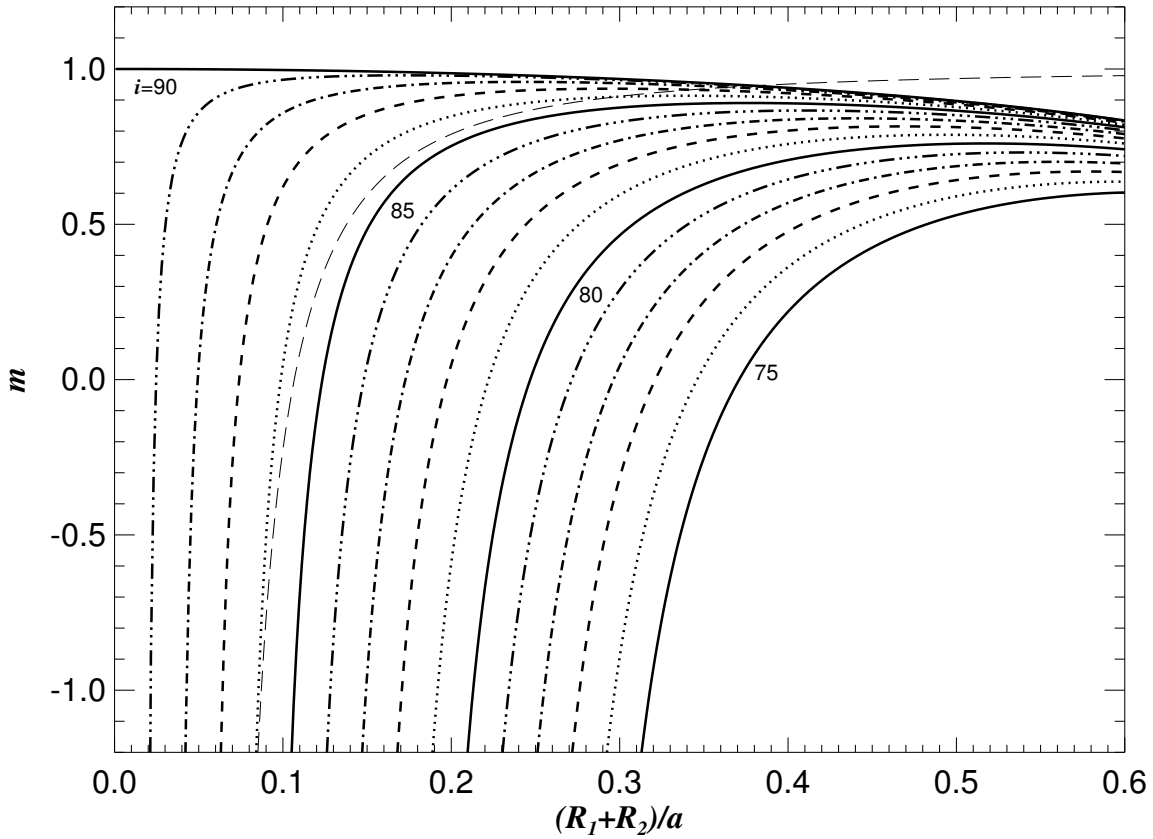

Figure A.3: The variation of the slope m for the relation $\frac{d_s - d_p}{d_s + d_p} = m\, e \sin\omega$. The values of the slope m represent linear fits using equations A.19 and A.20 for small eccentricity for a range in assumed values of the relative sum of the radii $(R_1 + R_2)/a$ and inclination i. Relations for constant i are shown for $i = 75°$ to $i = 90°$ (bottom to top) in steps of 1°. The thin, long-dashed line in the middle represents the first order approximation from equation A.17 for the case of $i = 85°$.

A.20. Our method uses a folded magnitude light curve that is binned in orbital phase. Each eclipse is identified and rescaled into a form with magnitude set to zero in the out-of-eclipse region and one at maximum eclipse depth. Then the eclipse curve is subdivided into 18 depth points at 5% intervals from 0.05 to 0.9, and the eclipse bisector is determined at each depth point. The bisector midpoints are extrapolated to the eclipse core to estimate the phase of

the eclipse, and the bisector widths are extrapolated to the out-of-eclipse level to find the duration of the eclipse. Although this estimate of duration is an underestimate of the actual duration, it is sufficient for use in the difference over sum ratio to find $e \sin \omega$. We caution that the scheme assumes that the stars are spherical, ignoring the tidal distortions that are often present in close binaries. Nevertheless, the method offers useful starting estimates for e and ω for use in light curve modeling programs like ELC.

```
pro findecc,obs,inc,ra,phase,mag
; estimate eccentricity and longitude of periastron
; Input:
; obs    = filename of three column light curve [phase,mag,error]
;          helpful if this is repeated by one cycle in phase
; inc    = assumed inclination [deg]
; ra     = assumed (R_p + R_s)/a
; Output:
; phase  = grid of light curve phases
; mag    = grid of magnitudes for above
;

; Read in lightcurves
; ---------------------------

dummy = dblarr(3)
phase = dblarr(100000)
mag = dblarr(100000)

; If Kepler light curve must convert to phases
; If ELCdataU.fold must add phases 1.0-2.0
; Assume done.

openr,2,obs
k = 0L
while (not eof(2)) do begin

    readf,2,dummy
    phase(k) = dummy(0)
    mag(k) = dummy(1)
    k = k + 1
```

```
endwhile

close,2

phase = phase(0:k-1)
mag = mag(0:k-1)

; User selection of regions
print,' ***Primary Eclipse***'
plot,phase,mag,yrange=[max(mag),min(mag)]
print,' Select starting boundary for primary eclipse ...'
cursor,x1,y & wait,0.5
print,' Select ending boundary for primary eclipse ...'
cursor,x2,y & wait,0.5
gobs=where((phase ge x1) and (phase le x2))
po=phase(gobs)
mo=mag(gobs)

; Fit for phase and duration
pflag=1
fitecl,po,mo,pflag,pmin1,epmin1,dur1,edur1
a=' '
read,' Press return to continue ...',a

; User selection of regions
print,' ***Secondary Eclipse After Primary Eclipse***'
plot,phase,mag,yrange=[max(mag),min(mag)]
print,' Select starting boundary for secondary eclipse ...'
cursor,x1,y & wait,0.5
print,' Select ending boundary for secondary eclipse ...'
cursor,x2,y & wait,0.5
gobs=where((phase ge x1) and (phase le x2))
po=phase(gobs)
mo=mag(gobs)

; Fit for phase and duration
fitecl,po,mo,pflag,pmin2,epmin2,dur2,edur2

; First approximation:
; Calculate e cos w from
; e cos w = pi/2 * (phase shift of sec) - (phase shift of pri)

dshift=pmin2-pmin1-0.5d
ecosw = !pi/2.*dshift
```

```
eecosw= !pi/2.*sqrt(epmin1^2 + epmin2^2)

; eclipse durations

d_pri = dur1
d_sec = dur2

incrad = inc*(!pi/180.)

delta = cos(incrad)/ra
deltasq = delta^2
dratio=(d_sec - d_pri)/(d_sec + d_pri)
dcorr=(2.-deltasq)/(2.-3.*deltasq)
esinw =dratio * dcorr
eesinw=0.5*sqrt(edur1^2+edur2^2)/dur1 * abs(dcorr)

print,' '
print,' First order estimates:'
print,' e*cosw =',ecosw, ' +/- ',eecosw,format='(a,f8.5,a,f7.5)'
print,' e*sinw =',esinw, ' +/- ',eesinw,format='(a,f8.5,a,f7.5)'

;
; Calculate estimated eccentricity and omega (longitude of periastron)
; ---------------------------------------------------------------------

geteo,ecosw,eecosw,esinw,eesinw,ecc,eecc,omega,eomega1,eomega2

; Updated small ecc estimates from Ecc Paper
;-----------------------------------------------
print,' '
print,' Second order estimates:' ; *** revised

; New ecosw estimate to include inc. from Ecc paper
ecosw2 = ecosw/(1 + 0.2828*(cos(incrad))^2)
eecosw2=eecosw/(1 + 0.2828*(cos(incrad))^2)

; Call tkmod to get estimate of m for
; (d_sec - d_pri)/(d_sec + d_pri) = m * e sin w
tkmod,ra,inc,esw,dr,sl
esinw2=dratio/sl
eesinw2=abs(eesinw/dcorr/sl)
print,' e*cosw =',ecosw2, ' +/- ',eecosw2,format='(a,f8.5,a,f7.5)'
print,' e*sinw =',esinw2, ' +/- ',eesinw2,format='(a,f8.5,a,f7.5)'

;
```

```
; Calculate estimated eccentricity and omega (longitude of periastron)
; ---------------------------------------------------------------------

geteo,ecosw2,eecosw2,esinw2,eesinw2,ecc,eecc,omega,eomega1,eomega2

return
end

;;;;;;;;;;;;;;;;;;;;;;;;;;;;;;;;;;;;;;;;;;;;;;;;;;;;;;;;;;;;;;;;;;;;;;;;;;;

pro fitecl,p,m,pflag,pmin,epmin,dur,edur
; Compare an observed and model eclipse
; to determine a phase shift and
; phase expansion/contraction parameter.
; Use with findecc.pro to estimate
; eccentricity and omega.
; This version uses a bisector fits
; to find eclipse center and duration.
;
; Input:
; p      = observed phases around eclipse
; m      = observed magnitude around eclipse
; pflag  = 0 for no plot, 1 for plot
;
; Output:
; pmin   = phase of central eclipse
; epmin  = uncertainty in phase of central eclipse
; dur    = eclipse phase duration
; edur   = uncertainty in eclipse phase duration

; find fitting regions
d1=deriv(p,m)
; check for NaN
xc=finite(d1,/nan)
bad=where(xc eq 1,cnt)
if (cnt gt 0) then begin
   good=where(xc eq 0)
   d1t=interpol(d1(good),p(good),p)
   d1=d1t
   endif
g1=where(d1 gt 0.1*max(d1)) ; entering branch
g2=where(d1 lt 0.1*min(d1)) ; exiting branch

; get local rectification
hw=0.5*(p(max(g2))-p(min(g1))) ; half width
```

```
pc=0.5*(p(max(g2))+p(min(g1))) ; center
; left side points
gl=where((p-pc) lt (-1.1*hw),cnt)
n3=fix(cnt/3.)
n1=0
n2=3*n3-1
pl=rebin(p(n1:n2),3)
ml=rebin(m(n1:n2),3)
  ; right side points
gr=where((p-pc) gt (1.1*hw),cnt)
n3=fix(cnt/3.)
n1=n_elements(p)-3*n3
n2=n_elements(p)-1
pr=rebin(p(n1:n2),3)
mr=rebin(m(n1:n2),3)
mfit=spline([pl,pr],[ml,mr],p)
mr=m-mfit

; normalize
mr=mr/max(mr(min(g1):max(g2)))

; get bisectors and width
depth=findgen(18)/20.+0.05 ; depth points from 0.05 to 0.9
p1=interpol(p(g1),mr(g1),depth) ; fading branch
p2=interpol(p(g2),mr(g2),depth) ; brightening branch
pc=0.5*(p2+p1) ; center
pd=p2-p1 ; width

; fit for center at core
c=poly_fit(depth,pc,1)
pmin=c(0)+c(1)
fit=poly(depth,c)
epmin=stddev(pc-fit)

; test for errors in center estimate
gd1=indgen(6)*3
c1=poly_fit(depth(gd1),pc(gd1),1)
pmin1=c1(0)+c1(1)
gd2=indgen(6)*3+1
c2=poly_fit(depth(gd2),pc(gd2),1)
pmin2=c2(0)+c2(1)
gd3=indgen(6)*3+2
c3=poly_fit(depth(gd3),pc(gd3),1)
pmin3=c3(0)+c3(1)
pmint=[pmin1,pmin2,pmin3]
```

```
epmin=epmin>(max(pmint)-min(pmint))
epmin=epmin>(0.00001)

if (pflag eq 1) then begin
   plot,p,mr,yrange=[1.1,-0.1],ystyle=1
   for i=0,17 do oplot,[p1(i),p2(i)],[depth(i),depth(i)]
   oplot,pc,depth,psym=1
   oplot,[pmin],[1.],psym=4,symsize=2
   endif

; fit for width at 0 = proxy for eclipse duration
c=poly_fit(depth-0.5,pd,2)
dur=c(0)-0.5*c(1)+0.25*c(2)
if (pflag eq 1) then oplot,[-0.5,0.5]*dur+pmin,[-0.05,-0.05],linestyle=1

; test for errors
c1=poly_fit(depth(gd1),pd(gd1),2)
dur1=c(0)-0.5*c(1)+0.25*c(2)
c2=poly_fit(depth(gd2),pd(gd2),2)
dur2=c(0)-0.5*c(1)+0.25*c(2)
c3=poly_fit(depth(gd3),pd(gd3),2)
dur3=c(0)-0.5*c(1)+0.25*c(2)
durt=[dur1,dur2,dur3]
edur=(max(durt)-min(durt))
edur=edur>(0.00001)

print,' Eclipse phase =    ',pmin, ' +/- ',epmin,format='(a,f9.6,a,f9.6)'
print,' Eclipse duration = ', dur, ' +/- ', edur,format='(a,f9.6,a,f9.6)'

return
end

;;;;;;;;;;;;;;;;;;;;;;;;;;;;;;;;;;;;;;;;;;;;;;;;;;;;;;;;;;;;;;;;;;;;;;;;;;;;;;;

pro geteo,ecosw,eecosw,esinw,eesinw,ecc,eecc,omega,eomega1,eomega2
; find eccentricity and omega from e cos omega and e sin omega
; Input:
; ecosw  = e cos omega
; eecosw = uncertainty in above
; esinw  = e sin omega
; eesinw = uncertainty in above
; Output:
; ecc    = eccentricity
; eecc   = uncertainty in above
; omega  = longitude of periastron [deg]
```

```
; eomega1 = +uncertainty in above
; eomega2 = -uncertainty in above

ecc = sqrt(esinw^2+ecosw^2)
eecc=sqrt(esinw^2*eesinw^2 + ecosw^2*eecosw^2)/(ecc>0.000001)

omega = (180./!pi)*atan(esinw,ecosw)
if (omega lt 0.) then omega = omega + 360.
esw=[-1.,0.,1.]*eesinw+esinw
ecw=[-1.,0.,1.]*eecosw+ecosw
om=fltarr(3,3)
for is=0,2 do begin
   for ic=0,2 do begin
      omegat = (180./!pi)*atan(esw(is),ecw(ic))
      if (omegat lt 0.) then omegat = omegat + 360.
      om(is,ic)=omegat
      endfor
   endfor

; check for continuity over positive x-axis
if ((ecosw gt 0.) and (esinw gt 0.) and (eesinw gt esinw))
then om(0,*)=om(0,*)-360.
if ((ecosw gt 0.) and (esinw lt 0.) and (eesinw gt abs(esinw)))
then om(2,*)=om(2,*)+360.
eomega1=max(om)-omega
eomega2=omega-min(om)
if ((eesinw^2+eecosw^2) gt (esinw^2+ecosw^2)) then begin
   eomega1=180.
   eomega2=180.
   endif

print,' ecc   = ',ecc, ' +/- ',eecc,format='(a,f6.4,a,f6.4)'
print,' omega = ',omega,' ^+',eomega1,' _-',eomega2,format='(a,f6.2,a,f6.2,a,f6.2)'

return
end

;;;;;;;;;;;;;;;;;;;;;;;;;;;;;;;;;;;;;;;;;;;;;;;;;;;;;;;;;;;;;;;;;;;;;;;;;;;;

pro tkmod,rsum,incl,esw,dr,sl
; find ratio of difference to sum of eclipse durations
; using expression from Kipping et al. 2010, MNRAS, 407, 301, eq. 15
; Input:
; rsum  = (R_p+R_s)/a
; incl  = inclination (deg)
```

```
; Output:
; esw   = grid of e sin omega values
; dr    = (Ts-Tp)/(Ts+Tp) for esw grid
; sl    = slope in relation dr = sl * (e sin omega)

esw=(findgen(51)-25.)/1000.
inclr=incl/180. * !pi
ci=cos(inclr)
si=sin(inclr)

ecc=sqrt(2.)*esw ; simple estimator
rp=(1.-ecc^2)/(1.+esw)
rs=(1.-ecc^2)/(1.-esw)
bp=asin(sqrt((rsum^2-rp^2*ci^2)>0.)/(rp*si))
bs=asin(sqrt((rsum^2-rs^2*ci^2)>0.)/(rs*si))
tp=(rp^2*bp)/(sqrt(1.-ecc^2)*!pi )
ts=(rs^2*bs)/(sqrt(1.-ecc^2)*!pi )
dr=(ts-tp)/(ts+tp)
gp=where((rsum^2-rp^2*ci^2) lt 0.,cntp)
gs=where((rsum^2-rs^2*ci^2) lt 0.,cnts)
nesw=n_elements(esw)
if (cntp gt 0) then print,' No pri ecl at ',esw(gp)
if (cnts gt 0) then print,' No sec ecl at ',esw(gs)
g=where(((rsum^2-rp^2*ci^2) ge 0.) and ((rsum^2-rs^2*ci^2) ge 0.), cnt)
if (cnt gt 2) then c=poly_fit(esw(g),dr(g),1) else c=[0.,0.]
sl=c(1)

return
end

;;;;;;;;;;;;;;;;;;;;;;;;;;;;;;;;;;;;;;;;;;;;;;;;;;;;;;;;;;;;;;;;;;;;;;;;

pro tkgrid,rsum,incl,slope
; form grid of slope terms over rsum and inclination
slope=fltarr(500,16)
rsum=(findgen(500)+0.5)/500.*0.80
incl=findgen(16)+75.
for iincl=0,15 do begin

   for jrsum=0,499 do begin

      tkmod,rsum(jrsum),incl(iincl),esw,dr,sl
      slope(jrsum,iincl)=sl

      endfor
```

```
   endfor

return
end

;;;;;;;;;;;;;;;;;;;;;;;;;;;;;;;;;;;;;;;;;;;;;;;;;;;;;;;;;;;;;;;;;;;;;;;;;;;;

pro tkplot,rsum,incl,slope
; make a plot of the slope dependence

tkgrid,rsum,incl,slope
set_plot,'ps'
device,filename='tkplot.eps',/landscape,/encapsulated
!x.thick=2
!y.thick=2
!p.thick=2
!p.charsize=1.5
!p.font=0

ci=cos(incl/180.*!pi)
ls=[0,1,2,3,4,0,1,2,3,4,0,1,2,3,4,0]
plot,rsum,slope(*,0),xrange=[0.,0.6],yrange=[-1.2,1.2],/nodata,$
   xtitle='!8(R!D1!N+R!D2!N)/a!3',ytitle='!8m!3',xstyle=1,ystyle=1
for i=0,15 do begin
   g=where((slope(*,i) ne 0.),cnt)
   if (cnt gt 1) then oplot,rsum(g),slope(g,i),linestyle=ls(i),thick=5
   endfor

xyouts,0.012, 0.92,'!8i!3=90',size=1
xyouts,0.164, 0.52,'85',size=1
xyouts,0.276, 0.25,'80',size=1
xyouts,0.380,0.,'75',size=1

; example of simple approximation for i=85 deg
inclr=85./180.*!pi
ci=cos(inclr)
si=sin(inclr)
eps=ci/rsum
ss=(2.-3.*eps^2)/(2.-eps^2)
g=where(eps^2 lt 2.)
oplot,rsum(g),ss(g),linestyle=5,thick=0.3
device,/close
set_plot,'x'
```

```
return
end
```

APPENDIX B

Measuring Radial Velocities of *Kepler* Eclipsing Binaries

This appendix gives an overview of the procedures used to measure radial velocities for the eclipsing binaries in our sample. Section B.1 contains the IDL code `runRV.pro` which runs several subroutines to estimate spectroscopic parameters from the light curve parameters of Slawson et al. (2011), obtain synthetic spectra for the primary and secondary, perform double cross-correlation to measure the radial velocities, and fit a preliminary spectroscopic orbit. The cross-correlation procedure `makecctwo.pro` is given in Section B.2, where more details of its use are provided.

B.1 Radial Velocity Analysis Overview

The IDL procedure `runRV.pro` reads in a variety of parameters (via `readslawson.pro`) and employs subroutines to estimate radial velocities (`orbest.pro`) and trial velocity separations (via the fortran code `sbcm`) for cross-correlation, as well as to obtain and transform synthetic spectra to the observer's grid from the UVBLUE grid of high resolution model spectra (`sptrans.pro`), which includes the ranges $T_{\rm eff} = 3000, 15000\,{\rm K}$ ($\Delta = 500\,{\rm K}$), $\log g = 0.0, 0.5$ ($\Delta = 0.5\,{\rm dex}$), and $\log Z = -2.0, 0.5$ ($\Delta = 0.5$ dex). The procedure also lets the user specify regions of a spectrum, such as broad Balmer lines or interstellar features, to be replaced with continuum for the calculation of cross-correlation functions (CCFs). The cross-correlations between composite model spectra and the observed spectra are then carried out in `makecctwo.pro` (see next section), deriving radial velocities of both stellar components. Finally, a preliminary orbital fit determines spectroscopic orbital parameters

for both components. The fit is then examined and `sbcm` rerun manually, adjusting fixed and fitted parameters such as the eccentricity and systemic velocity, or omitting suspect velocities as necessary.

```
pro runRV,star,zp,ezp,zs,ezs
;
; Procedure to perform Radial Velocity Analysis for Kepler targets
; in double-lined spectroscopic binaries (R. Matson 4/2016)
;
; Assumes spectroscopic observations have been reduced, rectified, and
; collected in spectrum stacks binned on a log wavelength scale located
; in the current directory (e.g., K2305372.dat and K2305372.fits)
;
;
; Inputs:  star = string with KIC number of star to be analyzed
;
; Outputs: zp = radial velocities of the primary component
;          ezp = radial velocity errors of the primary component
;          zs = radial velocities of the secondary component
;          ezs = radial velocity errors of the secondary component
;
;

; Get eclipsing binary parameters from table of light curve (LC)
; results of Slawson et al. 2011. Returns: T_0, P, e sin omega,
; e cos omega, sin i, T_1, and T_2/T_1 in ebpar

readslawson,star,ebpar

stkfile = 'K'+strtrim(star,1)

; Use LC parameters in ebpar to estimate spectroscopic parameters.
;  Returns: V_0, K, e, omega, T(max V_r), and p for the pri and sec
;                  in sbpri/sbsec for preliminary orbits
;  Returns: Teff, log g, v sin i, linear limb darkening coeffs, instrumental
;                  broadening FHWM, dlambda/c for log wave grid, # of points
;                  in log wave grid, and starting wave in grid for the primary
;                  and secondary in sppri/spsec for spectral templates

orbest,stkfile,ebpar,sbpri,sbsec,sppri,spsec,fratio
;sbpri/sbsec = inputs for sbcm
```

```
;sppri/spsec = inputs for sptrans

; Option to manually update temperatures and get new parameter estimates

tpans = 'n'
read,' '
read,'Adjust temps (y/[n])? ',tpans

if tpans eq 'y' then begin
   read,'Enter new T1, T2 = ',nt1,nt2
   ebpar(5) = nt1
   ebpar(6) = nt2/nt1
   print,'Updated temps = ',ebpar(5),'',ebpar(6)*ebpar(5)
   print,''
   print,'Re-running orbest: '
   orbest,stkfile,ebpar,sbpri,sbsec,sppri,spsec,fratio

endif

; Option to manually update the flux ratio (used once an improved
; flux ratio was determined by finding the maximum cross-correlation
; peaks over a grid of flux ratios in findfrcc.pro)

frans = 'n'
read,' '
read,'Adjust fratio (y/[n])? ',frans

if frans eq 'y' then begin
   read,'Enter new flux ratio = ',fr
   fratio = fr
   print,'Updated fratio = ',fratio
endif

; Options to read in updated T_0 and P from Gies et al. 2015,
; adjust T_0 to phase of maximum velocity (T_0 + 0.75*P), and
; set e & omega to 0 to fit a circular orbit if desired

giesans = 'y'
read,'Get P and T0 from Gies et al. 2015? ([y]/n)',giesans
if giesans eq 'y' then begin

readcol,'~rmatson/research/Binaries/Pros/KeplerRV/Gies2015_EBpar.txt', $
kic,int,ext,t0,te,p,format='A,A,A,D,A,D'

kictest = strmid(kic,0,1)
```

```
for i = 0,81 do begin
    if (kictest(i) eq '0') then begin
kic(i) = strmid(kic(i),1,7)
    endif else begin
kic(i) = strmid(kic(i),0,8)
    endelse
endfor

g = where (kic eq star)

tzerop = t0(g(0))+(0.75*p(g(0)))
tzeros = t0(g(1))+(0.75*p(g(1)))
sbpri(4) = tzerop
sbpri(5) = p(g(0))
sbsec(4) = tzeros
sbsec(5) = p(g(1))
endif

eom = 'n'
read,'Set e & omega to zero (y/[n])? ',eom
if eom eq 'y' then begin
    sbpri(2) = 0.0
    sbpri(3) = 0.0
    sbsec(2) = 0.0
    sbsec(3) = 0.0
endif

; Print estimated spectroscopic parameters to screen & file
print,sbpri,sbsec
print,sppri,spsec

openw,1,'ccparms.dat'
printf,1,sbpri
printf,1,sbsec
printf,1,sppri
printf,1,spsec
printf,1,'fratio = ',fratio
close,1

; Create files for (via makesbcm.pro) and run orbital fitting procedure
; sbcm to predict radial velocities for estimating velocity separations
; of composite spectra for use in cross-correlations

makesbcmin,stkfile,sbpri,sbsec
```

```
print,'Running sbcm for the primary...'
spawn,'cp sbcm.in.pri sbcm.in'
spawn,'~gies/Fortran/Orbits/sbcm'
spawn,'cp sbcm.out sbcm.out.pri'

colorset
window,0,xsize=1000,ysize=800

; Get synthetic spectrum from UVBLUE grid for the primary, transform to
; observer's grid (via sptrans.pro) and save file, then plot for visual inspection

read,'Getting model templates... '
sptrans,sppri,'model.pri',lambda,fm
plot,lambda,fm
wait = ''
print,'Model spectra for primary'
read,'Hit enter to continue...',wait

; Get synthetic spectrum from UVBLUE grid for the secondary, transform to
; observer's grid (via sptrans.pro) and save file, then plot for visual inspection

sptrans,spsec,'model.sec',lambda2,fm2
plot,lambda2,fm2
wait = ''
print,'Model spectra for secondary'
read,'Hit enter to continue...',wait

; Read in spectrum stack and review spectra

readstk,w,ss,t,stkfile,origin

revans = 'y'
read,'Review stack for problems in spectra ([y]/n)? ',revans

if revans  eq 'y' then begin

again = 'y'
repeat begin
   for i = 0,n_elements(t)-1. do begin
      plot,ss(*,i) & wait,1
   endfor
   read,'Repeat? ',again
endrep until again eq 'n'

endif
```

```
; Make file (ccomit.dat) with regions to be omitted for cross correlation
; (i.e., select regions with wide Balmer lines to be omitted)

ans='n'
read,'Use current ccomit.dat file (y/[n])? ',ans

if ans eq 'n' then begin
   read,'Spectrum for omit regions: ',omit

   plot,ss(*,omit)

   no = 0.
   read,'Number of regions to omit for cross correlation? ',no

   openw,1,'ccomit.dat'
   printf,1,no
   read,'Select regions to omit:'

   for i = 0,no-1. do begin
      cursor,xa,y & print,xa & wait,1
      cursor,xb,y & print,xb & wait,1
      if xa lt 0. then xa = 0.
      if xb gt 1733. then xb = 1732.
      printf,1,xa,xb
   endfor

   close,1

endif

; Set variables for synthetic spectra files and estimated orbital parameters
rfp = 'model.pri.fits'
rfs = 'model.sec.fits'
sbp = 'sbcm.out.pri'
sbs = 'sbcm.out.sec'

; Perform cross-correlation of stacked spectra (w,ss) against model spectra
; (rfp,rfs) using estimated flux ratio (fratio) and estimated velocity separations
; (sbp, sbs). Returns the velocity vector for ccfs (vel), matrix of ccfs (cc),
; offset ccf maxima (ccfmax), ccf maxima to measure goodness of fit (ccftop),
; and velocities and errors for the primary (zp, ezp) and secondary (zs,ezs).

makecctwo,w,ss,rfp,rfs,fratio,sbp,sbs,nfit,vel,cc,ccfmax,ccftop,zp,ezp,zs,ezs
print,'Primary velocities: ',zp
```

```
print,'Secondary velocities: ',zs
print,' '
print,'Fratio = ',fratio
print,'Max ccf values: ',ccftop
print,'Average ccfmax = ',mean(ccftop)
print,stkfile

; Create input files for spectrosocpic orbital fit and run sbcm

makesbcmin,stkfile,sbpri,sbsec,zp,ezp,zs,ezs

print,'Running sbcm for the primary...'
spawn,'cp sbcm.in.pri sbcm.in'
spawn,'~gies/Fortran/Orbits/sbcm'
spawn,'cp sbcm.out sbcm.out.pri'

print,'Running sbcm for the secondary...'
spawn,'cp sbcm.in.sec sbcm.in'
spawn,'~gies/Fortran/Orbits/sbcm'
spawn,'cp sbcm.out sbcm.out.sec'

end
```

Additional programs referenced in `runRV.pro` that are given in Section B.2:

```
@/nfs/morgan/users/rmatson/research/Binaries/Pros/KeplerRV/makecctwo.pro
@/nfs/morgan/users/rmatson/research/Binaries/Pros/KeplerRV/readsbcm.pro
@/nfs/morgan/users/rmatson/research/Binaries/Pros/KeplerRV/readstk.pro

;Also compile to run manually for final fitted orbit...
@/nfs/morgan/users/rmatson/research/Binaries/Pros/psbcm2residerr.pro
;(Plot radial velocities and orbital fit of both components)
@/nfs/morgan/users/rmatson/research/Binaries/Pros/sbcm2latex_printall.pro
;(Print velocities, errors, and O-C residuals from fit in latex form)
@/nfs/morgan/users/rmatson/research/Binaries/Pros/KeplerRV/sbcm2err.pro
;(Calculate errors on  M_1 sin^3 i and M_2 sin^3 i and calculate M_1, M_2, a
; if inclination is available)

;;;;;;;;;;;;;;;;;;;;;;;;;;;;;;;;;;;;;;;;;;;;;;;;;;;;;;;;;;;;;;;;;;;;;;;;;;;

pro orbest,stkfile,ebpar,sbpri,sbsec,sppri,spsec,fratio

; estimate spectroscopic parameters from
; light curve parameters
```

```
; Input:
; stkfile  = name of (path and) root name for spectrum stack
; For ebpar, use readslawson.pro to read the
; following parameters for a given target.
; ebpar    = dblarr(7)
; ebpar(0) = T(BJD-2400000.) for primary minimum
; ebpar(1) = P, period
; ebpar(2) = e sin omega
; ebpar(3) = e cos omega
; ebpar(4) = sin i, sin(inclination)
; ebpar(5) = T1, Teff primary
; ebpar(6) = T2/T1
;
; Output: for sbcm
; sbpri    = dblarr(6)
; sbpri(0) = V_0 = 0 for now
; sbpri(1) = K_1
; sbpri(2) = e
; sbpri(3) = omega + 180
; sbpri(4) = T(peri) or T(max V_r)
; sbpri(5) = P
; sbsec    = dblarr(6)
; sbsec(0) = V_0 = 0 for now
; sbsec(1) = K_2
; sbsec(2) = e
; sbsec(3) = omega
; sbsec(4) = T(peri) or T(max V_r)
; sbsec(5) = P
;
; Output: for sptrans
; sppri    = dblarr(8)
; sppri(0) = teff  = effective temperature
; sppri(1) = logg  = log gravity
       ; sppri(2) = vsini = v sin i in km/s
       ; sppri(3) = eps   = linear limb darkening coefficient
; sppri(4) = fwhm  = instrumental broadening FHWM (km/s)
; sppri(5) = dl    = dlambda/c for log wave grid
; sppri(6) = nl    = number of points for log wave grid
; sppri(7) = wave0 = starting wavelength for log wave grid
; spsec    = dblarr(8)
; spsec(0) = teff  = effective temperature
; spsec(1) = logg  = log gravity
       ; spsec(2) = vsini = v sin i in km/s
       ; spsec(3) = eps   = linear limb darkening coefficient
; spsec(4) = fwhm  = instrumental broadening FHWM (km/s)
```

```
; spsec(5) = dl    = dlambda/c for log wave grid
; spsec(6) = nl    = number of points for log wave grid
; spsec(7) = wave0 = starting wavelength for log wave grid
;
; Additional output:
; fratio   = F_2 / F_1 = flux ratio

sbpri=dblarr(6)
sbsec=dblarr(6)

; eccentricity
ecc=sqrt(ebpar(2)^2 + ebpar(3)^2)
sbpri(2)=ecc
sbsec(2)=ecc

; omega
omega=atan(ebpar(2),ebpar(3))
if (omega lt 0.) then omega=omega+2.*!pi

; period
sbpri(5)=ebpar(1)
sbsec(5)=ebpar(1)

; masses
teffs=[ebpar(5),ebpar(5)*ebpar(6)]
openr,1,'/nfs/morgan4/gies/Kepler/RV/lsmassteff.dat'
; mass, Teff, radius
d=fltarr(3,358)
readf,1,d
close,1
mass=interpol(d(0,*),d(1,*),teffs)
mtot=total(mass)
q=mass(1)/mass(0)

; estimate K
pyr=365.2421988d ; year in days
au=1.495978715d8 ; AU in km
dsec=24.*3600.   ; seconds per day
psec=ebpar(1)*dsec
a=(mtot*(ebpar(1)/pyr)^2)^(1./3.) *au ; semimajor axis in km
k=2.*!pi *a*ebpar(4)/psec/sqrt(1.-ecc^2)
sbpri(1)=k*q/(1.+q)
sbsec(1)=k/(1.+q)

; estimate epoch and longitude of periastron
```

```
if (ecc eq 0.) then begin       ; circular orbit case
   sbpri(4)=ebpar(0)+0.75*ebpar(1)
   sbsec(4)=ebpar(0)+0.25*ebpar(1)
   endif else begin             ; eccentric orbit case
      sbpri(3)=omega
      sbsec(3)=omega+!pi
      if (sbsec(3) gt 2.*!pi ) then sbsec(3)=sbsec(3)-2.*!pi
      nuecl=0.5*!pi - omega
      if (nuecl lt 0.) then nuecl=nuecl+2.*!pi
      trueanomaly,ecc,[nuecl],phecl
      sbpri(4)=ebpar(0)-phecl(0)*ebpar(1)
      sbsec(4)=ebpar(0)-phecl(0)*ebpar(1)
      endelse

; Print useful parameters
print, ' Teff estimates = ',teffs
print, ' Mass estimates = ',mass
radius=interpol(d(2,*),d(1,*),teffs)
print, ' Radius estimates = ',radius
logg=4.43775+alog10(mass)-2.*alog10(radius)
print, ' log g  estimates = ',logg
wave=4311. ; Angstroms
fratio=planck(wave,teffs(1))/planck(wave,teffs(0))
fratio=fratio*(radius(1)/radius(0))^2
print, ' Flux ratio = ',fratio
vsini=50.634*radius*ebpar(4)/ebpar(1)
print, ' V sin i = ',vsini
; limb darkening from Wade and Rucinski fot T>5200
; and from Claret 2011 for T<5200
teps=[3.5,4.0,4.5,5.0,5.5,6.0,6.5,7.0,7.5,8.0,8.5,9.0,9.5]
eps =[713,803,897,854,827,749,691,641,583,523,618,564,527]
teps=[teps,10.0,10.5,11.0,11.5,12.0,12.5,13.0,14.0,15.0]
eps =[ eps, 500, 477, 461, 446, 433, 421, 409, 393, 379]
teps=[teps,16.0,17.0,18.0,20.0,22.5,25.0,30.0]*1000.
eps =[ eps, 369, 360, 353, 340, 322, 302, 282]
eps =float(eps)/1000.
epss=interpol(eps,teps,teffs)
print,' Linear limb darkening coefficients (4311 Angstroms) = ', epss

; Create parameter vectors for sptrans
readstk,wave,stk,times,stkfile
nl=n_elements(wave)
dl=(alog10(wave(nl-1))-alog10(wave(0)))*alog(10.)/(nl-1.)
fwhm=2.5*dl*2.997925d5 ; assume FWHM = 2.5 pixels
```

```
sppri = dblarr(8)
sppri(0) = teffs(0)
sppri(1) = logg(0)
        sppri(2) = vsini(0)
        sppri(3) = epss(0)
sppri(4) = fwhm     ; instrumental broadening FHWM (km/s)
sppri(5) = dl       ; dlambda/c for log wave grid
sppri(6) = nl       ; number of points for log wave grid
sppri(7) = wave(0)  ; starting wavelength for log wave grid

spsec = dblarr(8)
spsec(0) = teffs(1)
spsec(1) = logg(1)
        spsec(2) = vsini(1)
        spsec(3) = epss(1)
spsec(4) = fwhm     ; instrumental broadening FHWM (km/s)
spsec(5) = dl       ; dlambda/c for log wave grid
spsec(6) = nl       ; number of points for log wave grid
spsec(7) = wave(0)  ; starting wavelength for log wave grid

return
end

;;;;;;;;;;;;;;;;;;;;;;;;;;;;;;;;;;;;;;;;;;;;;;;;;;;;;;;;;;;;;;;;;;;;;;;;;;;;;;;

        pro trueanomaly,e,nu,ph
        ;returns ph=phases for nu=true anomaly

        n=n_elements(nu)
        add=fltarr(n)
        newquad=where(nu ge !pi,count)
        if (count gt 0) then add(newquad)=!pi
        p1=tan(nu/2.)
        p1=p1*sqrt((1.-e)/(1.+e))
        p1=2.*(atan(p1)+add)
        p2=e*sqrt(1.-e^2)*sin(nu)/(1.+e*cos(nu))
        ph=(p1-p2)/(2.*!pi)
        return
        end

;;;;;;;;;;;;;;;;;;;;;;;;;;;;;;;;;;;;;;;;;;;;;;;;;;;;;;;;;;;;;;;;;;;;;;;;;;;;;;;

pro readslawson,kidin,ebpar,kid,t0,p,teff,logg,contam, $
                    tratio,sumrad,ecc,omega,incldeg
; read in data on eclipsing binaries from the catalog of
```

```
; Slawson et al. 2011AJ....142..160S
;
; Input:
; kidin  = Kepler input catalog number for star of interest
;
; Output:
; ebpar  = eclipsing binary parameters for use with orbest.pro
; [remaining params optional, useful for target selection]
; kid    = Kepler identification number
; t0     = epoch of primary eclipse (BJD-2400000)
; p      = period (d)
; teff   = effective temperature of primary
; logg   = log g of primary
; contam = contamination param (blending with nearby objects)
; tratio = T_2 / T_1
; sumrad = (R_1 + R_2)/a
; ecc    = eccentricity
; omega  = longitude of periastron of primary
; incldeg= orbital inclination in degrees

n=1423  ; detached and semidetached

kid   =dblarr(n)
t0    =dblarr(n)
p     =dblarr(n)
type  =intarr(n)
teff  =fltarr(n)
logg  =fltarr(n)
contam=fltarr(n)
tratio=fltarr(n)
sumrad=fltarr(n)
esinom=fltarr(n)
ecosom=fltarr(n)
sininc=fltarr(n)

openr,1,'~rmatson/research/Binaries/Pros/KeplerRV/slawson.txt'
a=' '
for i=1,45 do readf,1,a

for i=0,n-1 do begin
   readf,1,a
   kid(i)=double(strmid(a,0,11))
   t0(i) =double(strmid(a,12,12))
   p(i)  =double(strmid(a,25,11))
   dsd=strmid(a,38,2)
```

```
   if (dsd eq 'SD') then type(i)=1
   test=strmid(a,53,5)
   if (test ne '     ') then teff(i)=float(test)
   test=strmid(a,59,5)
   if (test ne '     ') then logg(i)=float(test)
   test=strmid(a,74,5)
   if (test ne '     ') then contam(i)=float(test)
   test=strmid(a,80,7)
   if (test ne '       ') then tratio(i)=float(test)
   test=strmid(a,88,7)
   if (test ne '       ') then sumrad(i)=float(test)
   test=strmid(a,104,8)
   if (test ne '        ') then esinom(i)=float(test)
   test=strmid(a,113,8)
   if (test ne '        ') then ecosom(i)=float(test)
   test=strmid(a,131,7)
   if (test ne '       ') then sininc(i)=float(test)
   endfor
close,1

; eccentricity
ecc=sqrt(esinom^2 + ecosom^2)

; omega
omega=atan(esinom,ecosom)
g=where(omega lt 0.,cnt)
if (cnt gt 0) then omega(g)=omega(g)+2.*!pi

; inclination
incl=asin(sininc<1.)
incldeg=180.*incl/!pi

; selection criteria
g=where(kid eq kidin,cnt)
if (cnt lt 1) then print, ' Target not found' else begin
   ebpar=dblarr(7)
   ebpar(0)=t0(g(0))
   ebpar(1)=p(g(0))
   ebpar(2)=esinom(g(0))
   ebpar(3)=ecosom(g(0))
   ebpar(4)=sininc(g(0))
   ebpar(5)=teff(g(0))
   ebpar(6)=tratio(g(0))
   endelse
```

```
; ebpar    = dblarr(7)
; ebpar(0) = T(BJD-2400000.) for primary minimum
; ebpar(1) = P, period
; ebpar(2) = e sin omega
; ebpar(3) = e cos omega
; ebpar(4) = sin i, sin(inclination)
; ebpar(5) = T1, Teff primary
; ebpar(6) = T2/T1

return
end

;;;;;;;;;;;;;;;;;;;;;;;;;;;;;;;;;;;;;;;;;;;;;;;;;;;;;;;;;;;;;;;;;;;;;;;;;;;;;;;

pro makesbcmin,stkfile,sbpri,sbsec,zp,ezp,zs,ezs
; create sbcm.in files for stack and
; preliminary elements from orbest.pro.
; Also may be used to create input files for fits
; if last four parameters used in call to procedure.
; Assumes nominal weights from errors and fits only
; for gamma = systemic velocity and K = semiamplitude.

; Input:
; stkfile = root name of spectrum stack
; sbpri   = primary orbital parameters from orbest.pro
; sbsec   = secondary orbital parameters from orbest.pro
; [optional parameters to add measured velocities]
; zp      = velocities for primary
; ezp     = uncertainties in above
; zs      = velocities for secondary
; ezs     = uncertainties in above
;
; Output:
; files sbcm.in.pri and sbcm.in.sec

readstk,w,ss,t,stkfile
nsp=n_elements(t)
vp=fltarr(nsp)
wp=fltarr(nsp)+1.
vs=fltarr(nsp)
ws=fltarr(nsp)+1.

npar=N_PARAMS()

if (npar gt 3) then begin
```

```
   ;  Fit for gamma, K using measured velocities
   vp=zp
   wp=1./ezp^2
   mwp=mean(wp)
   wp=wp/mwp
   vs=zs
   ws=1./ezs^2
   mws=mean(ws)
   ws=ws/mws
   endif

openw,1,'sbcm.in.pri'
printf,1,' Preliminary elements for primary'
printf,1,' 0 0 0'
if (npar eq 3) then printf,1,'000000000000' else printf,1,'010100000000'
printf,1,sbpri,format='(4d10.5,d12.4,d12.6)'
for i=0,nsp-1 do printf,1,t(i)-2400000.d,vp(i),wp(i),format='(d12.4,2f8.2)'
printf,1,0.,0.,0.,format='(d12.4,2f8.2)'
close,1

openw,1,'sbcm.in.sec'
printf,1,' Preliminary elements for secondary'
printf,1,' 0 0 0'
if (npar eq 3) then printf,1,'000000000000' else printf,1,'010100000000'
printf,1,sbsec,format='(4d10.5,d12.4,d12.6)'
for i=0,nsp-1 do printf,1,t(i)-2400000.d,vs(i),ws(i),format='(d12.4,2f8.2)'
printf,1,0.,0.,0.,format='(d12.4,2f8.2)'
close,1

return
end

;;;;;;;;;;;;;;;;;;;;;;;;;;;;;;;;;;;;;;;;;;;;;;;;;;;;;;;;;;;;;;;;;;;;;;;;;;;;;;;;

pro sptrans,sppar,fileout,lambda,fm
; read in optical line spectrum from UVBLUE
; and transform to observer's grid

; Input:
; sppar = dblarr(8)
; sppar(0) = teff  = effective temperature
; sppar(1) = logg  = log gravity
        ; sppar(2) = vsini = v sin i in km/s
        ; sppar(3) = eps   = linear limb darkening coefficient
; sppar(4) = fwhm  = instrumental broadening FHWM (km/s)
```

```
; sppar(5) = dl    = dlambda/c for log wave grid
; sppar(6) = nl    = number of points for log wave grid
; sppar(7) = wave0 = starting wavelength for log wave grid
; fileout  = name of output file with spectrum (string variable)

; Output:
; lambda   = wavelength grid
; fm       = model spectrum
; FITS file named fileout.fits

teff  = sppar(0)
logg  = sppar(1)
        vsini = sppar(2)
        eps   = sppar(3)
fwhm  = sppar(4)
dl    = sppar(5)
nl    = sppar(6)
wave0 = sppar(7)

; get data for Teff, log g on standard grid
fluxinterpolate,teff,logg,0.,w,s
binlog,w,s,dl,nl,wave0,lambda,f ; log grid

; convolve for rotational broadening
dvel=dl*2.997925d5
if (vsini le 10.) then frot=f else begin
           broadg,dvel,vsini,eps,grot
   ngrot=n_elements(grot)
   ff=[fltarr(ngrot)+1.,f,fltarr(ngrot)+1.]
   frot=convol(ff,grot)
   frot=frot(ngrot:ngrot+nl-1)
   endelse

; convolve for instrumental broadening
fwhmpix=fwhm/dvel
gsmooth,frot,fm,fwhmpix

; rectify again with a linear fit
g=indgen(nl)
for j=1,3 do begin ; iterative deletion of low points
   c=poly_fit(lambda(g),fm(g),1)
   fit=poly(lambda,c)
   res=fm-fit
   g=where(res gt -0.01)
   endfor
```

```
fm=fm/fit

; write results
writefits,fileout+'.fits',fm

return
end

@/nfs/morgan/users/rmatson/research/Binaries/Pros/KeplerRV/binlog.pro
@/nfs/morgan/users/rmatson/research/Binaries/Pros/KeplerRV/broadg.pro
@/nfs/morgan/users/rmatson/research/Binaries/Pros/KeplerRV/gsmooth.pro
@/nfs/morgan/users/rmatson/research/Binaries/Pros/KeplerRV/fluxinterpolate.pro
@/nfs/morgan/users/rmatson/research/Binaries/Pros/KeplerRV/readUVBLUE.pro

;;;;;;;;;;;;;;;;;;;;;;;;;;;;;;;;;;;;;;;;;;;;;;;;;;;;;;;;;;;;;;;;;;;;;;;;;;;;;;;;;;;;;;;;
```

B.2 Cross-Correlation Procedures

Radial velocities were measured using the IDL code `makecctwo.pro`, which is given below. This procedure calculates a series of test cross-correlation functions using trial velocity separations for the primary and secondary components around the predicted separation, which was determined from a preliminary orbital fit based on the spectroscopic parameters estimated from the light curve (via `makesbcmin` and `sbcm` in `runRV.pro`, see Section B.1). We omit regions of the spectrum with broad absorption lines or where data do not exist due to the smaller wavelength ranges in Lowell and DAO spectra. To smooth the edges created by omitting portions of the spectrum we used a Tukey or tapered cosine window (`tukey.pro`, `tukeywindow.pro`). The program then determines cross-correlation functions (`crosscoresb2.pro`) for 35 trial separations, and plots the peak CCF strength as a function of offset. The optimal separation is selected from the apex of the CCF strength vs. offset plot using the IDL `deriv` function. The adopted separation is then used to compute a final

CCF to determine the absolute position of the primary and secondary. This entire procedure is repeated for each spectrum.

```
pro makecctwo,w,ss,rfp,rfs,fr,sbp,sbs,vel,cc,pixo,ccfmax,ccftop,zp,ezp,zs,ezs
; Calculate cross-correlation functions.
; Use entire spectrum but blank-out problem regions
; from input file.
;
; Input:
;       w    = wavelength grid
;       ss   = stacked spectrum (from rdstk)
;       rfp  = name of reference spectrum for primary
;       rfs  = name of reference spectrum for secondary
;       fr    = flux ratio F2/F1
;       sbp  = sbcm.out file for primary
;       sbs  = sbcm.out file for secondary
; Output:
;       vel  = velocity vector for cc functions
;       cc   = matrix of cc function (401,n_spectra)
;       ccfmax = matrix of offset ccf maxima (34,n_spectra)
;       ccftop = vector of ccf maxima (n_spectra) to measure goodness of fit
;       zp   = vector of primary velocities
;       ezp  = vector of primary velocity errors
;       zs   = vector of secondary velocities
;       ezs  = vector of secondary velocity errors
; Version: 1 March 93 (Gies, Penny, Thaller)
; Revision: June 5, 2006 by Gies.  Change to dvel:
;   Program was designed for log wavelength input.
;   Linear wavelength input can be used with caution.
;   Program defines effective dvel = delta(lambda)/lambda*c
;   from pixels that are NOT blanked-out in the ccomit ranges.
;   Since lines to be measured are in the non-blanked-out regions,
;   this will be satisfactory for one line or lines of comparable strength.
; Version: 25 September 2011 (Gies)
;   makecctwo is for SB2 systems and uses two templates for pri, sec
; Version: 07 August 2012 (Gies)
;   Corrected bug with error estimates.
; Version: 03 June 2016 (Gies)
;   Matson version with more offset positions
; Version: 17 June 2016 (Gies)
;   Added tukey window function to smooth the omit regions
; Version: 23 June 2016 (Gies)
;   Background subtraction option for secondary velocity errors.
```

```
;   Takes lesser of standard and Kurtz et al. 1992 sec. error estimates.
;   Uses IDL deriv for maximum, so no need for nfit.
   ;   Adopted smp=100 pixels for transition regions to minimize
;   systematic effects.
; Version: 06 July 2016 (Gies)
;   Background from ccf minima rather than local fit difference.
;   This produces more realistic errors.

; Get list of blank regions
; blank=0.
blankans=' '
print,' *** CROSS CORRELATION FUNCTIONS ***'
nw=long(n_elements(w))
read,' Omit problem regions listed in a file (y or [n])? ', blankans
if (blankans eq 'y') then begin
   blankf=' '
   read,' Name of file with problem regions? ', blankf
   openr,1,blankf
   readf,1,nblank
   nblank=fix (nblank)
   blank=lonarr(2,nblank) ; starting, ending pixels to blank
   readf,1,blank
   close,1
   ; blank=blank+200   ; account for padding of first 200 points
   smp=100. ; trial smoothing size for window edge
   tukeywindow,blank,nw,smp,ww
   endif

; get good pixels in original grid
;nw=long(n_elements(w))
;goodw=findgen(nw)
;if (blankans eq 'y') then begin
;   blankspec=fltarr(nw)
;   blanko=blank-200  ; original
;   for j=0,nblank-1 do blankspec(blanko(0,j):blanko(1,j))=1.0
;   goodw=where(blankspec eq 0.)
;   endif

; get velocity increments
; check for linear or log increments
dw=deriv(w)
if (abs(dw(nw-2)-dw(1)) gt 0.01) then begin
   ; log scale
   dloglam=mean(deriv(alog10(w)))
   dvel=dloglam*alog(10.)*2.997925E5
```

```
   print,' Velocity increment = ',dvel,' km/s'
   endif else begin
      ; linear scale
      print,' Warning: using linear wavelength scale and average
                wavelength for velocity step.'
      wav=mean(w(goodw))
      dwav=mean(dw(goodw))
      dvel=dwav/wav*2.997925E5
      print,' Velocity increment = ',dvel,' km/s'
      endelse

; Set up vectors and matrix
vel=dvel*(findgen(401)-200.)
nsp=n_elements(ss(0,*))
cc=fltarr(401,nsp)
ccfmax=fltarr(35,nsp) ;11*17
ccfmin=fltarr(35,nsp) ;11*17
zero=fltarr(nsp)
ezero=fltarr(nsp)

; Pad input stack with unity
s=fltarr(nw+400,nsp)+1.0
win=fltarr(nw+400)
for i=0,nsp-1 do s(200,i)=ss(*,i)
if (blankans eq 'y') then begin
   win(200)=ww
           for i=0,nsp-1 do s(0,i) = 1.-(1.-s(*,i))*win
   endif

; get starting velocities
readsbcm,sbp,data,c
vcalp=reform(data(2,*))
readsbcm,sbs,data,c
vcals=reform(data(2,*))
aest=fltarr(nsp,2)   ; predicted pixel offsets
aest(*,0)=vcalp/dvel
aest(*,1)=vcals/dvel
dest=fix(aest(*,1)-aest(*,0)) ; estimated pixel shifts of sec from pri
 print,dest

; get flux contributions
rp=1./(1.+fr)
rs=fr/(1.+fr)
wm=mean(w)
```

```
zp=fltarr(nsp)
ezp=fltarr(nsp)
zs=fltarr(nsp)
ezs=fltarr(nsp)
ans=' '

; get template spectra
refp=readfits(rfp)
refs=readfits(rfs)

ccftop = fltarr(nsp)
ccfsig = fltarr(nsp)
pixo=fltarr(35,nsp)
gsig=[indgen(100),indgen(100)+300]
; Calculate cc functions
for i=0,nsp-1 do begin
   print,' '
   print,'spectrum number',i

   ; check model normalization
   smod=rp*refp+rs*refs
   ;sratio=ss(*,i)/smod
   ;coeff=poly_fit(w-wm,sratio,1)
   ;srfit=poly(w-wm,coeff)
   srfit=mean(ss(*,i))/mean(smod)

   ; get pixel offset grid
   pixo(0,i)=indgen(35)-17+dest(i) ;11,5*17,8

   ; loop for different offsets
   for j=0,34 do begin ;10*16

      smod=rp*refp+rs*shift(refs,pixo(j,i))
      smod=smod*srfit

      r=fltarr(nw+400)+1.0
      r(200)=smod
      if (blankans eq 'y') then begin
         ;for k=0,nblank-1 do r(blank(0,k):blank(1,k))=1.0
         r=1.-(1.-r)*win
         endif

      ;plot,s(*,i)
      ;oplot,r-0.2,linestyle=1
      ;wait,3
```

```
   crosscoresb2,s(*,i),r,401,fr,f,z,ezerop,ezeros
   ccfmax(j,i)=max(f)
   ccfmin(j,i)=min(f)>0.
   plot,vel,f,xtitle='Delta velocity',ytitle='ccf',yrange=[-0.2,1.0],ystyle=1
   xyouts,-4000.,0.8,' OFFSET = '+string(pixo(j)*dvel,format="(f6.1)")
   wait,0.02

   endfor

ccfsig(i)=stddev(f(gsig))

; determine best offset

; find local maximum
pshcal=(vcals(i)-vcalp(i))/dvel
ipixo=interpol(findgen(35),pixo(*,i),pshcal+[-6.,6.])
ip1=fix(ipixo(0))>0
ip2=fix(ipixo(1))<34
goodpix=ip1+indgen(ip2-ip1+1)
top=max(reform(ccfmax(goodpix,i)))
iptop=ip1+!c
if ((iptop lt 1) or (iptop gt 33)) then begin
   print, ' zero too close to edge of cc function !'
   print, ' returning 0 ...'
   ptop=0.
   ezero=0.
   endif else begin
      ix=iptop
      localmax,pixo(*,i),ccfmax(*,i),ix,x1,x2
      ptemp=interpol(pixo(*,i),findgen(35),[x1])
      ptop=ptemp(0)
      ;  ctest=spline(pixo(*,i),ccfmax(*,i),[ptop])
      ;cmax=ctest(0) ; for ccftop usage below
      ;ctop=ctest(0)-min(ccfmax(*,i))
      ; *** test
      ;  ctop=ctest(0)-mean(ccfmin(*,i))
      ;  good=where(r ne 1.0,neff)
      ;  ezero=-neff*2.*x2*ctop/(1.-ctop^2)
      ;  ezero=1./sqrt(ezero)
      ; Kurtz et al. 1992 expression FWHM=6 pixels
      ;  ezerok=6.0*3./8./(1.+abs(ctest(0)-min(ccfmax(*,i)))/ccfsig(i))
      ;  print, ' sec errors: ', ezero,ezerok
      ;  ezero=ezero<ezerok ; error should not exceed Kurtz estimate
```

```
      endelse

plot,pixo(*,i)*dvel,ccfmax(*,i),xtitle='Secondary Offset', $
   ytitle='Max(ccf)',$
   yrange=[min(ccfmax(*,i)),max(ccfmax(*,i))]
oplot,pixo(*,i)*dvel,ccfmax(*,i),psym=1
oplot,[ptop,ptop]*dvel,[-1,2]
oplot,[vcals(i)-vcalp(i),vcals(i)-vcalp(i)],[-1,2],linestyle=1
azero=' '
read,' Zero weight this secondary measurement (y or [n])? ',azero
if (azero eq 'y') then goto,fsh

answer='n'
read,' Select a different peak and change slope (y or [n])? ',answer
if (answer eq 'y') then begin

   ; local rectification
   print,' Select rectification point to left of peak ...'
   cursor,x1,y1 & wait, 1.
   print,' Select rectification point to right of peak ...'
   cursor,x2,y2
   coeff=poly_fit([x1,x2],[y1,y2],1)
   localfit=poly(pixo(*,i)*dvel,coeff)
   oplot,pixo(*,i)*dvel,localfit
   wait,1.
   ;aa=' '
   ;read,' Press enter to continue ...',aa

   ccfmaxtemp=ccfmax(*,i)-localfit
   plot,pixo(*,i)*dvel,ccfmaxtemp,xtitle='Secondary Offset',$
      ytitle='Max(ccf)',$
      yrange=[min(ccfmaxtemp),max(ccfmaxtemp)]
   oplot,pixo(*,i)*dvel,ccfmaxtemp,psym=1
   ; oplot,[ptop,ptop]*dvel,[-1,2]
   oplot,[vcals(i)-vcalp(i),vcals(i)-vcalp(i)],[-1,2],linestyle=1

   print,' Select new peak ...'
   cursor,xx,yy & wait, 1.
   pixvel=xx/dvel
   pixtop=interpol(findgen(35),pixo(*,i),[pixvel]) ;11*17
   pixtop=fix(pixtop(0)+0.5)
   ix=pixtop
   localmax,pixo(*,i),ccfmaxtemp,ix,x1,x2
   ptemp=interpol(pixo(*,i),findgen(35),[x1])
   ptop=ptemp(0)
```

```
      ;ctest=spline(pixo(*,i),ccfmaxtemp,[ptop])
      ;ctop=ctest(0)
         ; *** test
         ;  ctest=spline(pixo(*,i),ccfmax(*,i),[ptop])
         ;  ctop=ctest(0)-mean(ccfmin(*,i))
      ;  good=where(r ne 1.0,neff)
      ;  ezero=-neff*2.*x2*ctop/(1.-ctop^2)
      ;  ezero=1./sqrt(ezero)
      ; Kurtz et al. 1992 expression FWHM=6 pixels
      ;  ctest=spline(pixo(*,i),ccfmaxtemp,[ptop])
      ;  ezerok=6.0*3./8./(1.+abs(ctest(0))/ccfsig(i))
      ;  print, ' sec errors: ', ezero,ezerok
      ;  ezero=ezero<ezerok ; error should not exceed Kurtz estimate
      oplot,[ptop,ptop]*dvel,[-1,2]
      wait,1.

      endif

   ; run ccf at best offset
fsh:    fshift,refs,ptop,refss
   smod=rp*refp+rs*refss
   smod=smod*srfit

   r=fltarr(nw+400)+1.0
   r(200)=smod
   if (blankans eq 'y') then begin
      ; for k=0,nblank-1 do r(blank(0,k):blank(1,k))=1.0
      r=1.-(1.-r)*win
      endif

   crosscoresb2,s(*,i),r,401,fr,f,z,ezerop,ezeros
   cc(0,i)=f
   zp(i)=dvel* z
   ezp(i)=dvel*ezerop
   zs(i)=dvel*(z+ptop)
   ezs(i)=dvel*ezeros
   if (azero eq 'y') then ezs(i)=-99.

   ff=spline(vel,f,[zp(i)])
   ccftop(i) = ff(0)

   endfor

; write results
print,' '
```

```
print,' Mean of ccftop = ',mean(ccftop)

name = 'makecctwo5.dat'
nameans = 'n'
newname = ' '

read,' Change name of makecctwo5.dat output file (y/[n])? ',nameans
if nameans eq 'y' then begin
           read,'Enter new file name: ',newname
           name = newname
   endif

        openw,2,name
for i=0,nsp-1 do begin
   printf,2,zp(i),ezp(i),zs(i),ezs(i)
   endfor
close,2

return
end

;;;;;;;;;;;;;;;;;;;;;;;;;;;;;;;;;;;;;;;;;;;;;;;;;;;;;;;;;;;;;;;;;;;;;;;;;;;

pro localmax,x,f,ix,x1,x2
; use IDL deriv to find the local max position, curvature
; Input:
; x  = x vector
; f  = y vector
; ix = closest index to max
; Output:
; x1 = position of max
; x2 = second derivative at x1

df=deriv(x,f)
ddf=deriv(x,df)

if (df(ix) lt 0.) then i1=ix-1
if (df(ix) ge 0.) then i1=ix

xint=interpol([i1,i1+1.],[df(i1),df(i1+1)],[0.])
x1=xint(0)
xint=interpol([ddf(i1),ddf(i1+1)],[i1,i1+1.],[x1])
x2=xint(0)

return
```

```
end

;;;;;;;;;;;;;;;;;;;;;;;;;;;;;;;;;;;;;;;;;;;;;;;;;;;;;;;;;;;;;;;;;;;;;;;;

pro crosscoresb2,a,z,n,fr,c,zero,ezerop,ezeros
; cross-correlation with error estimates
; Zucker 2003, MNRAS, 342, 1291
; assumes some padding on ends so that edge effects are negligible
; Uses IDL deriv.pro to find maximum position
; This version for SB2 application with makecctwo5.pro
; Input:
; a     = spectrum to measure
; z     = template spectrum
; n     = number of points in ccf (odd)
; fr    = flux ratio
; Output:
; c     = ccf
; zero  = shift of spectrum from template in pixels
; ezerop = error in shift allocated to primary
; ezeros = error in shift allocated to secondary

; get offsets
n=fix(n)
nd2=fix((n-1.)/2.)
s=indgen(n)-nd2

; form continuum subtracted spectra
ntot=n_elements(a)
fn=a-mean(a)
gn=z-mean(z)
sf2=total(fn^2)/ntot
sg2=total(gn^2)/ntot
sf=sqrt(sf2)
sg=sqrt(sg2)

; form ccf
c=fltarr(n)
for i=0,n-1 do begin
   gns=shift(gn,s(i))
   c(i)=total(fn*gns)/ntot/sf/sg
   endfor
g=[indgen(20),n-1-reverse(indgen(20))]
back=mean(c(g))
c=(c-back)/(1.-back)
```

```
; find peak
top=max(c)
toppix=!C
nlim=n-3
if ((toppix lt 2) or (toppix gt nlim)) then begin
   print, ' zero too close to edge of cc function !'
   print, ' returning 0 ...'
   zero=0.
   ezero=0.
   endif else begin

      ix=toppix
      localmax,findgen(n),c,ix,x1,x2
      ptemp=interpol(s,findgen(n),[x1])
      zero=ptemp(0)
      ctest=spline(s,c,ptemp)
      ctop=ctest(0)
      good=where(z ne 1.0,neff)
      ctopp=ctop/(1.+fr)
      ctops=ctop*fr/(1.+fr)
      ezerop=-neff*2.*x2*ctopp/(1.-ctopp^2)
      ezerop=1./sqrt(ezerop)
      ezeros=-neff*2.*x2*ctops/(1.-ctops^2)
      ezeros=1./sqrt(ezeros)

      endelse
return
end

;;;;;;;;;;;;;;;;;;;;;;;;;;;;;;;;;;;;;;;;;;;;;;;;;;;;;;;;;;;;;;;;;;;;;;;;;;;

pro fshift,ospec,pshift,sspec
; fractional shift
; Input:
; ospec   = observed spectrum
; pshift  = pixel shifts
; Output:
; sspec   = shifted spectrum

np=n_elements(ospec)  ; # pixels

; Weighting factors
is1=fix(pshift)
if (pshift lt 0.) then is2=is1-1 else is2=is1+1
w2=abs(pshift-is1)
```

```
w1=1.-w2

npp=np+1000
rs=fltarr(npp)+1.     ; pad both sides with unity
rs(500)=ospec
cs=w1*shift(rs,is1) + w2*shift(rs,is2)
sspec=cs(500:np+499)

return
end

;;;;;;;;;;;;;;;;;;;;;;;;;;;;;;;;;;;;;;;;;;;;;;;;;;;;;;;;;;;;;;;;;;;;;;;;;;;

pro readstk,wave,stk,times,star,origin
; read in a spectrum stack
; data from *.fits
; header info from *.dat
; last parameter used if origin data is included in *.dat

; get data stack
stk=readfits(star+'.fits',/silent)

; open associated information file
openr,1,star+'.dat'

; get dimensions
readf,1,npix     ; number of spectral pixels
readf,1,nspec    ; number of spectra
npix=long(npix)
nspec=long(nspec)

; get wavelength vector
wave=dblarr(npix)
readf,1,wave

; get times of observations
times=dblarr(nspec)
readf,1,times

; origin data
if (n_params() eq 5) then begin
   origin=intarr(nspec)
   readf,1,origin
   endif
```

```
close,1

   return
end

;;;;;;;;;;;;;;;;;;;;;;;;;;;;;;;;;;;;;;;;;;;;;;;;;;;;;;;;;;;;;;;;;;;;;;;;;;;;

pro readsbcm,file,data,c
;file=' '
;read,' Name of file? ', file
openr,1,file
; get number of observations
j='          '
while (strmid(j,1,9) ne 'NUMBER OF') do readf,1,j
num=fix(strmid(j,17,3))
; get data block
j='                                   '
while ((strmid(j,7,4) ne 'date') and (strmid(j,7,4) ne 'DATE')) do readf,1,j
data=dblarr(7,num)
readf,1,data
for i=1,4 do readf,1,j
c=fltarr(3,100)
readf,1,c
close,1
; Add phase wrap around
ph=fltarr(num)
vo=fltarr(num)
good=fltarr(num)
for i=0,num-1 do ph(i)=data(4,i)
for i=0,num-1 do vo(i)=data(1,i)
for i=0,num-1 do good(i)=data(6,i)
order=sort(ph)
ph=ph(order)
vo=vo(order)
good=good(order)
lo=where(ph lt 0.2,countl)
hi=where(ph gt 0.8,counth)

phw=ph
vow=vo
goodw=good
if (countl gt 0) then begin
   phw=[phw,ph(lo)+1.]
   vow=[vow,vo(lo)]
   goodw=[goodw,good(lo)]
```

```
   endif
if (counth gt 0) then begin
   phw=[ph(hi)-1.,phw]
   vow=[vo(hi),vow]
   goodw=[good(hi),goodw]
   endif

; phw=[ph(hi)-1.,ph,ph(lo)+1.]
; vow=[vo(hi),vo,vo(lo)]
; goodw=[good(hi),good,good(lo)]
c(0,*)=findgen(100)*0.01+0.01
pc=fltarr(100)
vc=fltarr(100)
for i=0,99 do pc(i)=c(0,i)
for i=0,99 do vc(i)=c(2,i)
lo=where(pc lt 0.2)
hi=where(pc gt 0.8)
pcw=[pc(hi)-1.,pc,pc(lo)+1.]
vcw=[vc(hi),vc,vc(lo)]
return
end

;;;;;;;;;;;;;;;;;;;;;;;;;;;;;;;;;;;;;;;;;;;;;;;;;;;;;;;;;;;;;;;;;;;;;;;;;;;

pro tukey,nw,smp,window,w1,w2
; construct a tukey window for smoothing edges
; https://en.wikipedia.org/wiki/Window_function#Spectral_analysis
; Input:
; nw      = pixel width of window
; smp     = smoothing pixel width < nw/2
; Output:
; window  = window function
; w1      = smoothing only on RHS
; w2      = smoothing only on LHS

window=fltarr(nw)+1.
w1=fltarr(nw)+1.
w2=fltarr(nw)+1.
sm=smp<(nw/2.)
nsmp=fix(sm)
for i=0,nsmp-1 do window(i)=0.5*(1.+cos((i/(sm-1.)-1.)*!pi))
for i=nw-nsmp-2,nw-1 do window(i)=window(nw-1-i)

for i=0,nsmp-1 do w2(i)=window(i)
for i=nw-nsmp-2,nw-1 do w1(i)=window(i)
```

```
return
end

;;;;;;;;;;;;;;;;;;;;;;;;;;;;;;;;;;;;;;;;;;;;;;;;;;;;;;;;;;;;;;;;;;;;;;;;;;;;;;;;

pro tukeywindow,blank,nw,smp,ww
; create a combined Tukey window using
; pixels from ccomit file
; assume omit regions are ordered by increasing pixel number
; use before padding with unity
nblank=n_elements(blank(0,*))
ww=fltarr(nw)

; check need for extra window at start
if (blank(0,0) gt smp) then begin
   ; add window region at start
   n1=0
   n2=blank(0,0)
   n=n2-n1+1
   tukey,n,smp,w,w1,w2
   ww(n1)=w1
   endif

; window regions to the right of each blank
if (nblank ge 2) then begin
   for i=0,nblank-2 do begin
      ; next window to right
      n1=blank(1,i)
      n2=blank(0,i+1)<(nw-1)
      n=n2-n1+1
      tukey,n,smp,w,w1,w2
      ww(n1)=w
      endfor
   endif

; check need for extra window at end
if (blank(1,nblank-1) lt (nw-1-smp)) then begin
   ; add window region at end
   n1=blank(1,nblank-1)
   n2=nw-1
   n=n2-n1+1
   tukey,n,smp,w,w1,w2
   ww(n1)=w2
   endif
```

```
return
end

;;;;;;;;;;;;;;;;;;;;;;;;;;;;;;;;;;;;;;;;;;;;;;;;;;;;;;;;;;;;;;;;;;;;;;;;
```

APPENDIX C

Using ELC to Model *Kepler* Light Curves

This appendix outlines the general approach used to fit *Kepler* light curves with ELC. As discussed in Chapter 4, we fit the radial velocities and *Kepler* light curve separately due to the differences in the relative weights of the data. When fitting the radial velocities we fixed the inclination, eccentricity, and longitude of periastron based on preliminary values from the light curve, and the period using the value derived by Gies et al. (2015). The mass ratio (Q), velocity semi-amplitude of the primary (primK), and velocity zero point (gamma velocity) were allowed to vary to find the best solution.

After an optimized solution was found for the radial velocities, we used the derived values to constrain the fit of the light curve. Thus, the mass ratio, velocity semi-amplitude of the primary, and velocity zero point were held fixed. Once the inclination is determined, these values, along with the period, set the scale of the binary (i.e., the semi-major axis is uniquely determined). We also fixed the primary temperature (Teff1) according to the tomography results. The light curve model is then fit for the inclination (finc), temperature ratio (temprat), and fractional radii (frac1, frac2), which sets the sizes of the stars. Solutions converged best when we also fit for the reference epoch ($T_{\rm conj}$), which along with the eccentricity and longitude of periastron set the shape and orientation of the orbit. We initially set the eccentricity and longitude of periastron to zero and 90°, respectively, before allowing them to vary (see Section 4.4.3.1).

In ELC, stellar surfaces are divided up into tiles using a polar coordinate system with N_α

latitude rows equally spaced in angle and $4 \times N_\beta$ longitude points per latitude row equally spaced in angle (Orosz & Hauschildt 2000). When fitting high signal-to-noise light curves like those from *Kepler*, higher precision models requiring more tiles over the stellar surface are needed. We therefore use N_α and N_β values of 60 and 20, respectively. Specific intensities for each surface element are then specified by filter integrated intensities for different values of $T_{\rm eff}$ and $\log g$ at each emergent angle μ (where $\mu = 1$ at the center of the stellar disk and $\mu = 1$ at the stellar limb). For *Kepler* light curves, the specific intensities are calculated using the *Kepler* bandpass and accessed via the U filter position in ELC (icnU). We can also specify the 'dphase' parameter, which is the number of degrees the binary is turned in space while computing light curve points. A value of 0.5 therefore computes light curves for 720 points during one orbit. For KIC 5738698 ($P = 4.808$ days) we used 1.0 or 0.5 for preliminary results, but a 'dphase' value of 0.1 was used for the final fitting as it corresponds to light curves calculated approximately every 10 minutes, which could then be binned into 29.4244 minute intervals to mimic the *Kepler* long cadence data. This binning can be automatically performed by ELC if the 'bin size for light curves' parameter is specified. ELC also corrects the flux at each phase for the contamination present in *Kepler* light curves due to the flux from other stars recorded in the target aperture. The *Kepler* contamination parameter, k, is the fractional level of contamination, reported by the *Kepler* Data Search database at MAST (see Section 4.4.3.1). An example `ELC.inp` file from KIC 5738698 is shown below.

```
 60                Nalph1
 20                Nbet1
  60               Nalph2
 20                Nbet2
0.000000000        fill1
0.000000000        fill2
  1.000000         omega1
  1.000000         omega2
   0.500000        dphase
   0.9612300000    Q
86.33313           finc
  6792.00          Teff1
  6740.54          Teff2
0.067610           Tgrav1
0.068047           Tgrav2
 2.00000           betarim
0.000000           rinner
0.750000           router
30000.0            tdisk
-0.7500            xi
 90                Ntheta
 60                Nradius
0.3300             alb1
0.3300             alb2
 2                 Nref
   0.00100         log10(Lx)
    4.8087739600   Period
 0.32000           fm
      16.74426     separ
   7.622100        gamma velocity
  -5000.00         t3
  -5.00000         g3
   -0.100000       SA3
    0.000000       density in g/cc
    0.000000       onephase
    3.450000       usepot1
    2.860000       usepot2
 55691.815575666   T0
0                  idraw
1                  iecheck
0                  idint
1                  iatm
1                  ism1
1 0 0 0 0 0 0 0    icnU,icnB,icnV,icnR,icnI,icnJ,icnH,icnK
0                  iRVfilt
```

```
0                   ionephase
0                   isquare
0                   iusepot
0                   ifixgamma (currently inactive)
 2                  ilaw  (1=linear law, 2=logarithmic law,
                           3=square root law, 4=quad law,
                           >10 for power series)
 3600.0    0.6617  0.1455  0.6523  0.1328  0.6674  0.2152  0.6618  0.1764
 4500.0    0.6350  0.2420  0.6350  0.2420  0.0000  0.0000  0.0000  0.0000
 5550.0    0.6710  0.1950  0.6710  0.1950  0.7240  0.2633  0.7240  0.2633
 6700.0    0.6350  0.2420  0.6350  0.2420  0.0000  0.0000  0.0000  0.0000
 8700.0    0.6710  0.1950  0.6710  0.1950  0.0000  0.0000  0.0000  0.0000
12000.0    0.6350  0.2420  0.6350  0.2420  0.0000  0.0000  0.0000  0.0000
16200.0    0.6350  0.2420  0.6350  0.2420  0.0000  0.0000  0.0000  0.0000
22000.0    0.6350  0.2420  0.6350  0.2420  0.0000  0.0000  0.0000  0.0000
0.00067780          eccentricity
  51.08260000       argument of peristron in degrees
 0.00000000         pshift
    0.000000        asini (projected semimajor axis in seconds)
    0.000000        median fit (geneticELC only)
    0.000000        sw7 (currently inactive)
    0.000000        sw8 (currently inactive)
    0.000000        sw9 (currently inactive)
0                   ikeep (1 to put eclipse at phase 0.0)
0                   isynch (1 to keep rotation synchronous at periastron)
0                   ispotprof
3                   igrav
1                   itime
   200              MonteCarlo (0 for interpolation, >10 for Monte Carlo)
0                   ielite
-1.0000000          Temperature factor spot 1, star 1
 -1.0000000         Latitude of spot 1, star 1 (degrees)
 -1.0000000         Longitude of spot 1, star 1 (degrees)
 -1.0000000         Angular radius of spot 1, star 1 (degrees)
-1.0000000          Temperature factor spot 2, star 1
 -1.0000000         Latitude of spot 2, star 1 (degrees)
 -1.0000000         Longitude of spot 2, star 1 (degrees)
 -1.0000000         Angular radius of spot 2, star 1 (degrees)
-1.0000000          Temperature factor spot 1, star 2
 -1.0000000         Latitude of spot 1, star 2 (degrees)
 -1.0000000         Longitude of spot 1, star 2 (degrees)
 -1.0000000         Angular radius of spot 1, star 2 (degrees)
-1.0000000          Temperature factor spot 2, star 2
 -1.0000000         Latitude of spot 2, star 2 (degrees)
 -1.0000000         Longitude of spot 2, star 2 (degrees)
```

```
 -1.0000000         Angular radius of spot 2, star 2 (degrees)
-1.0000000          Temperature factor spot 1, disk
 -1.0000000         Azimuth of spot 1, disk (degrees)
 -1.0000000         Radial cutoff of spot 1, disk (0 <= r_cut <=1)
 -1.0000000         Angular size of spot 1, disk (degrees)
-1.0000000          Temperature factor spot 2, disk
 -1.0000000         Azimuth of spot 2, disk (degrees)
 -1.0000000         Radial cutoff of spot 2, disk (0 <= r_cut <=1)
 -1.0000000         Angular size of spot 2, disk (degrees)
  0.000000000       primmass (star 1 mass in solar masses)
  86.199200000      primK (K-velocity of star 1 in km/sec)
   0.000000000      primrad (star 1 radius in solar radii)
     0.000000000    ratrad (ratio of star 1 radius and star 2 radius)
0.109701225000      frac1 (fractional radius star 1: R_1/a)
0.102688726018      frac2 (fractional radius star 2: R_2/a)
 0.000000000        ecosw (phase difference between eclipses)
 0.9924238          temprat (T_2/T_1)
0                   idark1
0                   idark2
     0              Npoly (0 for numerical)
0                   ifasttrans (>0 for fast transit mode)
0                   ialign (0 for rotation aligned with orbit)
1                   ifastgen (1 for fast genetic mode)
0                   isw23 (currently inactive)
5                   frac switch (>1 to enable ELCratio.???? files)
 0.0000  0.0000  0.0000  0.0000  0.0000  0.0000  0.0000  0.0000  0.0000
 0.0000  0.0000  0.0000  0.0000  0.0000  0.0000  0.0000  0.0000  0.0000
 0.0000  0.0000  0.0000  0.0000  0.0000  0.0000  0.0000  0.0000  0.0000
 0.0000  0.0000  0.0000  0.0000  0.0000  0.0000  0.0000  0.0000  0.0000
 0.0000  0.0000  0.0000  0.0000  0.0000  0.0000  0.0000  0.0000  0.0000
 0.0000  0.0000  0.0000  0.0000  0.0000  0.0000  0.0000  0.0000  0.0000
 0.0000  0.0000  0.0000  0.0000  0.0000  0.0000  0.0000  0.0000  0.0000
 0.0000  0.0000  0.0000  0.0000  0.0000  0.0000  0.0000  0.0000  0.0000
 86.4700000         axis_I (inclination of rotation axis if ialign=1)
  0.0000000         axis_beta (angle of rotation axis wrt to orbit if ialign=1)
      0.0000000     t_start
      0.0000000     t_end
 0.0000000           asini error
0.00000000          reference phase for disk fraction
0.00000000          radfill1 (set to use fill1 in terms of R_eff
0.00000000          radfill2 (set to use fill2 in terms of R_eff
   29.4244          bin size for light curves (minutes)
    0.0000          bin size for RV curves (minutes)
0.0150000           Kepler contamination
 55692.33477000     Tconj
```

```
0.00                beam1 (Doppler boost factor, star 1)
0.00                beam2 (Doppler boost factor, star 2)
0                   isw25 (currently inactive)
0                   isw26 (currently inactive)
     0              Nterms for fast analytic
1                   set to 1 to fit for Tconj
0                   set to 1 to fit for e*cos(omega), e*sin(omega)
0                   isw30 (currently inactive)
0                   isw31 (currently inactive)
0                   isw32 (currently inactive)
0                   isw33 (currently inactive)
0                   isw34 (currently inactive)
  0.00000000        e*cos(omega)
  0.00000000        e*sin(omega)
  0.00000000        sw42 (currently inactive)
  0.00000000        sw43 (currently inactive)
  0.00000000        sw44 (currently inactive)
  0.00000000        sw45 (currently inactive)
  0.00000000        sw46 (currently inactive)
  0.00000000        sw47 (currently inactive)
  0.00000000        sw48 (currently inactive)
  0.00000000        sw49 (currently inactive)
```

The second input file used by ELC is `gridloop.opt`, which specifies which parameters are being fit and the parameter ranges and/or the number of iterations depending on the type of optimizer used. First, the names of the files with the light and/or radial velocity curves to be fit are listed in order of the Johnson filter (U, B, V, R, I, J, H, K) the data correspond to. As mentioned above, the U filter has been replaced with the *Kepler* bandpass in this version of ELC, so we list the light curve file there. The light curve can be given in Julian dates or phases, with the 'itime' parameter in `ELC.inp` set to 1 for Julian dates. The next two lines are used for the radial velocity files for the primary and secondary. Next, the number of parameters to be fit is specified, followed by the ELC names for each parameter. The next part is specific to the optimization routine used. For the genetic algorithm used in this

dissertation, the minimum and maximum values for each of the fitted parameters are given in three columns. In the first two lines, the third column specifies how many generations to explore for the best fit and how many members in each generation, in the remaining lines the third column is set to 1. An example file for KIC 5738698 is shown below.

```
5738698lctmag.txt
none
none
none
none
none
none
none
none
none
 9
temprat
eccentricity
l1
q1
inclination
l1
argper
q2
Tconj
     0.9918000000     0.992800000        100
     0.0003000000    0.0015000000        100
     0.3000000000    0.3800000000          1
     0.1095000000     0.112000000          1
    86.100000000     86.500000000          1
     0.3000000000    0.3800000000          1
     45.000000000    80.000000000          1
     0.1000000000     0.103900000          1
  55692.000000000  55692.60000000          1
```

The outputs from ELC are extensively recorded in a variety of output files. The fitted parameter values and chi-squared statistics from each iteration are recorded in `generation.1000###` files, while astrophysical parameters, such as the mass and radius of each star, and chi-squared statistics for each fit are recorded in `ELCparm.1000###` files. Also computed are the best-fit light (and/or radial velocity) curves, output in the files `modelU.linear` and `modelU.mag` for the *Kepler* bandpass, as well as `ELCdataU.fold`, which contains the input data folded to the current best-fit model.